

UC Berkeley

UC Berkeley Electronic Theses and Dissertations

Title

Slow Magnetic Relaxation in f-Element Complexes: A Tale of Dipolar Interactions, Symmetry, and Magnetic Hysteresis

Permalink

<https://escholarship.org/uc/item/9j83c940>

Author

Meihaus, Katie Ruth

Publication Date

2015

Peer reviewed|Thesis/dissertation

Slow Magnetic Relaxation in f-Element Complexes:
A Tale of Dipolar Interactions, Symmetry, and Magnetic Hysteresis

by

Katie Ruth Meihaus

A dissertation submitted in partial satisfaction of the

requirements for the degree of

Doctor of Philosophy

in

Chemistry

in the

Graduate Division

of the

University of California, Berkeley

Committee in charge:

Professor Jeffrey R. Long, Chair
Professor Richard A. Andersen
Professor Alessandra Lanzara

Spring 2015

Slow Magnetic Relaxation in f-Element Complexes:
A Tale of Dipolar Interactions, Symmetry, and Magnetic Hysteresis

© 2015

Katie Ruth Meihaus

Abstract

Slow Magnetic Relaxation in f-Element Complexes:

A Tale of Dipolar Interactions, Symmetry, and Magnetic Hysteresis

by

Katie Ruth Meihaus

Doctor of Philosophy in Chemistry

University of California, Berkeley

Professor Jeffrey R. Long, Chair

This dissertation describes the results of research into some of the subtle and not-so-subtle factors that govern slow magnetic relaxation in lanthanide and actinide complexes. Single-molecule magnetism is only now entering its third decade, while the lanthanides and actinides in particular have only been a part of the field for about the last decade and half a decade, respectively. Within this time, the study of slow magnetic relaxation in f-element systems has proven to be a rich and complex area of research. *Chapter 1* sets out to provide some historical context for the state of the f-elements in the field today as well as to highlight some of the most impressive systems in the literature. Some of the themes introduced in Chapter 1 will be relevant to the research discussed in subsequent chapters.

Chapter 2 describes the detailed magnetic characterization of $\text{U}(\text{H}_2\text{BPz}_2)_3$, only the second actinide molecule found to exhibit slow magnetic relaxation, in magnetically dilute form. The results of variable-temperature and variable-field ac susceptibility measurements reveal that dipolar interactions are implicit in speeding up molecular slow relaxation and also facilitate very slow intermolecular relaxation that leads to magnetic hysteresis at low temperatures. When placed in the context of some relevant literature, the results of this study suggest that the intermolecular relaxation and observed hysteresis may be unrecognized, though common, phenomena among low-nuclearity U^{III} molecules exhibiting slow magnetic relaxation.

Chapter 3 describes a detailed study of the role of donor atom influence and dipolar interactions on slow magnetic relaxation in two series of uranium and lanthanide compounds with nitrogen and carbon donor atoms, respectively. Through a combination of magnetic susceptibility characterization and lanthanide $M_{5,4}$ -edge XANES, EPR, and ^1H NMR spectroscopies, it is found that the carbon donor facilitates slower magnetic relaxation for all metal ions in the investigated temperature and frequency range. Thus, in addition to symmetry, the identity of the donor atom is revealed to be another tunable parameter in the design of f-element complexes exhibiting slow magnetic relaxation.

Chapter 4 describes full magnetic characterization of concentrated and magnetically dilute samples of the bis(cyclooctatetraenide) complex $[\text{Er}(\text{COT})_2]^-$. The high symmetry ligand field afforded by the two COT^{2-} groups leads to exceptionally slow magnetic relaxation for Er^{III} , with magnetic blocking at 9.25 K and magnetic hysteresis as high as 10 K. Magnetic dilution also

leads to an unprecedented opening of the hysteresis loop for this molecule at low temperatures, demonstrating that dipolar or intermolecular interactions can affect slow magnetic relaxation in some anomalous ways, by analogy with Chapter 2.

Finally, *Chapter 5* changes gears slightly and investigates slow magnetic relaxation in the series of N_2^{3-} radical-bridged complexes $\{[(Me_3Si)_2N)_2Ln(THF)]_2(\mu-N_2)K\}$ (for $Ln = Gd^{III}, Tb^{III}, Dy^{III}$). Inner-sphere coordination of the K^+ counter-ion in these complexes leads to bending of the Ln-radical-Ln unit, which is planar in the previously reported parent complexes $\{[(Me_3Si)_2N)_2Ln(THF)]_2(\mu-N_2)\}^-$ exhibiting an outer-sphere potassium ion. While the parent complexes hold records for both blocking temperature and magnetic coupling strength, bending of the core in $\{[(Me_3Si)_2N)_2Ln(THF)]_2(\mu-N_2)K\}$ introduces non-negligible intramolecular lanthanide-lanthanide coupling that competes with the lanthanide-radical interaction. This competition results in depressed magnetic moments and faster magnetic relaxation for the anisotropic lanthanides, revealing that even a seemingly simple counter-ion can be used to tune slow magnetic relaxation.

Table of Contents

Acknowledgements.....	iii
Dedication.....	viii
Chapter 1: An Introduction to the Lanthanides and Actinides in Single-Molecule Magnetism 1	
Section 1.1. Introduction.....	2
Section 1.2. Characterization of Slow Magnetic Relaxation in Molecules.....	5
Section 1.3. The f-Elements in Single-Molecule Magnetism.....	8
Section 1.4. Lanthanide Single-Ion Anisotropy in Molecular Magnetism.....	10
Section 1.5. Actinides in Single-Molecule Magnetism.....	19
Section 1.6. Slow Magnetic Relaxation and Exchange in Multinuclear Actinide Complexes.....	27
Section 1.7. Conclusions and Outlook.....	30
Section 1.8. References.....	31
Chapter 1 Appendix.....	42
Chapter 2: The Role of Dipolar Interactions in Slow Magnetic Relaxation in the Trigonal Prismatic Complex $U(H_2BPz_2)_3$ and Relevance for other Actinide Compounds 43	
Section 2.1. Introduction.....	44
Section 2.2. Experimental Section.....	46
Section 2.3. Results and Discussion.....	47
Section 2.4. Conclusions and Outlook.....	53
Section 2.5. Acknowledgements.....	53
Section 2.6. References.....	53
Chapter 2 Appendix.....	56
Chapter 3: Influence of Pyrazolates vs <i>N</i>-Heterocyclic Carbene Ligands on the Slow Magnetic Relaxation of Homoleptic Trischelate Lanthanide(III) and Uranium(III) Complexes 61	
Section 3.1. Introduction.....	62
Section 3.2. Experimental Section.....	63
Section 3.3. Results and Discussion.....	67
Section 3.4. Conclusions and Outlook.....	82
Section 3.5. Acknowledgements.....	83
Section 3.6. References.....	83
Chapter 3 Appendix.....	89
Chapter 4: Magnetic Blocking above 9 K in Salts of the Bis(η^8-cyclooctatetraenide) Complex $[Er(COT)_2]^-$ 119	
Section 4.1. Introduction.....	120
Section 4.2. Experimental Section.....	120
Section 4.3. Results and Discussion.....	123
Section 4.4. Conclusions and Outlook.....	130
Section 4.5. Acknowledgements.....	131
Section 4.6. References.....	131

Chapter 4 Appendix	134
Chapter 5: Influence of N Inner-Sphere K^+ Ion on the Magnetic Behavior of N_2^{3-} Radical-Bridged Dilanthanide Complexes	142
Section 5.1. Introduction.....	143
Section 5.2. Experimental Section	143
Section 5.3. Results and Discussion	144
Section 5.4. Conclusions and Outlook	151
Section 5.5. Acknowledgements.....	151
Section 5.6. References.....	152
Chapter 5 Appendix	154

Then how should I begin?...¹

It has taken nearly six years to get three little letters after my name. Six years represents many things, for instance: 1) just under $\frac{1}{3}$ of my age at the start of the PhD; 2) the average life-expectancy of a scorpion; 3) the amount of time it would take to sail around the world 48 times; 4) only 6% of the average life expectancy of a Monegasque;² and 5) 0.12% of the age of the world's oldest tree. Nothing I have been able to accomplish in this time, inexplicably both too long and too short, would have been possible without the support of an army of people.

I am grateful to my advisor Prof. Jeff Long for many things, not the least of which has been the opportunity to work in his lab, on a project I have loved, pursuing different avenues with more or less complete independence. Jeff has a great drive for doing creative chemistry and doing it extremely well. His admirably high standards have motivated me to seek excellence in all areas of research and take pride even in seemingly little things, like an aesthetically pleasing presentation or table of contents graphic. In addition to the science, I will take away some other fond memories with Jeff: e.g. smoking Swisher Sweets outside of Lewis Hall; his moral support in beer chugging contests; football games at Tilden Park; and group outings where his generosity made food and beer bountiful. Of late as I have toggled between future directions, Jeff has remained patient and supportive and this has also been a gift. I want to also acknowledge Jen Long – she is a wonderful person and every year endures 30+ people in the Long home over the course of 12 solid hours for the group holiday party, one of my favorite times of the year.

Before Jeff, there was my undergraduate advisor Trevor Hayton at UC Santa Barbara, a new professor when I joined his group in 2007. Many of the skills I took to Berkeley – including some grounding in and excitement for uranium chemistry, familiarity with air-free chemistry, and an appreciation for NMR spectroscopy – I learned directly from Trevor. He has continued to be a support throughout my PhD.

My parents, Terry and David, have been a constant source of encouragement and have lent their ears and hearts numerous times when I have needed to talk, or rant, or cry. I would not have made it through without their support. I am indebted to many other people in my family, immediate and extended, because at one point or another each has offered their love and encouragement. In particular, I want to thank my Aunt Cis, who has been a staunch support for as long as I can remember, and was the sole reason I even applied to and went to college. Even before this, a small seed was planted by my teacher for first semester online high school chemistry, Mrs. Rathbun, who told me she thought I had a knack for the subject. Without the encouragement of both these women, I would not be where I am today.

Three senior graduate students from the group offered their guidance, example, and seemingly boundless wisdom in the ways of magnetism. Dave Harris was a great resource when it came to all manner of science and graduate school insights, and I will fondly remember the few times I (nearly) beat him in beer chugging contests. An immense amount of what I learned my first two years, including general molecular magnetism, how to write a paper, and how to think about f-element electronic structure, was due in large part to Jeff Rinehart. Jeff's creative approach to chemistry (and the world, well-illustrated through some awesome and incredibly strange drawings) is something I have aspired to. I also learned from Jeff how useful Photoshop can be, both as a tool for improving manuscript graphics and as an artistic outlet. Joe Zadrozny, a softy with a crusty demeanor, had a huge impact in my time here. I am indebted to him for many things, including his wisdom in magnetism and all things SQUID-related and the time he spent

editing my early writing. Joe is also a great friend, and his encouragement and advice during some frustrating and transformative times have helped me to keep a level head.

I have been especially fortunate to share five plus years of grad school with the cohorts in my year Eric, Xioawen, and Dana. There is no small probability I would be leaving here in a straight jacket, sans degree, had it not been for the company of Eric Bloch. I have met few people as dedicated and loyal to those in their life, and to their work, as this guy. I am grateful for his friendship and his daily wisdom and calm, and for really stressful days when he would either hand me a piece of dry ice to smash into his lab bench (surprisingly satisfying if done correctly), or a shot of peppermint schnapps. He has gone on to excel as a post-doc and I am excited to see what is in store for him in the future. I am also grateful for his wife, Lynn, and her friendship. She is a phenomenal traveling companion, and we spent many relaxing baking extravaganzas together around Thanksgiving and Christmas. The rest of their family, Atom, Tinker, and Hoppy, also afforded a catharsis I think only four- (or three-) legged, furry creatures can.

Xiaowen Feng is a knowledgeable magnetochemist and something of an artist when it comes to recrystallization. He has succeeded in taking his science in some very creative and prosperous directions, and this has been motivating in my own research. He also introduced me to hot pot and grilled chicken hearts with coriander, both of which are delicious. It has been great to get to know Dana Levine over the years and to witness her dedication, persistence, and success as she has forged new ground in our group, pursuing bioinorganic chemistry in a lab of bio novices. Her positive outlook has been such an encouragement to me, and she can rock out impressively to AC/DC and Led Zeppelin.

The Long group was a bit dude-heavy when I joined in 2009 and Zoey Herm's presence was a boon. Zoey came to be a wonderful desk mate and friend, and I have immense admiration for her dedication to her science and perhaps more, her drive to apply it to benefit those outside of the academic sector. Many conversations with Zoey shaped how I have thought about grad school, how I handled shitty days, and how I kept perspective. She takes a genuine interest in others and throughout her PhD maintained an impressive work-life balance that I am still striving for. I also learned from her the magical powers of keeping a bag of chocolate chips handy.

For my first few months in lab I thought Brian Wiers was completely insane, but over the last six years I have come to know him as an exceptionally creative and talented scientist and a kindred spirit. I think I also understand now, in part, his urge to run barreling down an empty hallway in Lewis or Latimer. I have learned much from Brian, from a fantastic pep talk outside of Kips late one evening in my formative years, to random discussions about science, religion, and equal wealth distribution. His calmly-given perspective has often left me re-evaluating my own for the better. Additionally, no group clean up will be as memorable as the time he donned a full-body white lab suit, taped it around his ankles, wrists, and neck, and left only a small opening for an inlet of air.

I am glad my last few years have brought Tom McDonald as a desk mate – we have shared many a mutually frustrated rant over crap like paper or thesis formatting and proposal writing, and he has offered insightful feedback when I have needed to spew thoughts about the future. He has an intensity and certainty in his approach to science that I admire, and is also a well-spring of advice about travel and good places around the Bay Area for food and beer.

The entering students in 2010 were Jarad Mason, David Zee, and Jordan Axelson. Jarad and Eric used to have a contest to see who could get to lab first every morning (and before anyone else), and to my knowledge Jarad often won this contest. Even after Eric graduated, Jarad has managed to be one of the first, if not the first, into lab every day, even on the weekends. This is

one small example of the kind of dedication he puts into his work. I am also grateful to Jarad for lending an ear and his advice many times within the last year as I have wrestled with next steps, and for his bountiful candy drawer, which has also been instrumental in maintaining my sanity. My most poignant memory of David Zee will be the many times he has wandered into the group room with nothing but a long “Sigggghh” escaping from his mouth. It is an evocative declaration that I think many of us can relate to. David is a fun guy with impeccable taste in plaid and brightly colored pants. I admire his enthusiasm for science and his success in catalysis, arguably one of the more challenging areas in lab. Pet sitting for his affectionately demanding cat, Florence, has also satiated my occasional desire for a furry friend. Jordan Axelson is another kindred spirit and her friendship has been a rock over these years. I can talk with her about pretty much anything under the sun and receive thoughtful and non-judgmental feedback. She also introduced me to one of the greatest bands of all time, Con Bro Chill. In many ways I would not be who I am today without her friendship. Of late, many Sunday evenings have been spent relaxing in her company, usually with some wine or ice cream, making Monday feel pretty approachable. Jordan is a dedicated chemist with a passion for improving the way science is taught and brought to the masses, and I think if anyone has a shot at being the “Neil deGrasse Tyson of Chemistry,” it is this gal.

Fall of 2011 brought Dianne Xiao, Miguel Gonzales, and Mike Aubrey blazing through, and I have found them to be some of the most diligent and dedicated in lab. Dianne is balls to the wall with her chemistry, and I think one of the hardest working persons in the group. Along with Jarad, Dianne is one of the first to Lewis Hall in the mornings and often one of the few remaining in the later evening. She is a bit of a firecracker, and may try to distract you with the occasionally well-delivered sarcasm or amusingly biting remark, and I also see her as one of the most genuine and thoughtful in lab. For such a petite individual, she can also hold her liquor astoundingly well. Miguel is a wizard at solving crystal structures and thinks deeply about his chemistry, and I am grateful for his thoughtful input on a number of occasions when I have been wrestling through topics both within and outside of chemistry. He often speaks up at group meetings with insightful questions or suggestions, and cares equally about the group’s recreational success as evidenced by his invention of a mean cocktail that is deliciously fruity and deceptively strong. Mike is an incredibly intelligent and talented guy, and takes a quiet and observant approach with his science. I think he must also hold the record for most proposals written as a graduate student in the group. Talking with Mike has been encouraging on a number of occasions and I have felt a strong sense of camaraderie with him when the plight of grad school or general frustrations of academia have felt particularly acute.

After this year, the fate of the magnetism subgroup will rest predominantly in the hands of graduate students Lucy Darago and Philip Bunting, who joined the group in 2012 along with Matt Kapelewski and Douglas Reed. All of them have been a joy to have around, and I have shared some entertaining lunchtime and druntime conversations with Doug and Matt. When Lucy joined the lab, there was talk that she was the new version of me, deriving from the fact that she also hails from UCSB, is petite, blonde, blue-eyed, and studying magnetism. This is about as far as the comparison goes, however, as Lucy has already distinguished herself as a far superior scientist in many ways. She has tackled lanthanide chemistry with abandon and new insights, part of a general fearlessness in her approach to research that will serve her well. Aside from the science, Lucy has great energy and takes a genuine interest in others and I am grateful for her friendship. Phil reminds me in some ways of Joe, not simply because his space and desk used to belong to Joe, (or because he still keeps a stash of random solvents and reagents in

bombs in a special drawer), but because of his quiet, intense manner of working and the methodical way he approaches his chemistry. He is also the most fearless with a Schlenk line out of the entire magnetism cohort. Phil and I have had many magnetism conversations, and I have benefited from his perspective. He is working diligently to carry the torch of transition metal magnetism, and I am excited to see where his research takes him.

Many hard-working undergraduates have spent their early research years in the group, but David Gygi is leaving a legacy that will be hard to beat. I have had the privilege of overlapping with him throughout his four years here, and the time and energy he has invested into research puts many grad students (me included) and post-docs to shame. Gygi is an incredibly talented guy with perhaps an unreasonably level head, and a devotion to his science that is matched by a genuine interest in and desire to serve others, I think a rare combination. I am looking forward to seeing where his PhD takes him.

One of many visiting researchers to come through the lab was Valentina Columbo (now Prof.), who was here just six months and became a wonderful friend. She was a source of wisdom and encouragement as I was adjusting to life in graduate school, and her wedding in Como, Italy afforded my first excuse to travel to Europe.

Kathy Bean, Jeff's administrative assistant of many years, was an incredible resource. Whether doing something as simple as shipping a chemical or as complicated as putting together an NSF proposal, her knowledge and support made these tasks a relative breeze. I will fondly remember her stories from working in government, her penchant for eating ice in the afternoons, and amusing interactions brought on by the fact that she is slightly hard of hearing. Additionally, she offered some perhaps generally useful life wisdom, after I asked what she was looking forward to doing in her retirement. I can only paraphrase, but she expressed: after working for the last 50 or so years of her life, she was looking forward to having to do *absolutely nothing*. When I retire, I plan to do it like Kathy.

More recently, Julia, Mercedes, Rodi, Jon, Kristen, and Rebecca have joined the ranks. Their presence as well as their energy and enthusiasm for research have been heartening in my old and sometimes embittered state. I have also crossed paths with a number of awesome post-docs during my time here. I would not be who I am today were it not in part for Elizabeth Montalvo, a fantastic person and chemist. Working with Elizabeth was instrumental in helping me see where I could be more patient and take things in stride, habits that are useful to practice certainly in science but also life in general. Jeff van Humbeck introduced me to the subtle euphoria brought on by hummus spiced with cumin, and was full of good (non-chemistry) book recommendations. Michael Nippe was always a joy to talk with, and would let me bum the occasional cigarette. I am glad to have had his feedback both in matters of science and steps beyond the PhD. Selly Demir is a phenomenal synthetic chemist, and has been generous with her advice and encouragement over many occasions when the future has seemed opaque. Keith (Benjamin) Keitz has been a great addition to the group and a gracious, if unwitting, sounding board for some of my runaway mental processes. Alexander Tskhovrebov has become a fast and close friend. It has been nice to engage with a new person about magnetism and to share some of the knowledge bouncing around in my head. Much time spent in his company has been a breath of fresh air while shedding helpful light as I hunt for new perspective and direction.

A number of others outside of the group have offered their support on this trek. Shane Yost's friendship will always be dear to me, and it was in huge part because of him that I survived my first year. It has been wonderful having two friends from UCSB, Yael Itzkowitz and Amanda Wahnich, in the Bay Area in the last few years. Their friendships have stuck the test of time, and

stealing away from Berkeley and the lab on occasion to spend time with them has facilitated some much needed mental recuperation.

In the department, Prof. Dick Andersen has been an unofficial mentor, and his stalwart dedication to leaving no ends untied in his chemistry has influenced the way I approach my own. I have had numerous enjoyable discussions with him about what is important in science and I will remember these fondly. I have also been fortunate to learn from Wayne Lukens at Lawrence Berkeley Lab. Wayne's knowledge of lanthanide and actinide chemistry, electronic structure, and EPR is extensive. Throughout the course of a lengthy collaboration and even after, he has been incredibly patient and generous with his time. I have come to a deeper understanding of my work through our interactions. I am also grateful to have collaborated with Stefan Minasian at LBL. His insights into some of the research in this document, manuscript writing, his patience, and general wisdom about graduate school and beyond have been a blessing. Without his support, a large portion of my PhD efforts would not have seen the light of day.

Six years here has also given me a lot of time to break glassware and in doing so I was able to meet and befriend Jim Breen, the resident glass blower in the Chemistry Department. It has been enjoyable to talk with him on numerous occasions, to have his perspective about what exists beyond the academic bubble, and to bug him to eat my extra baked goods. I have also personally consumed some few thousand liters of liquid helium while here, which has brought me to know Kinfe Lita in the Liquid Air Plant. He is a selfless and grounded individual with a wild laugh, and chatting with him is always a pleasure. Finally, messing around with uranium chemistry introduced me to Jeff Cromwell, a campus radiation safety specialist. Jeff has been great fun to interact with and transformed the once-dreaded experience of biannual rad safety surveys.

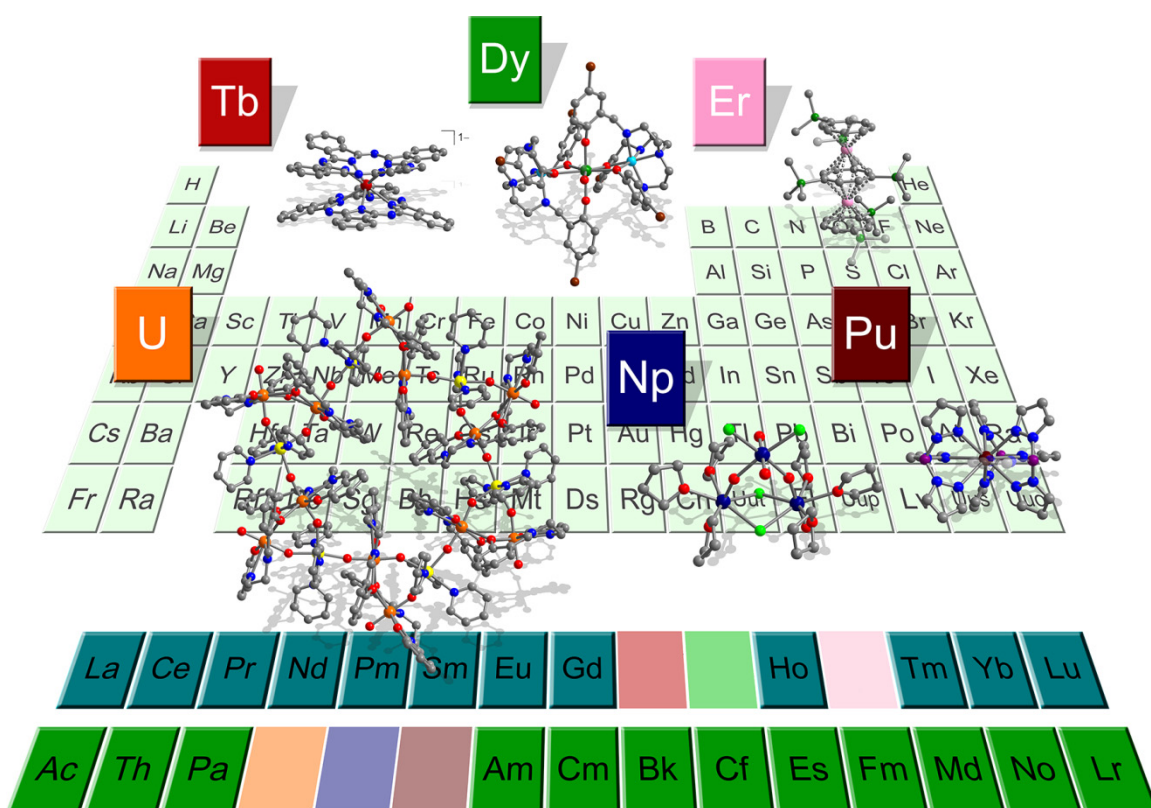
I could continue this section indefinitely, but might then miss the filing deadline. At the risk of waxing too much on the mushy side of things: even more than the science, I feel like grad school has catalyzed a life-long learning process (emphasis on life-long) that is teaching me how to embrace others and approach every aspect of life. This is perhaps what I am most grateful for, and the learning opportunity remains boundless. I am particularly fond of this quote from Kurt Vonnegut that I thought might provide a decent, if abrupt, end to this ridiculous tome of acknowledgments. In some ways it sums up the plight of grad school, and the support and love I have felt from so many:

“Many people need desperately to receive this message: ‘I feel and think much as you do, care about many of the things you care about, although most people do not care about them. You are not alone.’”

- (1) ...*To spit out all the butt-ends of my days and ways?* – T.S. Eliot, from The Love Song of J. Alfred Prufrock, a masterpiece on the human condition and perhaps my favorite poem.
- (2) Incidentally, as of 2014, Monaco had the highest life expectancy of any country in the world. In the same estimate, the US fell at #42, below Andorra (#7), Iceland (#20), and the Faroe Islands (#34) (source: www.cia.gov).

Dedicated to
Mom, Dad, Sister, and Brothers
Family and Friends

Chapter 1: An Introduction to the Lanthanides and Actinides in Single-Molecule Magnetism



1.1 Introduction

Magnetic phenomena have fascinated scientists ever since the discovery by the ancient Greeks that a peculiar kind of stone from the island of Magnesia exerted an inexplicable attractive force on iron.¹ The twentieth century was the stage for the development of the theory of magnetism and the best permanent magnets known today, which can be characterized by their propensity to display magnetic hysteresis, a phenomenon that has been exploited in systems ranging from wind-turbines and electric motors to computer hard drives. The most commonly used materials largely consist either of extended metal oxides such as magnetite (Fe_2O_3) or transition metal lanthanide solids ($\text{Nd}_2\text{Fe}_{14}\text{B}^2$ and SmCo_5^3) wherein the large magnetic anisotropies of the 4f ions couple with transition metals via itinerant electrons to generate incredibly hard magnets.

Around the same time, interest was growing in the area of molecular magnetic materials. Here, the motivation was a “bottom-up” design approach – that is by first controlling the spin of a molecular cluster unit, such clusters could be assembled together to form bulk materials with more synthetic control than solid state techniques would allow. In 1993, one of these clusters $\text{Mn}_{12}\text{O}_{12}(\text{CH}_3\text{COO})_{16}(\text{H}_2\text{O})_4$ was found to display magnetic hysteresis to 3 K due to the slow magnetic relaxation through an energy barrier, U , determined by the electronic structure of the isolated molecule (Figure 1.1).⁴ Magnetic hysteresis was a phenomenon previously unheard of in discrete systems and this discovery sparked the development of the field known as single-molecule magnetism. Owing to their unique amalgamation of bulk and nanoscale properties and their highly tunable nature, single-molecule magnets are often touted as possible replacements for bulk magnets in a variety of applications^{5,6} such as spintronic⁷ or quantum computing devices.⁸ Recent work suggests that such ideas do not necessarily present impossible goals, though single-molecule magnetism is still very exploratory in nature and the synthesis and characterization of new molecules is the bread and butter of current research.

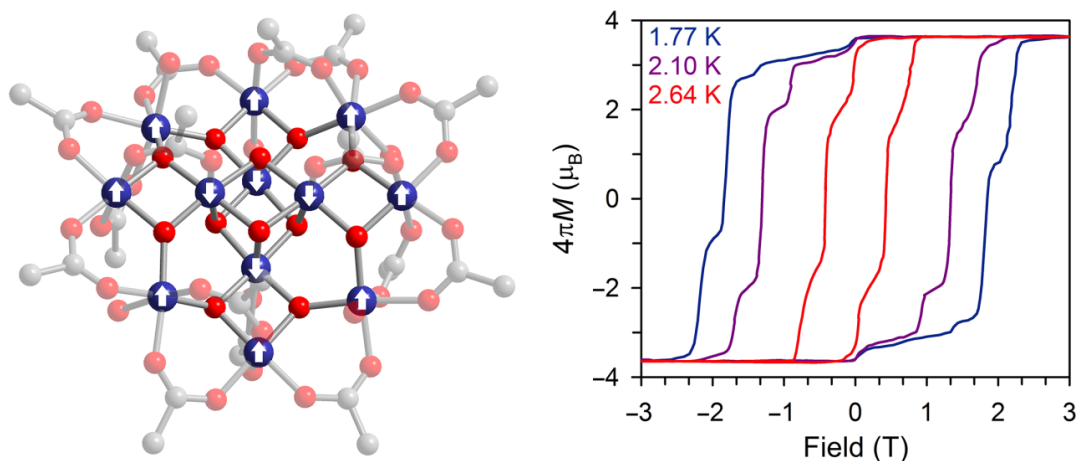


Figure 1.1. (Left) Molecular structure of the first single-molecule magnet, $\text{Mn}_{12}\text{O}_{12}(\text{CH}_3\text{COO})_{16}(\text{H}_2\text{O})_4$. Blue, red, and grey spheres represent $\text{Mn}^{\text{III}}/\text{Mn}^{\text{IV}}$, O, and C atoms, respectively. Hydrogen atoms have been omitted for clarity. The central four $S = 3/2$ Mn^{IV} centers couple antiferromagnetically through oxo-bridges with peripheral the $S = 2$ Mn^{III} centers, leading to an overall molecular spin $S = 10$. (Right) Variable-field magnetization measurements on a single crystal of $\text{Mn}_{12}\text{O}_{12}(\text{CH}_3\text{COO})_{16}(\text{H}_2\text{O})_4$. The steps in the hysteresis loops are due to resonant tunneling of the magnetization as described in the text.^{4,29}

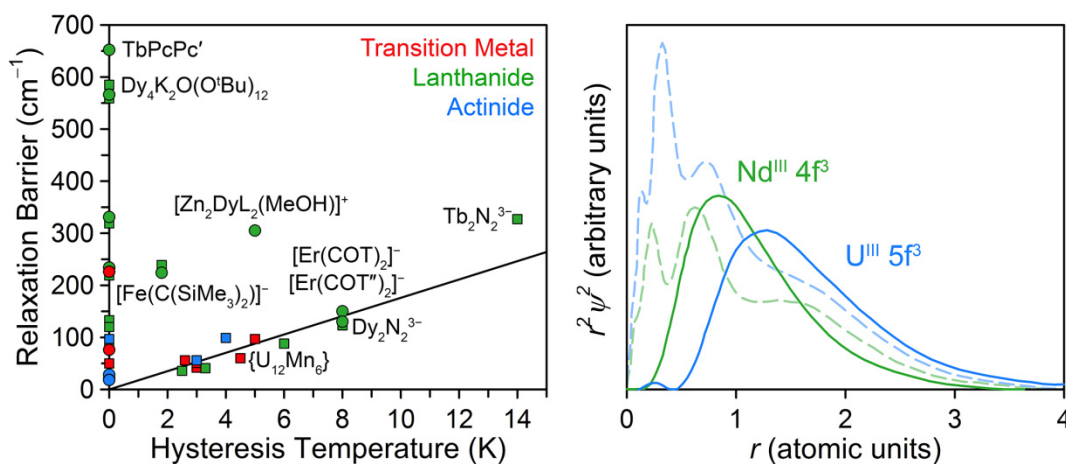
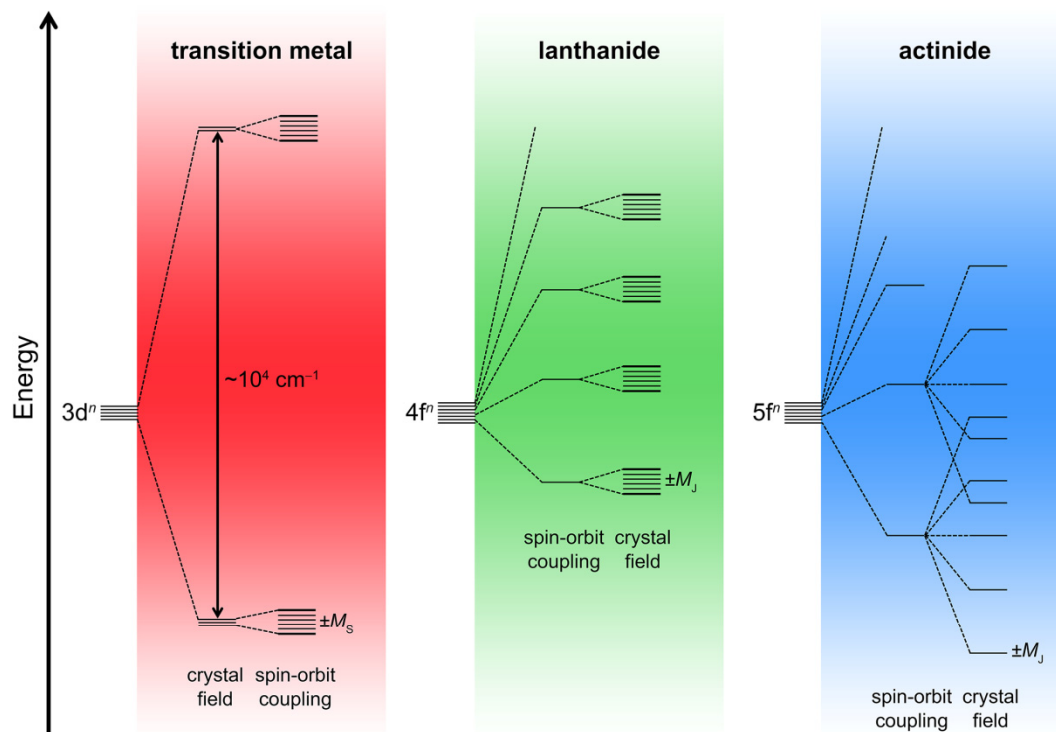


Figure 1.2. (Top) Simplified electronic energy level diagrams demonstrating the effects of the crystal field and spin-orbit coupling on transition metal, lanthanide, and actinide complexes and the resulting splitting of M_S or M_J levels. (Bottom left) Plot of relaxation barrier versus hysteresis temperature for select single-molecule magnets (see also Table 1.1); here, the hysteresis temperature is defined as the highest temperature for which remnant magnetization is observed for a given molecule. Circles correspond to systems with a single paramagnetic center while squares represent compounds with two or more paramagnetic centers. The black line indicates values of the barrier and hysteresis temperature for a relaxation time of 100 s, assuming a thermally-activated mechanism with $\tau_0 = 1 \times 10^{-9}$ s (Section 1.2). (Bottom right) Radial probability distribution functions for trivalent neodymium and uranium (adapted from Ref 42). Solid blue and green lines represent the probability distributions for the three valence f electrons of Nd^{III} and U^{III}, respectively, relative to their core electrons (dashed lines).

Table 1.1. Some of the highest performing single-molecule magnets and corresponding figures of merit.

Category	Molecule	U_{eff} (cm^{-1})	τ_0 (s)	Hysteresis T (K) ^a	Sweep Rate ($\text{mT}\cdot\text{s}^{-1}$)	Ref
Multinuclear Transition Metal	$[(\text{Co}(1\text{-hfpip}))_2(\text{D2py}_2(\text{TBA}))_2]$	97	1.6×10^{-9}	5	35	141
	$\text{Mn}_6\text{O}_2(\text{sao})_6(\text{O}_2\text{CPh})_2(\text{EtOH})_4$	60	2×10^{-10}	4.5	140	141
	$\text{Mn}_{12}\text{O}_{12}(\text{O}_2\text{CCH}_2\text{Br})_{16}(\text{H}_2\text{O})_4$	56	3.4×10^{-8}	2.6		141
	$[\text{Mn}_{21}\text{DyO}_{20}]$	51	2×10^{-12}	3	70	141
	$[(\text{TPyA})_2\text{Fe}^{\text{II}}_2(\text{N}^{\text{Ph}}\text{L})]^{+\text{b}}$	50	2.7×10^{-10}	0		141
Mononuclear Transition Metal	$\text{Mn}_{12}\text{O}_{12}(\text{O}_2\text{CMe})_{16}(\text{H}_2\text{O})_4$	42	2.1×10^{-7}	3	2.2	4
	$[\text{Fe}(\text{C}(\text{SiMe}_3)_3)_2]^-$	226	1.3×10^{-9}	0		36
	$[\text{Co}^{\text{II}}\text{Co}^{\text{III}}_3\text{L}''_6]^{-\text{c}}$	76	1×10^{-7}	0		141
	$[\text{Co}(\text{SPh})_4]^{2-}$	21	1×10^{-7}	0		141
	$[\text{Dy}_4\text{K}_2\text{O}(\text{O}^i\text{Bu})_{12}]$	585 ^d	$6.6 \times 10^{-11\text{e}}$	0		16a
	$[\text{Dy}_5\text{O}(\text{O}^i\text{Pr})_{13}]$	559 ^d	$4.7 \times 10^{-10\text{e}}$	0		60
	$[\text{Fe}_2\text{DyL}'_2(\text{H}_2\text{O})]^+$	319	1.11×10^{-10}	0		49c
	$\text{Er}_2(\text{COT}''')_3$	232 ^f	1.9×10^{-10}	1.8	2.2	78
	$[\{[(\text{Me}_3\text{Si})_2\text{N}]_2(\text{THF})\text{Tb}\}_2\text{N}_2]^-$	227	8.2×10^{-9}	14	0.9	13
	$\text{K}_2(\text{THF})_4[\text{Er}_2(\text{COT})_4]$	213 ^g	5×10^{-9}	0		78
Multinuclear Lanthanide	$[\{\text{Cp}^*\text{Ln}(\mu\text{-SSiPh}_3)_2\}_2]$	133	2.3×10^{-7}	0		142
	$[\{[(\text{Me}_3\text{Si})_2\text{N}]_2(\text{THF})\text{Dy}\}_2\text{N}_2]^-$	123	8.9×10^{-9}	8	80	88
	$[(\text{Cp}^*\text{Dy})_2(\mu\text{-bpym})]^+$	88	1.03×10^{-7}	6	2	90
	$[\text{Ln}(\text{Me}_5\text{trenCH}_2)(\mu\text{-H})_3\text{Ln}(\text{Me}_6\text{tren})]^{2+}$	85	1.04×10^{-7}	0		142
	$\{[(\text{Me}_3\text{Si})_2\text{N}]_2\text{Ln}(\text{THF})_2(\mu\text{-N}_2)\text{K}\}$	41	3.89×10^{-6}	3.3	1	89
	$[(\text{Cp}^*\text{Dy})_2(\mu\text{-tppz})]^+$	35.9	2.1×10^{-7}	2.5	3	91
	TbPcPc'	652	9.11×10^{-10}	0		40
	Tb^iPc_2	556	3.83×10^{-12}	0		20a
	$[\text{Cp}^*\text{Dy}(\text{BPh}_4)]$	331	1×10^{-9}	0		69
	$[\text{Zn}_2\text{DyL}_2(\text{MeOH})]^+$	305		5	20	33a
Mononuclear Lanthanide	$\text{Dy}(\text{sal})(\text{NO}_3)(\text{MeOH})\text{ZnL}_3$	234	1.1×10^{-9}	0		58a
	$\text{ErCp}^*(\text{COT})$	224 ^h	8.17×10^{-11}	1.8	0.92	72
	$[\text{Er}(\text{COT})_2]^-$	150	6.9×10^{-8}	8	0.78	75
	$[\text{Er}(\text{COT}''')_2]^-$	130	4.0×10^{-8}	8	2.2	77
	$[\{[\text{UO}_2(\text{salen})]_2\text{Mn}(\text{Py})_3\}_6]$	99	3×10^{-12}	4	4	136a
	$[\text{NpO}_2\text{Cl}_2][\text{NpO}_2\text{Cl}(\text{THF})_3]_2$	97		0		43
	$\{\text{UO}_2\text{Mn}_2\}^+$	56	5.02×10^{-10}	3	1.3	138
Mononuclear Actinide ⁱ	$\text{Np}(\text{COT})_2$	28.5	1.1×10^{-5}	0		116
	$\text{U}(\text{Ph}_2\text{BPz}_2)_3$	20	1×10^{-7}	0		10
	$[\text{UTp}^{\text{Me}2}_2(\text{bipy})]$	19.8	3.28×10^{-7}	0		111
	PuTp_3	18.3	2.9×10^{-7}	0		119
	$[\text{U}(\text{OSi}(\text{O}^i\text{Bu})_3)_4]^-$	18	2.6×10^{-7}	0		113

^a Highest reported hysteresis temperature where the loop is open at zero applied field. ^b $\text{N}^{\text{Ph}}\text{LH}_2 = \text{N}, \text{N}', \text{N}'', \text{N}'''$ -tetraphenyl-2,5-diamino-1,4-diiiminobenzoquinone. ^c $\text{H}_2\text{L}'' = R$ -4-bromo-2-((2-hydroxy-1-phenylethylimino)methyl)phenol. ^d Magnetically dilute sample. ^e Reported only for concentrated sample. ^f From solution measurement in cyclopentane; solid state $U_{\text{eff}} = 224 \text{ cm}^{-1}$; these values are lower than reported in cm^{-1} , but calculated from the reported Kelvin values and the relationship between K and cm^{-1} , $1 \text{ K} = 0.695 \text{ cm}^{-1}$. Assuming accurate values in Kelvin, the values in cm^{-1} are erroneously high. ^g Determined for relaxation between 19 and 32 K. For lower temperatures, a second relaxation process with $U_{\text{eff}} = 118(1) \text{ cm}^{-1}$. Based on the reported value in Kelvins, $U_{\text{eff}} = 213 \text{ cm}^{-1}$, not 219 cm^{-1} as reported. ^h A second Orbach relaxation process was observed with $U_{\text{eff}} = 137 \text{ cm}^{-1}$ and $\tau_0 = 3.13 \times 10^{-9} \text{ s}$. ⁱ Reported barriers for these systems are under H_{dc} except for $\text{U}(\text{Ph}_2\text{BPz}_2)_3$ and $[\text{UTp}^{\text{Me}2}_2(\text{bipy})]$ ($[\text{Tp}^{\text{Me}2}]^- = \text{dimethyltris}(\text{pyrazolyl})\text{borate anion}$, $\text{bipy} = \text{bipyridine}$).

In the two decades following the discovery of $\text{Mn}_{12}\text{O}_{12}$ and a host of transition metal-based compounds, the field has grown to encompass the study of the lanthanides⁹ and even the actinides.¹⁰ This transformation has brought with it inherent synthetic challenges due to the different electronic structures of these elements and the unique contributions of spin-orbit coupling and ligand field (Figure 1.2). Even with such diversity, some dominant trends are clear among the highest performing systems. A number of these compounds, many of them discovered within the last five years, are highlighted in Figure 1.2 (see also Table 1.1) wherein relaxation barrier is plotted as a function of hysteresis temperature.¹¹ Notably, the largest relaxation barriers and highest hysteresis temperatures to date are all associated with complexes wherein single-ion magnetic anisotropy has been maximized or strong magnetic coupling of two or more metal centers is engineered via a radical bridge.¹² Still, molecular blocking temperatures today are rather low, with the current record of 14 K established in 2011.¹³ For other molecular systems that approach this value, the hysteresis loops are generally characterized by loss of remnant magnetization at zero field, associated with rapid relaxation processes such as tunneling of the magnetization.¹⁴ These processes,¹⁵ elaborated on below, can also prevent observation of the full barrier, U , as defined by the zero-field splitting of the ground S or J term.¹⁶ Tunneling and other “through-barrier” processes limit the performance of current single-molecule magnets, and make it difficult to predict upper bounds for their properties. For instance, consider that there are molecules already known with extremely high relaxation barriers, such as $\text{Dy}_4\text{K}_2\text{O}(\text{O}^t\text{Bu})_{12}$ discussed below ($U_{\text{eff}} = 585 \text{ cm}^{-1}$ in magnetically dilute form).^{16a} In principle, such a magnet should be useful in devices at temperatures up to 28 K, assuming only thermal relaxation of the magnetization. However, hysteresis is observed only to 5 K for this molecule with almost no remnant magnetization, and fast relaxation leads to relatively facile moment reorientation above this temperature. It is clear that equally as important as asking questions such as “how high” (barrier and blocking temperature) and “how long” (relaxation time), a better understanding of relaxation phenomena is necessary for known molecules, such that new systems with improved properties can be obtained. In this chapter a general introduction to the field of single-molecule magnetism will be provided, with emphasis on the role of lanthanides and actinides, which will be the predominant players in the research described in the subsequent chapters. First, the general characterization of single-molecule magnets will be described. Next, the events leading up to the discovery of lanthanide and actinide single-molecule magnets will be briefly outlined. Finally, several recent literature benchmarks will be discussed to illustrate the current state of the field and put into context the work that will be discussed in this dissertation.

1.2 Characterization of Slow Magnetic Relaxation in Molecules

Molecular slow magnetic relaxation is readily introduced by considering the example of $\text{Mn}_{12}\text{O}_{12}$. Composed of a tetranuclear cluster of Mn^{IV} surrounded by a periphery of Mn^{III} ions (Figure 1.1), antiferromagnetic coupling between the core and the outer ring of manganese ions leads to an overall $S = 10$ ground state. Spin-orbit coupling then acts as a minor perturbation splitting the degenerate M_S states in the absence of an applied field (Figure 1.2 and Figure 1.3, left). Due to the presence of a large, uniaxial magnetic anisotropy within the molecule, the $M_S = \pm 10$ states are lowest in energy and separated by a barrier, U , from the highest excited state $M_S = 0$. This existence of a doubly-degenerate ground state, separated by an energy barrier U , is a hallmark of single-molecule magnets, and in the absence of facile relaxation pathways between ground states, magnetic hysteresis can be observed at temperatures below U .

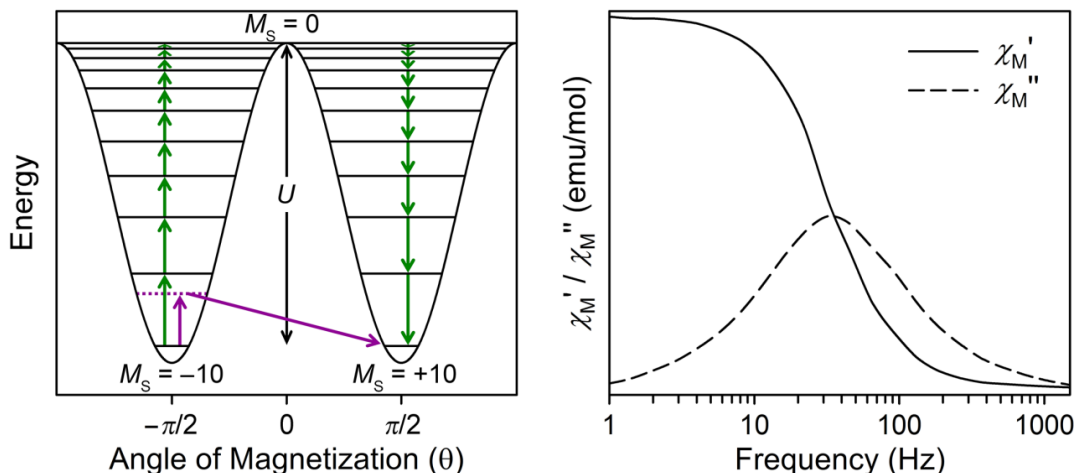


Figure 1.3. (Left) Double-well energy diagram for an $S = 10$ system with full Orbach and Raman relaxation processes highlighted with green and purple arrows, respectively. (Right) Plot of the in-phase (χ_M' , solid line) and out-of-phase (χ_M'' , dashed line) components of the magnetic susceptibility versus frequency of the ac field for a typical SQUID Magnetometer.

The splitting of the $2S + 1$ M_S states in zero applied field for $\text{Mn}_{12}\text{O}_{12}$ ¹⁷ can be described by the phenomenological crystal field Hamiltonian $\hat{H}_{CF} = D\hat{S}_Z^2 + E(\hat{S}_x^2 - \hat{S}_y^2)$, where D and E are the axial and transverse zero-field splitting parameters, respectively. In the case of a negative D parameter, the maximal $M_S = \pm S$ states will be lowest in energy, while if D is positive then minimal M_S states will be stabilized.¹⁸ For a perfectly axial system, $E = 0$, and in general for systems with negligible transverse magnetic anisotropy the E term may be neglected, and the relaxation barrier for the molecule given by $U = |D|S^2$ or $U = |D|(S^2 - 1/4)$ (for integer and half-integer spins, respectively). Considering $\text{Mn}_{12}\text{O}_{12}$ with $S = 10$ and $D = -0.5 \text{ cm}^{-1}$,¹⁹ the former relation yields a theoretical barrier of 50 cm^{-1} that agrees with the value of $U_{\text{eff}} = 42 \text{ cm}^{-1}$ first obtained experimentally from susceptibility measurements.⁴

The observation of magnetic hysteresis in $\text{Mn}_{12}\text{O}_{12}$ sparked the moniker single-molecule magnet, and indeed the highest hysteresis temperature for a molecule (or blocking temperature) is one of the best metrics for evaluating the performance of these systems. Due to different techniques for measuring magnetic hysteresis, however (SQUID magnetometry, micro-SQUID measurements,¹⁸ and X-ray Magnetic Circular Dichroism,²⁰ to name a few) and the variable time-scales that can be achieved with these approaches, a normalizing definition for blocking temperature is the temperature at which a given molecule demonstrates a relaxation time of 100 s.¹⁸ This temperature often corresponds to the maximum hysteresis observed for a single-molecule magnet. Even still, the wide, square loops characteristic of hard bulk magnets are rarely displayed by single-molecule magnets, due to the presence of rapid zero-field relaxation that leads to little or no remnant magnetization and coercive field (M_R and H_C).²¹

As it turns out, for the vast majority of single-molecule magnets, characteristic relaxation times are on the order of milliseconds, and magnetic blocking occurs well below 1.8 K. In these cases, slow magnetic relaxation can be observed via ac susceptibility measurements, wherein a sample is exposed to a small oscillating magnetic field of magnitude not much larger than that found at the surface of the earth (4-10 Gauss).²² By varying the frequency of this oscillating field, it is possible to probe for the presence of slow magnetic relaxation in a molecular species. If the molecule does not possess a barrier to moment reorientation within the given time-scale

(typically 1-1500 Hz, though as high as 10,000 Hz with some instruments), a constant magnetic susceptibility value will be observed over the entire frequency range. This value should correspond with that of the static magnetic susceptibility at the same temperature, measured in the presence of a dc magnetic field.

On the other hand, if a molecule possesses a barrier to reorientation of the magnetization, then at some resonant frequency and corresponding relaxation time, τ , the magnetic susceptibility will demonstrate a lag in response to oscillating magnetic field (Figure 1.3, right). In this case, the in-phase magnetic susceptibility, χ_M' , will drop off as the out-of-phase component of the magnetic susceptibility, χ_M'' , grows in (see the Appendix to this chapter for explicit formulae for χ_M' and χ_M'').²³ This relaxation of the magnetization is mediated by phonons and occurs via one or more varieties of spin-lattice relaxation. The ideal mode of relaxation is via thermal excitation over the energy barrier for the molecule (Figure 1.3, left, green arrows). This process is known as thermally-activated or Orbach relaxation, and can be identified by its characteristic temperature dependence, given by Equation 1.1.

$$\tau^{-1} = \tau_0^{-1} \cdot \exp(-U_{\text{eff}}/k_B T) \quad (1.1)$$

Here, τ is the relaxation time of the magnetic moment at a given temperature; U_{eff} denotes the relaxation barrier of the molecule; and τ_0^{-1} is the attempt frequency. If a system relaxes via an Orbach mechanism, then a plot of $\ln(\tau)$ versus $1/T$ should be a straight line with intercept equal to τ_0 and a slope of U_{eff}/k_B . Designing systems that show Orbach relaxation and maximizing U_{eff} is in principle also a way to maximize hysteresis temperature; that is, if the barrier is far above room temperature, then “blocking” of the magnetization (i.e. isolation of the moment in one of the potential wells in Figure 1.3) and magnetic hysteresis may also be observable at high temperatures. However, even for systems in which the ground S or J manifold is spread over several hundred cm^{-1} , the observed relaxation barrier through ac susceptibility measurements is typically a fraction of this value (hence the “ U_{eff} ” delineation), corresponding to relaxation via a low-lying excited state. Thus, in addition to simply targeting molecules that show larger U_{eff} values, a great deal of effort is being put toward understanding why for many systems relaxation through the full barrier U is not accessible.^{24,25}

The attempt frequency, τ_0^{-1} , is another parameter that finds itself with a rather imprecise definition. Classically, this quantity can be understood as the frequency of an oscillating particle (the magnetic moment) within one of the potential wells in Figure 1.3. The higher the frequency, and correspondingly the smaller the value of τ_0 , the greater the number of “attempts” made at this over-barrier transition and the greater the likelihood of such a transition. For systems demonstrating thermally-activated relaxation through a real excited state, τ_0 will often range from 10^{-9} to 10^{-12} s, though this can be variable.^{26,27} When τ_0 falls outside of this range in either direction, this is an indication that there are contributions from other relaxation processes.²⁸ The most common of these is tunneling of the magnetization, which can occur at very low temperatures between ground states, or between degenerate excited states.^{14,29} For mononuclear systems with a Kramers ion ($S = \text{half-integer}$) or any molecule with non-integer spin, a doubly-degenerate ground state is guaranteed in the absence of an applied field and ground state tunneling is forbidden in the absence of other perturbations. However, tunneling can also arise due to mixing of ground states, whether due to inherent symmetry, dipolar interactions, or hyperfine interactions.^{14,30} If ground state tunneling is facile, this can short-circuit slow relaxation, and in these cases application of a small dc field will offset the potential wells in

Figure 4 such that slow magnetic relaxation may be observed. Two other spin-lattice mechanisms deserve attention here, and these are Raman ($\tau \propto CT^n$) and direct ($\tau \propto CT$) processes, respectively. Raman relaxation occurs via a virtual excited state (Figure 1.3, left, pink arrows), created by coupling to different vibrational modes within the crystal, and will lead to experimental “relaxation barriers” that do not correspond to real molecular excited states.³¹ Direct relaxation can only be observed in the presence of a magnetic field and corresponds to relaxation between ground states; this process can be identified by large τ_0 (again variable, but commonly $> 10^{-5}$).

It is possible that one or more of these mechanisms may be active over a given temperature range, and this can be most readily detected when there is curvature in a plot of $\ln(\tau)$ versus $1/T$ toward low temperatures. Suffice it to say that identifying the relaxation mechanism and true barrier³² from ac susceptibility measurements alone is challenging. Recognition of this is becoming more wide-spread in the literature however, and many attempts have been made to identify and quantify other relaxation mechanisms.^{31,33} This is certainly the first step forward in better understanding these additional mechanisms and tailoring systems to shown only Orbach relaxation.

1.3 The f-Elements in Single-Molecule Magnetism

From the expressions given in Section 1.2, i.e. $U = |D|S^2$ or $U = |D|(S^2 - 1/4)$, it would appear that U should depend heavily on the size of the molecular spin ground state. Indeed, for many years the dominant design strategy was to assemble clusters of increasing nuclearity to target larger S and therefore U . The most impressive realization of this effort was a Mn_{19} cluster with an enormous $S = 83/2$ ground state. However, the relative orientations of the manganese Jahn-Teller axes contributed to a low molecular anisotropy and no experimentally observed barrier.³⁴ Seminal work by Neese and Pantazis later shed light on this and similar observations, namely that increasing S did not generally afford clusters with enhanced barriers or hysteresis, due to an implicit inverse relationship between D and S^2 .³⁵ Thus rather than targeting compounds with larger S , a more viable strategy would be to pursue complexes with enhanced magnetic anisotropy. Recent advances in transition metal single-molecule magnetism have demonstrated that a promising route to enhance magnetic anisotropy is to focus on tailoring the ligand field for a single metal ion. Indeed, the $S = 3/2$ Fe^{I} molecule $[\text{Fe}(\text{C}(\text{SiMe}_3)_3)_2]^-$ currently holds the record for both relaxation barrier ($U_{\text{eff}} = 226 \text{ cm}^{-1}$) and hysteresis temperature (6.5 K) for any transition metal species.³⁶ The combination of the low coordination number and oxidation state of the Fe center leads to a configuration wherein the partially-filled $d_{x^2-y^2}$ and d_{xy} orbitals are nearly degenerate (Figure 1.4), leading to large unquenched orbital angular momentum and magnetic anisotropy. The magnetic anisotropy is so great for this compound that the ground state is best described in terms of the total angular momentum quantum number, $J = 9/2$ ($L = 2$, $S = 3/2$) in a manner analogous to lanthanide systems (Figure 1.2). Over the temperature range 20-29 K, the relaxation data could be fit to an Arrhenius law, however the presence of pronounced curvature below 20 K suggested the presence of non-Orbach relaxation mechanisms. Notably, lower temperature relaxation times were accessible via Mössbauer measurements and allowed quantification of Raman relaxation and characterization of Orbach relaxation via the first ($M_J = 5/2$) and second ($M_J = 3/2$) excited states (Figure 1.4).³⁷

By far, the most successful means to enhance magnetic anisotropy within a molecule has been to take advantage of the unique properties of the lanthanide ions. Indeed due to their limited

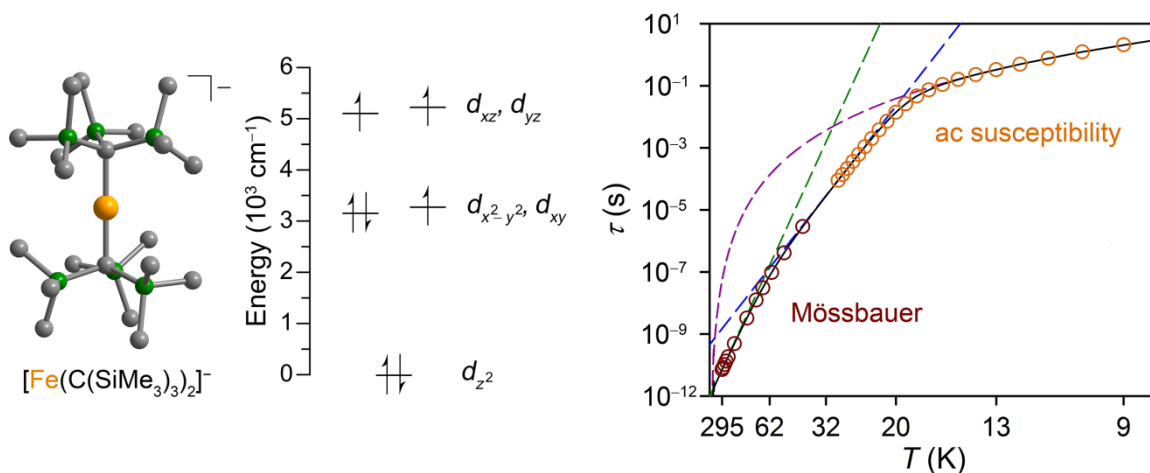


Figure 1.4. (Left) X-ray structure of $[\text{Fe}(\text{C}(\text{SiMe}_3)_3)_2]^-$ and energy level splitting of the d-orbitals as determined by ab initio calculations. Orange, grey, and green spheres represent Fe, C, and Si, respectively; H atoms have been omitted for clarity. (Right) Full range of temperature-dependent relaxation data collected for $[\text{Fe}(\text{C}(\text{SiMe}_3)_3)_2]^-$ utilizing both ac susceptibility measurements (orange circles) and Mössbauer (red circles), revealing two thermally-activated relaxation processes (green and blue dashed lines) and Raman relaxation (pink dashed line).^{36,37}

radial extension beyond the [Xe] core (Figure 1.2, bottom right), the 4f orbitals participate little in covalent bonding thus generating large unquenched orbital moments and strong spin-orbit coupling across the series. Correspondingly, the lanthanides possess some of the largest magnetic anisotropies in the periodic table. Spin-orbit coupling is the dominant perturbation of the free ion state, and thus a spin-only description of the crystal field splitting as described above for transition metal systems no longer applies. The ground state is defined by the total angular momentum quantum number J ($|L - S|$ for $n < 7$ and $L + S$ for $n > 7$), which is further split into $2J + 1$ states by the crystal field (Figure 1.2). The discovery of the first lanthanide single-molecule magnets⁹ came somewhat inadvertently in the course of determining ligand field parameters (B_q^k)³⁸ for lanthanide phthalocyanine complexes, when Ishikawa and coworkers found that the crystal field split the ground J in such a way that the maximal M_J was lowest in energy and separated by as much as a few hundred wave numbers from the first excited M_J doublet.³⁹ This energy level structure resembled the splitting of the M_S levels within multinuclear transition metal systems, and magnetic characterization revealed that indeed the pseudo- D_{4d} symmetric complexes $[\text{LnPc}_2]^-$ ($\text{Ln} = \text{Tb}, \text{Dy}, \text{Ho}$; Pc^{2-} = phthalocyanine dianion) are single-molecule magnets, with the largest experimental barrier corresponding to the highly anisotropic Tb^{III} congener (Figure 1.5, left, $U_{\text{eff}} = 230 \text{ cm}^{-1}$).⁹ Fast-forward just over ten years and lanthanide compounds currently exhibit the largest relaxation barrier (652 cm^{-1})⁴⁰ and blocking temperature (14 K)¹³ of any single-molecule magnet.

While the actinides are an exotic choice, their spin-orbit coupling energies far exceed those of the lanthanides,⁴¹ and the greater radial extension of the 5f over the 4f orbitals (Figure 1.2, bottom right)⁴² introduces the possibility of covalency and strong magnetic exchange.⁴³ Such a seemingly opportune melding of the properties of lanthanides and transition metals has led to the actinides being frequently touted as a promising new route to single-molecule magnets with higher blocking temperatures. Research into this area is still developing, and the systems studied to date have revealed a complexity not yet encountered with 3d or 4f forerunners. The first system to be discovered was the mononuclear U^{III} complex, $\text{U}(\text{Ph}_2\text{BPz}_2)_3$,¹⁰ which had been

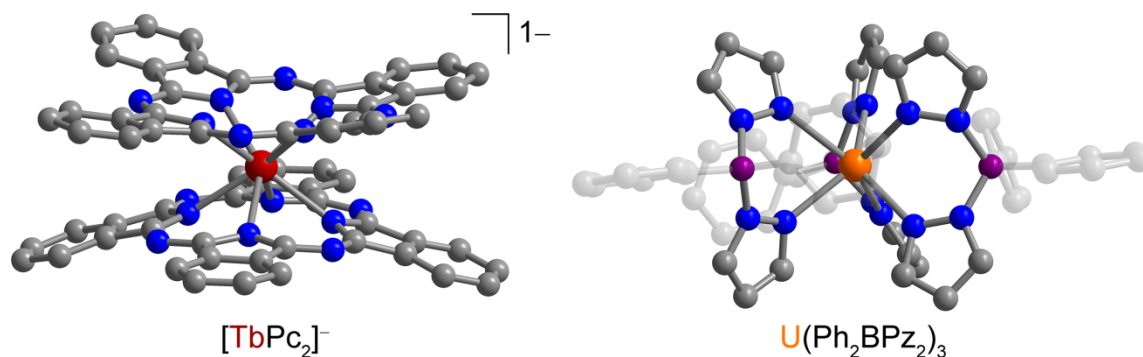


Figure 1.5. Molecular structures of the first lanthanide and actinide single-molecule magnets $[\text{TbPc}_2]^-$ (left)⁹ and $\text{U}(\text{Ph}_2\text{BPz}_2)_3$ (right),^{10,44} respectively. Red, orange, blue, purple, and grey spheres represent Tb, U, N, B, and C atoms, respectively; H atoms are omitted for clarity.

synthesized many years prior and found to possess a trigonal prismatic geometry arising from the coordination of the three bidentate diphenyl(bispyrazolyl)borate ligands (Figure 1.5, right).⁴⁴ The realization of slow relaxation in this complex was not serendipitous, however. Indeed, it was observed that the nitrogen atoms above and below the plane of the uranium center presented a pseudo-axial ligand field somewhat analogous to $[\text{LnPc}_2]^-$.⁹ Given that U^{3+} possesses a ground $J = 9/2$ with oblate-type anisotropy akin to anisotropic Tb^{3+} ,⁴⁵ it was reasoned that this ligand environment could potentially provide an effective strategy for engineering slow magnetic relaxation. Indeed, this complex exhibited temperature-dependent out-of-phase signal under zero applied magnetic field with a thermally-activated relaxation barrier of 20 cm^{-1} and $\tau_0 = 1 \times 10^{-9}$ s. While the U_{eff} value was more than an order of magnitude smaller than record lanthanide barriers at the time, this result opened up a new area of molecular magnetism based upon actinide ions. Slow relaxation in mononuclear actinide complexes can again be attributed to the splitting of the ground J by the ligand field, though the radial extension of the 5f orbitals may complicate this description in cases where the crystal field splitting energy is comparable with the spin-orbit coupling (see Figure 1.2).

1.4 Lanthanide Single-Ion Anisotropy in Molecular Magnetism

Early research into lanthanide single-molecule magnets focused on the study of mononuclear compounds with pseudo- D_{4d} symmetry after the demonstrated success of the $[\text{LnPc}_2]^-$ complexes.⁹ Mixed 4f- π d (or 4f-radical, *vide infra*) were also targeted with the intent of combining lanthanide anisotropy with more diffuse magnetic orbitals to engender strong exchange.⁴⁶ While a great body of synthetic chemistry has developed around the design of multinuclear systems, interactions between lanthanide and transition metal are generally weak⁴⁷ and slow relaxation derives from intramolecular coupling between transition metals⁴⁸ or from lanthanide single-ion anisotropy.⁴⁹ For multinuclear systems where lanthanides compose the only paramagnetic centers, the story is similar, and in fact weak coupling between lanthanide ions can be counterproductive in observing slow relaxation (see Section 1.5).^{16a,47c} Thus, a more promising strategy is to target systems with enhanced single-ion magnetic anisotropy. Within the last few years, the more rational design of highly anisotropic molecules become accessible with the realization that certain molecular symmetries can preferentially stabilize large angular momentum ground states for the lanthanides and engender large magnetic anisotropy.

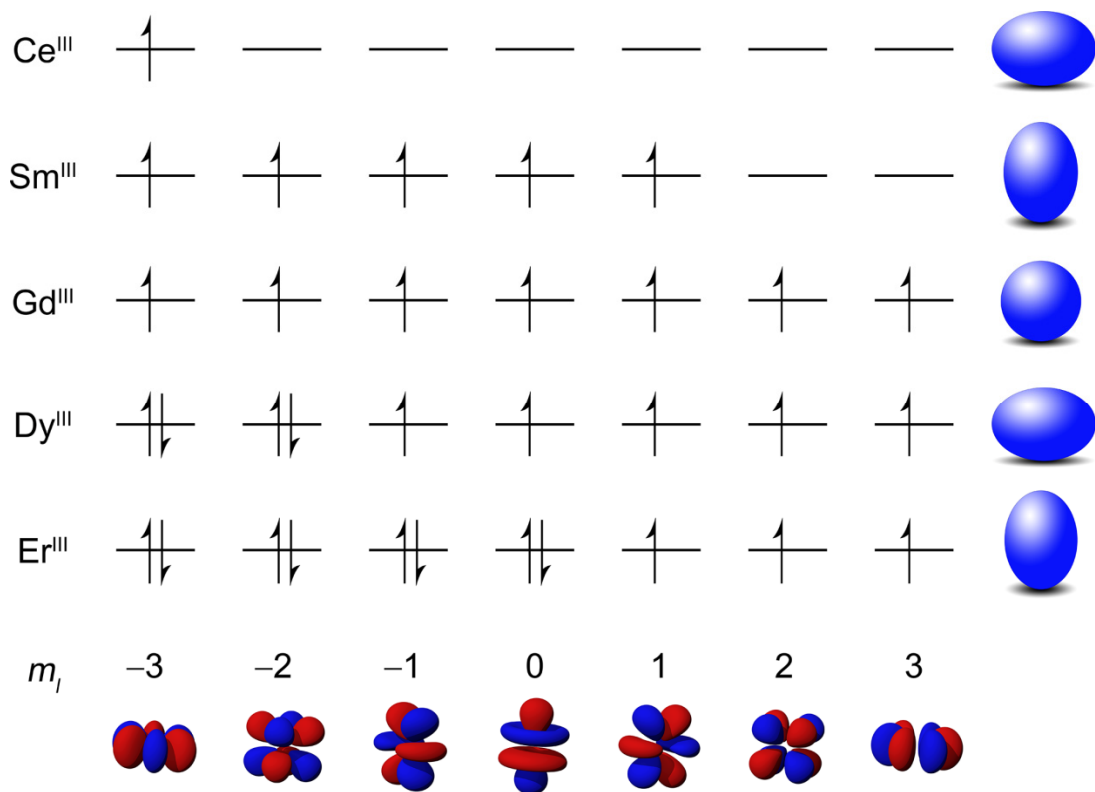


Figure 1.6. Qualitative picture of the shapes of the quadrupole moments for some oblate (Ce^{III} and Dy^{III}), prolate (Sm^{III} and Er^{III}) and isotropic (Gd^{III}) lanthanide ions. Adapted from Ref. 50.

To introduce the idea behind this transformation in the field, consider the fact that the 4f-electron density distribution for a given trivalent lanthanide possesses a shape (dictated by the sign of the so-called quadrupole moment) that is dependent on the f-electron count and corresponding filling of the f-orbitals (based on Hund's Rules). For instance, in the case of Sm^{III} (4f⁵, $S = 5/2$, $L = 5$, $J = 5/2$), the 4f electron cloud is axially elongated or prolate in shape, while for Dy^{III} (4f⁹, $S = 5/2$, $L = 5$, $J = 15/2$) the charge cloud has an axially compressed, or oblate, shape (Figure 1.6).⁵⁰ By virtue of their large spin-orbit coupling and the limited radial extension of the 4f orbitals, each trivalent ion can thus be well-characterized in the ground state by the total angular quantum number J ($= |L - S|$ for $nf < 7$ and $L + S$ for $nf > 7$), with the ligand field acting only as a minor perturbation that splits the J into its corresponding M_J sublevels ($-J \leq M_J \leq J$). While there is no a priori way to predict how these levels will split in a particular ligand field, the shapes of the 4f electron clouds can direct the synthetic chemist to potentially ideal symmetries to enhance lanthanide anisotropy. For instance, for oblate Nd^{III} (isoelectronic to U^{III}, 4f³, $S = 3/2$, $L = 6$, $J = 9/2$) an axial ligand field should engender large anisotropy along the same direction, due to the energetically unfavorable electrostatic interaction that results upon 180° reorientation of the magnetization (Figure 1.7). This very simple logic can also be extended to lanthanide ions with prolate electron density distributions, wherein an equatorial ligand field would enhance anisotropy. Considering the quadrupole moment as descriptive of the ground J state for a given lanthanide, one can further extract the electron density distributions of the M_J sublevels by calculating higher order magnetic anisotropy terms or multipoles. This was in fact done previously for the trivalent lanthanide ions,⁵¹ and has since been elegantly used to further

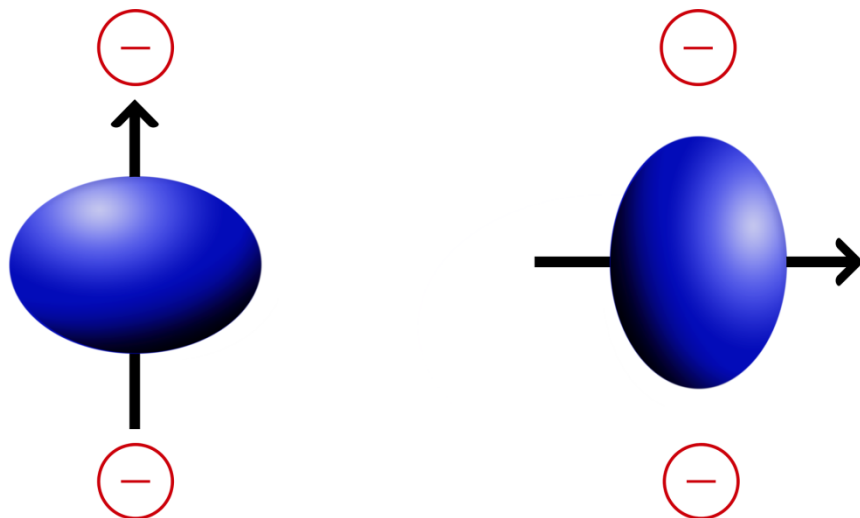


Figure 1.7. Qualitative representation of the magnetic anisotropy of an oblate lanthanide ion in a axial ligand field, adapted from Ref. 50. The lower energy configuration is represented on the left, where the magnetization axis points along the crystallographic symmetry axis, while the highest energy configuration occurs when the magnetization is orthogonal to the crystallographic axis.

establish a qualitative rationale for slow magnetic relaxation in many mononuclear lanthanide single-molecule magnets.⁴⁵

In addition to this qualitative approach, a handful of more comprehensive methods have been developed to describe the sublevel splitting in lanthanide complexes, extract ligand field parameters, and quantify magnetic anisotropy.^{52,53,54} For instance, using a Hamiltonian describing only the Zeeman interaction⁵⁵ and crystal field splitting, Ishikawa et al. determined the ligand field parameters and sublevel splitting for $[\text{LnPc}_2]^-$ through simultaneous fitting of magnetic susceptibility data and reproduction of ^1H NMR shifts across the latter half of the series.^{9b} More recently, *ab initio* calculations have become vogue in the characterization arsenal for a number of molecules⁵² as will be shown for a number of examples below, though these calculations are non-trivial. An arguably even more rigorous approach is to model the magnetism of a lanthanide (or actinide) molecule using a complete Hamiltonian accounting for the Zeeman and crystal field interactions as well as electron-electron repulsion and spin-orbit coupling. The program CONDON (*vide infra*) provides an exceptional platform for this purpose,⁵⁶ though its use also requires somewhat involved computations and is ideally best supported by spectroscopic measurements.⁵⁷ In principle any of these methods are accessible to the synthetic chemist with some additional effort, though the qualitative rationale above serves as an invaluable starting point and is indeed borne out by these more rigorous methods. For example, for a number of low-symmetry Dy^{III} compounds, *ab initio* and computational electrostatic models have concluded that the presence of a strong axial ligand field is responsible for the observed slow magnetic relaxation.^{54,58}

While the very basic ligand coordination (axial versus equatorial) is an important factor, molecular symmetry plays a crucial role in whether slow magnetic relaxation will be observed. Teasing out the contributions from these two factors can be a challenge, though it is instructive to examine some of the highest performing systems in the literature. For instance, the largest barrier to date for any single-molecule magnet is 652 cm^{-1} ($\tau_0 = 9.11 \times 10^{-10} \text{ s}$), discovered rather recently for the heteroleptic, neutral complex TbPcPc' ($\text{Pc}' = \text{tert-butylphenoxy-substituted}$

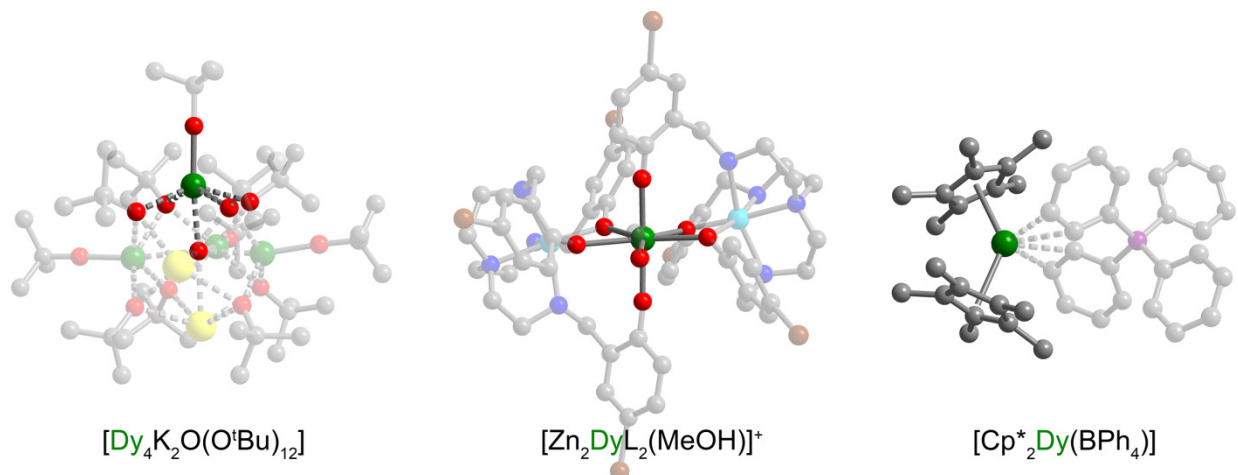


Figure 1.8. X-ray structures of $[\text{Dy}_4\text{K}_2\text{O}(\text{O}^t\text{Bu})_{12}]$, $[\text{Zn}_2\text{DyL}_2(\text{MeOH})]^+$, and $[\text{Cp}^*_2\text{Dy}(\text{BPh}_4)]$ as described in the text. Green, red, grey, yellow, blue, pale blue, burnt orange, and purple represent Dy, O, C, K, N, Zn, Br, and B atoms, respectively.^{16a,33a,69}

phthalocyanine dianion, Pc = phthalocyanine radical cation).^{40,59} While the ligand environment in this molecule can be observed as somewhat axial in nature, the pseudo- D_{4d} symmetry is also instrumental in generating a doubly-degenerate ground state for non-Kramers Tb^{III} .^{9,12a} Terbium bis(phthalocyanine) systems have certainly been hotly pursued in the literature, though lanthanide-based single-molecule magnets are known for over half of the series and slow magnetic relaxation is most common for Dy^{III} ($4f^9$, $J = 15/2$) in a wide variety of symmetries, no doubt due to its Kramers nature. Even still, the highest performing systems for Dy^{III} are few and often can be identified by highly axial ligand environments. More recently, a handful of impressive systems incorporating Er^{III} ($4f^{11}$, $J = 15/2$) have confirmed the utility of strongly equatorial ligand fields for this ion.

Slow Magnetic Relaxation for Dysprosium(III) in Axial Coordination Environments. The compounds $[\text{Dy}_5\text{O}(\text{O}^i\text{Pr})_{13}]$ ($\{\text{Dy}_5\}$)⁶⁰ and $[\text{Dy}_4\text{K}_2\text{O}(\text{O}^t\text{Bu})_{12}]$ ($\{\text{Dy}_4\text{K}_2\}$, see Figure 1.8)^{16a} exhibit the largest relaxation barriers to date for any Dy^{III} -containing system (Table 1.1). The first compound consists of a square pyramid of Dy^{III} ions, wherein each metal is coordinated axially by a terminal alkoxide ligand and a central $\mu_5\text{-O}^{2-}$, with the cluster itself held together by eight bridging alkoxides. Notably, the terminal alkoxide forms the shortest bond to each Dy^{III} in $\{\text{Dy}_5\}$ and $\{\text{Dy}_4\text{K}_2\}$ (by as much as 0.5 Å),^{16a} generating a predominantly axial ligand field. Such a ligand field should stabilize the $M_J = 15/2$ ground state for each Dy^{III} and indeed ab initio calculations suggested that the ground state is highly axial ($g_z > 19.8$ with $g_{x,y} < 0.001$)⁶¹ for both clusters, with the anisotropy axes of each Dy^{III} along the terminal alkoxide bond.

A single Orbach relaxation process was observed for the $\{\text{Dy}_5\}$ cluster with $U_{\text{eff}} = 337 \text{ cm}^{-1}$ ⁶² while $\{\text{Dy}_4\text{K}_2\}$ exhibited two relaxation processes with $U_{\text{eff}} = 481 \text{ cm}^{-1}$ and 220 cm^{-1} .^{16a} Interestingly, intracuster dilution to give $\{\text{DyY}_4\}$ and $\{\text{DyY}_3\text{K}_2\}$ in their respective Y^{III} matrices revealed only one relaxation feature for both compounds, with $U_{\text{eff}} = 559 \text{ cm}^{-1}$ ($\tau_0 = 6.6 \times 10^{-11} \text{ s}$) and 585 cm^{-1} ($\tau_0 = 4.7 \times 10^{-10} \text{ s}$), respectively, indicating that dipolar interactions play a role in the second relaxation process exhibited by $\{\text{Dy}_4\text{K}_2\}$. Based on ab initio determined sub-level splitting for each Dy^{III} site within the clusters, these barriers were ascribed to relaxation via a second excited M_J state, the first observation of its kind for a molecular species. Magnetic hysteresis was also observed as high as 7 K for both dilute species, though the loop is narrow and

closed at zero field. The associated tunneling of the magnetization would likely be remedied by synthesis of rigorously axially symmetric compounds, as suggested by some recent theoretical investigations. For instance, it was noted via ab initio calculations that a compound of the type $[\text{DyO}]^+$ would possess an enormous barrier due to perfectly axial Kramers doublets ($g_{x,y} = 0$) except for the highest energy $M_J = \pm 1/2$. Tunneling induced via transverse anisotropy would thus only occur via this highest excited state, allowing observation of the full barrier in excess of 2000 cm^{-1} .⁵²

While such a molecular compound is not synthetically realistic, an extreme realization of the axial ligand field that should be isolable was highlighted recently by Chilton et al.⁶³ The authors present structural characterization of a nearly linear Sm^{II} compound, coordinated by two bulky $[\text{N}(\text{Si}^{\text{i}}\text{Pr}_3)_2]^-$ ligands, and demonstrated through ab initio calculations that an analogous compound with anisotropic Dy^{III} would present an energy level structure very reminiscent of the $[\text{DyO}]^+$ species. Slow relaxation was predicted to occur primarily via the highest two excited states, which would result in an enormous relaxation barrier in excess of 1800 cm^{-1} . With such a barrier, magnetic blocking would occur even at room temperature, bringing a molecular system into the realm of bulk magnetic materials. As this calculation does not account for factors such as dipolar interactions, crystalline vibrational modes, and nuclear spin (all relevant for measurements on bulk samples), it is possible that a value of U_{eff} smaller than the full J splitting would be observed. Even still, this molecule presents an extremely exciting target for accessing an unprecedented relaxation barrier and blocking temperature for Dy^{III} .

Another notable molecule is $[\text{Zn}_2\text{DyL}_2(\text{MeOH})]^+$ ($L = 2,2'2''\text{-}(((\text{nitrilotris}(\text{ethane-2,1-diy}))\text{tris}(\text{azanediyl}))\text{tris}(\text{methylene}))\text{tris}(4\text{-bromophenol}))$), wherein the Dy^{III} sits in a pseudo- D_{5h} symmetric pocket (Figure 1.8, middle) and exhibits $U_{\text{eff}} = 305(3) \text{ cm}^{-1}$ and butterfly magnetic hysteresis to 12 K.^{33a} Upon desolvation to $[\text{Zn}_2\text{DyL}_2]^+$, the Dy^{III} center adopts pseudo- O_h symmetry and slow relaxation is only observable under a dc field with a temperature dependence suggesting contributions from Raman and direct processes.⁶⁴ In the context of this discussion, it is perhaps relevant to note that a comparison of the axial and equatorial bond lengths within each structure reveals a stronger axial coordination environment for $[\text{Zn}_2\text{DyL}_2(\text{MeOH})]^+$,⁶⁵ though symmetry is arguably the dominant player in the relaxation dynamics. Indeed, the differences in relaxation behavior can be rationalized by recognizing that in approximate D_{5h} symmetry, off-diagonal crystal field parameters B_q^k (see Footnote 36) are minimized relative to O_h symmetry, and correspondingly so is mixing of M_J states induced by these terms.⁶⁶ These results implicate state mixing in the observation of non-Orbach relaxation processes, highlighting the importance of targeting complexes with high axial site symmetry to target pure M_J doublets. However, a strongly axial ligand field is also equally of import to generate a maximal ground state. For instance, consider that $[\text{Dy}(\text{COT})_2]^-$ possesses high axial symmetry, though weak axial coordination, and as might be anticipated based on ab initio calculations, the ground state is nearly pure though non-maximal with $M_J = \pm 9/2$.⁶⁷

Under anaerobic conditions it was also possible to synthesize an Fe^{II} analogue of $[\text{Zn}_2\text{DyL}_2(\text{MeOH})]^+$, namely $[\text{Fe}_2\text{DyL}'_2(\text{H}_2\text{O})]^+$, ($L' = 2,2'2''\text{-}(((\text{nitrilotris}(\text{ethane-2,1-diy}))\text{tris}(\text{azanediyl}))\text{tris}(\text{methylene}))\text{tris}(4\text{-chlorophenol}))$) wherein the D_{5h} site symmetry is accomplished with a coordinated water molecule. As common for such systems with diamagnetic bridging ligands, magnetic interactions are weak in this complex and the impressive zero-field $U_{\text{eff}} = 319(9) \text{ cm}^{-1}$ ($\tau_0 = 1.11 \times 10^{-10} \text{ s}$) derives from Dy^{III} single-ion anisotropy.^{49c} This barrier is almost the same within error as that measured for $[\text{Zn}_2\text{DyL}_2(\text{MeOH})]^+$, though no magnetic hysteresis was observed due to quenching of magnetic anisotropy at low temperature.⁶⁸

We note finally here that the measured relaxation barriers for both the Zn^{II} and Fe^{II} complexes agree more closely with the second excited state separations predicted from ab initio calculations; thus, perhaps relaxation through the second excited state may also be favored for these compounds as was the case with $\{\text{Dy}_4\text{K}_2\}$ and $\{\text{Dy}_5\}$ (it is important, however, to not indiscriminately trust computational results as mentioned below). Indeed, targeting Dy^{III} compounds with anisotropic ligand fields enforced by one or two strong axial ligands appears to be a most promising route to enhancing slow relaxation through higher excited states.

A final compound that requires mention here is $[\text{Cp}^*\text{Dy}(\text{BPh}_4)]$ (Figure 1.8, right, $[\text{Cp}^*]^-$ = pentamethylcyclopentadienyl anion), which exhibits $U_{\text{eff}} = 331 \text{ cm}^{-1}$ ($\tau_0 = 1 \times 10^{-9} \text{ s}$) and butterfly magnetic hysteresis for $T \leq 5.3 \text{ K}$.⁶⁹ This molecule is unique in this discussion, lacking any clearly defined axial symmetry, however the $[\text{BPh}_4]^-$ group is only very weakly coordinated and therefore may be seen as contributing a weak transverse anisotropy, which may be implicit in the magnetization drop in the hysteresis without precluding a sizable relaxation barrier. This example will be illustrative below in the discussion of radical-bridged compounds.

Equatorially-Coordinated Erbium(III) Compounds. Though Tb^{III} and Dy^{III} have come to dominate single-molecule magnetism, among some of the earliest systems studied were $[\text{Er}(\text{W}_5\text{O}_{18})_2]^{9-}$ and $[\text{Er}(\text{SiW}_{11}\text{O}_{39})_2]^{13-}$.⁷⁰ These molecules were investigated along with the other later lanthanides due to their approximate D_{4d} symmetry, akin to $[\text{LnPc}_2]^-$, though only Er^{III} showed slow magnetic relaxation under zero dc field above 2 K, with $U_{\text{eff}} \sim 38 \text{ cm}^{-1}$. Notable for these molecules is the axial compression of the oxygen coordination sphere, relative to the coordinated nitrogen atoms in $[\text{LnPc}_2]^-$. Thus, the former can be considered to afford a more equatorial coordination environment favoring slow magnetic relaxation for Er^{III} .⁷¹ Just two years later, the molecule $\text{ErCp}^*(\text{COT})$ (COT^{2-} = cyclooctatetraenyl dianion) was found to relax slowly under zero dc field to temperatures as high as 22 K, a discovery that has since sparked a small surge in the study of Er^{III} compounds.⁷² Two Orbach mechanisms were characterized for this molecule with $U_{\text{eff}} = 224 \text{ cm}^{-1}$ ($\tau_0 = 8.17 \times 10^{-11} \text{ s}$) and 137 cm^{-1} ($\tau_0 = 3.13 \times 10^{-9} \text{ s}$), and were ascribed to two conformers in the crystal structure. This molecule also showed butterfly magnetic hysteresis as high as 5 K and for a 1:20 (Er:Y) magnetic dilution, the loop opened at zero dc field and 1.8 K with $M_R \sim 0.7 \mu_B$. The exceptional slow relaxation observed for this complex, relative to prior Er^{III} systems can be rationalized by considering that the conjugated π -system formed by the $[\text{Cp}^*]^-$ and COT^{2-} ligands creates a strong equatorial ligand field,⁷³ preferentially stabilizing $M_J = \pm 15/2$. Indeed, calculations using the program CONDON⁵⁶ as well as a recent combined study utilizing rotating angle magnetometry and ab initio calculations⁷⁴ confirmed the Ising nature of the ground state.

In lieu of the relaxation through higher excited states observed for $\{\text{Dy}_4\text{K}_2\}$ and $\{\text{Dy}_5\}$, it is interesting to consider more closely the predicted energy level separations for $\text{ErCp}^*(\text{COT})$. From ab initio, the ground to first excited separation (using a DFT-optimized structure) agrees only for the smaller experimental U_{eff} , and the total splitting within the ground J is predicted to be less than 300 cm^{-1} . In contrast using CONDON, the ground to first and second excited state separations were found to be 189 cm^{-1} ($M_J = \pm 13/2$) and $\sim 225 \text{ cm}^{-1}$ ($M_J = \pm 1/2$), which agree much better with the experimentally determined U_{eff} values, and raises the possibility that the two processes might derive from relaxation through the first and second excited states, rather than the two conformers in the crystal structure.⁷⁵ We note that the discrepancy in these two computational methods highlights the difficulty in accurately determining the electronic structure for these systems, and that in addition to taking great care in drawing too many conclusions from

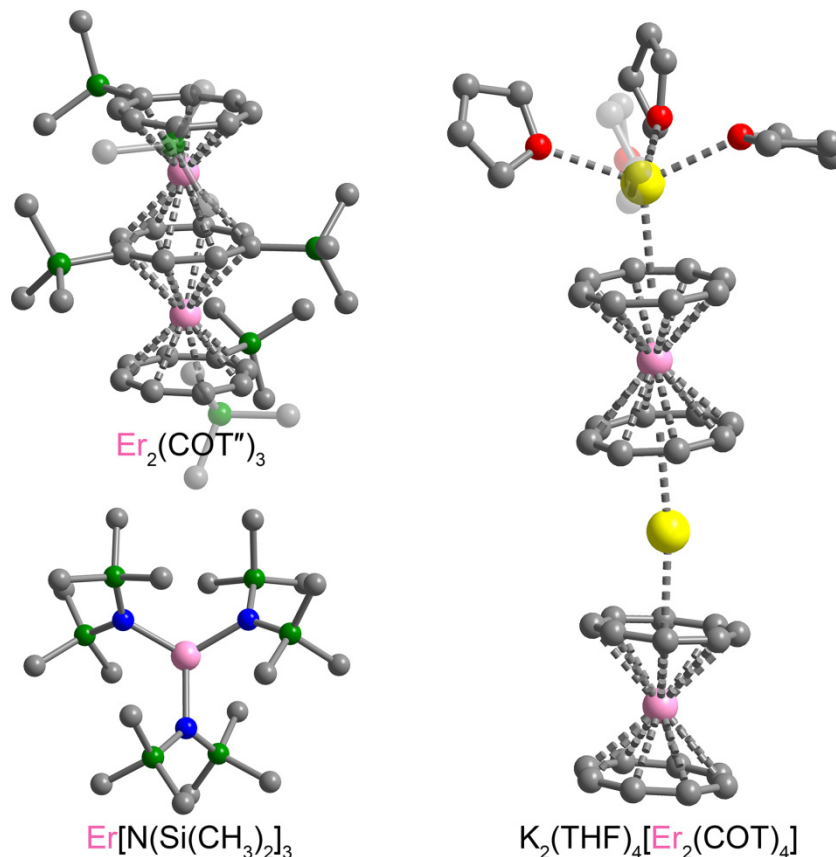


Figure 1.9. X-ray structures of $\text{Er}_2(\text{COT}'')_3$, $\text{K}_2(\text{THF})_4[\text{Er}_2(\text{COT})_4]$, and $\text{Er}[\text{N}(\text{SiMe}_3)_2]_3$ as described in the text. Pink, grey, red, blue, green, and yellow spheres represent Er, C, O, N, Si, and K atoms, respectively.^{78,80}

computations alone, a more complete computational model may be more appropriate to describe slow relaxation for f-element compounds.⁷⁶

Given the impressive properties of the $\text{ErCp}^*(\text{COT})$ molecule, it is interesting to consider how replacing the $[\text{Cp}^*]^-$ with COT^{2-} would maintain the equatorial coordination while enhancing molecular symmetry. This strategy will be discussed in Chapter 4, but an analogous system subsequently reported in the literature illustrates its promise. Indeed, by using the more soluble substituted COT^{2-} ligand 1,4-bis(trimethylsilyl)cyclooctatetraenide ($[\text{COT}'']^-$), the homoleptic complex $[\text{Er}(\text{COT}'')_2]^-$ could be isolated and was found to exhibit slow relaxation to 31 K with $U_{\text{eff}} = 130(1) \text{ cm}^{-1}$ ($\tau_0 = 4.0 \times 10^{-8} \text{ s}$) and open hysteresis to 8 K.⁷⁷ While no dilute samples were measured for this molecule, it is interesting to consider that magnetic dilution might also lead to opening of the hysteresis as observed for $\text{ErCp}^*(\text{COT})$.

Efforts to enhance the slow magnetic relaxation observed for these Er^{III} compounds led to the study of $\text{Er}_2(\text{COT}'')_3$ and $\text{K}_2(\text{THF})_4[\text{Er}_2(\text{COT})_4]$ (Figure 1.9).⁷⁸ While it was intended to examine the influence of any magnetic coupling of the highly anisotropic mononuclear units, the observed slow relaxation appears to derive from single-ion anisotropy. In the former compound, two Er^{III} ions are coordinated via a central $[\text{COT}'']^{2-}$ ligand with an $\text{Er}^{\text{III}} \cdots \text{Er}^{\text{III}}$ separation of 4.11 Å, while for the latter two $[\text{Er}(\text{COT})_2]^-$ units are bridged via a potassium cation with an $\text{Er}^{\text{III}} \cdots \text{Er}^{\text{III}}$ separation of 8.82 Å. Weak magnetic coupling present in $\text{Er}_2(\text{COT}'')_3$ ($J = -0.448 \text{ cm}^{-1}$

determined for the Gd^{III} analogue, see Ref. 143) leads to a low moment in the ground exchange doublet, while the excited exchange doublet possesses a much larger moment due to ferromagnetic interaction between Er^{III} centers. This crossover leads to a very different hysteresis behavior compared to the mononuclear compound, and even though hysteresis is observed to 12 K, the loop is open only slightly at 1.8 K and the coercive field is essentially zero. Thus, while it is possible the coupling may enhance the highest hysteresis temperature overall, the dinuclear species is a softer magnetic than the mononuclear compound. On the other hand, the observed $U_{\text{eff}} = 232 \text{ cm}^{-1}$, nearly twice that of the mononuclear analogue, and agrees with the second excited state separation for the individual Er^{III} centers. Similarly, for K₂(THF)₄[Er₂(COT)₄], the much larger Er^{III}...Er^{III} facilitates relaxation of single-ion origin and both the hysteresis to 12 K and $U_{\text{eff}} = 213 \text{ cm}^{-1}$ (19-32 K) arise from single-ion behavior, while the enhancements of both values were ascribed to a slightly different ligand field environment compared to [Er(COT)₂]⁻.⁷⁹ In spite of an enhanced barrier for K₂(THF)₄[Er₂(COT)₄], the hysteresis loop is closed at zero field for all temperatures.

A final recent success with Er^{III} is the complex Er[N(SiMe₃)₂]₃, exhibiting a slightly distorted trigonal planar arrangement of amide ligands. Under zero applied field, this molecule relaxes with $U_{\text{eff}} = 85 \text{ cm}^{-1}$,⁸⁰ a value that agrees quite well with a calculated first excited state separation of 82 cm⁻¹ determined by solving a crystal field Hamiltonian with parameters obtained from oriented single-crystal linear dichroism.⁸¹ While relaxation is clearly favored through the first excited state in the concentrated compound, ab initio computations predict that the experimental barrier could be as large as 331 cm⁻¹, due to most favorable relaxation through the fourth excited state in the absence of transverse anisotropy.⁸² These authors observed that while transversal magnetic moments between opposing Kramers doublets contribute in part to the lower observed barrier, magnetic dilution could significantly enhance U_{eff} .

In closing this section, we consider briefly the individual successes for Dy^{III} and Er^{III} systems. While Dy^{III} relaxation barriers are the largest, few systems exhibit magnetic hysteresis with remnant magnetization; however, a combination of magnetic dilution and isotopic enrichment with $I = 0$ nuclei is perhaps a viable strategy to enhance low temperature relaxation and remnant magnetization in some of these most promising systems (see Ref. 28). For the mononuclear Er^{III} species discussed above, open hysteresis is already observed for temperatures as high as 8 K, agreeing well with predicted relaxation times from the experimental barriers. Thus, in the appropriate ligand field Er^{III} shows great promise toward developing harder magnets based on single-ions, and again in these cases isotopic enrichment may very serve to even further enhance magnetic hysteresis. A common theme for both categories of compounds does arise when considering that relaxation consistently occurs via only the first or perhaps second excited M_J state. Though relaxation through the full J manifold remains elusive at this stage, targeting appropriate ligand fields and mitigating contributions from dipolar and hyperfine interactions continue to be exceedingly promising strategies in tandem.

Dinuclear Radical-Bridged Lanthanide Complexes. Undoubtedly, the most promising route thus far toward generating harder molecular magnets has been to target certain lanthanide-radical bridged compounds.⁸³ Notwithstanding extensive efforts in the design of compounds based on nitronyl nitroxide radicals,⁸⁴ only within the last three years has the use of air-free techniques led to the isolation of some exceptional lanthanide systems, the most successful incorporating the N₂³⁻ radical unit.⁸⁵ Compared to the larger nitronyl nitroxide radical,⁸⁶ where low-spin densities on the donor atoms gives rise to weak coupling, the more diffuse spin orbitals of the N₂³⁻ radical are better able to penetrate the core electron density of the lanthanide 4f orbitals, leading to very

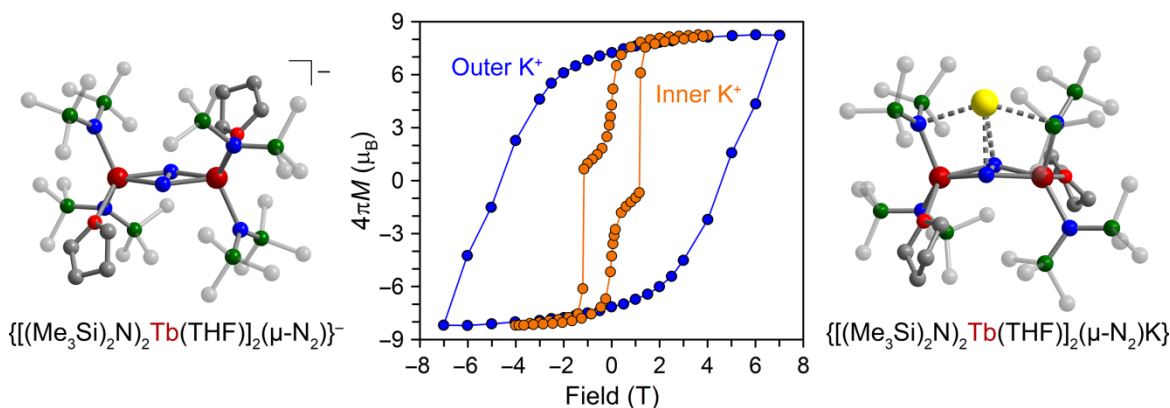


Figure 1.10. Comparison of the lowest temperature magnetic hysteresis data collected for $\{[(\text{Me}_3\text{Si})_2\text{N})_2\text{Tb}(\text{THF})]_2(\mu\text{-N}_2)\}^-$ (11 K, dark blue curve) and $\text{K}\{[(\text{Me}_3\text{Si})_2\text{N})_2\text{Tb}(\text{THF})]_2(\mu\text{-N}_2)\}$ (1.8 K, orange curve).^{13,88}

strong magnetic exchange.⁸⁷ This was first shown for the complexes $\{[(\text{Me}_3\text{Si})_2\text{N})_2\text{Ln}(\text{THF})]_2(\mu\text{-N}_2)\}^-$ (Ln = Gd, Tb, Dy, Ho, Er), composed of two lanthanide centers bridged by the N_2^{3-} radical and possessing a rigorously linear Ln- N_2^{3-} -Ln core. The Gd^{III} congener holds the record for strongest magnetic exchange in a lanthanide molecule ($J_{\text{Gd-radical}} = -27 \text{ cm}^{-1}$) while the Tb^{III} variant (Figure 1.10) exhibits $U_{\text{eff}} = 227.0(4) \text{ cm}^{-1}$ ($\tau_0 = 8.2 \times 10^{-9} \text{ s}$) and very square magnetic hysteresis to 14 K, the current record for any molecular species.^{13,88} The linear Ln- N_2^{3-} -Ln core is crucial to promote concerted magnetic exchange,⁸⁷ as will be discussed for the related complexes with an inner sphere potassium, $\{[(\text{Me}_3\text{Si})_2\text{N})_2\text{Ln}(\text{THF})]_2(\mu\text{-N}_2)\text{K}\}$ (Ln = Gd, Tb, Dy) in Chapter 5 (see Figure 1.10 for Tb^{III} analogue).⁸⁹

While the N_2^{3-} radical is exceptional in facilitating strong magnetic exchange, the synthetic challenge associated with its isolation and reactivity precludes its ready incorporation into other molecules or extended networks. Thus, effort has been directed to the study of more accessible redox active organic bridging ligands such as 2,2-bipyrimidine (bpym) and 2,3,5,6-tetrakis(2-pyridyl)pyrazine (tppz). The 2,2-bipyrimidine radical-bridged complexes $[(\text{Cp}^*_2\text{Ln})_2(\mu\text{-bpym})]^+$ (Ln = Gd, Tb, Dy, Figure 1.11) exhibit a linear Ln-radical-Ln unit analogous to the original N_2^{3-} species⁹⁰ and strong lanthanide radical coupling as indicated by static magnetic susceptibility measurements. Fitting of the dc susceptibility data obtained for the isotropic Gd^{III} analogue revealed weaker antiferromagnetic Ln-radical coupling with $J = -10 \text{ cm}^{-1}$, while the relaxation barriers exhibited by the Tb^{III} and Dy^{III} species were also smaller than for the N_2^{3-} compounds. Notable for this series is the fact that the Dy^{III} is the highest performer with $U_{\text{eff}} = 87.8(3) \text{ cm}^{-1}$ and magnetic hysteresis to 6.5 K.

With use of the larger tppz ligand it was possible to isolate the radical-bridged compounds $[(\text{Cp}^*_2\text{Ln})_2(\mu\text{-tppz})]^+$ and $[(\text{Cp}^*_2\text{Ln})_2(\mu\text{-tppz})]^-$ (Ln = Gd, Tb, Dy), wherein the tppz moiety is singly and triply-reduced, respectively (see Figure 1.11 for Dy^{III}). For these compounds, it becomes apparent that a large coupling constant, J , is a necessary though not sufficient condition for the observation of impressive slow magnetic relaxation. Indeed, for the Gd^{III} complexes of both series, the lanthanide-radical coupling strength was reported to be $J \sim -7 \text{ cm}^{-1}$, though only $[(\text{Cp}^*_2\text{Dy})_2(\mu\text{-tppz})]^+$ exhibits slow magnetic relaxation with $U_{\text{eff}} = 35.9(2) \text{ cm}^{-1}$. Additionally, while magnetic hysteresis is observed below 3.25 K, it is clear that this molecule is a much softer magnetic material than the related bpym compound.⁹¹ It is natural to ask, then, how future systems can be designed to exhibit both strong coupling and enhanced relaxation barriers. In this

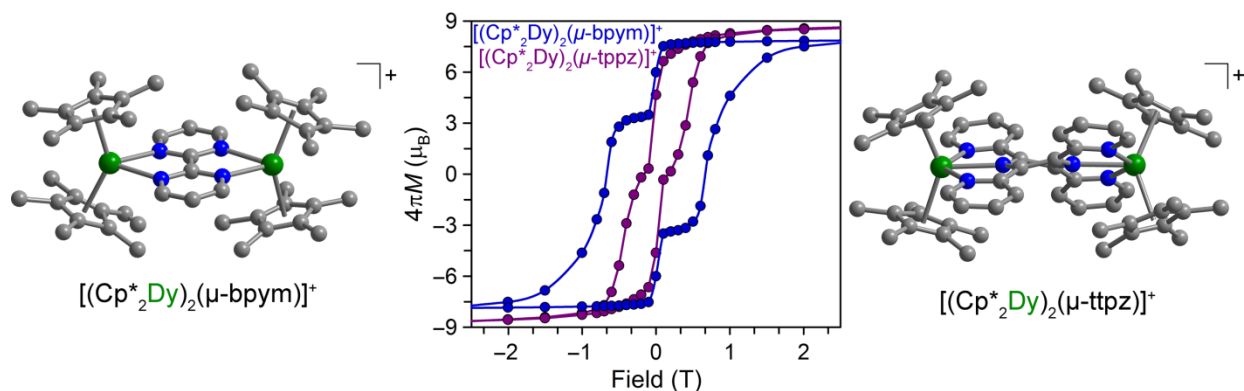


Figure 1.11. Comparison of the lowest temperature magnetic hysteresis data collected for $[(\text{Cp}^*_2\text{Dy})_2(\mu\text{-bpym})]^+$ (2 K, dark blue curve) and $[(\text{Cp}^*_2\text{Dy})_2(\mu\text{-ttpz})]^+$ (1.8 K, purple curve).^{90,91}

regard, the examples discussed above offer some interesting food for thought. Consider that the relaxation barrier exhibited by $[(\text{Cp}^*_2\text{Ln})_2(\mu\text{-bpym})]^+$ is smaller than that for $[\text{Cp}^*_2\text{Dy}(\text{BPh}_4)]$, while open hysteresis is observed to higher temperatures for the former. This can be rationalized by considering that upon replacement of the weakly coordinated $[\text{BPh}_4]^-$ ligand with the anionic bpym radical, the equatorial ligand field is enhanced, diminishing anisotropy.⁹² On the other hand, the radical facilitates strong coupling and a large moment, thus diminishing tunneling of the magnetization. In order to enhance coupling strength and anisotropy in tandem (i.e. diminish tunneling and increase the relaxation barrier), a suitable approach for an oblate ion such as Dy^{III} would be to design a compound wherein the radical bridge is also the source of a strong axial ligand field, which would then generate large anisotropy along the spin-coupling direction. Likewise, for a prolate ion such as Er^{III} , it is interesting to consider that bridging two $[(\text{COT}^{\text{II}})\text{Er}]^+$ moieties with a planar, π -conjugated radical would maintain an equatorial ligand field while promoting coupling along the most anisotropic direction of the molecule.

1.5 Actinides in Single-Molecule Magnetism

Actinide compounds were the last to join the ranks of single-molecule magnets and compose the smallest family, with only 21 complexes published to date.^{12c,93} As already mentioned, the actinides are unique given that in principle they combine the advantageous attributes of both the lanthanides and transition metals. The combination of qualities such as large magnetic anisotropy and the possibility for covalency, however, necessarily adds some new complexity. For instance, while covalency is advantageous for generating strong magnetic exchange, on the other hand it introduces a challenge in the rational design of mononuclear actinide complexes thus far not encountered with the lanthanides. This can be understood when considering the successful synthetic rationale in the design of mononuclear lanthanide systems as discussed above, namely choosing an appropriate ligand field symmetry such that a maximal M_J ground state electron density distribution is likely to be preferentially stabilized.^{45,58b,94} One main reason this approach has worked well for the lanthanides is that they do not participate in covalent bonding, and therefore their orbital angular momentum remains largely unquenched and the ligand field acts as a minor electrostatic perturbation that splits the degenerate M_J states within the ground J manifold. With the potential for covalency and therefore partial quenching of orbital angular momentum, such an approach for the actinides is less straightforward.⁹⁵ Taking a synthetic cue

Table 1.2. Comparison of spin-orbit coupling and crystal field splitting for isoelectronic U^{3+} and Nd^{3+} compounds; all values are reported in cm^{-1} .^a

Complex	ζ_{nf}	$N_v/\sqrt{4\pi}^b$	E (1 st excited M_J)	B_0^2
LaCl ₃ :U ³⁺	1607	634	208	260(64)
LaCl ₃ :Nd ³⁺	880	300	115	163
UTp ₃	1516	1386	270	-1124
NdTp ₃	881	514	107	-512

^a All values obtained from Ref. 42, 96 and references therein.

^b Measure of crystal field strength.

from recent developments in mononuclear transition metal complexes, a promising avenue for future mononuclear actinide systems could be to design low-coordinate complexes of weakly donating ligands, in order to maximize anisotropy. Given the oxo-philic nature and large ionic radii of the actinides (~ 0.95 - 1.05 Å for An^{3+}), however, such a goal will no doubt be a formidable synthetic challenge.

On the other hand, one advantage of covalency in actinide complexes may be the resulting larger overall crystal field splitting achieved when compared to isoelectronic lanthanide complexes.^{41,42,96} Table 1.2 compares values of the spin-orbit coupling interaction (ζ_{nf}), crystal field splitting, and B_0^2 crystal field parameter for two different compounds of U^{3+} and Nd^{3+} , obtained from parametric analysis of absorption and fluorescence spectra.⁹⁷ Both the spin-orbit coupling and crystal field parameters are nearly double for both uranium systems in comparison with their Nd^{3+} analogues. Accompanying a larger crystal field splitting is a larger magnitude for B_0^2 , which influences the sign and magnitude of the overall magnetocrystalline anisotropy.^{50,98} In turn, the larger crystal field also yields a larger separation between ground and first excited M_J states. Thus, much larger barriers and preferential Orbach relaxation might be accessible for the actinides compared to the lanthanides.^{45,58} This reasoning also suggests that the study of isoelectronic lanthanide complexes may provide a simple first pass in order to decipher potentially interesting actinide systems, especially for more challenging transuranic elements. For instance, when the study of an f^1 or f^3 actinide system is of interest, an isostructural Ce^{III} or Nd^{III} complex may serve as a good model.

The remarkable range of oxidation states accessible among the actinides is another potentially promising peculiarity. For instance, uranium is synthetically accessible in oxidation states ranging from +3 to +6, and even very recently +2.⁹⁹ Even considering only Kramers ions ($S =$ half integer), which are guaranteed to possess a doubly-degenerate $\pm M_J$ ground state in the absence of an applied field, then for the first half of the actinides there are twice as many potential magnetic centers than for the lanthanides. The very obvious caveat here is that this seeming abundance of choices is seriously limited by the accessibility and practicality of studying certain actinides. Only a handful of institutions in the world are equipped with all the means necessary to study transuranic single-molecule magnets, and the latter half of the 5f elements is perhaps entirely impractical due to the limitations of short half-lives and self heating. Not surprisingly, then, the study of slow relaxation among the actinides is dominated by the relatively stable and abundant ²³⁸U isotope. However, neptunium appears to be quite promising

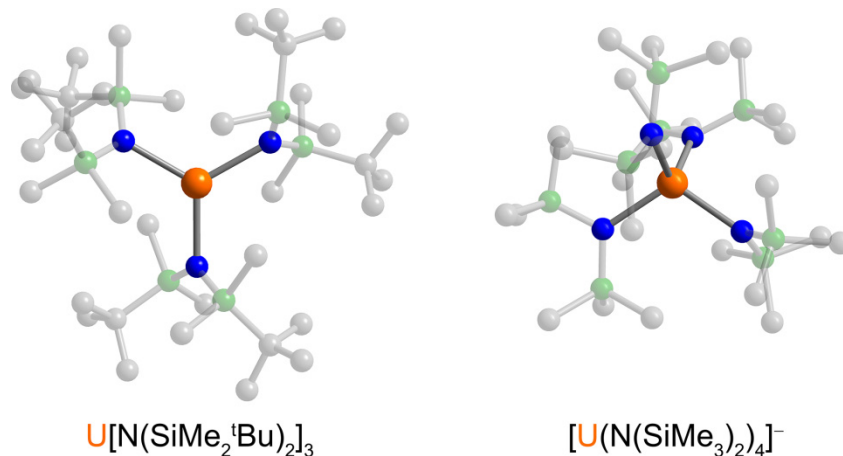


Figure 1.12. X-ray structures of $\text{U}[\text{N}(\text{SiMe}_2^t\text{Bu})_2]_3$ and $[\text{U}(\text{N}(\text{SiMe}_3)_2)_4]^-$ as described in the text. Orange, blue, grey, and green spheres represent U, N, C, and Si atoms, respectively.^{100,113}

in both mono- and multinuclear complexes. Thus, for an ambitious few, the first half of the series presents a fundamentally fascinating and exotic playground for molecular magnetism.

Mononuclear and Dinuclear Complexes. All but three of the known mono- or dinuclear actinide single-molecule magnets are based on U^{III} , a Kramers ion with a large total angular momentum ground state ($5f^3$, $J = 9/2$). The other systems are known with Np^{IV} (also $5f^3$), U^{V} ($5f^1$, $J = 5/2$), and Pu^{III} ($5f^5$, $J = 5/2$). Mononuclear complexes in particular are ideal for developing a more fundamental understanding of slow relaxation among the actinides, as these systems can be rationally designed and the absence of magnetic exchange simplifies computational modeling. As discussed at length for the lanthanides, maximizing single-ion anisotropy in the appropriate ligand field has allowed for the isolation of systems with impressive relaxation barriers and in some cases magnetic hysteresis. With spin-orbit coupling energies double the size of the lanthanides, it is perhaps surprising then that all mononuclear actinide systems studied thus far exhibit experimental U_{eff} values are $\leq 29 \text{ cm}^{-1}$ and for all but two complexes an applied field is necessary to observe slow magnetic relaxation. This is true for a range of coordination geometries and ions such as Pu^{III} , U^{III} , and U^{V} . At the same time, an uncannily common phenomenon is the observation of low-temperature magnetic hysteresis, despite ac relaxation times on the order of several milliseconds for most molecules at the same temperatures. For example, the recently isolated trigonal planar U^{III} molecule, $\text{U}(\text{N}^{**})_3$ (Figure 1.12, left, $\text{N}^{**} = \text{N}(\text{SiMe}_2^t\text{Bu})_2^-$),¹⁰⁰ exhibits butterfly magnetic hysteresis at 1.8 K, a surprising result given that the relaxation time at this temperature is only 45 ms (with $\tau_0 = 3.1 \times 10^{-7} \text{ s}$). As will be addressed in Chapter 2, there is evidence to suggest that this hysteresis is due to intermolecular interactions in the concentrated crystal, which are effectively “turned on” by large applied magnetic fields. Thus, for actinide systems in particular, extensive characterization of relaxation time at varying applied fields and measurements on dilute samples should perhaps become common methods of characterization.

Complexes of Uranium(III). Since the discovery of slow magnetic relaxation in $\text{U}(\text{Ph}_2\text{BPz}_2)_3$,^{10,44} scorpionate-based complexes of U^{III} have been predominant in the literature. As will be discussed in Chapter 2, it was of interest for example to examine the influence of ligand modifications on slow magnetic relaxation for trigonal prismatic U^{III} , which led to the study of $\text{U}(\text{Bp})_3$ ($[\text{Bp}]^- = [\text{H}_2\text{BPz}_2]^-$).¹⁰¹ Due to agostic $\text{U}\cdots\text{H}$ interactions, the trigonal prism of

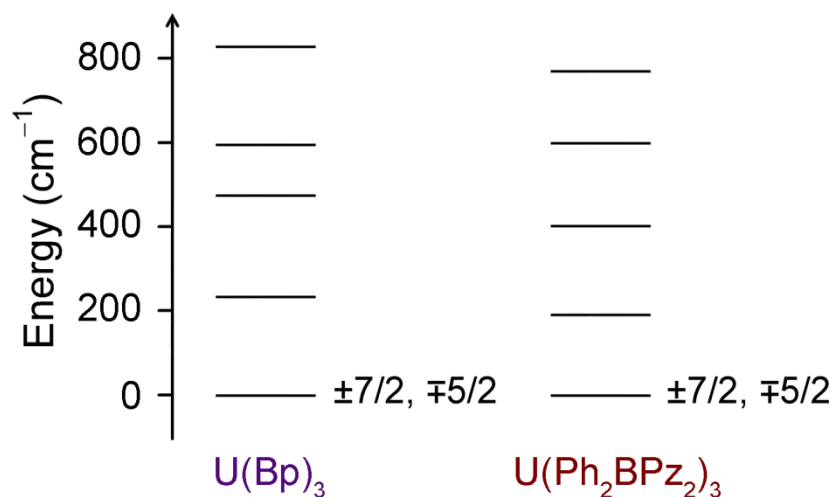


Figure 1.13. Comparison of the energy sublevel splitting within the ground $J = 9/2$ for $U(\text{Ph}_2\text{BPz}_2)_3$ and $U(\text{Bp})_3$ as determined in Ref. 104.

$U(\text{Bp})_3$ is elongated relative to $U(\text{Ph}_2\text{BPz}_2)_3$, and based on the qualitative rationale employed for the lanthanides above, this geometrical difference might serve as a starting point to understand the much smaller experimental barrier of 8 cm^{-1} for the former, observed only under an applied dc field.¹⁰² Notably, magnetic dilution in a $Y(\text{Bp})_3$ matrix does enhance the slow magnetic relaxation for $U(\text{Bp})_3$, leading to a near doubling of the thermally-activated barrier to 14.9 cm^{-1} for a 1:90 (U:Y) dilution (Chapter 2).¹⁰³ In the course of the latter studies on $U(\text{Bp})_3$, it was also found that for a 1:1 dilution, magnetic hysteresis could be observed as high as 3 K, a surprising result given the very short corresponding relaxation time (0.12 ms) determined by extrapolating Arrhenius data collected under $H_{\text{dc}} = 100 \text{ Oe}$. Elaboration on this phenomenon is continued in Chapter 2.

A recent computational investigation using a corrected crystal field model¹⁰⁴ was carried out on $U(\text{Ph}_2\text{BPz}_2)_3$ and $U(\text{Bp})_3$ to determine the wave functions and sublevel splitting of the ground $J = 9/2$ state. While this method predicts comparable ground to first excited state separations for the two complexes, the values are 190 and 230 cm^{-1} respectively, a shocking order of magnitude larger than the experimental U_{eff} values (Figure 1.13 and Table 1.3). This experimental and computational mismatch stands in stark contrast to the lanthanide systems discussed above, and is the rule and not the exception for mononuclear actinide-based single-molecule magnets. For instance, the field-induced single-molecule magnet UTp_3 presents the most extreme case of this discrepancy, as both spectroscopic and crystal field approaches predict a relaxation barrier of $U \sim 270 \text{ cm}^{-1}$ assuming relaxation through the first excited state, while the experimental “barrier” is nearly two orders of magnitude smaller at 3.8 cm^{-1} .¹⁰⁵

Given the predominance of N-donor scorpionate ligands, it became of interest to study how changing the donor atom within the same molecular symmetry might influence relaxation behavior. This investigation is detailed in Chapter 3, wherein study of the isostructural scorpionate complexes $U(\text{Bc}^{\text{Me}})_3$ ($[\text{Bc}^{\text{Me}}]^-$ = dihydrobis(methylimidazolyl)borate anion) and $U(\text{Bp}^{\text{Me}})_3$ ($[\text{Bp}^{\text{Me}}]^-$ = dihydrobis(methylpyrazolyl)borate anion) revealed that the more strongly-donating N-heterocyclic carbene engineers slower relaxation under an applied magnetic field with a much greater thermal dependence.¹⁰⁶ Even still, the apparent thermally activated experimental barrier for magnetically dilute $U(\text{Bc}^{\text{Me}})_3$ was only 23 cm^{-1} , notably very close to those determined for $U(\text{Ph}_2\text{BPz}_2)_3$ and $U(\text{Bp})_3$.

Table 1.3. Actinide single-molecule magnets (and one single-chain magnet) and diagnostic parameters.

Complex	$U_{\text{eff}}(\text{cm}^{-1})^{\text{a}}$	$U_{\text{calc}}(\text{cm}^{-1})$	τ_0 (s)	Crystal symmetry	Hysteresis (K) ^f	$\chi_{\text{r}} = \chi_{\text{dc}}^{\text{?h}}$	Ref.
U(Ph ₂ BPz ₂) ₃	20	190	$1 \times 10^{-7\text{e}}$	<i>P</i> -1		too large	10
U(Bp) ₃	16	230	4×10^{-7}	<i>C2/c</i>	3 ^g	yes	102,103
UTp ₃	3.8	270	7×10^{-5}	<i>P6₃/m</i>		too large	105
[UTp ^{Me2} ₂ (bipy)]I	18.2	137 ^c	1.4×10^{-7}	<i>C2/c</i>	0.32	yes	107
[UTp ^{Me2} ₂ (bipy)]	19.8 ^b		3.28×10^{-7}	<i>P2₁/c</i>	0.8	yes	111
[UTp ^{Me2} ₂]I	21.0	187 ^d	1.8×10^{-7}	<i>C2/m</i>	3	too large	108,109
U ₃ (THF) ₄	12.9		6.4×10^{-7}	<i>P2₁/c</i>		too large	112
U[N(SiMe ₃) ₂] ₃	22		10^{-11}	<i>P</i> -3 ₁ <i>c</i>		too large	112
[U(BIPM ^{TMS})(I ₂)(THF)]	16.3		2.9×10^{-7}	<i>P</i> -1		too large	112
U(Bc ^{Me}) ₃	23		1×10^{-7}	<i>R</i> -3		yes	106
U(Bp ^{Me}) ₃				<i>R</i> -3		yes	106
[U(OSi(O ^t Bu) ₃) ₄] ⁻	18		2.6×10^{-7}	<i>Pbca</i>		<i>i</i>	113
[U(N(SiMe ₃) ₂) ₄] ⁻	16		2.20×10^{-8}	<i>P2₁2₁2₁</i>		<i>i</i>	113
U(N**) ₃	14.9		3.1×10^{-7}	<i>C2/c</i>	1.8	too small	100
[U(BIPM ^{TMS})I] ₂ (μ-C ₆ H ₅ CH ₃)				<i>Fdd2</i>	1.8		114
UO(Tren ^{TIPS})	14.9		2.6×10^{-7}	<i>P2₁/c</i>	2.4	yes	115
{[UO ₂ (salen)] ₂ Mn(Py) ₃ } ₆	98.7		3×10^{-12}		4		136a
{UO ₂ Mn ₂ } ⁺	56		5.02×10^{-10}		3		138
[UO ₂ (salen)(Py)][Mn(Py) ₄](NO ₃)	93		3.1×10^{-11}		3		136b
Np(COT) ₂	28.5	1400	1.1×10^{-5}	<i>P2₁/n</i>	1.8		116
(Np ^{VI} O ₂ Cl ₂)[Np ^V O ₂ Cl(THF) ₃] ₂	97		not reported				43
PuTp ₃	18.3	332	2.9×10^{-7}	<i>P6₃/m</i>		too large	119

^a Obtained under H_{dc} except for U(Ph₂BPz₂)₃, [UTp^{Me2}₂(bipy)], {[UO₂(salen)]₂Mn(Py)₃}₆, {UO₂Mn₂}⁺, [UO₂(salen)(Py)][Mn(Py)₄](NO₃), and (Np^{VI}O₂Cl₂)[Np^VO₂Cl(THF)₃]₂.

^b Under zero dc field; under 500 Oe the barrier increases to 22.6 cm⁻¹ with $\tau_0 = 4.68 \times 10^{-8}$ s.

^c Average of the values calculated from SO-CASPT2 method and a corrected crystal field model (136 cm⁻¹ and 138 cm⁻¹, respectively).

^d Determined from the SO-CASPT2 method performed on the high-symmetry cationic structure, see Ref. 109.

^e The previously reported τ_0 value was 1×10^{-9} s; however re-plotting of the data revealed this to be an error, with the actual value equal to 1×10^{-7} s.

^f Maximum reported hysteresis temperature.

^g Hysteresis due to intermolecular interactions.

^h See Ref. 127.

ⁱ Dc and ac susceptibility data were reported at different fields, namely 5000 Oe and 500 Oe, respectively.

Two additional scorpionate-based complexes [UTp^{Me2}₂(bipy)]I¹⁰⁷ ([Tp^{Me2}]⁻ = hydrotris(dimethylpyrazolyl)borate anion, bipy = 2,2'-bipyridine) and [UTp^{Me2}₂]I^{108,109} were shown to relax slowly in the presence of a small dc field, with experimental relaxation barriers of 18.2 cm⁻¹ and 21.0 cm⁻¹, respectively. Following the same trend as above, these values are only a fraction of the calculated ground to first excited state gaps determined using the aforementioned crystal field approach or ab initio methods (Table 1.3). Notably, the 2,2'-bipyridine radical complex [UTp^{Me2}₂(bipy)],¹¹⁰ obtained from reduction of [UTp^{Me2}₂(bipy)]I with sodium amalgam, was found to relax slowly under zero dc field, with $U_{\text{eff}} = 19.8$ cm⁻¹.¹¹¹ This result is a promising indication that magnetic coupling can efficiently diminish tunneling of the magnetization even in mononuclear uranium complexes. For all three of the above complexes, magnetic hysteresis could furthermore be observed at low temperatures. While [UTp^{Me2}₂(bipy)]I and [UTp^{Me2}₂(bipy)] show hysteresis only below 1 K, [UTp^{Me2}₂]I presents a butterfly hysteresis loop as high as 3 K.

The uniformity among actinide single-molecule magnets is well exemplified in the remaining six mononuclear U^{III} complexes currently known in the literature. Indeed, the compounds $U_3(THF)_4$, $U[N(SiMe_3)_2]_3$, and $[U(BIPM^{TMS})(I_2)(THF)]$ ($BIPM^{TMS} = CH[PPh_2NSiMe_3]_2$) present remarkably similar relaxation with barriers of 12.9 cm^{-1} , 22 cm^{-1} , and 16.2 cm^{-1} , respectively, despite their different symmetries (Table 1.3). Although no calculated energy barriers are available for these complexes, the experimental relaxation barriers are small and similar to those reported for scorpionate-based systems. No magnetic hysteresis was observed for these samples, and while solution measurements confirmed the molecular origins of the slow magnetic relaxation, strangely the values of U_{eff} were smaller than determined for the concentrated species.¹¹² The three most recent U^{III} literature additions, namely $[U(OSi(O^tBu)_3)_4]^-$ and $[U(N(SiMe_3)_2)_4]^-$ (Figure 1.12, right) with tetrahedral symmetry¹¹³ and $U(N^{**})_3$, also exhibit slow relaxation only under H_{dc} with comparable relaxation barriers of 18 cm^{-1} , 16 cm^{-1} , and $14.9(1)\text{ cm}^{-1}$, respectively. For $U(N^{**})_3$, the relatively small relaxation barrier observed only under H_{dc} might be explained away by the predominantly $M_J = \pm 1/2$ ground state, verified by X- and Q-band EPR measurements at 5 K, however the ground state of the tetrahedral compounds was not determined, and further this logic does not hold for several systems incorporating scorpionate ligands wherein the ground state is dominated by $M_J = \pm 5/2$.¹⁰⁴ Heavy mixing of M_J states may be the culprit for the absence of zero-field slow relaxation for these latter molecules, and $U_{\text{eff}}/U \ll 0.01$ for all systems studied thus far reveals the possible significance of Raman relaxation (vide infra).

A final U^{III} complex reported to show slow magnetic relaxation under a dc field of 0.1 T was the dinuclear arene-bridged species $[U(BIPM^{TMS})I]_2(\mu\text{-C}_6\text{H}_5\text{CH}_3)$.¹¹⁴ The observed relaxation was very fast, however, such that peaks in the out-of-phase susceptibility were only apparent below 3 K and at high frequencies of the oscillating field, precluding the extraction of relaxation times. In spite of ac relaxation times on the order of a few milliseconds, a butterfly-shaped magnetic hysteresis loop was also reported for this complex at 1.8 K.

Complexes of Uranium(V), Neptunium(IV), and Pu(III). Three additional mononuclear systems illustrate the diversity accessible with actinides. The first of these is the C_{3v} symmetric uranium(V) complex $UO(\text{Tren}^{\text{TIPS}})$ ($\text{Tren}^{\text{TIPS}} = [N(\text{CH}_2\text{CH}_2\text{NSi}^i\text{Pr}_3)_3]^{3-}$), for which a pure $M_J = \pm 3/2$ ground state was inferred from magnetization and EPR studies.¹¹⁵ Slow magnetic relaxation was observed for this complex only under an applied dc field, with a relaxation barrier of 14.9 cm^{-1} , the same order of magnitude as observed for mononuclear U^{III} complexes. Despite a very small relaxation barrier, this U^V complex was also reported to show butterfly-shaped magnetic hysteresis loops as high as 2.4 K.

One of only two mononuclear transuranic systems displaying slow magnetic relaxation is the homoleptic bis(cyclcoctatetraenide) complex $Np(\text{COT})_2$, as probed under applied fields greater than 0.1 T.¹¹⁶ Notably, earlier characterization of this complex at 4.2 K using Mössbauer spectroscopy revealed magnetic splitting of the quadrupole doublet, which was attributed to the occurrence of slow spin-lattice relaxation.¹¹⁷ A rigorous ligand field analysis estimated the ground state of this complex to be predominantly $M_J = \pm 5/2$, separated from the first excited state by an enormous energy gap of $\sim 1400\text{ cm}^{-1}$. However, under an applied field of 0.3 T, an energy barrier of just 28.5 cm^{-1} was determined. Under larger applied fields ($> 5\text{ T}$), it was found that the relaxation times for this complex slow dramatically, leading to very steep Arrhenius behavior and the opening of a magnetic hysteresis loop above 5 T at 1.8 K. The fast relaxation at low fields was attributed to hyperfine interactions of the $M_J = \pm 5/2$ ground doublet with the $I = 5/2$ nuclear spin of ^{237}Np .¹¹⁸

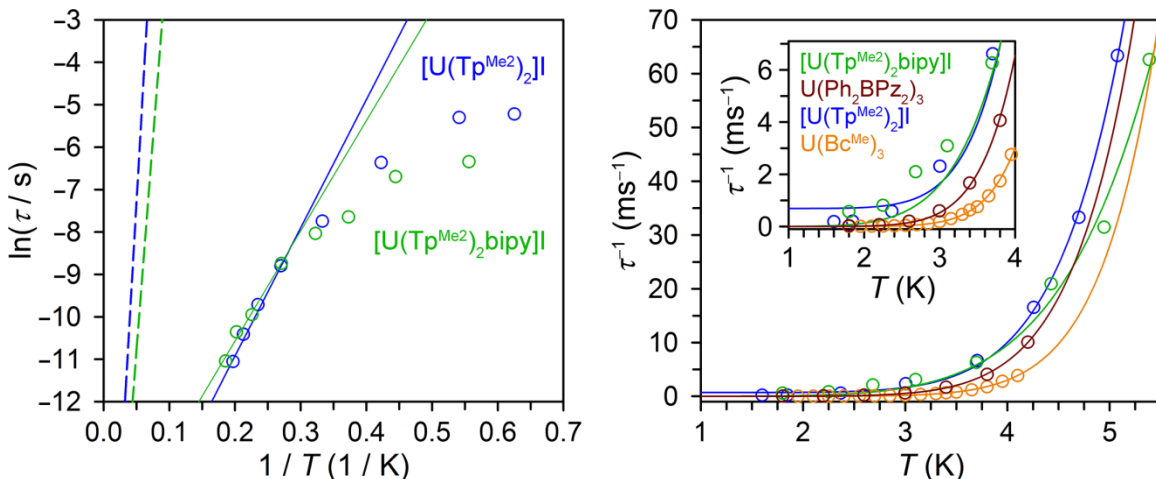


Figure 1.14. (Left) Plot of $\ln(\tau)$ versus $1/T$ for $[UTp^{Me2}]I$ ^{108,109} and $[UTp^{Me2}(bipy)]I$ ¹⁰⁷ ($H_{dc} = 500$ Oe). Circles represent experimental data, solid lines represent linear Arrhenius fits, and dashed lines represent the predicted Arrhenius behavior assuming calculated ground to first excited M_J separations of 187 cm^{-1} and 138 cm^{-1} , respectively, and a τ_0 of 1×10^{-9} s. (Right) Plot of the inverse relaxation time versus T for $[UTp^{Me2}]I$, $[UTp^{Me2}(bipy)]I$, $U(Bc^{Me})_3$,¹⁰⁶ and $U(Ph_2BPz_2)_3$.¹⁰ Circles represent the full range of temperature-dependent data and solid lines represent fits to a Raman relaxation process. Values of C/n were found to be $0.15(7) / 7.9(2)$; $2(1) / 6.2(5)$; $0.002(6) / 9.91(1)$; and $0.034(8) / 8.8(2)$ for each complex, respectively. In the case of $[UTp^{Me2}]I$ the fit was improved by also accounting for quantum tunneling of the magnetization with $\tau_{QTM} = 1.5(9)$ ms. (Inset) Expanded view of the low temperature fit region.

Recently, $PuTp_3$ was reported to show slow magnetic relaxation under a dc field of 100 Oe ($H_{ac} = 10$ Oe) and to temperatures as high as 12 K, with $U_{eff} = 18.3\text{ cm}^{-1}$. This compound represents the first plutonium-based single-molecule magnet, and possesses the same symmetry as its U^{III} congener. Accordingly, by using the same crystal field parameters as those obtained spectroscopically for UTp_3 (Ref. 92b), the authors were able to extract wave functions and energies of the sublevels within the ground $J = 5/2$ manifold. The ground state is predominantly $M_J = \pm 5/2$ and separated from a nearly pure excited $M_J = \pm 3/2$ by 332 cm^{-1} , almost 20 times that of the experimental barrier. The authors note that the relaxation mechanism is therefore more complex than for transition metal clusters (and importantly, also many lanthanide complexes).¹¹⁹

Fast Relaxation and U_{eff} Discrepancies. From the above survey, two distinct trends distinguish low-nuclearity actinide single-molecule magnets from their 4f predecessors. The first is the very small (and remarkably similar) U_{eff} values across all compounds, when available calculations predict much larger separations between the ground and first excited state M_J doublets. This difference is illustrated for $[UTp^{Me2}]I$ and $[UTp^{Me2}(bipy)]I$ in Figure 1.14, and is in contrast to many lanthanide complexes, wherein U_{eff} values have been found to correlate with the ground to first excited state energy gap.^{9,120}

For $Np(COT)_2$ the mismatch cannot be explained by hyperfine interactions, for even under large dc fields where these should be irrelevant, the experimental barrier is still only a fraction of the calculated value. For the uranium systems, the scenario is even more opaque. While ^{238}U has no nuclear spin, dipolar interactions may play a role in speeding up molecular relaxation, though measurements on magnetically dilute actinide molecules are sparse. If the predicted relaxation barriers are correct in their order of magnitude estimate, it appears that the relaxation observed

on the ac timescale must necessarily be some other spin-lattice relaxation process that is not truly thermally-activated.

With this in mind, we thought it illustrative to plot the inverse of the relaxation time, τ^{-1} , versus temperature for some of the aforementioned complexes, to gain insight into the relevance of Raman or direct processes. Interestingly, the whole range of temperature-dependent data for $[\text{UTp}^{\text{Me}_2}_2]\text{I}$ and $[\text{UTp}^{\text{Me}_2}_2(\text{bipy})]\text{I}$ can be fit quite well to a power dependence on temperature, e.g. $\tau^{-1} = CT^n$, corresponding to a two-phonon Raman process.¹²¹ The same procedure also provides very good fits for $\text{U}(\text{Ph}_2\text{BPz}_2)_3$ and even $\text{U}(\text{Bc}^{\text{Me}})_3$, discussed in Chapter 3 (Figure 1.14, right). Thus, in the characterization of future systems it will be important to evaluate the temperature-dependent relaxation data for all relevant relaxation processes in order to determine which is in fact the most reasonable. At this point of course, the lingering question remains as to why Orbach relaxation seems largely inaccessible in these systems.

One possible culprit is that for all of the mononuclear compounds discussed above, the ground M_J is non-maximal.¹²² Such a scenario is less than ideal, as a maximal M_J ground state corresponds to the largest projection of the angular momentum and therefore the greatest magnetic anisotropy. In the case of the homoleptic scorpionate systems, the ground state is also impure, due to symmetry-allowed mixing between $M_J = \pm^{5/2}$ and $M_J = \pm^{7/2}$.¹²³ This result derives from the presence of approximate C_{3h} or D_{3h} symmetry for most of these complexes,¹²⁴ which will always allow mixing of M_J states that differ by ± 6 due to the B_6^6 crystal field parameter.^{106,125} It may thus seem ideal to move away from ligands that enforce a trigonal prismatic geometry in pursuit of pure, larger magnitude ground states. However, as has been previously addressed in Ref. 104, the solution is not so simple, for instance in tetragonal symmetry the ground state will likely be of larger magnitude $M_J = \pm^{9/2}$ or $M_J = \pm^{7/2}$, though there will be heavy symmetry-allowed mixing with $M_J = \pm^{1/2}$.¹⁰⁴ One remedy is perhaps to move toward systems with much higher symmetry, such as D_{5h} or $C_{\infty v}$, wherein mixing of ground states will be less facile due to the reduction in crystal field parameters.^{33a} Either of these approaches would present non-trivial synthetic challenges.¹²⁶ Ultimately, a more rigorous understanding of the relationship between the temperature-dependent relaxation and the magnetic ground state will surely require more exotic experimental methods and computational analysis. Such an investigation will be worthwhile toward informing future synthetic designs.

Magnetic Hysteresis and Dipolar Interactions. The second trend for the foregoing complexes is the existence of magnetic hysteresis at low temperatures. The pervasive assumption here is that this hysteresis is due to molecular relaxation; however, as will be seen in Chapter 2, only for $\text{U}(\text{Bp})_3$ has the origin of magnetic hysteresis been thoroughly vetted and found to arise from intermolecular interactions, even at a separation of ~ 8.5 Å (importantly, this relaxation process is strongly field-dependant, and grows in magnitude with increasing applied fields). Therefore, the common logic that a separation of ~ 8 - 9 Å should preclude strong dipolar interactions is not wholly founded. In fact, before attempting the study of dilute samples, a very simple test can be performed to determine whether dipolar relaxation (in the form of fast or slow processes) deserves further attention. This test is to compare the isothermal susceptibility value (χ_T) with the static magnetic susceptibility value at the same temperature (χ_{dc}). If the ac relaxation process under study represents the major relaxation process, then these two susceptibility values should agree for a given temperature and range of magnetic fields. If instead χ_T is less than χ_{dc} , this suggests a slower relaxation process is also occurring, and perhaps dipolar interactions could play a role.¹²⁷ Without variable-field data for most of the compounds under consideration here, it is not possible to say whether dipolar interactions are important in the

relaxation and observed magnetic hysteresis. However, as the analysis in Chapter 2 suggests, the molecular origins of magnetic hysteresis are not definitive, and it seems important that dipolar interactions and the possibility of additional relaxation mechanisms be considered for these and future low-nuclearity systems.

1.6 Slow Magnetic Relaxation and Exchange in Multinuclear Actinide Complexes

While mononuclear complexes of the actinides have proven a tough nut to crack, the study of exchange-coupled systems has led to some early successes. Indeed, the three multinuclear exchange-coupled molecules studied to date exhibit moderate to large U_{eff} values and open magnetic hysteresis of molecular origin; thus, in this scenario the greater radial extension of the 5f orbitals and enhanced covalency are a great boon.

Magnetic exchange in actinide complexes has been known for over 20 years, since it was first observed in the dinuclear U^V species $[(\text{MeC}_5\text{H}_4)_3\text{U}]_2(\mu\text{-}1,4\text{-N}_2\text{C}_6\text{H}_4)$.¹²⁸ Even before the discovery of slow magnetic relaxation in $\text{U}(\text{Ph}_2\text{BPz}_2)_3$, exchange coupling was recognized as a potential route toward the design of actinide single-molecule magnets.^{129,130} Indeed, exchange constants estimated for complexes such as $[(\text{MeC}_5\text{H}_4)_3\text{U}]_2(\mu\text{-}1,4\text{-N}_2\text{C}_6\text{H}_4)$ ($J = 19(1) \text{ cm}^{-1}$), $(\text{cyclam})\text{Co}[(\mu\text{-Cl})\text{U}(\text{Me}_2\text{Pz})_4]_2$ ($15 \text{ cm}^{-1} \geq J \geq 48 \text{ cm}^{-1}$),¹³¹ and the arene-bridged U^{IV} complex $[\text{HC}(\text{SiMe}_2\text{Ar})_2(\text{SiMe}_2\text{-}\mu\text{-N})](\mu\text{-Ar})\text{U}(\text{Ts}^{\text{Xy}})$ ¹³² ($J = 20 \text{ cm}^{-1}$) rival coupling strengths in transition metal complexes, and are the same order of magnitude as the strong lanthanide-radical exchange observed for $[\{[(\text{Me}_3\text{Si})_2\text{N}]_2(\text{THF})\text{Gd}\}_2(\mu\text{-N}_2)]^-$ (vida supra) and by extension $[\{[(\text{Me}_3\text{Si})_2\text{N}]_2(\text{THF})\text{Tb}\}_2(\mu\text{-N}_2)]^-$, the single-molecule magnetic exhibiting the highest known blocking temperature.

At the same time, strong magnetic exchange is not a necessary prerequisite for the observation of slow magnetic relaxation. For instance, as mentioned above, magnetic exchange has been successfully demonstrated in a number of dinuclear lanthanide single-molecule magnets, though the bridging species are predominantly diamagnetic, and the coupling is therefore very weak.¹³³ As a consequence of this weak coupling, the resultant slow magnetic relaxation originates from single-ion anisotropy, and in fact sometimes the weak coupling can even hamper slow magnetic relaxation due to closely-spaced exchange coupled states that facilitate fast quantum relaxation.¹³³ Thus, strong exchange is crucial for achieving a well-isolated ground state, and thereby favoring the observation of slow magnetic relaxation. Indeed, only in the case of $[\{[(\text{Me}_3\text{Si})_2\text{N}]_2(\text{THF})\text{Ln}\}_2(\mu\text{-N}_2)]^-$ has very strong magnetic exchange been demonstrated to be essential to the observed relaxation.^{88,134} The nature of magnetic exchange is also of significant import, as suggested by recent DFT and ab initio calculations on these N_2^{3-} radical-bridged complexes. The calculations predict strong antiferromagnetic coupling for $\text{Ln} = \text{Tb}$, Dy , and Ho^{III} , but ferromagnetic coupling for $\text{Ln} = \text{Er}^{\text{III}}$, an interesting result given that the Er^{III} congener requires an applied field to observe slow relaxation on the ac time-scale, and displays the smallest relaxation barrier. Ultimately, however, these results suggest that slow magnetic relaxation should be accessible in multinuclear actinide complexes with an appropriate superexchange pathway.

Cation-Cation Interactions and Strong Magnetic Exchange. A well-established route to superexchange in actinide-containing multinuclear species is through cation-cation interactions, whereby the oxo-ligands of an actinyl unit (commonly uranyl(V)) interact with another metal center. This linkage effectively forms an oxo-bridge between metal centers and to date has been the most successful strategy toward strong coupling between U^V centers¹³⁵ and between U^V and

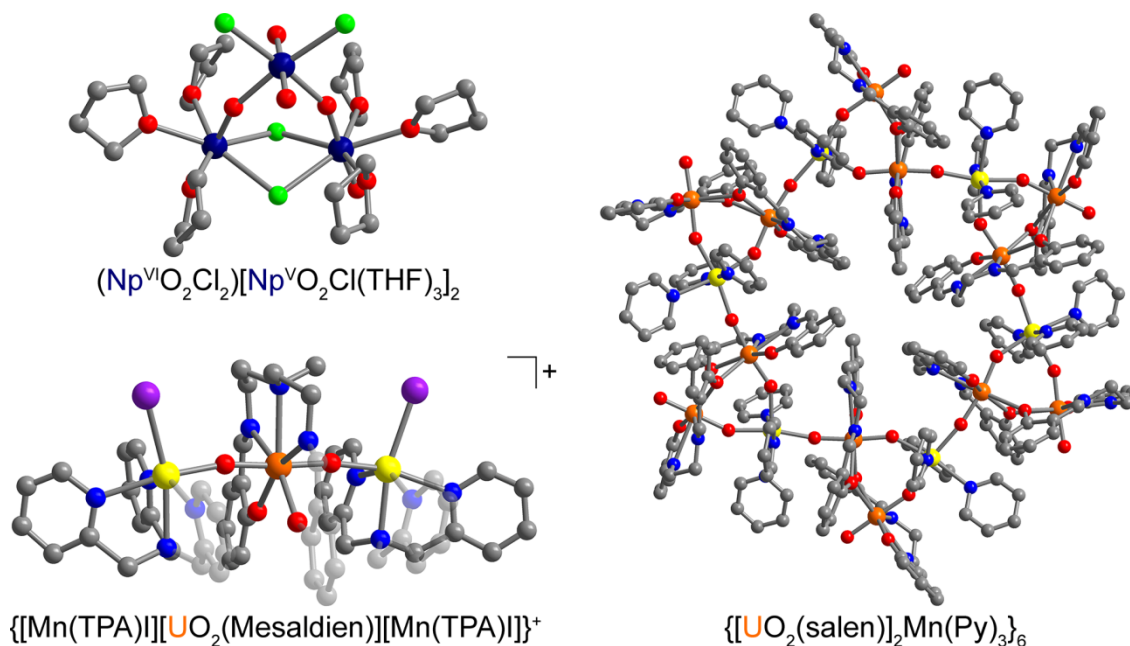


Figure 1.15. Molecular structures of the neptunium cluster $(\text{Np}^{\text{VI}}\text{O}_2\text{Cl}_2)[\text{Np}^{\text{V}}\text{O}_2\text{Cl}(\text{THF})_3]_2$ (top left),⁴³ MnUMn complex (bottom left),¹³⁸ and uranyl(V) wheel $\{[\text{UO}_2(\text{salen})]_2\text{Mn}(\text{Py})_3\}_6$ (right).^{136a} Dark blue, orange, yellow, green, red, purple, blue, and grey spheres represent Np, U, Mn, Cl, O, I, N, and C atoms, respectively; H atoms are omitted for clarity.

transition metal¹³⁶ or lanthanide centers.¹³⁷ Perhaps not surprisingly, then, the first multinuclear actinide complex to demonstrate both superexchange and slow magnetic relaxation was assembled through cation-cation interactions. The complex $(\text{Np}^{\text{VI}}\text{O}_2\text{Cl}_2)[\text{Np}^{\text{V}}\text{O}_2\text{Cl}(\text{THF})_3]_2$ is a triangular cluster made up of two chloride-bridged neptunyl(V) units at the base and a capping neptunyl(VI) unit (Figure 1.15). Considering the environment of the individual neptunyl moieties, it was found that all three neptunium centers experience a dominant axial ligand field due to strong, short, and nearly linear Np–O bonds of the neptunyl unit. Static magnetic susceptibility measurements on the trinuclear complex revealed a rise in the magnetic susceptibility below 25 K and 3 T, which was attributed to exchange coupling. This data could be fit by accounting for the strong axial ligand field and also antiferromagnetic exchange between neptunyl centers. Coupling between Np^{V} and Np^{VI} was found to be quite strong with $J = -7.51 \text{ cm}^{-1}$, while only very weak coupling occurs between Np^{V} centers, with $J = -0.39 \text{ cm}^{-1}$.⁴³

In addition to strong exchange, slow magnetic relaxation was observed for this complex under zero applied dc field and a 15 Oe ac field. The temperature-dependent relaxation behavior is approximated well by an Arrhenius law with $U_{\text{eff}} = 97 \text{ cm}^{-1}$ and lacks the marked deviation at low temperature demonstrated by the mononuclear complexes discussed above. Interestingly, the authors noted that the calculated energy gap corresponds well to the presence of an excited $M_J = \pm 5/2$ state of Np^{VI} , which would suggest that the slow magnetic relaxation originates from a single ion, and further exposes the potential promise in designing mononuclear complexes of Np^{VI} with dominant axial ligand fields.

The second actinide-based cluster to demonstrate magnetic exchange and slow magnetic relaxation was also assembled through cation-cation interactions, this time between uranyl(V) moieties and Mn^{II} centers.^{136a} The large, wheel-shaped cluster $\{[\text{UO}_2(\text{salen})]_2\text{Mn}(\text{Py})_3\}_6$ (Py = pyridine) depicted in Figure 1.15 was synthesized from the reaction of

[Cp*₂Co][UO₂(salen)(Py)] and Mn(NO₃)₂ in pyridine, in a 2:1 ratio. This molecule is structurally unique in that it is the largest actinide-based multinuclear complex and the first to be assembled through UO₂⁺ and Mn^{II} interactions. Additionally, the nature of the early metal cation was essential to the formation of such a high nuclearity complex, as the use of Ca^{II} was found to produce only a tetrameric uranyl(V) cluster. Interestingly, while for (Np^{VI}O₂Cl₂)[Np^VO₂Cl(THF)₃]₂ the cation-cation interactions necessarily occur between neptunium ions, the wheel complex is assembled in such a fashion that cation-cation interactions occur only between uranyl(V) units and Mn^{II} centers; individual uranyl(V) units are connected only via salen linkages. Static magnetic susceptibility data collected below 7 T revealed a sharp rise in $\chi_M T$ below ~60 K, similar to the susceptibility behavior observed for (Np^{VI}O₂Cl₂)[Np^VO₂Cl(THF)₃]₂. For the wheel complex, the behavior was also attributed to a combination of ligand field effects and coupling between metal centers; however, no modeling of the magnetic data was attempted due to the complexity of the system.

In addition to evidence of superexchange, blocking of the magnetization was observed for U₁₂Mn₆ in the form of magnetic hysteresis below 4.5 K. A drop in the magnetization at zero field occurs for all reported temperatures and is most pronounced at the lowest temperature of 2.25 K, indicative of quantum tunneling of the magnetization. On the ac time-scale, slow magnetic relaxation was observed between 5 and 10 K under zero dc field and a 10 Oe oscillating field. The resulting relaxation times could be fit well to an Arrhenius law to give $U_{\text{eff}} = 99 \text{ cm}^{-1}$ with a rather small $\tau_0 = 3 \times 10^{-12} \text{ s}$. As the authors alluded to, diamagnetic substitution of the Mn^{II} centers within the wheel with Cd^{II} or Zn^{II} would provide valuable insight into the exact nature and origins of the magnetic coupling. In addition, such an experiment would be an interesting probe of how the exchange coupling influences the observed slow magnetic relaxation.

While the complexity of U₁₂Mn₆ precluded quantification of magnetic coupling, for the molecule $\{[M(\text{TPA})\text{I}][\text{UO}_2(\text{Mesaldien})][M(\text{TPA})\text{I}]\}_2$ (Figure 1.15), magnetic susceptibility data could be fit with the Hamiltonian $\hat{H} = -2J(\hat{S}_{\text{Mn1}}\hat{S}_{\text{U}} + \hat{S}_{\text{U}}\hat{S}_{\text{Mn2}})$ to extract $J = 7.5 \text{ cm}^{-1}$, which might be considered an upper bound on the magnetic coupling for the wheel compound, given the larger Mn-O-U bond angles in the latter. This trinuclear species exhibited $U_{\text{eff}} = 56.3(3) \text{ cm}^{-1}$ ($\tau_0 = 5.02 \times 10^{-10} \text{ s}$) and hysteresis to 3 K. Magnetic characterization of the analogue with M = Cd^{II} revealed relaxation only under H_{dc} at high frequencies of the oscillating field, highlighting the likely importance of magnetic coupling in shutting down zero-field tunneling.¹³⁸

Gratifyingly, it was also found that by employing the same synthetic conditions used to isolate U₁₂Mn₆, but combining [Cp*₂Co][UO₂(salen)(Py)] and Mn(NO₃)₂ in a 1:1 ratio, the first actinide-based single-chain magnet could be isolated, namely [UO₂(salen)(Py)][Mn(Py)₄](NO₃).^{136b} This compound does not qualify as a single-molecule magnet, though its magnetic behavior is noteworthy and further illustrative of the utility of exchange in actinide systems. Indeed, below a temperature of 150 K, dc magnetic susceptibility data exhibit a sharp rise in $\chi_M T$, indicative of ferromagnetic coupling between the U^V and Mn^{II} centers. Moreover, ac susceptibility measurements under zero dc field revealed strong temperature and frequency dependence in the out-of-phase signal, χ_M'' , indicative of single-chain magnet behavior. This result was further supported by the observation of a linear regime in $\ln(\chi_M T)$ versus $1/T$. In addition to a large relaxation barrier of $U_{\text{eff}} = 93 \text{ cm}^{-1}$, an open magnetic hysteresis loop was observed for this compound as high as 3 K. Interestingly, the analogous Cd^{II}-containing chain was also found to show slow relaxation of the magnetization (under an applied dc field), undoubtedly due to the single-ion anisotropy associated with the U^V centers. As expected, the relaxation was significantly faster and less temperature-dependent than observed

for the UMn chain compound, although this result highlights the future utility of dominant axial ligand fields in mononuclear actinide complexes, as already demonstrated in the complex $\text{UO}(\text{Tren}^{\text{TIPS}})$. Indeed, mononuclear uranyl(V) complexes with weak equatorial ligands may present a worthwhile avenue for pursuit.

Targeting superexchange-coupled molecules thus appears to be a promising route in the design of actinide single-molecule magnets, and the small values of τ_0 observed in these systems, among other factors, indicate that the exchange is facilitating relaxation through primarily thermal means. Given the relative ambiguity of the role of magnetic coupling in the slow magnetic relaxation, however, future design of exchange-coupled molecules might benefit from a view towards smaller nuclearity clusters, for which diamagnetic substitution can be more readily performed. Additionally, as the use of paramagnetic bridging ligands in dinuclear lanthanide complexes has been proven the most successful route for exchange-coupled single-molecule magnets, a natural progression is the pursuit of analogous systems with actinide elements. While the N_2^{3-} radical is rather challenging synthetically, linkers such as bipyrimidine, pyrazine,¹³⁹ and phenazine¹⁴⁰ might serve as more suitable paramagnetic bridging species. As an example of the design of such structures, the mononuclear species $[\text{UTp}^{\text{Me}_2}_2(\text{bipy})]\text{I}$ stands as a useful building unit. Indeed, exchange of the bipyridine with bipyrimidine or other bridging N-heterocycles should facilitate the formation of a dinuclear complex that could be further reduced to form a radical-bridged species. The design and study of such simpler exchange-coupled structures is enticing both from a synthetic standpoint and toward a goal of expanding understanding of their unusual magnetic behavior.

1.7 Conclusions and Outlook

Of the many diverse approaches that have developed over the last two decades, it is clear that maximizing anisotropy and magnetic exchange are two of the most promising in the design of new single-molecule magnets; further by combining these individual approaches, it may be possible to enhance relaxation barriers and improve hysteresis behavior in the same molecule. While the area of lanthanide single-molecule magnetism is arguably well-established, there are no doubt improvements that will continue to be made and continued fine tuning of mononuclear systems in particular promises to lead to molecules with even more impressive relaxation barriers, and perhaps realization of relaxation through the full ground J manifold. Even though strategies such as isotopic enrichment with $I = 0$ nuclei and magnetic dilution are not currently state of the art for all studies in the literature, recognition of the sundry and sometimes subtle ways in which dipolar and hyperfine interactions can affect relaxation behavior will hopefully bring these more into the mainstream.

Actinide-based systems are proving to be richly complex in their relaxation behavior relative to the lanthanides, and a key step forward in their study will be the more rigorous characterization of relaxation dynamics in low-nuclearity species, including via dilution measurements, and particularly when a complex shows markedly different relaxation behavior depending on the applied magnetic field and/or temperature. Potentially promising mononuclear systems might be those with significantly higher axial site symmetries that may minimize state mixing and maximize orbital angular momentum. However, given the new challenges introduced with the use of the actinides, such as enhanced covalency and reactivity, it stands to reason that mononuclear complexes of these ions may be hard-pressed to succeed in the same way as their 4f forerunners. On the other hand, the few exchange-coupled systems studied suggest that

rationally-designed multinuclear complexes may be a more direct route to successful single-molecule magnets with the actinides, just as mononuclear species are arguably the most promising among the lanthanides. Finally, while outside the scope of synthetic chemistry, it is important to reemphasize that for the mononuclear actinide compounds, the models currently being used to describe electronic structure and understand molecular slow relaxation are in some ways insufficient, for example when solely relaxation through virtual excited states is observed on the ac time-scale. Indeed, for complexes of these metals and even for the lanthanides, perhaps more complete theoretical models are necessary to accurately describe electronic structure.^{56,76}

In the subsequent chapters in this dissertation, some of the themes that have been established here will be important for the molecules under discussion; for instance, the complexity of uranium slow magnetic relaxation will be examined in detail for U(Bp)₃ in Chapter 2. Expanding on the importance of symmetry and the ligand field in lanthanide systems, Chapter 3 will investigate the role of donor strength across two series of complexes for the later lanthanides and also U^{III}, here the role of non-Orbach relaxation mechanisms will also be discussed in detail. In Chapter 4, the importance of an equatorial coordination environment and dipolar interactions is investigated for Er^{III} in the homoleptic complex [Er(COT)₂]⁻, which is found to exhibit one of the highest blocking temperatures for a mononuclear system. Changing course slightly, Chapter 5 will investigate the relaxation dynamics and magnetic coupling in a new series of N₂³⁻ radical-bridged complexes, highlighting the importance of a linear Ln-radical-Ln bridge in promoting concerted exchange and slow relaxation.

1.8 References

- (1) Mattis, D. C. *The Theory of Magnetism I*; Springer-Verlag: Berlin, 1981; 1-37. Apparently, the origin of the name is debatable, however, and the magnet may have been named after an ancient Greek shepherd, Magnes.
- (2) Croat, J. J.; Herbst, J. F.; Lee, R. W.; Pinkerton, F. E. *J. Appl. Phys.* **1984**, *55*, 2078.
- (3) Strnat, K. J.; Hofer, G.; Olson, W.; Ostertag, W.; Becker, J. J. *J. Appl. Phys.* **1967**, *38*, 1001.
- (4) (a) Caneschi, A.; Gatteschi, D.; Sessoli, R. *J. Am. Chem. Soc.* **1991**, *113*, 5874. (b) Sessoli, R.; Tsai, H. L.; Schake, A. R.; Wang, S.; Vincent, J. B.; Folting, K.; Gatteschi, D.; Christou, G.; Hendrickson, D. N. *J. Am. Chem. Soc.* **1993**, *115*, 1804. (c) Sessoli, R.; Gatteschi, D.; Caneschi, A.; Novak, M. A. *Nature* **1993**, *365*, 141.
- (5) (a) Torres, F.; Hernández, J. M.; Bohigas, X.; Tejada, J. *Appl. Phys. Lett.* **2000**, *77*, 3248. (b) Sessoli, R. *Angew. Chem. Int. Ed.* **2012**, *51*, 43 and references therein.
- (6) (a) Liang, W.; Shores, M. P.; Bockrath, M.; Long, J. R.; Park, H. *Nature* **2002**, *417*, 725. (b) Jo, M.-H.; Grose, J. E.; Baheti, K.; Deshmukh, M. M.; Sokol, J. J.; Rumberger, E. M.; Hendrickson, D. N.; Long, J. R.; Park, H.; Ralph, D. C. *Nano Lett.* **2006**, *6*, 2014. (c) Heersche, H. B.; de Groot, Z.; Folk, J. A.; van der Zant, H. S. J.; Romeike, C.; Wegewijs, M. R.; Zoppi, L.; Barreca, D.; Tondello, E.; Cornia, A. *Phys. Rev. Lett.* **2006**, *96*, 206801. (d) Urdampilleta, M.; Nguyen, N.-V.; Cleuziou, J.-P.; Klyatskaya, S.; Ruben, M.; Wernsdorfer, W. *Int. J. Mol. Sci.* **2011**, *12*, 6656. (e) Thiele, S.; Vincent, R.; Holzmann, M.; Klyatskaya, S.; Ruben, M.; Balestro, F.; Wernsdorfer, W. *Phys. Rev. Lett.* **2013**, *111*, 037203.
- (7) (a) Komeda, T.; Isshiki, H.; Liu, J.; Zhang, Y.-F.; Lorente, N.; Katoh, K.; Breedlove, B. K.; Yamashita, M. *Nat. Commun.* **2011**, *2*, 217. (b) Urdampilleta, M.; Klyatskaya, S.;

- Cleuziou, J-P.; Ruben, M.; Wernsdorfer, W. *Nat. Mater.* **2011**, *10*, 502. (c) Candini, A.; Klyatskaya, S.; Ruben, M.; Wernsdorfer, W.; Affronte, M. *Nano Lett.* **2011**, *11*, 2634. (d) Clemente-Juan, J. M.; Coronado, E.; Gaita-Ariño, A. *Chem. Soc. Rev.* **2012**, *41*, 7464. (e) Ganzhorn, M.; Klyatskaya, S.; Ruben, M.; Wernsdorfer, W. *Nat. Nanotechnol.* **2013**, *8*, 165.
- (8) Aguilà, D.; Barrios, L. A.; Velasco, V.; Roubeau, O.; Repollés, A.; Alonso, P. J.; Sesé, J.; Teat, S. J.; Luis, F.; Aromí, G. *J. Am. Chem. Soc.* **2014**, *136*, 14215.
- (9) (a) Ishikawa, N.; Sugita, M.; Ishikawa, T.; Koshihara, S.-y.; Kaizu, Y. *J. Am. Chem. Soc.* **2003**, *125*, 8694. (b) Ishikawa, N.; Sugita, M.; Okubo, T.; Iino, T.; Kaizu, Y. *Inorg. Chem.* **2003**, *42*, 2440. (c) Ishikawa, N.; Sugita, M.; Ishikawa, T.; Koshihara, S.-y.; Kaizu, Y. *J. Phys. Chem. B* **2004**, *108*, 11265.
- (10) Rinehart, J. D.; Long, J. R. *J. Am. Chem. Soc.* **2009**, *131*, 12558.
- (11) Here, hysteresis temperature is defined as the highest temperature for which a compound demonstrates magnetic hysteresis with remnant magnetization at zero field. Thus, while many of the complexes represented in Figure 1.2 and Table 1.1 exhibit magnetic hysteresis, the majority of these loops are so-called “butterfly” in shape, where there is rapid relaxation at zero field, leading to no remnant magnetization.
- (12) (a) Woodruff, D. N.; Winpenny, R. E. P.; Layfield, R. A. *Chem. Rev.* **2013**, *113*, 5110. (b) Layfield, R. A. *Organometallics*, **2014**, *33*, 1084. (c) Magnani, N. *Int. J. Quantum Chem.* **2014**, *114*, 755. (d) Feltham, H. L. C.; Brooker, S. *Coord. Chem. Rev.* **2014**, *276*, 1. (e) Jiang, S.-D.; Wang, B.-W.; Gao, S. *Advances in Lanthanide Single-Ion Magnets*. In *Molecular Nanomagnets and Related Phenomenon*; Gao, S., Ed.; Springer-Verlag: Berlin, Heidelberg, 2014. (f) Milios, C. J.; Winpenny, R. E. P. *Cluster-Based Single-Molecule Magnets*. In *Molecular Nanomagnets and Related Phenomenon*; Gao, S., Ed.; Springer-Verlag: Berlin, Heidelberg, 2014.
- (13) Rinehart, J.; Fang, M.; Evans, W. J.; Long, J. R. *J. Am. Chem. Soc.* **2011**, *133*, 14236.
- (14) Gatteschi, D.; Sessoli, R. *Angew. Chem. Int. Ed.* **2003**, *42*, 268.
- (15) Yersin, H.; Strasser, J. *Coord. Chem. Rev.* **2000**, *208*, 331.
- (16) (a) Blagg, R. J.; Ungur, L.; Tuna, F.; Speak, J.; Comar, P.; Collison, D.; Wernsdorfer, W.; McInnes, E. J. L.; Chibotaru, L. F.; Winpenny, R. E. P. *Nat. Chem.* **2013**, *5*, 673. (b) Guo, Y.-N.; Ungur, L.; Granroth, G. E.; Powell, A. K.; Wu, C.; Nagler, S. E.; Tang, J.; Chibotaru, L. F.; Cui, D. *Sci. Rep.* **2014**, *4*, 1.
- (17) And, in principle, any orbitally non-degenerate transition metal ion or cluster see Ref. 18.
- (18) Gatteschi, D.; Sessoli, R.; Villain, J. *Molecular Nanomagnets*; Oxford University Press: Oxford, 2006.
- (19) Obtained from fitting magnetization data, see Ref 4a.
- (20) For example (a) Gonidec, M.; Biagi, R.; Corradini, V.; Moro, F.; De Renzi, V.; del Pennino, U.; Summa, D.; Muccioli, L.; Zannoni, C.; Amabilino, D. B.; Veciana, J. *J. Am. Chem. Soc.* **2011**, *133*, 6603. (b) Mannini, M.; Bertani, F.; Tudisco, C.; Malavolti, L.; Poggini, L.; Misztal, K.; Menozzi, D.; Motta, A.; Otero, E.; Ohresser, P.; Sainctavit, P.; Condorelli, G. G.; Dalcanale, E.; Sessoli, R. *Nat. Commun.* **2014**, *5*, 4582.
- (21) M_R = magnetization remaining after the field is swept from its maximum value back to zero dc field; H_C = dc field required to bring the sample moment back to zero.

- (22) The Gauss (G) is equivalent to the Ørsted, or Oe, in cgs units; Oe and Tesla, T, will be the unit of choice in this thesis and are related via $10,000 \text{ Oe} = 1 \text{ T}$.
- (23) At much higher frequencies, the field is oscillating too quickly for the magnet moment to respond either in or out of phase, leading to a zeroing of the magnetic susceptibility.
- (24) The exceptions to this observation are most exchange-coupled Mn clusters.
- (25) Other contributing factors might be dipolar interactions, mixing of M_S or M_J states, inherent molecular symmetry (and any resulting transverse magnetic anisotropy), vibronic coupling, hyperfine interactions, and even sample preparation (see for example Ref. 14, 18, and (a) Schenker, R.; Leuenberger, M. N.; Chaboussant, G.; Loss, D.; Güdel, H. U. *Phys. Rev. B* **2005**, *72*, 184403) and (b) Atanasov, M.; Zadrozny, J. M.; Long, J. R.; Neese, F. *Chem. Sci.* **2013**, *4*, 139.
- (26) Pedersen, K. S.; Bendix, J.; Clérac, R. *Chem. Commun.* **2014**, *50*, 4396 gives a very nice discussion of this variability in τ_0 .
- (27) Special thanks to Philip C. Bunting for pointing out this reference. Stöhr, J.; Siegmann, H. C. *Magnetism: From Fundamentals to Nanoscale Dynamics*; Springer: Heidelberg, Germany, 2006. As described on page 684, there is a so-called *intrinsic spin-lattice relaxation time* on the order to 100 ps (10^{-10} s), which corresponds to thermal equilibrium between phonons and electron spins. If the timescale is much longer, then the system is out of thermal equilibrium with the phonon bath. This correlates with $\tau_0 \gg 10^{-10}$ s, and the through barrier relaxation processes discussed above.
- (28) For example: spin-glass behavior, wherein below some transition temperature spin cooperation occurs in a non-ordered way, distinct from ferro- or antiferromagnets. These systems can also show slow relaxation in an ac field with $\tau_0 < 10^{-12}$ s. See Mydosh, J. A. *Spin Glasses: An Experimental Introduction*; Taylor and Francis: London, 1993.
- (29) Thomas, L.; Lionti, F.; Ballou, R.; Gatteschi, D.; Sessoli, R.; Barbara, B. *Nature* **1996**, *383*, 145.
- (30) Pointillart, F.; Bernot, K.; Golhen, S.; Le Guennic, B.; Guizouarn, T.; Ouahab, L.; Cador, O. *Angew. Chem. Int. Ed.* **2015**, *54*, 1504 and references therein. This study nicely shows that combined solid state magnetic dilution and enrichment of $[\text{Dy}(\text{tta})_3(\text{L})] \cdot \text{C}_6\text{H}_{14}$ ($\text{tta}^- = 2\text{-thenoyltrifluoroacetate}$, $\text{L} = 4,5\text{-bis}(\text{propylthio})\text{-tetrathiafulvaene-2-(2-pyridal)-benzimidazole methyl-2-pyridine}$) with $I = 0$ ^{164}Dy leads to a near 10,000-fold increase in the relaxation time at 2 K, as well as opening of the magnetic hysteresis loop at 0.46 K. However, the high temperature relaxation behavior (and therefore U_{eff}) was not affected by these strategies.
- (31) The first explicit characterization of a Raman relaxation process was for the complex $[\text{Dy}_4(\text{L})_4(\text{MeOH})_6]$ ($\text{H}_3\text{L} = 2\text{-hydroxy-3-methoxybenzoic acid} [(2\text{-hydroxy-3-methoxyphenyl)methylene] \text{hydrazide}$), which also exhibited Orbach relaxation with $U_{\text{eff}} = 120 \text{ cm}^{-1}$ and $\tau_0 = 1.2 \times 10^{-7}$ s, see Guo, Y.-N.; Xu, G.-F.; Gamez, P.; Zhao, L.; Lin, S.-Y.; Deng, R.; Tang, J.; Zhang, H.-J. *J. Am. Chem. Soc.* **2010**, *132*, 8538.
- (32) E.g. either the full energy splitting within the ground S or J , or even simply the ground to first excited state separation within a molecule.
- (33) (a) Liu, J.-L.; Chen, Y.-C.; Zheng, Y.-Z.; Lin, W.-Q.; Ungur, L.; Wernsdorfer, W.; Chibotaru, L. F.; Tong, M.-L. *Chem. Sci.* **2013**, *4*, 3310. (b) Pedersen, K. S.; Ungur, L.; Sigrist, M.; Sundt, A.; Schau-Magnussen, M.; Vieru, V.; Mutka, H.; Rols, S.; Weihe, H.; Waldmann, O.; Chibotaru, L. F.; Bendix, J.; Dreiser, J. *Chem. Sci.* **2014**, *5*, 1650.

- (34) Ako, A. M.; Hewitt, I. J.; Mereacre, V.; Clérac, R.; Wernsdorfer, W.; Anson, C. E.; Powell, A. K. *Angew. Chem. Int. Ed.* **2006**, *45*, 4926.
- (35) Neese, F.; Pantazis, D. A. *Faraday Discuss.* **2011**, *148*, 229.
- (36) Zadrozny, J. M.; Xiao, D. J.; Atanasov, M.; Long, G. J.; Grandjean, F.; Neese, F.; Long, J. R. *Nature Chem.* **2013**, *5*, 577.
- (37) Zadrozny, J. M.; Xiao, D. J.; Long, J. R.; Atanasov, M.; Neese, F.; Grandjean, F.; Long, G. J. *Inorg. Chem.* **2013**, *52*, 13123.
- (38) These parameters are the coefficients in the crystal field Hamiltonian describing the point-charge environment of the lanthanide ion, which in Wybourne notation is given by $\hat{H}_{CF} = \sum_{k=0}^6 \sum_{q=-k}^k B_q^k \hat{C}_q^k$ (\hat{C}_q^k are spherical tensor operators, see Wybourne, B. G. *Spectroscopic Properties of Rare Earths*; Wiley: New York, 1965). For high symmetry point groups such as $C_{\infty h}$ or $D_{\infty h}$, only the parameters B_0^2 , B_0^4 , and B_0^6 are allowed. Upon lowering the symmetry, off-diagonal parameters (in the matrix representation of the Hamiltonian, $q \neq 0$) become allowed, and these can induce mixing of M_J levels, leading to a decrease in magnetic anisotropy, depending on the molecular symmetry. See also Görller-Walran, C.; Binnemans, K. Rationalization of Crystal-Field Parameterization. In *Handbook on the Physics and Chemistry of Rare Earths, Vol 23*; Gschneidner Jr., K. A.; Eyring, L., Eds.; Elsevier: Amsterdam, 1996, pp 121-283.
- (39) (a) Ishikawa, N.; Iino, T.; Kaizu, Y. *J. Phys. Chem.* **2002**, *106*, 9543. (b) Ishikawa, N.; Iino, T.; Kaizu, Y. *J. Am. Chem. Soc.* **2002**, *124*, 11440.
- (40) Ganivet, C. R.; Ballesteros, B.; de la Torre, G.; Clemente-Juan, J. M.; Coronado, E.; Torres, T. *Chem. Eur. J.* **2013**, *19*, 1457.
- (41) Edelstein, N. *J. Alloys Compd.* **1995**, *223*, 197.
- (42) Crosswhite, H. M.; Crosswhite, H.; Carnall, W. T.; Paszek, A. P. *J. Chem. Phys.* **1980**, *72*, 5103.
- (43) Magnani, N.; Colineau, E.; Eloirdi, R.; Griveau, J.-C.; Caciuffo, R.; Cornet, S. M.; May, I.; Sharrad, C. A.; Collison, D.; Winpenny, R. E. P. *Phys. Rev. Lett.* **2010**, *104*, 197202.
- (44) Maria, L.; Campello, M. P.; Domingos, Á.; Santos, I.; Andersen, R. *J. Chem. Soc. Dalton Trans.* **1999**, 2015.
- (45) Rinehart, J. D.; Long, J. R. *Chem. Sci.*, **2011**, *2*, 2078.
- (46) Benelli, C.; Gatteschi, D. *Chem. Rev.* **2002**, *102*, 2369 and references therein.
- (47) (a) Sessoli, R.; Powell, A. K. *Coord. Chem. Rev.* **2009**, *253*, 2328; (b) Feltham, H. L. C.; Brooker, S. *Coord. Chem. Rev.* **2014**, *276*, 1. (c) Liu, W.; Shi, W.; Cheng, P. *Coord. Chem. Rev.* **2014**, DOI: 10.1016/j.ccr.2014.10.004.
- (48) Ledezma-Gairaud, M.; Grangel, L.; Aromí, G.; Fujisawa, T.; Yamaguchi, A.; Sumiyama, A.; Sañudo, E. C. *Inorg. Chem.* **2014**, *53*, 5878.
- (49) For example: (a) Papatriantafyllopoulou, C.; Wernsdorfer, W.; Abboud, K. A.; Christou, G. *Inorg. Chem.* **2011**, *50*, 421. (b) Langley, S. K.; Chilton, N. F.; Ungur, L.; Moubaraki, B.; Chibotaru, L. F.; Murray, K. S. *Inorg. Chem.* **2012**, *51*, 11873. (c) Liu, J.-L.; Wu, J.-Y.; Chen, Y.-C.; Mereacre, V.; Powell, A. K.; Ungur, L.; Chibotaru, L. F.; Chen, X.-M.; Tong, M.-L. *Angew. Chem. Int. Ed.* **2014**, *53*, 12966.
- (50) For example, Skomski, R. *Simple Models of Magnetism*; Oxford University Press: Oxford, 2008.
- (51) Sievers, J. Z. *Phys. B: Condens. Matter Quanta* **1982**, *45*, 289.
- (52) Ungur, L.; Chibotaru, L. F. *Phys. Chem. Chem. Phys.* **2011**, *13*, 20086.

- (53) Baldoví, J. J.; Borrás-Almenar, J. J.; Clemente-Juan, J. M.; Coronado, E.; Gaita-Ariño, A. *Dalton Trans.* **2012**, *41*, 13705.
- (54) Chilton, N. F.; Collison, D.; McInnes, E. J. L.; Winpenny, R. E. P.; Soncini, A. *Nat. Commun.* **2013**, *4*, 2551.
- (55) That is, the splitting of degenerate S or J states upon application of a static magnetic field.
- (56) (a) Schilder, H.; Lueken, H. *J. Magn. Magn. Mater.* **2004**, *281*, 17. (b) Speldrich, M.; Schilder, H.; Lueken, H.; Kögerler, P. *Isr. J. Chem.* **2011**, *51*, 215.
- (57) These include Inelastic Neutron Scattering, heat capacity measurements, and Near Infrared Spectroscopy.
- (58) (a) Watanabe, A.; Yamashita, A.; Nakano, M.; Yamamura, T.; Kajiwara, T. *Chem. Eur. J.* **2011**, *17*, 7428. (b) Chilton, N. F.; Langley, S. K.; Moubaraki, B.; Soncini, A.; Batten, S. R.; Murray, K. S. *Chem. Sci.* **2013**, *4*, 1719. (c) Aravena, D.; Ruiz, E. *Inorg. Chem.* **2013**, *52*, 13770.
- (59) This compound is notably a neutral species, unlike the original $[\text{LnPc}_2]^-$. Following characterization of these anionic species, it was shown that one or two electron oxidation to form $[\text{TbPc}_2]^0$ (and $[\text{Pc}(\text{OH}_{25}\text{C}_{12})_8]_2\text{Tb}$) or $[\{\text{Pc}(\text{OEt})_8\}_2\text{Tb}]^+$ led to enhancement of the original $U_{\text{eff}} = 230 \text{ cm}^{-1}$ to 410 cm^{-1} or 550 cm^{-1} (and reduction in τ_0) due to the contraction of the coordination sphere of the Tb^{III} . See also the magnetometry and surface study of $^1\text{Pc}_2\text{Tb}$ on graphite in Ref. 20a for which $U_{\text{eff}} = 556 \text{ cm}^{-1}$. These results may also be interpreted as nice experimental confirmation of this simple crystal field model, wherein enhancing the ligand field by bringing the axial charges closer to the oblate electron density of the Tb^{III} also enhances the magnetic anisotropy.
- (60) Blagg, R. J.; Muryn, C. A.; McInnes, E. J. L.; Tuna, F.; Winpenny, R. E. P. *Angew. Chem., Int. Ed.* **2011**, *50*, 6530.
- (61) For free Dy^{III} , the g -value for the lowest Kramers doublet $M_J = 15/2$ is 20; ab initio calculations on the perfectly axial $[\text{DyO}]^+$ (Ref. 52) gave $g_{\parallel} = 19.908$ with $g_{\perp} = 0$. Thus, the ground state for both $\{\text{Dy}_4\text{K}_2\}$ and $\{\text{Dy}_5\}$ is also dominated by $M_J = 15/2$. See Ref. 125 for a discussion of the anisotropic g -tensor.
- (62) A second process was also observed as a small shoulder at very low temperatures and could be tentatively fit to give $U_{\text{eff}} = 32.4(5) \text{ cm}^{-1}$.
- (63) Chilton, N. F.; Goodwin, C. A. P.; Mills, D. P.; Winpenny, R. E. P. *Chem. Commun.* **2015**, DOI: 10.1039/C4CC08312A.
- (64) This is despite a comparable ground to first excited state separation of $\sim 290 \text{ cm}^{-1}$ for both complexes, as determined from ab initio calculations, Ref. 33a.
- (65) Average axial distances in $[\text{Zn}_2\text{DyL}_2(\text{MeOH})]^+$ and $[\text{Zn}_2\text{DyL}_2]^+$ are 2.208(7) Å and 2.186(8), respectively, while average equatorial distances are 2.393(6) Å and 2.298(8) Å, respectively.
- (66) Calculations also revealed a highly axial ground state for the former, with $g_{x,y} = 0$, compared to $g_{x,v} = 0.01$ for the desolvated compound.
- (67) Ungur, L.; Le Roy, J. J.; Korobkov, I.; Murugesu, M. Chibotaru, L.F. *Angew. Chem. Int. Ed.* **2014**, *53*, 4413.
- (68) Based on Mössbauer characterization at 3 K under $H_{\text{dc}} = 6 \text{ T}$; this result again serves to emphasize the utility of enhancing lanthanide anisotropy in the absence of other magnetic interactions that can complicate or diminish slow relaxation.
- (69) Demir, S.; Zadrozny, J. M.; Long, J. R. *Chem. Eur. J.* **2014**, *20*, 9524.

- (70) (a) AlDamen, M. A.; Clemente-Juan, J. M.; Coronado, E.; Martí-Gastaldo, C.; Gaita-Ariño, A. *J. Am. Chem. Soc.* **2008**, *130*, 8874. (b) AlDamen, M. A.; Cardona-Serra, S.; Clemente-Juan, J. M.; Coronado, E.; Gaita-Ariño, A.; Martí-Gastaldo, C.; Luis, F.; Montero, O. *Inorg. Chem.* **2009**, *48*, 3467.
- (71) The first explicit recognition of the advantage of an equatorial ligand field for Er^{III} sparked the study of the macrocyclic compound [Er^{III}Zn^{II}₃(L)(OAc)(NO₃)₂(H₂O)_{1.5}(MeOH)_{0.5}]; even still this molecule only exhibited slow relaxation under $H_{dc} = 1000$ Oe with $U_{eff} = 5.6(3)$ cm⁻¹, see Yamashita, A.; Watanabe, A.; Akine, S.; Nabeshima, T.; Nakano, M.; Yamamura, T.; Kajiwara, T. *Angew. Chem. Int. Ed.* **2011**, *50*, 4016.
- (72) Jiang, S.-D.; Wang, B.-W.; Sun, H.-L.; Wang, Z.-M.; Gao, S. *J. Am. Chem. Soc.* **2011**, *133*, 19286.
- (73) Le Roy, J. J.; Jeletic, M.; Gorelsky, S. I.; Korobkov, I.; Ungur, L.; Chibotaru, L. F.; Murugesu, M. *J. Am. Chem. Soc.* **2013**, *135*, 3502.
- (74) Boulon, M.-E.; Cucinotta, G.; Liu, S.-S.; Jiang, S.-D.; Ungur, L.; Chibotaru, L. F.; Gao, S.; Sessoli, R. *Chem. Eur. J.* **2013**, *19*, 13726.
- (75) Indeed, for [Er(COT)₂]⁻ discussed in Chapter 4, changes to the immediate coordination sphere did not lead to detectable differences in ac relaxation behavior, see Meihaus, K. R.; Long, J. R. *J. Am. Chem. Soc.* **2013**, *135*, 17952.
- (76) van Leusen, J.; Speldrich, M.; Schilder, H.; Kögerler, P. *Coord. Chem. Rev.* **2014**, DOI: 10.1016/j.ccr.2014.10.011.
- (77) Le Roy, J. J.; Korobkov, I.; Murugesu, M. *Chem. Commun.* **2014**, *50*, 1602.
- (78) Le Roy, J. J.; Ungur, L.; Korobkov, I.; Chibotaru, L.F.; Murugesu, M. *J. Am. Chem. Soc.* **2014**, *136*, 8003.
- (79) In addition to the latter U_{eff} , a second relaxation process is observed from 7-12 K with $U_{eff} = 118(1)$ cm⁻¹. The two processes are ascribed to the individual Er^{III} centers, however we wonder if it is also possible that relaxation through the first and second excited states for a single Er^{III} is being observed. Indeed, if the two processes corresponded to the individual Er^{III} centers, they might be anticipated to exhibit similar magnitudes in χ_M'' , though in fact the larger observed barrier represents a much greater proportion of the total susceptibility of the sample. A similar discrepancy in the magnitude of χ_M'' was observed for the two relaxation modes of {Dy₄} (see Ref. 16a).
- (80) Zhang, P.; Zhang, L.; Wang, C.; Xue, S.; Lin, S.-Y.; Tang, J. *J. Am. Chem. Soc.* **2014**, *136*, 4484.
- (81) Reddmann, H.; Guttenberger, C.; Amberger, H.-D. *J. Organomet. Chem.* **2000**, *602*, 65.
- (82) Singh, S. K.; Gupta, T.; Shanmugam, M.; Rajaraman, G. *Chem. Commun.* **2014**, *50*, 15513.
- (83) Demir, S.; Jeon, I.-R.; Long, J. R.; Harris, T. D. *Coord. Chem. Rev.* **2014**, DOI: 10.1016/j.ccr.2014.10.012.
- (84) (a) Poneti, G.; Bernot, K.; Bogani, L.; Caneschi, A.; Sessoli, R.; Wernsdorfer, W.; Gatteschi, D. *Chem. Commun.* **2007**, 1807. (b) Xu, J.-X.; Ma, Y.; Xu, G.-F.; Wang, C.; Liao, D.-Z.; Jiang, Z.-H.; Yan, S.-P.; Li, L.-C. *Inorg. Chem. Commun.* **2008**, *11*, 1356. (c) Xu, J.-X.; Ma, Y.; Liao, D.-z.; Xu, G.-F.; Tang, J.; Wang, C.; Zhou, N.; Yan, S.-P.; Cheng, P.; Li, L.-C. *Inorg. Chem.* **2009**, *48*, 8890. (d) Tian, H.; Liu, R.; Wang, X.; Yang, P.; Li, Z.; Li, L.; Liao, D. *Eur. J. Inorg. Chem.* **2009**, *2009*, 4498. (e) Zhou, N.; Ma, Y.; Wang,

- C.; Feng Xu, G.; Tang, J.-K.; Xu, J.-X.; Yan, S.-P.; Cheng, P.; Li, L.-C.; Liao, D.-Z. *Dalton Trans.* **2009**, 8489. (f) Zhou, N.; Ma, Y.; Wang, C.; Xu, G.-F.; Tang, J.; Yan, S.-P.; Liao, D.-Z. *J. Solid State Chem.* **2010**, *183*, 927. (g) Wang, X.-L.; Li, L.-C.; Liao, D.-Z. *Inorg. Chem.* **2010**, *49*, 4735. (h) Pointillart, F.; Bernot, K.; Poneti, G.; Sessoli, R. *Inorg. Chem.* **2012**, *51*, 12218.
- (85) Evans, W. J.; Fang, M.; Zucchi, G.; Furche, F.; Ziller, J. W.; Hoekstra, R. M.; Zink, J. I. *J. Am. Chem. Soc.* **2009**, *131*, 11195.
- (86) Luneau, D.; Rey, P. *Coord. Chem. Rev.* **2005**, *249*, 2591.
- (87) Rajeshkumar, T.; Rajaraman, G. *Chem. Commun.* **2012**, *48*, 7856.
- (88) Rinehart, J. D.; Fang, M.; Evans, W. J.; Long, J. R. *Nat. Chem.* **2011**, *3*, 538.
- (89) Meihaus, K. R.; Corbey, J. F.; Fang, M.; Ziller, J. W.; Long, J. R.; Evans, W. J. *Inorg. Chem.* **2014**, *53*, 3099 and references therein.
- (90) Demir, S.; Zadrozny, J. M.; Nippe, M.; Long, J. R. *J. Am. Chem. Soc.* **2012**, *134*, 18546.
- (91) Demir, S.; Nippe, M.; Gonzalez, M. I.; Long, J. R. *Chem. Sci.* **2014**, *5*, 4701.
- (92) This logic might also serve to rationalize the absence of slow magnetic relaxation for the radical trianion species $[(\text{Cp}^*_2\text{Ln})_2(\mu\text{-tppz})]^-$, wherein the greater equatorial charge density might introduce large transverse anisotropy.
- (93) Meihaus, K. R.; Long, J. R. *Dalton Trans.* **2015** Advance Article, DOI: 10.1039/C4DT02391A.
- (94) Le Roy, J. J.; Korobkov, I.; Murugesu, M. *Chem. Commun.* **2014**, *50*, 1602. This is of course only one first step in a possible route to accessing systems showing slow relaxation and large relaxation barriers. Additional factors such as large axial anisotropy and nearly collinear ground and first excited state anisotropy axes have been shown to promote slow relaxation through thermally activated means. However, these attributes are often only determined computationally, after synthesis and ac susceptibility characterization, in order to further rationalize observed magnetic relaxation behavior.
- (95) The potential for covalency poses an additional challenge in the theoretical description of actinide-based complexes that is not an issue for the lanthanides. Alternatively, stronger metal-ligand interactions may aid in more fine-tuning of the electronics and therefore magnetic relaxation than is possible with the lanthanides.
- (96) (a) Reddmann, H.; Apostolidis, C.; Walter, O.; Amberger, H.-D. *Z. Anorg. Allg. Chem.* **2006**, *632*, 1405. (b) Apostolidis, C.; Morgenstern, A.; Rebizant, J.; Kanellakopoulos, B.; Walter, O.; Powietzka, B.; Karbowski, M.; Reddmann, H.; Amberger, H.-D. *Z. Anorg. Allg. Chem.* **2010**, *636*, 201.
- (97) The spin-orbit coupling constant ζ_{nf} is a coefficient used to describe the magnitude of the interaction between the spin magnetic moment of an individual electron with the magnetic field generated by its motion around the nucleus; the crystal field parameters B_q^k are obtained from transformation of corresponding coefficients within the crystal field Hamiltonian, where $k = 1 \dots 7$ and $q = 0 \dots 6$ increasing in integer values, see G6rlller-Walrand, C.; Binnemans, K. *Handbook of the Physics and Chemistry of the Rare Earths, Vol. 23*, Gschneidner Jr., K. A. and Eyrin, L. Elsevier, Amsterdam, 1996, 121-283. The sign and magnitude of B_0^2 is relevant as it influences the sign and magnitude of the magnetic anisotropy, see Ref. 98. $N_V/\sqrt{4\pi}$ of course represents the strength of the crystal field experienced by U^{3+} or Nd^{3+} due to the perturbation of the nf electrons by those of the Cl^- or $[\text{Tp}]^-$ (tris(pyrazolyl)borate anion) ligands.

- (98) Szytuła, A. and Leciejewicz, J. *Handbook of Crystal Structures and Magnetic Properties of Rare Earth Intermetallics*, CRC Press, Boca Raton, Florida, 1994.
- (99) (a) MacDonald, M. R.; Fieser, M. E.; Bates, J. E.; Ziller, J. W.; Furche, F.; Evans, W. J. *J. Am. Chem. Soc.* **2013**, *135*, 13310. (b) La Pierre, H. S.; Scheurer, A.; Heinemann, F. W.; Hieringer, W.; Meyer, K. *Angew. Chem. Int. Ed.* **2014**, *53*, DOI: 10.1002/ange.201402050.
- (100) Goodwin, C. A. P.; Tuna, F.; McInnes, E. J. L.; Liddle, S. T.; McMaster, J.; Vitorica-Yrezabal, I. J.; Mills, D. P. *Chem. Eur. J.* **2014**, *20*, 14579.
- (101) Sun, Y.; Takats, J.; Eberspacher, T.; Day, V. *Inorg. Chim. Acta* **1995**, *229*, 315.
- (102) Rinehart, J. D.; Meihaus, K. R.; Long, J. R. *J. Am. Chem. Soc.* **2010**, *132*, 7572.
- (103) Meihaus, K. R.; Rinehart, J. D.; Long, J. R. *Inorg. Chem.* **2011**, *50*, 8484.
- (104) Baldoví, J. J.; Cardona-Serra, S.; Clemente-Juan, J. M.; Coronado, E.; Gaita-Ariño, A. *Chem. Sci.* **2013**, *4*, 938. This corrected model was used to improve previous approaches that treat the ligands as point charges and therefore does not account for potential overlap and covalency.
- (105) Rinehart, J. D.; Long, J. R. *Dalton Trans.* **2012**, *41*, 13572.
- (106) Meihaus, K. R.; Minasian, S. G.; Lukens, Jr., W. W.; Kozimor, S. A.; Shuh, D. K.; Tylliszczak, T.; Long, J. R. *J. Am. Chem. Soc.* **2014**, *136*, 6056.
- (107) Antunes, M. A.; Pereira, L. C. J.; Santos, I. C.; Mazzanti, M.; Marçalo, J.; Almeida, M. *Inorg. Chem.* **2011**, *50*, 9915.
- (108) Coutinho, J. T.; Antunes, M. A.; Pereira, L. C. J.; Bolvin, H.; Marçalo, J.; Mazzanti, M.; Almeida, M. *Dalton Trans.* **2012**, *41*, 13568.
- (109) It should be mentioned here that the same authors recently reported the very interesting result that $\text{UTp}^{\text{Me}_2}\text{I}$ can actually form three different structures depending on the crystallization conditions (see (a) Antunes, M. A.; Santos, I. C.; Bolvin, H.; Pereira, L. C. J.; Mazzanti, M.; Marçalo, J.; Almeida, M. *Dalton Trans.* **2013**, *42*, 8861 and (b) Sun, Y. M.; McDonald, R.; Takats, J.; Day, V. W.; Eberspacher, T. A. *Inorg. Chem.* **1994**, *33*, 4433). Two of these structures involve an inner-sphere iodide ligand, while the third is a high symmetry structure wherein the iodide is outer-sphere and shortening of the U–N bond lengths is concomitant with a decrease in crowding around the uranium center. Crystal field modeling of the magnetic data for this compound by Baldoví et al. (Ref. 104) was performed using the originally reported structure by Sun et al. with an inner-sphere iodide. However, as reported in Ref. 109a, powder diffraction data support that the reported magnetism corresponds with the high symmetry cationic form $[\text{UTp}^{\text{Me}_2}\text{I}]$. While *ab initio* computations on all three structures reveal differences in the separation between ground and first excited M_J states for each complex, nonetheless these values compare well with Ref 104, are all the same order of magnitude, and significantly larger than the experimentally determined barrier of 21.0 cm^{-1} .
- (110) Kraft, S. J.; Fanwick, P. E.; Bart, S. C. *Inorg. Chem.* **2010**, *49*, 1103.
- (111) Coutinho, J. T.; Antunes, M. A.; Pereira, L. C. J.; Marçalo, J.; Almeida, M. *Chem. Commun.* **2014**, *50*, 10262.
- (112) Moro, F.; Mills, D. P.; Liddle, S. T.; van Slageren, J. *Angew. Chem. Int. Ed.* **2013**, *52*, 3430.
- (113) Pereira, L. C. J.; Camp, C.; Coutinho, J. T.; Chatelain, L.; Maldivi, P.; Almeida, M.; Mazzanti, M. *Inorg. Chem.* **2014**, *53*, 11809.

- (114) Mills, D. P.; Moro, F.; McMaster, J.; van Slageren, J.; Lewis, W.; Blake, A. J.; Liddle, S. T. *Nat. Chem.* **2011**, *3*, 454.
- (115) King, D. M.; Tuna, F.; McMaster, J.; Lewis, W.; Blake, A. J.; McInnes, E. J. L.; Liddle, S. T. *Angew. Chem. Int. Ed.* **2013**, *52*, 4921.
- (116) Magnani, N.; Apostolidis, C.; Morgenstern, A.; Colineau, E.; Griveau, J.-C.; Bolvin, H.; Walter, O.; Caciuffo, R. *Angew. Chem. Int. Ed.* **2011**, *50*, 1696.
- (117) Karraker, D.; Stone, J. A.; Jones, Jr., E. R.; Edelstein, N. *J. Am. Chem. Soc.* **1970**, *92*, 4841.
- (118) One additional low-nuclearity system not mentioned above is the molecule $[\text{UO}_2\text{Dy}(\text{py})_2(\text{L})_2]_2$ (L = Pacman ligand) from Ref. 135b, which was found to show a butterfly-shaped magnetic hysteresis loop at 3 K. The authors attributed the observed slow relaxation of the magnetization to Dy^{III} single-ion anisotropy, thus it is not included under the category of actinide single-molecule magnets here, where slow relaxation is inherently assumed to arise predominantly from the actinide metal center(s).
- (119) Magnani, N.; Colineau, E.; Griveau, J.-C.; Apostolidis, C.; Walter, O.; Caciuffo, R. *Chem. Comm.* **2014**, *50*, 8171.
- (120) For example Ref. 45; in some cases, the measured energy barrier corresponds to relaxation via higher excited states if level crossing is not allowed from the first excited state, for instance Ref. 78 and 16a. It should also be noted, however, that while correlations between M_J separations and U_{eff} have been observed for lanthanide complexes, this is not always the case, and again it is important to consider alternative spin-lattice relaxation processes, for example see Ref. 33b. As is noted in the latter reference, a given ac frequency and temperature range may limit the observation of Orbach relaxation, and this process should not be taken for granted in mononuclear systems.
- (121) The exponent n ranges most commonly from 5-9, with values of 8 or 9 typically corresponding with Kramers ions such as U^{III} .
- (122) Another point to briefly touch on here is the assumption of idealized symmetry both in crystal field models and in the simulation of EPR data. This protocol is useful in obtaining a model, but also can be less directly informative when the actual molecular symmetry is significantly lower (as in the case of $[\text{UTp}^{\text{Me}_2}_2(\text{bipy})]\text{I}$ and $[\text{UTp}^{\text{Me}_2}_2]\text{I}$, modelled with D_{5h} symmetry). In the absence of computations, it is also important that careful consideration of experimental and literature data be considered before making claims regarding properties such as magnetic ground state. Consider for example the case of C_{3v} symmetric complex $\text{UO}(\text{Tren}^{\text{TIPS}})$. Based on the absence of an EPR signal for this complex and experimental magnetization data, the authors assume a pure $M_J = \pm 3/2$ ground state. For a pure ground state though, it is hard to rationalize tunnelling of the magnetization at zero field since, if dipolar interactions are null, then there is no other mechanism by which tunnelling should be expected to arise in a Kramers system with a pure ground state. However, isoelectronic Ce^{III} has been studied in C_{3v} symmetry, and the ground M_J doublet is not pure, and further it does not contain any contribution from $M_J = \pm 3/2$. Thus, there is likely more complexity to the magnetization dynamics in $\text{UO}(\text{Tren}^{\text{TIPS}})$ than first appears.
- (123) Demonstrated through EPR for $\text{U}(\text{Bc}^{\text{Me}})_3$ and $\text{U}(\text{Bp}^{\text{Me}})_3$ (Chapter 3) and computationally for the other complexes.

- (124) This is reasonable given the trigonal prismatic geometry around the uranium center in these complexes; only UTp_3 possesses crystallographically-imposed D_{3h} symmetry.
- (125) Abragam, A.; Bleaney, B. *Electron Paramagnetic Resonance of Transition Ions*; Clarendon Press: Oxford, 1970.
- (126) Another interesting consideration is the design of low-coordinate, high site symmetry complexes with low crystal symmetry. Ref. 58b presents calculations on the internal fields experienced by Dy^{III} centers in mononuclear β -diketonate complexes. Due to the greater number of symmetry operations and therefore molecular orientations in $P2_1/c$ versus $P-1$, a single Dy^{III} center in the former complex experiences two different internal fields, whereas for the $P-1$ symmetry, only one type of internal field is present.
- (127) If χ_T is more than χ_{dc} , this of course indicates a calculation error, as the in-phase susceptibility can never exceed the total magnetic susceptibility for the molecule. Unfortunately, for many of the literature compounds, comparison of χ_T to χ_{dc} at the same temperature revealed calculation errors in over half of the complexes, strongly suggesting a need for more careful workup and also analysis of experimental data.
- (128) Rosen, R. K.; Andersen, R. A.; Edelstein, N. M. *J. Am. Chem. Soc.* **1990**, *112*, 4588.
- (129) Rinehart, J. D.; Harris, T. D.; Kozimor, S. A.; Bartlett, B. M.; Long, J. R. *Inorg. Chem.* **2009**, *48*, 3382 and references therein.
- (130) Lukens, W. W.; Walter, M. D. *Inorg. Chem.* **2010**, *49*, 4458.
- (131) Rinehart, J. D.; Bartlett, B. M.; Kozimor, S. A.; Long, J. R. *Inorg. Chim. Acta.* **2008**, *361*, 3534.
- (132) Patel, D.; Moro, F.; McMaster, J.; Lewis, W.; Blake, A. J.; Liddle, S. T. *Angew. Chem. Int. Ed.* **2011**, *50*, 10388.
- (133) Habib, F.; Murugesu, M. *Chem. Soc. Rev.* **2013**, *42*, 3278 and references therein.
- (134) Lukens, W. W.; Magnani, N.; Booth, C. H. *Inorg. Chem.* **2012**, *51*, 10105.
- (135) (a) Chatelain, L.; Mougel, V.; Pécaut, J.; Mazzanti, M. *Chem. Sci.* **2012**, *3*, 1075. (b) Arnold, P. L.; Jones, G. M.; Odoh, S. O.; Schreckenbach, G.; Magnani, N.; Love, J. B. *Nat. Chem.* **2012**, *4*, 221.
- (136) (a) Mougel, V.; Chatelain, L.; Pécaut, J.; Caciuffo, R.; Colineau, E.; Griveau, J.-C.; Mazzanti, M. *Nat. Chem.*, **2012**, *4*, 1101. (b) Mougel, V.; Chatelain, L.; Hermle, J.; Caciuffo, R.; Colineau, E.; Tuna, F.; Magnani, N.; De Geyer, A.; Pécaut, J.; Mazzanti, M. *Angew. Chem. Int. Ed.* **2014**, *53*, 819.
- (137) (a) Arnold, P. L.; Hollis, E.; White, F. J.; Magnani, N.; Caciuffo, R.; Love, J. B. *Angew. Chem. Int. Ed.* **2011**, *50*, 887. (b) Arnold, P. L.; Hollis, E.; Nichol, G. S.; Love, J. B.; Griveau, J.-C.; Caciuffo, R.; Magnani, N.; Maron, L.; Castro, L.; Yahia, A.; Odoh, S. O.; Schreckenbach, G. *J. Am. Chem. Soc.* **2013**, *135*, 3841.
- (138) Chatelain, L.; Walsh, J. P. S.; Pécaut, J.; Tuna, F.; Mazzanti, M. *Angew. Chem. Int. Ed.* **2014**, *126*, 13652.
- (139) Mehdoui, T.; Berthet, J.-C.; Thuéry, P.; Ephritikhine, M. *Eur. J. Inorg. Chem.* **2004**, 1996.
- (140) Evans, W. J.; Takase, M. K.; Ziller, J. W.; DiPasquale, A. G.; Rheingold, A. L.; *Organometallics*, **2009**, *28*, 236.
- (141) (a) $Mn_{12}O_{12}(O_2CCH_2Br)_{16}(H_2O)_4$: Tsai, H.-L.; Chen, D.-M.; Yang, C.-I.; Jwo, T.-Y.; Wur, C.-S.; Lee, G.-H.; Wang, Y. *Inorg. Chem. Commun.* **2001**, *4*, 511. (b) $Mn_6O_2(saO)_6(O_2CPh)_2(EtOH)_4$: Milios, C. J.; Alina, V.; Wernsdorfer, W.; Moggach, S.;

- Parsons, S.; Perlepes, S. P.; Christou, G.; Brechin, E. K. *J. Am. Chem. Soc.* **2007**, *129*, 2754. (c) $[\text{Mn}_{21}\text{DyO}_{20}] \equiv [\text{Mn}_{21}\text{DyO}_{20}(\text{OH})_2(\text{tBuCO}_2)_{20}(\text{HCO}_2)_4(\text{NO}_3)_3(\text{H}_2\text{O})_7]$: Papatriantafyllopoulou, C.; Wernsdorfer, W.; Abboud, K. A.; Christou, G. *Inorg. Chem.* **2011**, *50*, 421. (d) $[\text{Co}(\text{SPh})_4]^{2-}$: Zadrozny, J. M.; Long, J. R. *J. Am. Chem. Soc.* **2011**, *133*, 20732. (e) $[(\text{Co}(\text{1-hfpip})_2)_2(\text{D2py}_2(\text{TBA}))_2]$: Yoshihara, D.; Karasawa, S.; Koga, N. *Polyhedron* **2011**, *30*, 3211. (f) $[\text{Co}^{\text{II}}\text{Co}^{\text{III}}_3\text{L}_6]^-$: Zhu, Y.; Cui, C.; Zhang, Y.; Jia, J.; Guo, X.; Gao, C.; Qian, K.; Jiang, S.; Wang, B.; Wang, Z.; Gao, S. *Chem. Sci.* **2013**, *4*, 1802. (g) $[(\text{TPyA})_2\text{Fe}^{\text{II}}_2(\text{N}^{\text{Ph}}\text{L})]^+$: Jeon, I.-R.; Park, J. G.; Xiao, D. J.; Harris, T. D. *J. Am. Chem. Soc.* **2013**, *135*, 16845.
- (142) (a) $[\{\text{Cp}'_2\text{Ln}(\mu\text{-SSiPh}_3)\}_2]$: Tuna, F.; Smith, C. A.; Bodensteiner, M.; Ungur, L.; Chibotaru, L. F.; McInnes, E. J. L.; Winpenny, R. E. P.; Collison, D.; Layfield, R. A. *Angew. Chem. Int. Ed.* **2012**, *51*, 6976. (b) $[\text{Ln}(\text{Me}_5\text{trenCH}_2)(\mu\text{-H})_3\text{Ln}(\text{Me}_6\text{tren})]^{2+}$: Venugopal, A.; Tuna, F.; Spaniol, T. P.; Ungur, L.; Chibotaru, L. F.; Okuda, J.; Layfield, R. A. *Chem. Commun.* **2013**, *49*, 901.
- (143) As there are different conventions for reporting J values, in this work $J < 0$ indicates antiferromagnetic coupling while $J > 0$ indicates ferromagnetic.

Chapter 1 Appendix

Formulae for χ_M' and χ_M'' assuming a distribution of relaxation times, τ .

$$\chi'(v) = \chi_S + (\chi_T - \chi_S) \frac{1 + (2\pi\nu\tau)^{1-\alpha} \sin\left(\frac{\pi\alpha}{2}\right)}{1 + 2(2\pi\nu\tau)^{1-\alpha} \sin\left(\frac{\pi\alpha}{2}\right) + (2\pi\nu\tau)^{2-2\alpha}}$$

$$\chi''(v) = (\chi_T - \chi_S) \frac{(2\pi\nu\tau)^{1-\alpha} \cos\left(\frac{\pi\alpha}{2}\right)}{1 + 2(2\pi\nu\tau)^{1-\alpha} \sin\left(\frac{\pi\alpha}{2}\right) + (2\pi\nu\tau)^{2-2\alpha}}$$

Using the above expressions, ac susceptibility data (left panel of Figure A1) can be fit to extract the relaxation time, τ , and the parameters χ_T , χ_S , and α for a given temperature (and applied field if relevant), all ≥ 0 . The parameters χ_T and χ_S are the isothermal and adiabatic susceptibilities, respectively. In the high-frequency limit, when the moment cannot exchange energy with the environment, the susceptibility takes on the value χ_S ; in general for a molecule with uniform relaxation, χ_S should be very close to zero irrespective of temperature and applied field. A value for χ_S significantly larger than zero is indicative of further relaxation processes at frequencies beyond the measureable limit. The parameter χ_T corresponds to the susceptibility when the moment is in equilibrium with the phonon bath. As mentioned above, χ_T should also correspond to the value of the static susceptibility at the same temperature if all low-frequency relaxation processes are accounted for. χ_T will depend on temperature but should exhibit negligible field-dependence. The parameter α represents the distribution of relaxation times and can range from 0 to 1; values close to zero indicate uniform relaxation that occurs primarily via one mechanism. See Ref. 18, pp. 69-75, for a detailed discussion of ac susceptibility.

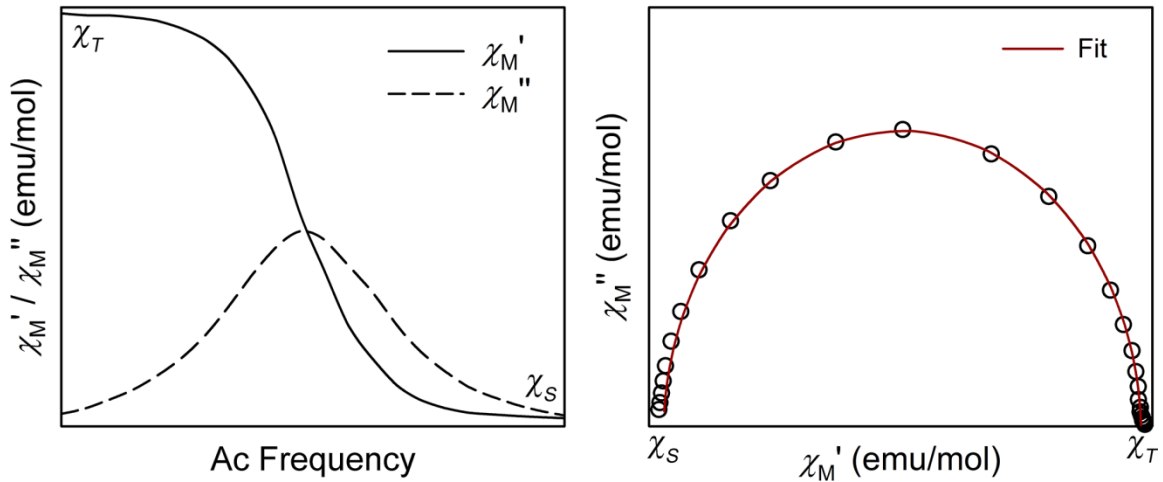
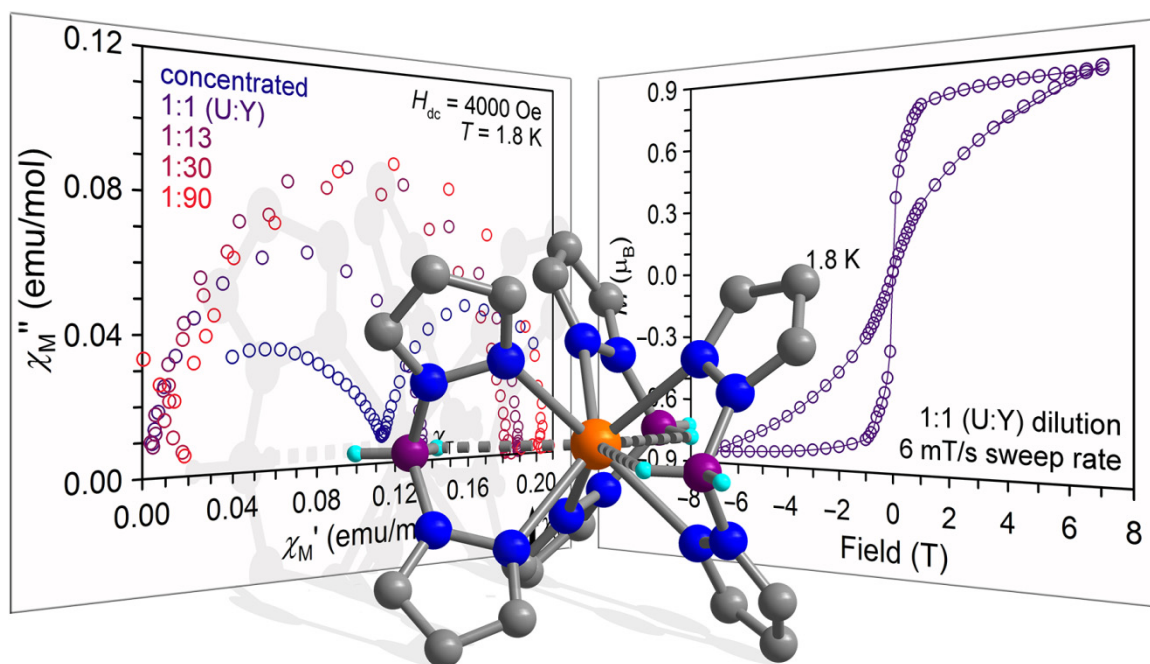


Figure 1.A1. (Left) Plot of the in-phase (χ_M' , solid line) and out-of-phase (χ_M'' , dashed line) components of the magnetic susceptibility versus frequency of the ac field for a typical SQUID Magnetometer, as shown above. (Right) Plot of χ_M'' versus χ_M' , a so-called Argand or Cole-Cole plot.

Chapter 2: The Role of Dipolar Interactions in Slow Magnetic Relaxation in the Trigonal Prismatic Complex $U(H_2BPz_2)_3$ and Relevance for other Actinide Compounds



2.1 Introduction

As discussed in Chapter 1, in 2009 the trigonal prismatic U^{III} compound $U(Ph_2BPz_2)_3$ ¹ was found to exhibit slow magnetic relaxation under zero dc field, with $U_{eff} = 20 \text{ cm}^{-1}$ and $\tau_0 = 1 \times 10^{-7} \text{ s}$, introducing the actinides into single-molecule magnetism. A subsequent study sought to discern how slight electronic changes made via modification to the bis(pyrazolyl)borate framework would influence relaxation behavior at the uranium center. By replacing the ancillary phenyl groups with hydrogen atoms, one obtains the complex $U(Bp)_3$ (Figure 2.1, $[Bp]^-$ = dihydrobis(pyrazolyl)borate anion) wherein a hydrogen atom on each boron center interacts agostically with uranium as confirmed by infrared spectroscopy.² Such an interaction leads to a tricapped trigonal prismatic coordination geometry, wherein the trigonal prism of $U(Bp)_3$ is elongated relative to $U(Ph_2BPz_2)_3$ due to the presence of the equatorial electron density around the uranium center.³ In addition to contributing to this axial elongation, replacement of the phenyl groups with hydrogen atoms results in a decrease in the nearest-neighbor $U \cdots U$ separations, from 10.791(2) Å in $U(Ph_2BPz_2)_3$ to 8.167(2) Å in $U(Bp)_3$.

Ac susceptibility characterization of $U(Bp)_3$ with a 4 Oe driving field over frequencies ranging from 1-1500 Hz revealed no out-of-phase signal, in contrast to $U(Ph_2BPz_2)_3$.³ From Chapter 1, we can recall that the absence of zero-field signal is a common occurrence in slowly relaxing molecular systems due to the presence of fast quantum tunnelling. If tunnelling is the predominant reason for rapid relaxation at zero field, then application of a small dc field can short-circuit this process by bringing the magnetic ground states out of resonance, allowing for the observation of slow magnetic relaxation. Indeed, upon application of dc fields greater than or equal to 30 Oe at 1.8 K, slow magnetic relaxation was observed for $U(Bp)_3$, as indicated by the appearance of out-of-phase magnetic susceptibility, χ_M'' , within the ac frequency range of 1-1500 Hz. The relaxation time was observed to increase with increasing field until reaching a maximum at 300 Oe, followed by a gradual decline with higher applied fields (Figure 2.1, right). Even still, the field-dependent relaxation time was two orders of magnitude faster than previously reported for $U(Ph_2BPz_2)_3$ (Figure 2.1) and $\alpha \geq 0.19$ at each field for $U(Bp)_3$, indicating contributions from other relaxation mechanisms (Chapter 1 Appendix). Analysis of variable-temperature ac susceptibility at 100 Oe revealed weak temperature dependence with $U_{eff} = 8 \text{ cm}^{-1}$ and $\tau_0 = 1.2 \times 10^{-6} \text{ s}$ (Figure 2.A1 and Figure 2.3, blue circles), while the same data collected at a larger field of 5000 Oe was found to vary insignificantly with temperature. Given the weak temperature-dependence of the direct process,⁴ it was observed that this might be the mechanism dominant at 5000 Oe, while at 100 Oe there might be competition between direct relaxation and Orbach relaxation, a possibility supported by the rather large value of τ_0 .

Intriguingly, for fields larger than 500 Oe the maximum in χ_M'' moved to higher frequencies and decreased in magnitude, concomitant with a decrease in the maximum value of χ_M' at the lowest frequency (1 Hz). A convenient way of visualizing this transformation is to look at the field-dependent Cole-Cole plots (χ_M'' versus χ_M') for varying fields. For instance, as field is increased from 500 Oe to 5000 Oe (Figure 2.A2), the corresponding Cole-Cole plots shift to higher frequencies and the intercept of each curve with the χ_M' axis begins to deviate significantly from the value of the static magnetic susceptibility at the same temperature. In the absence of additional relaxation phenomena on the ac scale, however, the χ_T value should always agree with the value of the static susceptibility at the same temperature.⁵ This deviation is indicative of a second relaxation process occurring on a slower time scale, which can in fact be partially visualized as a tail in the Cole-Cole plots at low frequencies (Figure 2.A2). By scanning

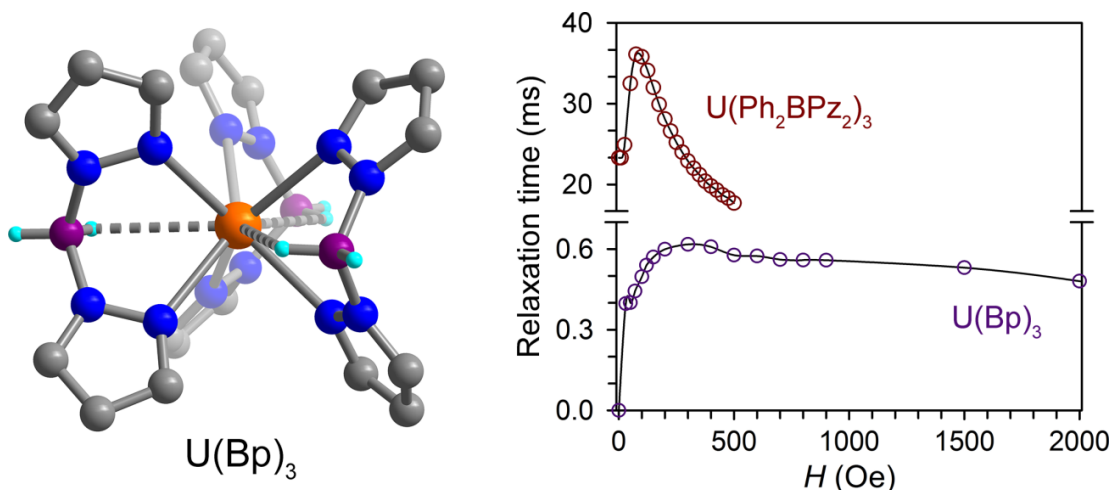


Figure 2.1. (Left) X-ray crystal structure of $\text{U}(\text{Bp})_3$;⁶ orange, grey, blue, purple, and pale blue spheres represent U, C, N, B, and H atoms, respectively; all other hydrogen atoms have been omitted for clarity. (Right) Comparison of the field-dependent relaxation data for $\text{U}(\text{Ph}_2\text{BPz}_2)_3$ and $\text{U}(\text{Bp})_3$ collected at 1.8 K.^{1,3}

over the absolute frequency range of the magnetometer (0.06 Hz to 1500 Hz), one can indeed see a fully resolved second Cole-Cole plot corresponding to this slow process (Figure 2.A3). Overlaying the χ_M'' versus frequency curves for a few fields also nicely reveals the transition from the high frequency process to the low frequency process with an isosbestic point around 5 Hz (Figure 2.2). While the faster relaxation process could be correlated with temperature-dependent and/or direct relaxation, this much slower process was an anomaly for f-element systems and could not readily be identified, though it was observed to slow extensively with increasing applied fields and exhibited little temperature dependence (Figure 2.A5).³

It was of interest to unravel the source(s) of this unconventional relaxation behavior, and in doing so it was relevant to consider the above-noted structural distortions for $\text{U}(\text{Bp})_3$, namely the expansion of the trigonal prism and the closer inter-ion distances relative to $\text{U}(\text{Ph}_2\text{BPz}_2)_3$. While any role played by the former distortion is difficult to address in the absence of theoretical analysis, the impact of the closer inter-ion distances is something that can be probed experimentally by studying magnetically dilute samples of $\text{U}(\text{Bp})_3$ within an appropriate diamagnetic matrix. Indeed, such an experiment is important due to the relevance of dipolar interactions in magnetic relaxation for multinuclear transition metal systems^{6,7} and also highly anisotropic lanthanide compounds,⁸ as first demonstrated by Ishikawa and co-workers when they characterized magnetically dilute samples of $[\text{LnPc}_2]^-$ ($\text{Ln} = \text{Dy}, \text{Tb}$) and observed a drastic shift in the frequency dependence of the ac magnetic susceptibility relative to the concentrated samples.^{8a} Such studies are particularly important as harnessing magnetic properties of molecular origin becomes increasingly of interest,⁹ while the majority of magnetic characterization of new molecules is conducted on bulk samples wherein intermolecular interactions can influence observed properties. Thus, acquiring a better understanding of intermolecular interactions and an ability to interpret their effects on molecular-based magnetic relaxation is crucial.

In this chapter we describe the results of magnetic measurements on varying magnetic dilutions of $\text{U}(\text{Bp})_3$, which reveal that dipolar interactions not only enhance molecular relaxation rates, but also are implicit in this second anomalous relaxation pathway. Indeed, with dilution of $\text{U}(\text{Bp})_3$, a near two-fold increase is observed for the value of U_{eff} while the second relaxation pathway is

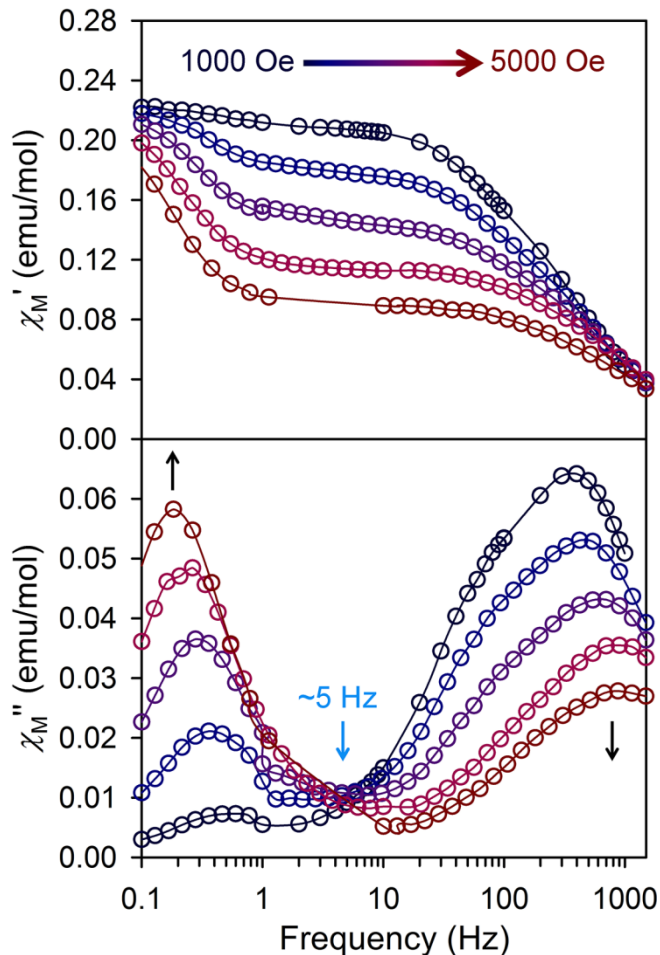


Figure 2.2. Variable field in- and out-of-phase susceptibility data for $\text{U}(\text{Bp})_3$ collected at 1.8 K for fields of 1000, 2000, 3000, 4000, and 5000 Oe, over the frequency range 0.1-1500 Hz. As indicated by the black lines, the high frequency peak gives way to a much slower relaxation process. This transition is marked by an isosbestic point at ~ 5 Hz.³

initially slowed down further, leading to unprecedented magnetic hysteresis arising from intermolecular relaxation. We finally propose, within the context of some recent literature on mononuclear U^{III} single-molecule magnets, that this intermolecular relaxation may not be restricted to $\text{U}(\text{Bp})_3$.

2.2 Experimental Section

All reactions and subsequent manipulations were performed under anaerobic and anhydrous conditions in a nitrogen atmosphere using a glove box or Schlenk technique. THF, hexanes, and toluene were dried by passage over activated molecular sieves using a Vacuum Atmospheres solvent purification system. $\text{U}(\text{Bp})_3$ and $\text{Y}(\text{Bp})_3$ were prepared from literature procedures.^{2,10} A modification of the method of Trofimenko¹¹ was used for the synthesis of dihydrobis(dimethylpyrazolyl)borate. UI_3 was prepared by modification of the method of Cloke and Hitchcock.¹² Fine uranium powder was prepared by synthesis of UH_3 ¹³ and subsequent removal of hydrogen under dynamic vacuum at 400 °C. Heating of the fine metal powder with a

stoichiometric amount of HgI_2 in a sealed tube at 320 °C for two days afforded the triiodide starting material. Anhydrous C_6D_6 was purchased from Cambridge Isotopes Laboratories, freeze-pump-thawed and stored over activated 4 Å molecular sieves prior to use. Dihydrobis(pyrazolyl)borate was purchased from Strem Chemicals and purified by recrystallization from THF/hexanes. NMR spectra were recorded on a Bruker AVB 400 or Bruker AV 300 spectrometer. IR spectra were recorded on a Perkin Elmer Avatar Spectrum 400 FTIR Spectrometer equipped with ATR. Elemental analyses were performed by the Micro-Mass Facility at the University of California, Berkeley on a Perkin-Elmer 2400 Series II combustion analyzer.

Magnetic Measurements. Magnetic samples were prepared by adding crystalline powder compound to a 5 mm inner diameter/7 mm outer diameter quartz tube with raised quartz platform. Sufficient liquid eicosane (at 60 °C) was added to saturate and cover the samples to prevent crystallite torquing and provide good thermal contact between the sample and the bath. The tubes were fitted with Teflon sealable adapters, evacuated on a Schenk line or using a glove box vacuum pump, and flame sealed under vacuum. Interestingly, issues with sample torquing became more prevalent with greater dilutions.

Magnetic susceptibility measurements were collected using a Quantum Design MPMS2 SQUID magnetometer. Dc susceptibility data measurements were performed at temperatures ranging from 2.0 to 300 K, using an applied field of 1000 Oe. The amount of and $\text{U}(\text{Bp})_3$ present in each dilute sample was confirmed by adjusting the mass of the paramagnetic material until the low temperature portions of the dilute dc susceptibility curves overlapped with that of the neat compound. The starting mass estimate was determined from the as-crystallized ratio of diamagnetic to paramagnetic compound. Ac magnetic susceptibility measurements were performed using a 4 Oe switching field. All data were corrected for diamagnetic contributions from the core diamagnetism estimated using Pascal's constants to give $\chi_D = -0.00030064$ emu/mol ($\text{U}(\text{Bp})_3$), -0.00026664 emu/mol ($\text{Y}(\text{Bp})_3$), and -0.00024306 emu/mol (eicosane).

Temperature dependent ac susceptibility measurements were performed at 100 Oe for $\text{U}(\text{Bp})_3$, at which field the relaxation time approaches a maximum. Dilution dependent relaxation data was also collected at an applied field of 4000 Oe, representing the optimum field at which both processes are comparable in magnitude. Cole-Cole plots were fitted using formulae describing χ_M' and χ_M'' in terms of frequency, constant temperature susceptibility (χ_T), adiabatic susceptibility (χ_S), relaxation time (τ), and a variable representing the distribution of relaxation times (α).¹⁴ All data fitted to α values of ≤ 0.37 .

2.3 Results and Discussion

Crystalline samples of $\text{U}(\text{Bp})_3$ diluted in a diamagnetic matrix of $\text{Y}(\text{Bp})_3$ were prepared in U:Y molar ratios of 1:1 (56% U), 1:13 (9% U), 1:30 (4% U), and 1:90 (1% U) to examine the relevance of intermolecular interactions on the observed slow magnetic relaxation. The study of samples with larger dilution ratios was rendered difficult by instrument sensitivity (2.3 mg of $\text{U}(\text{Bp})_3$ for the highest dilution corresponds to $\sim 10^{-12}$ μ_B). Ac magnetic susceptibility data collected under a dc field of 100 Oe revealed a drastic dilution dependence of the relaxation time as observed in Figure 2.3. At 1.8 K, a 1:1 dilution leads to a shift in χ_M'' of nearly two orders of magnitude from the concentrated sample, and the out-of-phase signal continues to shift to lower frequencies while growing in magnitude with increasing dilution, confirming its molecular origin. This change in χ_M'' is also accompanied by a decrease in the high frequency value of χ_M' ,

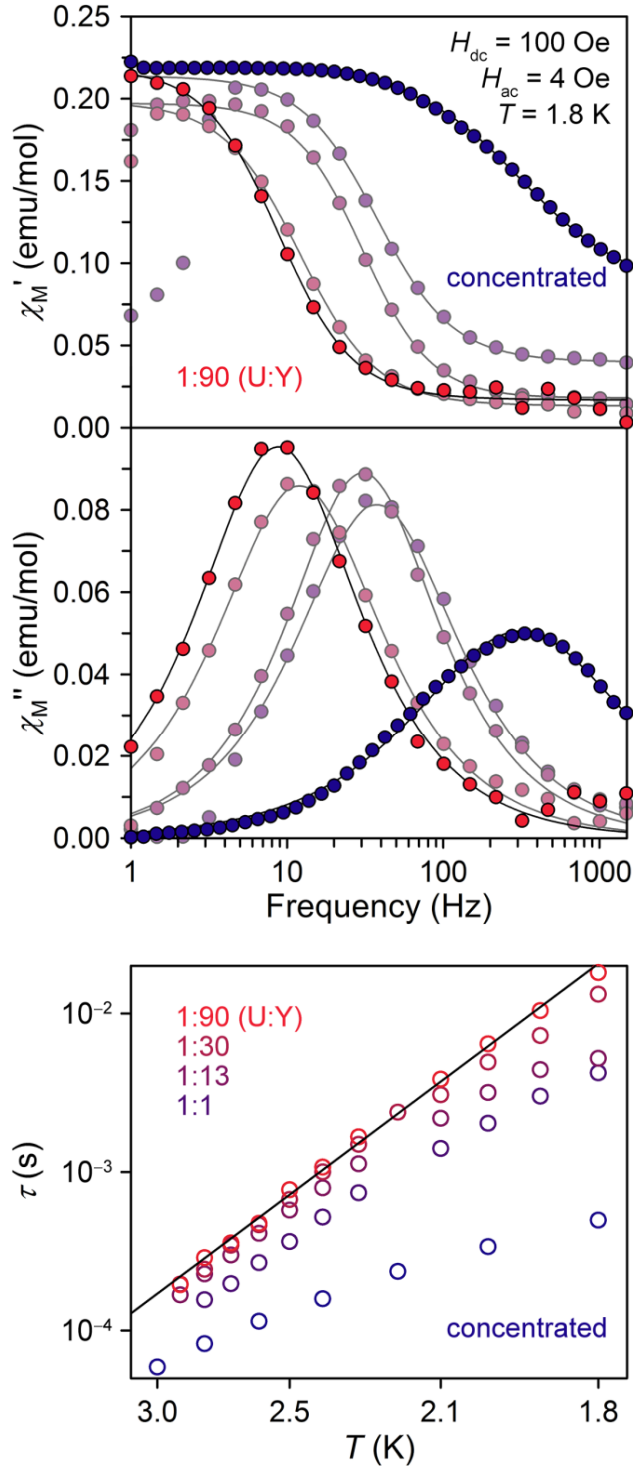


Figure 2.3. (Top) Plot of the in- and out-of-phase susceptibility (χ_M' and χ_M'') versus the frequency of the oscillating field for $\text{U}(\text{Bp})_3$ and magnetically dilute samples with molar U:Y ratios of 1:1, 1:13, 1:30, and 1:90, revealing the increasing uniformity of the magnetic relaxation as U^{III} ions are separated. (Bottom) Plot of the relaxation time (log scale) versus T (inverse scale) for the varying dilutions of $\text{U}(\text{Bp})_3$. For the highest dilution, the range of data was fit to an Arrhenius law to give $U_{\text{eff}} = 14.9(3) \text{ cm}^{-1}$ with $\tau_0 = 1.3(2) \times 10^{-7} \text{ s}$.^{8h}

which indicates that the relaxation grows more uniform as unresolved and more rapid relaxation processes are extinguished with dilution.

Temperature-dependent ac susceptibility data were also collected for each of the dilute samples under $H_{dc} = 100$ Oe to compare with the concentrated species. A plot of the relaxation time versus temperature is shown in the lower part of Figure 2.3 for all dilutions over temperatures ranging from 1.8 to 3 K. With increasing dilution, the relaxation time grows increasingly temperature-dependent and at the highest dilution, the small range of temperatures can be fit to a straight line giving $U_{eff} = 14.9(3) \text{ cm}^{-1}$ with $\tau_0 = 1.3(2) \times 10^{-7}$ s. The experimental barrier thus nearly doubled from the concentrated species and the τ_0 value decreased by an order of magnitude. It is possible then that the direct process, which was postulated above to be active in the concentrated sample, may derive at least in part from internal fields due to nearby paramagnetic ions in the concentrated sample. This is not too surprising given that dipolar fields can be as strong as 100 Oe.⁶

Ac susceptibility data were also collected for dilute samples at 1.8 K and 4000 Oe to examine the influence of dilution on the low frequency process, which begins to dominate at this field. The Cole-Cole plots obtained from these measurements are plotted together in Figure 2.4, with the undiluted data for comparison. Upon a 1:1 dilution, the slower process is no longer visible within the frequency range probed (0.06-1500 Hz), and χ_T for this curve again does not match the value of χ_{dc} at 1.8 K, thus this process has slowed down even further with dilution and is no longer accessible within the ac time-scale. Variable field magnetization measurements performed at a sweep rate of 6 mT/s on the 1:1 sample support this rationale, revealing hysteresis at 1.8 K and as high 3 K (Figure 2.4, right, and Figure 2.A7). The loop displays no remnant magnetization, however, as the moment of the sample rapidly plummets to zero upon removal of the field. Such a shape to the hysteresis loop mirrors the strong field dependence of this process as seen in field-dependent ac measurements on the concentrated sample. Perhaps ironically, while this result is the first observation of magnetic hysteresis for a mononuclear uranium

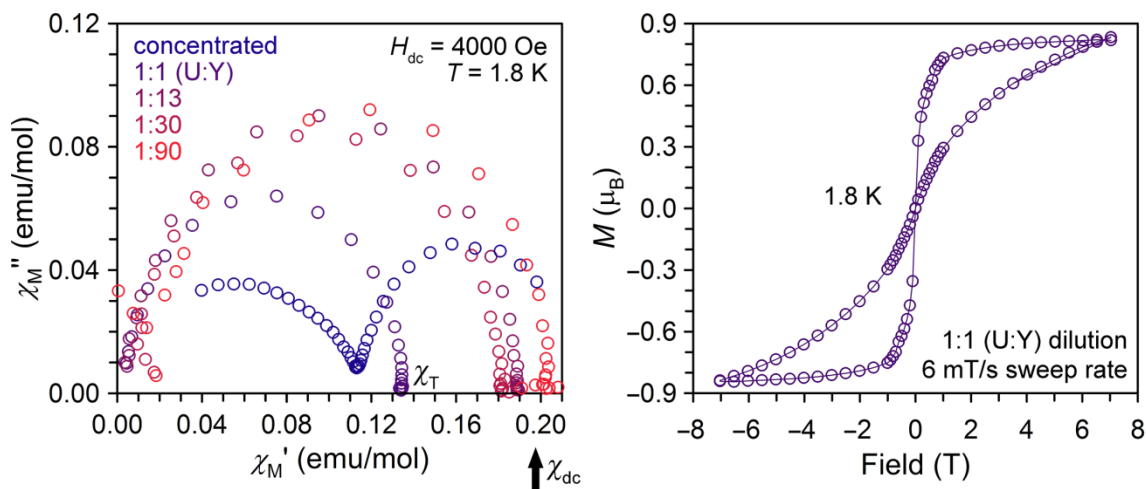


Figure 2.4. (Left) Cole-Cole plots collected at 1.8 K under an applied field of 4000 Oe for increasing magnetic dilutions of $\text{U}(\text{Bp})_3$ in a matrix of $\text{Y}(\text{Bp})_3$. With increasing dilution, the low frequency process moves first out of the ac time-scale (purple circles, 1:1 dilution) and is eventually extinguished (red circles, 1:90 dilution). When all relaxation processes are accounted for, the isothermal susceptibility value χ_T agrees with the static susceptibility χ_{dc} value at the same temperature. (Right) Variable-field magnetization data collected for the 1:1 dilution at 1.8 K.^{8h}

Table 2.1. Mononuclear uranium compounds showing slow magnetic relaxation and magnetic hysteresis at low temperatures.

Compound	$U_{\text{eff}}(\text{cm}^{-1})^{\text{a}}$	τ_0 (s)	Hysteresis (K) ^b	τ (ms) ^c	An...An (Å) ^d	Ref.
[UTp ^{Me2} ₂ (bipy)]I	18.2	1.4×10^{-7}	0.32	10^{31}	9.4550(4)	19a
[UTp ^{Me2} ₂ (bipy)]	19.8 ^e	3.28×10^{-7}	0.8	10^{12}	10.6670(5)	19f
[UTp ^{Me2} ₂]I	21.0	1.8×10^{-7}	3	$\leq 5^{\text{f}}$	8.3714(2)	19c,d
UO(Tren ^{TIPS})	14.9	2.6×10^{-7}	2.4	2	8.2995(9)	19e
U(N ^{**}) ₃	14.9	3.1×10^{-7}	1.8	46	9.0282(4)	19g
[(U(L) ₂ (I)) ₂ (μ-C ₆ H ₅ CH ₃)] ^g	–	–	1.8	$\leq 2^{\text{h}}$	4.2836(5) ⁱ	19b
U(Bp) ₃	14.9	1.3×10^{-7}	3	0.12	8.546(2)	This work

^a Obtained under $H_{\text{dc}} \leq 1000$ Oe except for [UTp^{Me2}₂(bipy)]. ^b Maximum reported hysteresis temperature. ^c Relaxation time at the hysteresis reported hysteresis temperature extrapolated from published Arrhenius parameters. ^d Nearest-neighbor distance in sample of interest. ^e Under zero dc field; under 500 Oe the barrier increases to 22.6 cm^{-1} with $\tau_0 = 4.68 \times 10^{-8}$ s. ^f From the reported τ_0 , $\tau \sim 5$ ms, see Ref. 20. ^g L = HC(PPh₂NSiMe₃)₂; while this compound is dinuclear, the slow magnetic relaxation arises from single-ion effects given the absence of magnetic coupling in $\chi_M T$. ^h Maxima in χ_M'' are only observed for frequencies greater than 1200 Hz and temperatures above 2 K, thus the given 1.8 K relaxation time represents an upper bound. ⁱ Intramolecular distance within dinuclear structure, intramolecular nearest-neighbor = 10.5425(9) Å.

compound, it is likely the hysteresis does not derive from the observed ac molecular relaxation, due to the short associated time-scales of the latter (0.004 s at 1.8 K and 100 Oe). Interestingly, variable-field magnetization measurements on the 1:13 sample also revealed a very narrow hysteresis loop at 1.8 K, though it was open for a smaller field range (1 and 2.5 T) and closed for higher temperatures; hysteresis is completely shut down for higher dilutions. Notably, these results reveal that the much slower process observed in concentrated U(Bp)₃ is not molecular in origin, and that there is an optimal nearest-neighbor separation (~ 8.5 Å)¹⁵ at which it is slowest. While this intermolecular relaxation is clearly strongly field- and distance-dependent, its mechanism is still unclear.

Notably, recent simultaneous fitting of magnetic susceptibility ($\chi_M T$ versus T) and 1.8 K Magnetization (M versus H) data for (UBp)₃ using the program CONDON^{16,17} required inclusion of a small $zJ = -0.38 \text{ cm}^{-1}$ for improved fits below 10 K, suggesting weak antiferromagnetic interactions between molecules. (The fitting also revealed a ground to first excited M_J separation $\sim 150 \text{ cm}^{-1}$, with the ground state composed of an admixture of $M_J = \pm 5/2$ and $\pm 7/2$, consistent with the computational results discussed in Chapter 1). In the absence of further experimental characterization such a parameter ought to be considered with some caution, though it suggests that dipolar induced magnetic order is relevant in the observed hysteresis for U(Bp)₃. Magnetic order due to dipole-dipole interactions has been characterized for other single-molecule magnets such as Fe₈ ([Fe₈O₂(OH)₁₂(tacn)₆]⁸⁺, tacn = 1,4,7-triazacyclononane),¹⁸ though ordering occurs at temperatures in the range of a few hundred millikelvin and is not reported to coincide with slow relaxation of molecular origin.¹⁸ Thus, the phenomenon observed for U(Bp)₃ appears to be unique.

It is interesting in light of these results to examine the handful of other uranium molecules showing single-ion slow magnetic relaxation and hysteresis at low temperatures.¹⁹ These compounds are listed in Table 2.1 along with their experimentally determined effective relaxation barriers and other relevant parameters. The first two compounds consist of trivalent uranium coordinated by dimethyltris(pyrazolyl)borate and neutral or radical anion bipyridine

ligands, and for these the relaxation time at the highest reported hysteresis temperatures (as extrapolated from the Arrhenius parameters) is long enough to allow for the observation of magnetic hysteresis.^{19a,f} For the remaining compounds, however, the Arrhenius relaxation time at the highest reported hysteresis temperatures is only on the order of milliseconds. Notably, these molecules are quite distinct both in structure and oxidation state: in [UTp^{Me2}]₂I, the crystal symmetry is *C2/m* and the U^{III} center sits along a two-fold axis, mirror plane, and is the site of inversion symmetry;^{19c,d} the compound UO(Tren^{TIPS}) consists of U^V (5f¹) in three-fold symmetry;^{19e} the U^{III} centers in the dinuclear species possess no clear site symmetry and are not related by inversion;^{19b} and finally U(N^{**})₃^{19g} adopts a trigonal planar geometry, unprecedented among tris(amide) actinide complexes.

For the first three compounds, no variable-field ac data is provided and thus it is challenging to analyze the relevance of intermolecular interactions in the observed magnetic hysteresis. Indeed, only upon scanning ac fields larger than 500 Oe was the intermolecular relaxation “turned on” for U(Bp)₃, and the low frequencies measurements necessary to fully visualize this process were not used for the above studies. However, it is relevant to note that the hysteresis loops for UO(Tren^{TIPS}) and [UTp^{Me2}]₂I in particular open only above fields of 1 T,^{19c-e} whereas the ac dynamics are investigated at fields ≤ 1000 Oe. In the case of [(U(L)₂(I))₂(μ-C₆H₅CH₃)],^{19b} the hysteresis loop is open above 1000 Oe, though the ac relaxation was so fast at 1000 Oe that χ_M'' peaks were present only at frequencies of ~500 Hz. These observations indicate that with increasing applied fields the relaxation dynamics are changing drastically for these systems and that at the same temperature, a component of the magnetic susceptibility is relaxing much more slowly than the relaxation being observed on the ac time-scale.

Consider more closely the case of [UTp^{Me2}]₂I:^{19c,d} from the Arrhenius data reported at 500 Oe, it is apparent that below ~3.5 K, the relaxation grows steadily temperature-independent. Extrapolating the given Arrhenius parameters ($U_{\text{eff}} = 21.0 \text{ cm}^{-1}$ and $\tau_0 = 4.3 \times 10^{-8} \text{ s}^{20}$), the relaxation time at 3 K is ≤ 5 ms, seemingly too fast to allow for the observation of magnetic hysteresis. The caveat of course is that the opening of the hysteresis loop for this compound occurs at ~ 1 T, and ac relaxation data is not provided for this field. However, in the absence of hyperfine interactions²¹ or other fast relaxation processes at lower fields, it is unlikely that the temperature-dependent ac relaxation at 0.05 T should differ significantly from the same measured under a 1 T field. Even if increasing the field lengthens the low-temperature relaxation, it should still follow the determined Arrhenius law, and one should not expect to see hysteresis given the corresponding relaxation times. This discrepancy arises from two assumptions: (i) there is no additional fast relaxation process that would significantly speed up the relaxation at fields below 1 T and (ii) the measured temperature-dependent relaxation data is truly representative of relaxation between M_J states. For the first point, a simple dilution can be performed to rule out any fast molecular relaxation due to dipolar fields.

In the second case, we know from Chapter 1 that the observed temperature-dependent relaxation in all mononuclear actinide compounds deviates significantly from what is expected based on calculations of the splitting within the ground J . If the hysteresis is in fact molecular, however, temperature-dependent relaxation collected at 1 T might more closely represent the calculated M_J separation for this species, or at least show a dramatic lengthening of τ . Therefore, the measurement of temperature-dependent relaxation data at 1 T should reflect this slower relaxation and the Arrhenius behavior should change dramatically. If instead, the Arrhenius data at 1 T follows the curvature of that at 0.05 T, then this is strong evidence that the hysteresis is extra-molecular. Performing higher field ac scans would aid in confirming or ruling out this

possibility for $[\text{UTp}^{\text{Me}_2}]_2$. With only a few simple additional experiments, then, it would be possible to obtain a more thorough understanding of the relaxation dynamics in this system, though the characterization already for these compounds indicates a strong field-dependence of the relaxation, and is in support of the possibility of an intermolecular relaxation process as in the case of concentrated $\text{U}(\text{Bp})_3$.

As it turns out, $\text{U}(\text{N}^{**})_3$ ^{19g} is the only compound in Table 2.1 for which variable field ac data is supplied. Analogous to the field-dependent Cole-Cole plots for $\text{U}(\text{Bp})_3$ (Figures 2.A2 and 2.A3), the value of χ_T decreases for $\text{U}(\text{N}^{**})_3$ also decreases with increasing field, indicating that at lower frequencies there are one or more additional relaxation mechanisms are being “turned on” by the field. For instance, at 1.8 K and under $H_{\text{dc}} = 600$ Oe (also the field used in ac susceptibility measurements), $\chi_T \sim 0.27$ emu/mol; upon increasing the field to 5000 Oe, the value of χ_T has shrunk to ~ 0.13 emu/mol, while static magnetic susceptibility data reported for $H_{\text{dc}} = 5000$ Oe at 2 K revealed $\chi_M \sim 0.2$ emu/mol $> \chi_T$. These results provide some compelling evidence that the hysteresis is also not molecular for this molecule.

It is important to address the perhaps ostensibly analogous observation of butterfly hysteresis for some transition metal clusters, wherein there is no slow magnetic relaxation or where the observed molecular relaxation should preclude this phenomenon.²² For these systems, the hysteresis has been found to arise due to a phonon bottleneck,²³ though most are set apart from the molecules discussed here due to the fact that hysteresis is only observed at high fields (> 7 T) and/or low temperatures (< 1.5 K). In the case of the dinuclear Fe^{II} species $(\text{Et}_4\text{N})_3\text{Fe}_2\text{F}_9$,²⁴ magnetic characterization of an oriented single crystal sealed under nitrogen gas revealed magnetic hysteresis at 1.8 K and to fields as high as 2 T, more reminiscent of that exhibited by $\text{U}(\text{Bp})_3$. From dc relaxation measurements, it was also possible to extract $U_{\text{eff}} = 1.5 \text{ cm}^{-1}$ and $\tau_0 = 70$ s, though the corresponding process was clearly not thermally activated. No hysteresis was observed upon subsequent magnetic characterization of two separate samples prepared with better thermal contact,²⁵ confirming the presence of a phonon bottleneck in the original sample. In the case of $\text{U}(\text{Bp})_3$, however, all samples that were measured were restrained under vacuum with eicosane, a hydrocarbon matrix that should promote heat transfer between lattice and phonons. Additionally, the trend in the relaxation data (i.e. the disappearance of the slow process with dilution) was consistent across all prepared samples. Given how this phenomenon has been observed for uranium systems in the literature with similar restraints (such as $[\text{UTp}^{\text{Me}_2}]_2$ in frozen hexanes or $\text{UO}(\text{Tren}^{\text{TIPS}})$ in eicosane), a phonon bottle neck seems unlikely.

A final interesting category encompasses the lanthanide compounds $\text{Ln}(\text{OH})_3$ ($\text{Ln} = \text{Tb}, \text{Dy}, \text{Ho}$),²⁶ dysprosium ethyl sulfate $(\text{Dy}(\text{CH}_3\text{CH}_2\text{SO}_4)_3 \cdot 9\text{H}_2\text{O}, \text{DyEtS})$,²⁷ and terbium arsonate²⁸, for which paramagnetic relaxation studies were performed in the late 1900s. Ac susceptibility measurements conducted below or near their ferromagnetic ordering temperatures of these compounds (< 2 K) revealed two relaxation domains in the Cole-Cole plots and the low frequency relaxation process was attributed to domain wall movement. While the probed frequencies and temperatures differ significantly from those in the ac experiments described here, consider that both $\text{U}(\text{Bp})_3$ and salts such as DyEtS are molecular solids and small inter-ion separations characterize both concentrated species (8.167(2) Å vs. 7.0122(6) Å for $\text{U}(\text{Bp})_3$ and DyEtS , respectively). Such a simplistic comparison must certainly be made with caution, as for instance the relaxation observed for the lanthanide compounds results from a spontaneously (dipole-induced) ordered ferromagnetic phase, whereas the “ordering” phenomenon in $\text{U}(\text{Bp})_3$ requires application of a magnetic field. However, in both molecules dipolar interactions are implicit in the observed slow phenomenon. Such a comparison certainly re-emphasizes the care

that must be used when assuming observed dynamic relaxation is molecular.

On a final note, it is relevant to mention one other mononuclear actinide single-molecule magnet in this discussion, namely $\text{Np}(\text{COT})_2$ (Np^{IV} , $5f^3$).²⁹ This compound shows low-temperature slow relaxation for applied fields greater than 0.5 T, and an open magnetic hysteresis loop above 5 T at 1.8 K. This hysteresis is ascribed to a process dominant at high fields and distinct from a faster, low-field process for which a relaxation barrier of $U_{\text{eff}} = 28 \text{ cm}^{-1}$ was extracted. Both relaxation processes are assumed to be molecular. However, while the provided linear fit of the 7 T Arrhenius data gives a large barrier to magnetic relaxation of $\sim 471 \text{ cm}^{-1}$, the corresponding τ_0 value is shockingly small at $\sim 7 \times 10^{-19} \text{ s}$ (Fig. 2.A8). Such a small value is typically not associated with slowly-relaxing molecular species but rather relaxation in spin glasses, and it can often be challenging to distinguish the two.¹⁴ Spin glasses are furthermore often characterized by magnetic hysteresis loops that fail to show saturation and exhibit an out-of-phase signal with little frequency dependence. Both of these are characteristics displayed by $\text{Np}(\text{COT})_2$ under large applied fields. For a field of 5 T, the low temperature relaxation time spikes below $\sim 11 \text{ K}$ and, as the authors note, becomes frequency-independent. Thus, for the relaxation under large applied fields and the observed magnetic hysteresis, it is perhaps relevant also to consider the role of intermolecular interactions.

2.4 Conclusions and Outlook

The foregoing results demonstrate the significance of dipolar interactions in $\text{U}(\text{Bp})_3$, with likely relevance to other mononuclear actinide single-molecule magnets in the literature. Indeed, dipolar interactions are effective at speeding up molecular relaxation for this molecule, as for many lanthanides systems; more uniquely, these interactions also conspire to facilitate a slow relaxation process that appears unprecedented for such molecular systems. This process may derive from weak, field-induced antiferromagnetic coupling between molecules, and with an optimal U...U separation of $\sim 8.5 \text{ \AA}$, this process is slowed so significantly as to be observable via magnetic hysteresis measurements. These results further highlight the importance of understanding the factors that moderate slow magnetic relaxation for mononuclear single-molecule magnets with large unquenched orbital moments and anisotropy, and of accurately reporting molecular rather than ensemble properties. With an eye toward the future of possibly constructing single-molecule magnet memory storage and computing devices, the study of intermolecular relaxation effects is particularly critical, since dipolar interactions can heavily influence quantum coherence times.³⁰

2.5 Acknowledgements

This research was funded by NSF Grant No. CHE-06170633. The NSF Graduate Research Fellowship Program is acknowledged for support of K.R.M, Dr. Antonio DiPasquale for x-ray structure assistance, and McDonald's Corporation for the drinking straws used in magnetic sample loading.

2.6 References

- (1) (a) L. Maria, M. P. Campello, Á. Domingos, I. Santos, and R. Andersen, *J. Chem. Soc., Dalton Trans.* **1999**, 2015. (b) Rinehart, J. D.; Long, J. R. *J. Am. Chem. Soc.* **2009**, *131*, 12558.

- (2) Y. Sun, J. Takats, T. Eberspacher, and V. Day, *Inorg. Chim. Acta*, 1995, **229**, 315.
- (3) J. D. Rinehart, K. R. Meihaus, and J. R. Long, *J. Am. Chem. Soc.*, 2010, **132**, 7572.
- (4) Recall, $\tau_{\text{direct}} \propto T$ or T^2 , from Chapter 1.
- (5) This is assuming no strong dependence of the static magnetic susceptibility on applied field, which is the case for $\text{U}(\text{Bp})_3$ (see Figure 2.A4).
- (6) Gatteschi, D.; Sessoli, R. *Angew. Chem. Int. Ed.* **2003**, *42*, 268.
- (7) (a) Wernsdorfer, W.; Bhaduri, S.; Tiron, R.; Hendrickson, D. N.; Christou, G. *Phys. Rev. Lett.* **2002**, *89*, 197201. (b) Affronte, M.; Lasjaunias, J. C.; Wernsdorfer, W.; Sessoli, R.; Gatteschi, D.; Heath, S. L.; Fort, A.; Rettori, A. *Phys. Rev. B* **2002**, *66*, 064408. (c) Wernsdorfer, W.; Caneschi, A.; Sessoli, R.; Gatteschi, D.; Cornia, A.; Villar, V.; Paulsen, C. *Phys. Rev. Lett.* **2000**, *84*, 2965. (d) Wernsdorfer, W.; Ohm, T.; Sangregorio, C.; Sessoli, R.; Maily, D.; Paulsen, C. *Phys. Rev. Lett.* **1999**, *82*, 3903. (e) Prok'ev, N. V.; Stamp, P. C. E. *Phys. Rev. Lett.* **1998**, *80*, 5794.
- (8) For example: (a) Ishikawa, N.; Sugita, M.; Ishikawa, T.; Koshihara, S.-y.; Kaizu, Y. *J. Am. Chem. Soc.* **2003**, *125*, 8694. (b) Ishikawa, N.; Sugita, M.; Ishikawa, T.; Koshihara, S.-y.; Kaizu, Y. *J. Phys. Chem. B* **2004**, *108*, 11265. (c) Lin, P.-H.; Burchell, T. J.; Clérac, R.; Murugesu, M. *Angew. Chem. Int. Ed.* **2008**, *47*, 8848. (d) Luis, F.; Martínez-Pérez, M. J.; Montero, O.; Coronado, E.; Cardona-Serra, S.; Martí-Gastaldo, C.; Clemente-Juan, J. M.; Sesé, J.; Drung, D.; Schurig, T. *Phys. Rev. B* **2010**, *82*, 060403. (e) Jiang, S.-D.; Wang, B.-W.; Su, G.; Wang, Z.-M.; Gao, S. *Angew. Chem. Int. Ed.* **2010**, *49*, 7448. (f) Layfield, R. A.; McDouall, J. J. W.; Sulway, S. A.; Tuna, F.; Collison, D.; Winpenny, R. E. P. *Chem. Eur. J.* **2010**, *16*, 4442. (g) Habib, F.; Lin, P.-H.; Long, J.; Korobkov, I.; Wernsdorfer, W.; Murugesu, M. *J. Am. Chem. Soc.* **2011**, *133*, 8830. (h) Meihaus, K. R.; Rinehart, J. D.; Long, J. R. *Inorg. Chem.* **2011**, *50*, 8484.
- (9) (a) Vitali, L.; Fabris, S.; Conte, M. A.; Brink, S.; Ruben, M.; Baroni, S.; Kern, K. *Nano Lett.* **2008**, *8*, 3364. (b) Bogani, L.; Wernsdorfer, W. *Nature Mat.* **2008**, *7*, 179. (c) Candini, A.; Klyatskaya, S.; Ruben, M.; Wernsdorfer, W.; Affronte, M. *Nano Lett.* **2011**, *11*, 2634. (d) Sanvito, S. *Nature Mat.* **2011**, *10*, 484. (e) Uradampilleta, M.; Klyatskaya, S.; Kleuziou, J.-P.; Wernsdorfer, W. *Nature Mat.* **2011**, *10*, 502. (f) Mannini, M.; Bertani, F.; Tudisco, C.; Malavolti, L.; Poggini, L.; Misztal, K.; Menozzi, D.; Motta, A.; Otero, E.; Ohresser, P.; Saintavit, P.; Condorelli, G. G.; Dalcanale, E.; Sessoli, R. *Nat. Commun.* **2014**, *5*, 4582.
- (10) Reger, D. A.; Lindeman, J. A.; Lebioda, L. *Inorg. Chem.* **1988**, *27*, 1890.
- (11) Trofimenko, S. *J. Am. Chem. Soc.* **1967**, *89*, 6288.
- (12) Cloke, F. G. N.; Hitchcock, P. B. *J. Am. Chem. Soc.* **2002**, *124*, 9352.
- (13) Spedding, F. H.; Newton, A. S.; Warf, J. C.; Johnson, O.; Nottorf, R. W.; Johns, I. B.; Daane, A. H. *Nucleonics* **1949**, *4*, 4.
- (14) Gatteschi, D.; Sessoli, R.; Villain, J. *Molecular Nanomagnets*; Oxford University Press: Oxford, 2006.
- (15) Based on the removal of nearest-neighbors, based on the intermolecular distances from the crystal structure of concentrated $\text{U}(\text{Bp})_3$.
- (16) CONDON: (a) Schilder, H.; Lueken, H. *J. Magn. Magn. Mater.* **2004**, *281*, 17. (b) Speldrich, M.; Schilder, H.; Lueken, H.; Kögerler, P. *Isr. J. Chem.* **2011**, *51*, 215.
- (17) Fitting of magnetic data for $\text{U}(\text{Bp})_3$: van Leusen, J.; Speldrich, M.; Schilder, H.; Kögerler, P. *Coord. Chem. Rev.* **2014**, DOI: 10.1016/j.ccr.2014.10.011.

- (18) (a) Martínez-Hidalgo, X.; Chudnovsky, E. M.; Aharony, A. *Europhys. Lett.* **2001**, *55*, 273; see also Ref. 20-23 from this paper for other examples of dipolar ordering or theoretical investigations. (b) Burzurí, E.; Luis, F.; Ballou, R.; Ressouche, E.; Montero, O.; Campo, J.; Maegawa, S. *Phys. Rev. Lett.* **2011**, *107*, 097203.
- (19) (a) Antunes, M. A.; Pereira, L. C. J.; Santos, I. C.; Mazzanti, M. Marçalo, J.; Almeida, M. *Inorg. Chem.* **2011**, *50*, 9915. (b) Mills, D. P.; Moro, F.; McMaster, J.; van Slageren, J.; Lewis, W.; Blake, A. J.; Liddle, S. T. *Nature Chem.* **2011**, *3*, 454. (c) Coutinho, J. T.; Antunes, M. A.; Pereira, L. C. J.; Bolvin, H.; Marçalo, J.; Mazzanti, M.; Almeida, M. *Dalton Trans.* **2012**, *41*, 13568. (d) Antunes, M. A.; Santos, I. C.; Bolvin, H.; Pereira, L. C. J.; Mazzanti, M.; Marçalo, J. Almeida, M. *Dalton Trans.* **2013**, *42*, 8861. (e) King, D. M.; Tuna, F.; McMaster, J.; Lewis, W.; Blake, A. J.; McInnes, E. J. L.; Liddle, S. T. *Angew. Chem. Int. Ed.* **2013**, *52*, 4921. (f) Coutinho, J. T.; Antunes, M. A.; Pereira, L. C. J.; Marçalo, J.; Almeida, M. *Chem. Commun.* **2014**, *50*, 10262. (g) Goodwin, C. A. P.; Tuna, F.; McInnes, E. J. L.; Liddle, S. T.; McMaster, J.; Vitorica-Yrezabal, I. J.; Mills, D. P. *Chem. Eur. J.* **2014**, *20*, 14579.
- (20) In re-plotting the Arrhenius data from Ref. 19c, we obtained a U_{eff} value of 21.2 cm^{-1} from fitting the highest four temperatures to an Arrhenius law, which agrees with the reported value. However, the corresponding $\tau_0 = 4.3 \times 10^{-8} \text{ s}$, rather than the reported $\tau_0 = 1.8 \times 10^{-7} \text{ s}$. Therefore, this former value was used to determine the corresponding 3 K relaxation time. Even using the Arrhenius parameters exactly as reported, the relaxation time at 2 K is $\sim 5 \text{ ms}$, rapid for the observation of magnetic hysteresis.
- (21) ^{238}U has no nuclear spin.
- (22) (a) Chiorescu, I.; Wernsdorfer, W.; Müller, A.; Bögge, H.; Barbara, B. *Phys. Rev. Lett.* **2000**, *84*, 3454. (b) Waldmann, O.; Koch, R.; Schromm, S.; Müller, P.; Bernt, I.; Saalfrank, R. W. *Phys. Rev. Lett.* **2002**, *89*, 246401. (c) Inagaki, Y.; Asano, T.; Ajiro, Y.; Narumi, Y.; Kindo, K.; Cornia, A.; Gatteschi, D. *J. Phys. Soc. Jpn.* **2003**, *72*, 1178. (d) Schenker, R.; Leuenberger, M. N.; Chaboussant, G.; Loss, D.; Güdel, H. U. *Phys. Rev. B.* **2005**, *72*, 184403.
- (23) Spin-lattice relaxation requires energy (heat) transfer between the spins and lattice phonons and transfer also between the phonons and the sample helium bath. A phonon bottleneck occurs when there is insufficient heat transfer between the phonons and the bath, such as can occur in a scenario where insufficient or no crystallite restraint is used. See van Vleck, J. H. *Phys. Rev.* **1941**, *59*, 724.
- (24) Schenker, R.; Leuenberger, M. N.; Chaboussant, G.; Güdel, H. U.; Loss, D. *Chem. Phys. Lett.* **2002**, *358*, 413.
- (25) Single crystals restrained with Apiezon grease and crushed powder sealed in a gelatin capsule.
- (26) Schlachetzki, A.; Eckert, J. *Phys. Stat. Sol. (A)* **1972**, *11*, 611.
- (27) Cooke, A. H.; Edmonds, D. T.; Finn, C. B. P.; Wolfe, W. P. *Proc. Roy. Soc. A.* **1968**, *306*, 335.
- (28) Müller, P. H.; Kasten, A.; Schienle, M. *Phys. Stat. Sol. (B)* **1983**, *119*, 239.
- (29) Magnani, N.; Apostolidis, C.; Morgenstern, A.; Colineau, E.; Griveau, J.-C.; Bolvin, H.; Walter, O.; Caciuffo, R. *Angew. Chem. Int. Ed.* **2011**, *50*, 1696.
- (30) Stamp, P. C. E. Gaita-Ariño, A. *J. Mat. Chem.* **2009**, *19*, 1718.

Chapter 2 Appendix

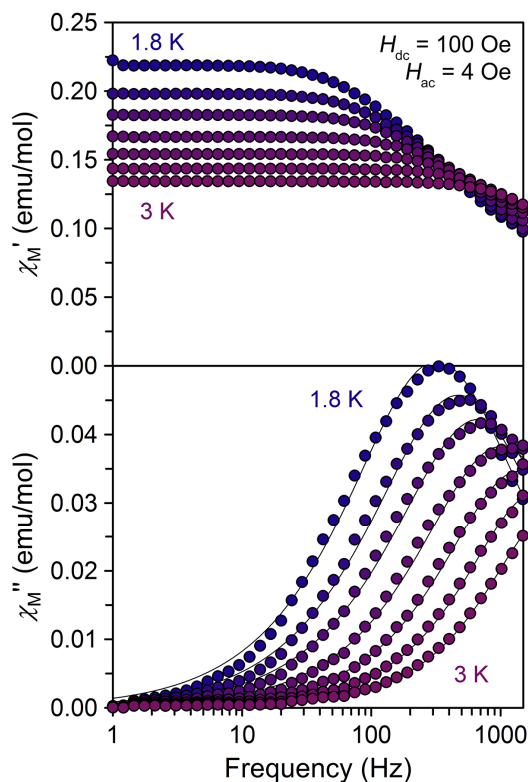


Figure 2.A1. Plot of the in-phase (χ_M') and out-of-phase (χ_M'') molar magnetic susceptibility versus the frequency of the oscillating field for concentrated $\text{U}(\text{Bp})_3$ for a range of temperatures and a 100 Oe dc field. Solid lines are guides for the eyes.

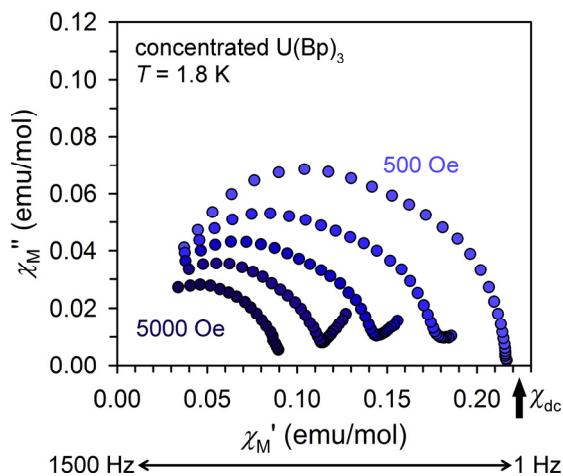


Figure 2.A2. Cole-Cole plots for the concentrated $\text{U}(\text{Bp})_3$ collected at 1.8 K and varying fields over the indicated frequency range. The static susceptibility value at 1.8 K and 1000 Oe is indicated by a black arrow. With increasing field, the Cole-Cole peak moves to higher frequencies, suggesting a slower relaxation process is growing in on a much slower time-scale (lower frequencies).

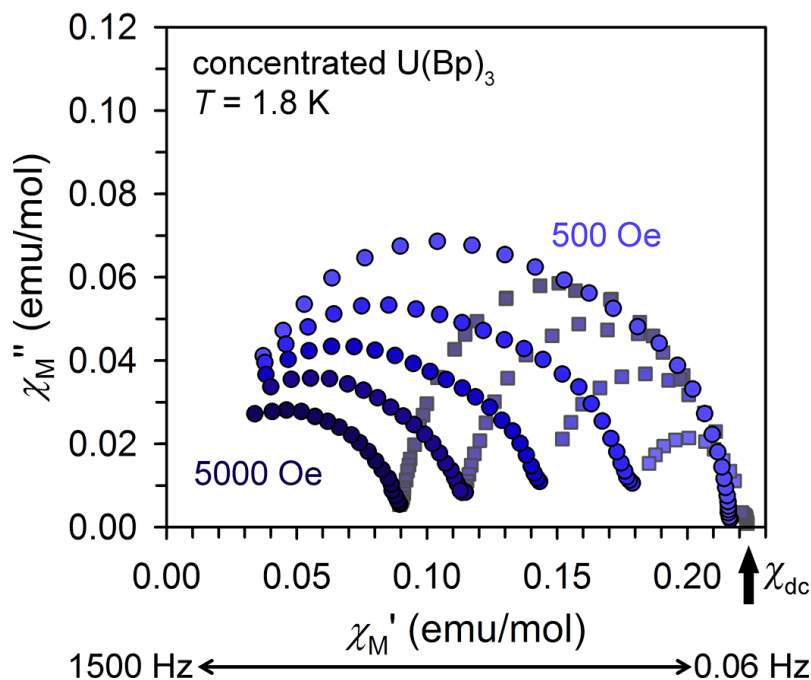


Figure 2.A3. Cole-Cole plots for the concentrated U(Bp)_3 collected at 1.8 K and varying fields, with the static susceptibility value at 1.8 K and 1000 Oe indicated by a black arrow. The low to high frequency range now extends from 0.06-1500 Hz, revealing the second slower process (faded squares).

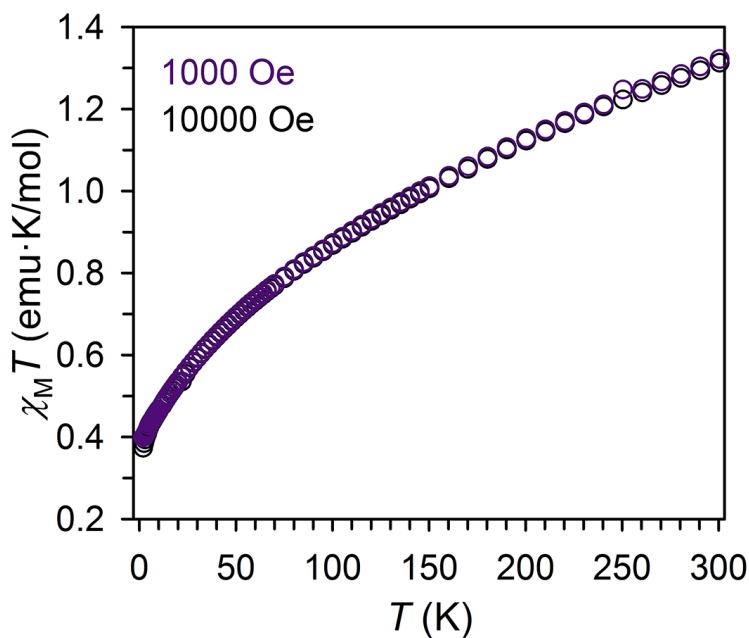


Figure 2.A4. Plot of the magnetic susceptibility times temperature ($\chi_M T$) versus temperature for U(Bp)_3 at fields of 0.1 T (purple circles) and 1 T (black circles).

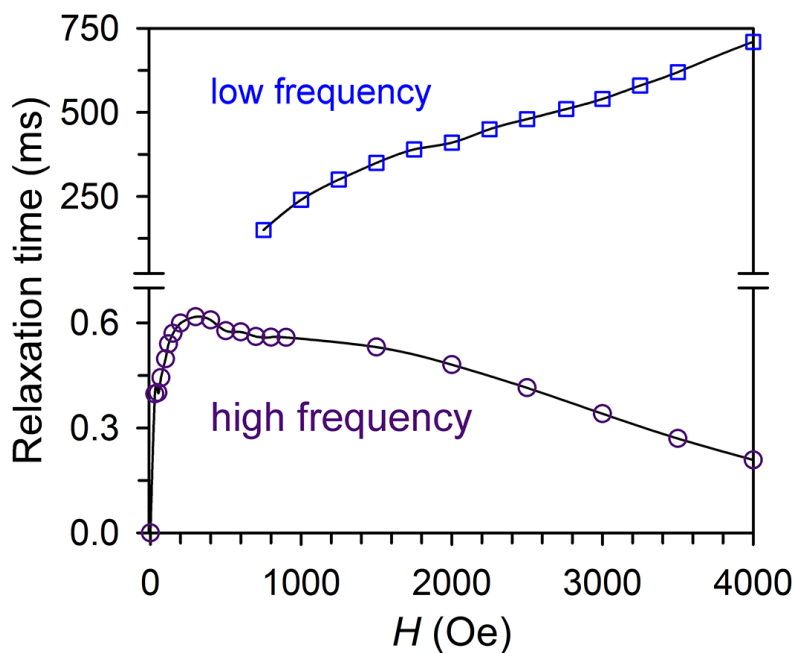


Figure 2.A5. Comparison of the field-dependent relaxation time at 1.8 K for the low and high frequency relaxation processes observed for $U(Bp)_3$.

Table 2.A1. Values of the relaxation time (τ) and α for $U(Bp)_3$ at 100 Oe and varying temperatures.

T (K)	1:1 dilution		1:13		1:30		1:90	
	τ (s)	α	τ (s)	α	τ (s)	α	τ (s)	α
1.8	0.0042	0.0428	0.0052	0.0023	0.0132	0.0478	0.0181	0.0369
1.9	0.0030	0.0253	0.0044	0.0216	0.0072	0.0345	0.0104	0.0506
2	0.0020	0.0215	0.0032	0.0388	0.0049	0.0386	0.0064	0.0230
2.1	0.0014	0.0169	0.0022	0.0306	0.0031	0.0342	0.0039	0.0281
2.2	–	–	–	–	0.0024	0.0624	–	–
2.3	0.0007	0.0175	0.0011	0.0297	0.0015	0.0212	0.0017	0.0521
2.4	0.0005	0.0190	0.0008	0.0277	0.0010	0.0268	0.0011	0.0381
2.5	0.0004	0.0225	0.0006	0.0171	0.0007	0.0286	0.0008	0.0100
2.6	0.0003	0.0186	0.0004	0.0302	0.0005	0.0349	0.0005	0.0542
2.7	0.0002	0.0238	0.0003	0.0245	0.0003	0.0401	0.0005	0.0542
2.8	0.0002	0.0207	0.0002	0.0159	0.0002	0.0237	0.0003	0
2.9	–	–	0.0002	0.0213	0.0002	0.0008	0.0002	0

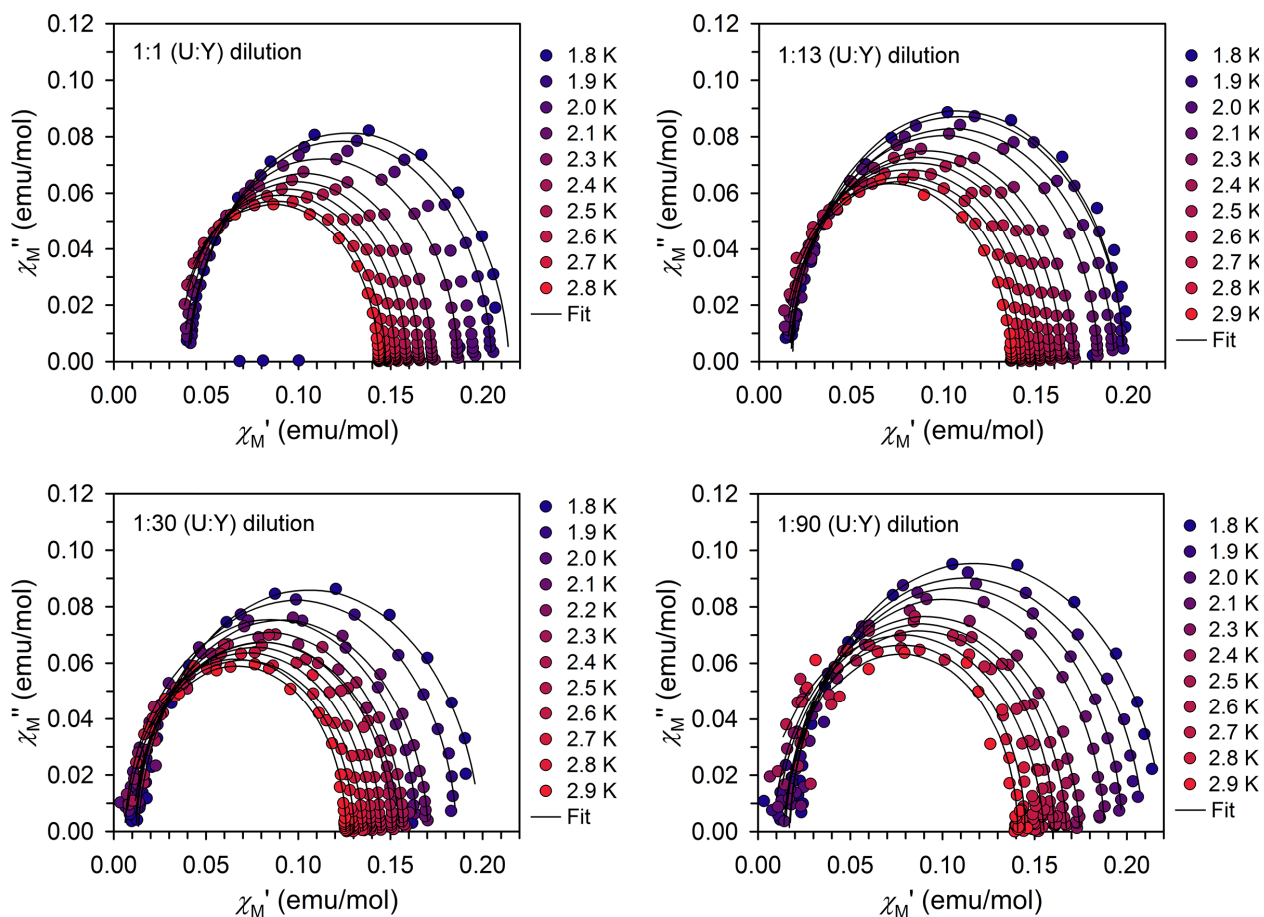


Figure 2.A6. Cole-Cole plots for the (U:Y) 1:1, 1:13, 1:30 and 1:90 dilutions of U(Bp)_3 , collected at 100 Oe and varying temperatures. Experimental data points are represented by colored circles and the points representing the fit are connected by solid black lines.

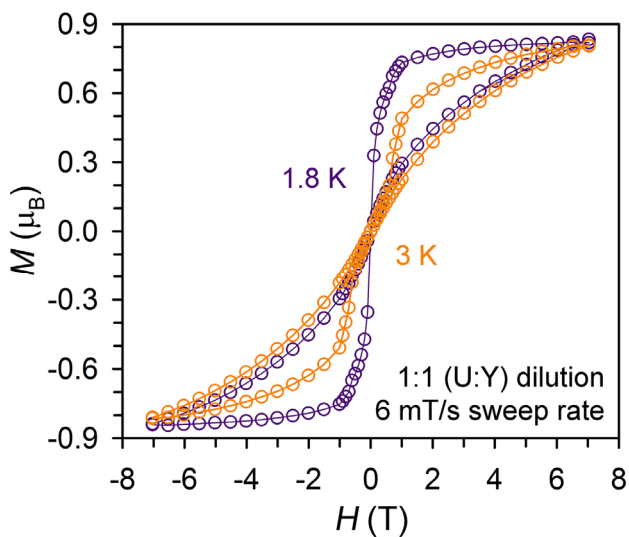


Figure 2.A7. Variable-field magnetization data collected at 1.8 K and 3 K between 7 T and -7 T for the 1:1 dilution of U(Bp)_3 .

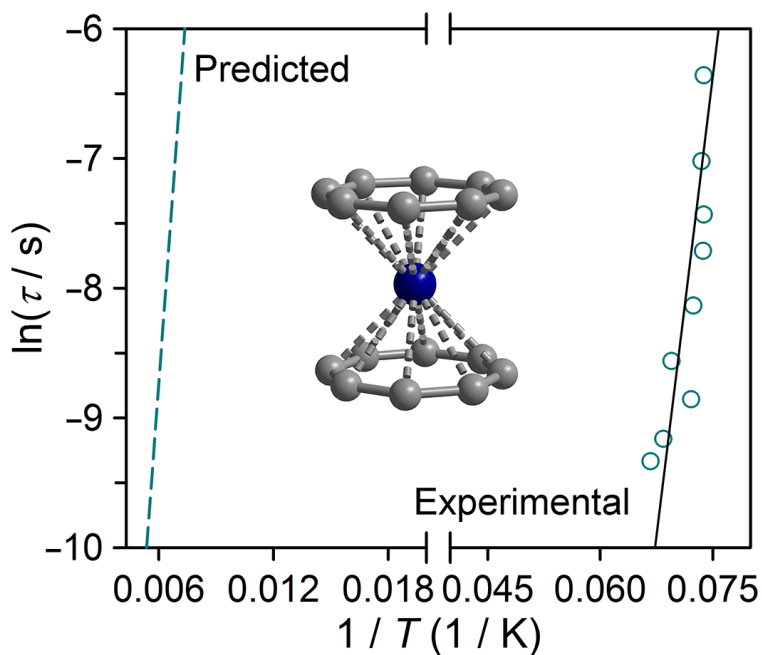
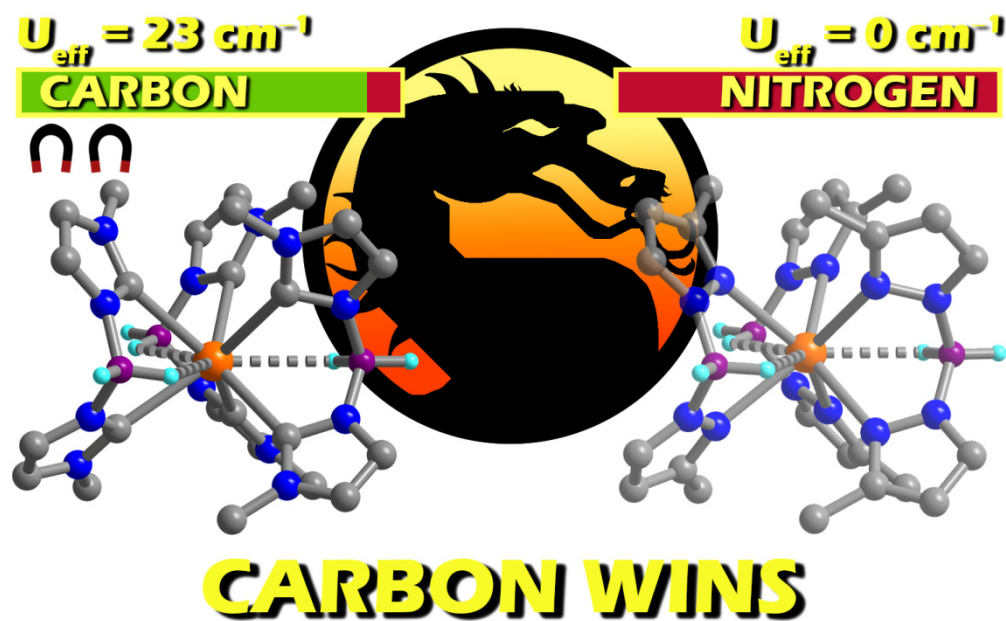


Figure 2.A8. Plot of $\ln(\tau)$ versus $1/T$ for $\text{Np}(\text{COT})_2$ (molecular structure inset) under $H_{\text{dc}} = 7$ T. Circles represent experimental data and the solid line represents a linear fit to an Arrhenius law, giving $U_{\text{eff}} = 471 \text{ cm}^{-1}$ and $\tau_0 = 7 \times 10^{-19}$ s. The dashed cyan line represents the predicted Arrhenius behavior assuming a calculated ground to first excited energy splitting of 1400 cm^{-1} and $\tau_0 = 1 \times 10^{-9}$ s.

Chapter 3: Influence of Pyrazolate vs *N*-Heterocyclic Carbene Ligands on the Slow Magnetic Relaxation of Homoleptic Trischelate Lanthanide(III) and Uranium(III) Complexes



3.1 Introduction

As has already been discussed, when considering the design of mononuclear single-molecule magnets of the lanthanides, the site symmetry around the metal center is of utmost importance in dictating the magnitude of the axial magnetic anisotropy and observed slow relaxation.¹ Recall the two Dy^{III} compounds $[\text{Zn}_2\text{DyL}_2]^+$ (O_h symmetry) and $[\text{Zn}_2\text{DyL}_2(\text{MeOH})]^+$ (D_{5h} symmetry) discussed in Chapter 1, which will interconvert via addition or removal of methanol.² While $[\text{Zn}_2\text{DyL}_2(\text{MeOH})]^+$ relaxes slowly under zero dc field with $U_{\text{eff}} = 305(3) \text{ cm}^{-1}$ and hysteresis to 12 K, $[\text{Zn}_2\text{DyL}_2]^+$ relaxes only in the presence of a dc field with $U_{\text{eff}} = 44(2) \text{ cm}^{-1}$. Ab initio calculations have demonstrated that both compounds possess comparable ground to first excited doublet splittings (289.9 cm^{-1} versus 294.8 cm^{-1} , respectively), though while the methanol coordinated compound has a highly axial ground doublet, $[\text{Zn}_2\text{DyL}_2]^+$ has non-negligible transverse anisotropy. The latter observation aids in rationalizing the much smaller observed relaxation barrier for $[\text{Zn}_2\text{DyL}_2]^+$, which appears to be heavily influenced by Raman and direct relaxation processes.²

In contrast, for mononuclear uranium (and actinide) complexes, the influence of symmetry on magnetic anisotropy and slow relaxation is still poorly understood. Mononuclear U^{III} compounds have been studied with a wide variety of geometries, including trigonal prismatic ($\text{U}(\text{Ph}_2\text{BPz}_2)_3$, ideal D_{3h} symmetry),³ tetrahedral ($[\text{U}(\text{OSi}(\text{O}^{\text{tBu}})_3)_4]^+$, ideal T_d symmetry),⁴ distorted triangular dodecahedral ($[\text{U}(\text{Tp}^*)_2\text{bipy}]^+$, ideal D_{2d} symmetry),⁵ and pentagonal bipyrimidal (ideal C_{2v} symmetry),⁶ though all species demonstrate very similar relaxation behavior with anisotropy barriers commonly between 15 and 23 cm^{-1} . Given these results and the demonstrated importance of covalency in actinide electronic structure and bonding,⁷ it seems insufficient even from a qualitative standpoint to consider ligand donor atoms as simple point charges interacting with an actinide ion (recall the discussion in Chapter 1). Indeed, it is interesting to consider that enhanced covalency may lead to partial quenching of orbital angular momentum and magnetic anisotropy for the actinides, as is common with mononuclear transition metal compounds.⁸ These possibilities have yet to be addressed directly in the literature and will no doubt require comprehensive experimental and computational efforts working in tandem. At the same time, an interesting question arises that the synthetic chemist is well-equipped to begin answering, namely: what influence, if any, does the donor atom have on slow relaxation in uranium and actinide compounds? Given the greater possibility for covalency among the actinides, it is interesting to consider that perhaps simply by changing the donor atom within a given symmetry, slow magnetic relaxation could be selectively tuned, thus presenting a new approach to the design of actinide-based single-molecule magnets. Moreover, while covalency is not expected to be a significant factor in lanthanide bonding, it is conceivable that changing the electrostatic properties of the ligand environment for these ions, via the use of soft rather than hard donors, may influence magnetic properties.

The vast majority of lanthanide- and actinide-based single-molecule magnets to date feature ligands with hard nitrogen or oxygen donors, while *N*-donor scorpionate ligands represent the majority of mononuclear U³⁺ single-molecule magnets, which incorporate either bis(pyrazolyl)borate or hydrotris(dimethylpyrazolyl)borate ligands.⁹ Dy^{III} can also exhibit slow magnetic relaxation as a homoleptic trischelate complex of the dihydrobis(dimethylpyrazolyl)borate ligand.^{9c} Notably, recent efforts have also demonstrated the utility of softer carbon-^{1b,10,11} and even sulfur-based donor ligands¹² in designing single-molecule magnets for a number of the lanthanides, though no study has directly compared the influence of

these softer donors with nitrogen or oxygen on slow magnetic relaxation. In this chapter, we present the first investigation of donor influence on slow magnetic relaxation for two series of f-element complexes, $M(\text{Bc}^{\text{Me}})_3$ and $M(\text{Bp}^{\text{Me}})_3$ ($M = \text{Y, Tb, Dy, Ho, Er, and U}$) incorporating the highly tunable scorpionate ligand.¹³ The compound $M(\text{Bc}^{\text{Me}})_3$ consists of a homoleptic ligand field of *N*-heterocyclic carbene donors ($\text{Bc}^{\text{Me}} = \text{dihydrobis(methylimidazolyl)borate}$), while $M(\text{Bp}^{\text{Me}})_3$ ($\text{Bp}^{\text{Me}} = \text{dihydrobis(methylpyrazolyl)borate}$) is assembled from the more common pyrazolate donor. $M(\text{Bc}^{\text{Me}})_3$ and $M(\text{Bp}^{\text{Me}})_3$ represent all new compounds, while $M(\text{Bc}^{\text{Me}})_3$ are the first examples of *N*-heterocyclic carbene complexes for Tb^{3+} and Dy^{3+} , as well as the first examples of homoleptic *N*-heterocyclic carbene complexes for any f-element. The results of magnetic characterization reveal that, while field-induced slow magnetic relaxation occurs for both series of complexes incorporating Tb^{3+} , Dy^{3+} , and U^{3+} , the relaxation time is orders of magnitude slower for $M(\text{Bc}^{\text{Me}})_3$ and experimental relaxation barriers are more than double for $M(\text{Bc}^{\text{Me}})_3$ compared to $M(\text{Bp}^{\text{Me}})_3$, revealing that ligand donor influence is significant for the lanthanides as well as uranium. Additional spectroscopic characterization indicates that this slower relaxation indeed arises from greater magnetocrystalline anisotropy, as engineered through the stronger axial ligand field of the *N*-heterocyclic carbene.

3.2 Experimental Section

All reactions and subsequent manipulations were performed under anaerobic and anhydrous conditions in a nitrogen-atmosphere glove box or on a nitrogen-atmosphere Schlenk line. THF, toluene, diethyl ether, and hexanes were dried by passage over activated molecular sieves using a custom-built solvent system. Anhydrous dimethoxyethane (DME) was purchased from Sigma Aldrich and further purified by distillation over sodium benzophenone ketyl, followed by several freeze-pump-thaw cycles to removed dissolved gases. UI_3 was prepared by a modification of the method of Cloke and Hitchcock.¹⁴ Fine uranium powder was synthesized by preparation of UH_3 ¹⁵ followed by removal of hydrogen under dynamic vacuum at 400 °C. Subsequent heating of the resulting metal powder with a stoichiometric amount of HgI_2 in a sealed tube under vacuum at 320 °C for 2 days afforded the black UI_3 starting material.

Lithium diisopropyl amide (LDA) was prepared by the dropwise addition of one equivalent of 1.6 M *n*-butyllithium to a stirring solution of diisopropyl amine in anhydrous hexanes at -78 °C. Solid white LDA was isolated via canula filtration, and subsequently washed several times with hexanes. Sodium diisopropyl amide (NaDA) was prepared as previously described by combining LDA with sodium tert-butoxide in hexanes at room temperature.¹⁶ The compound $\text{K}[\text{Bp}^{\text{Me}}]$ was prepared according to a literature method by heating potassium borohydride with an excess of two equivalents of 3-methylpyrazole at 120 °C.¹⁷ Crystals of $\text{K}[\text{Bp}^{\text{Me}}]$ used in metathesis reactions to form $M(\text{Bp}^{\text{Me}})_3$ were isolated through recrystallization from a THF solution layered with hexanes. $\text{Li}[\text{Bc}^{\text{Me}}]$ ¹⁸ was prepared in a manner similar to that previously described for $\text{Li}[\text{Bc}^{\text{tBu}}]$.¹⁹ THF-*d*₈ was purchased from Cambridge Isotopes Laboratories and stored over NaK prior to use. Anhydrous LnCl_3 was purchased from Strem Chemicals and diisopropyl amine, 1.6 M solution of *n*-butyllithium in hexanes, 1-methylimidazole, borane dimethylamine, I_2 , 3-methylpyrazole, and potassium borohydride were purchased from Sigma Aldrich. Iodine was purified by sublimation and 3-methylpyrazole was purified by vacuum distillation. All other chemicals were used as received.

NMR spectra were recorded on a Bruker AV 600 spectrometer. IR spectra were recorded on a Perkin Elmer Avatar Spectrum 400 FTIR Spectrometer equipped with ATR. Elemental analyses

were performed by the Micro-Mass Facility at the University of California, Berkeley on a Perkin-Elmer 2400 Series II combustion analyzer. Quartz tubes used for magnetic samples were custom-made by D&G Glassblowing, Inc.

Li/Na[Bc^{Me}]. Diethyl ether (15 mL) chilled at $-34\text{ }^{\circ}\text{C}$ was added to a stirring mixture of $[\text{H}_2\text{B}(\text{MeIm})_2]\text{I}$ and LDA or NaDA (2 equivalents) in a reaction vial. After stirring for 3 h, a crystalline white solid deposited in the case of the LDA reaction, while a pale yellow solution and a beige powder resulted from the NaDA reaction. Attempts to isolate pure $\text{Li}[\text{Bc}^{\text{Me}}]$ through recrystallization were not successful, likely due to the similar solubility of LiI . Rather, what is isolated upon recrystallization is a 1:1 mixture of $\text{Li}[\text{Bc}^{\text{Me}}]$ and LiI , cocrystallized with ~ 1 equiv of diethyl ether, as confirmed by elemental analysis. The presence of ~ 1 coordinated diethyl ether molecule is also confirmed by ^1H NMR of the as-isolated crystalline solid. Clean metathesis reactions resulted when using the solid mixture of LiI and $\text{Li}[\text{Bc}^{\text{Me}}]$ isolated directly by in vacuo removal of diethyl ether solvent and diisopropylamine formed in the reaction. Subsequent removal of Li^+ salts formed in the compound synthesis was achieved by extraction with DME. The absence of additional (organic) impurities beyond the LiI byproduct in the starting $\text{Li}[\text{Bc}^{\text{Me}}]$ material was confirmed by ^1H NMR (δ , 400 MHz, THF-*d*₈): 3.623 (s, 6H, Me); 6.585 (s, 2H, ring); 6.806 (s, 2H, ring). A resonance due to the borate hydrogen atoms was not observed. Calculated for $\text{C}_{12}\text{H}_{22}\text{BILi}_2\text{N}_4\text{O}$ (%) C: 36.96, H: 5.69, N: 14.37; found (%) C: 37.43, H: 5.35, N: 15.66 and (duplicate) C: 36.98, H: 5.56, N: 15.98. This formulation, with one LiI molecule and one coordinated diethyl ether, provided the best match to the obtained elemental analysis.

The Na^+ salt could be readily isolated as highly temperature-sensitive pale yellow needles by diethyl ether extraction of the beige solid formed in the reaction and storage of the resulting solution at $-34\text{ }^{\circ}\text{C}$ (0.175 g, 54% yield). The purity of these crystals was confirmed by elemental analysis. Calculated for $\text{C}_8\text{H}_{12}\text{BN}_4\text{Na}$ (%) C: 48.52, H: 6.12, N: 28.30; found (%) C: 48.89, H: 5.93, N: 28.19. ^1H NMR (δ , 400 MHz, THF-*d*₈): 3.557 (s, 6H, Me); 6.574 (d, 2H, ring); 6.798 (d, 2H, ring). The Na^+ salt was found to be much more reactive than the Li^+ salt and was not used as a ligand source.

$\text{M}(\text{Bp}^{\text{Me}})_3$ (M = Y, Tb, Dy, Ho, Er, U). At room temperature, a solution of 3 equivalents of $\text{K}[\text{Bp}^{\text{Me}}]$ in 6 mL THF was added to a stirring slurry of 1 equivalent MX_3 in 4 mL THF. The solution rapidly took on the characteristic color of the final corresponding metal complex over the course of ligand addition, and a fine white precipitate formed in solution. After reacting for 3 h, the solution was filtered over 2 cm diatomaceous earth, the solvent removed in vacuo, and the resulting residue re-dissolved in 10 mL diethyl ether with several drops of THF. The solution was filtered again over celite, layered with hexanes, and stored at $-34\text{ }^{\circ}\text{C}$. Crystals of $\text{M}(\text{Bp}^{\text{Me}})_3$ would typically form within 1-3 days. Low to moderate yields were obtained from a single crystallization, based on metal halide starting material: 0.135 g (0.692 mmol) of YCl_3 gave 0.170 g of $\text{Y}(\text{Bp}^{\text{Me}})_3$ (40%); 0.0747 g (0.282 mmol) of TbCl_3 gave 0.0778 g of $\text{Tb}(\text{Bp}^{\text{Me}})_3$ (40%); 0.0996 g (0.371 mmol) of DyCl_3 gave 0.0838 g of $\text{Dy}(\text{Bp}^{\text{Me}})_3$ (46%); 0.132 g (0.485 mmol) of HoCl_3 gave 0.025 g of $\text{Ho}(\text{Bp}^{\text{Me}})_3$ (7%); 0.0923 g (0.337 mmol) of ErCl_3 gave 0.0900 g of $\text{Er}(\text{Bp}^{\text{Me}})_3$ (39%); and 0.150 g (0.242 mmol) of UCl_3 gave 0.110 g of $\text{U}(\text{Bp}^{\text{Me}})_3$ (59%). We note that the reported crystalline yield for $\text{Ho}(\text{Bp}^{\text{Me}})_3$ is quite low, and much lower than the other complexes. This value is that obtained from a first recrystallization, and is consistently observed, while the crude powder yield(s) appear to be much greater. We ascribe this low yield to greater solubility of this complex in the crystallization solvents used. Calculated for $\text{C}_{24}\text{H}_{36}\text{B}_3\text{N}_{12}\text{Y}$ (%) C: 46.95, H: 5.91, N: 27.38; found (%) C: 46.96, H: 6.03, N: 27.06. Calculated for

$C_{24}H_{36}B_3N_{12}Tb$ (%) C: 42.14, H: 5.31, N: 24.57; found (%) C: 42.09, H: 5.20, N: 24.24. Calculated for $C_{24}H_{36}B_3DyN_{12}$ (%) C: 41.92, H: 5.29, N: 24.45; found (%) C: 41.63, H: 4.99, N: 24.11. Calculated for $C_{24}H_{36}B_3HoN_{12}$ (%) C: 41.78, H: 5.26, N: 24.36; found (%) C: 42.05, H: 5.21, N: 24.15. Calculated for $C_{24}H_{36}B_3ErN_{12}$ (%) C: 41.64, H: 5.24, N: 24.28; found (%) C: 41.49, H: 5.22, N: 24.09. Calculated for $C_{24}H_{36}B_3N_{12}U$ (%) C: 37.78, H: 4.76, N: 22.03; found (%) C: 37.80, H: 4.70, N: 21.80.

$M(Bc^{Me})_3$ (M = Y, Tb, Dy, Ho, Er, U). Separate slurries of 1 equivalent of MX_3 (M = Y, Tb, Dy, Ho, Er, U; X = I or Cl) in 6 mL THF and ~3 equivalents²⁰ of $LiI \cdot Li[Bc^{Me}]$ in 6 mL diethyl ether were chilled at -34 °C. With stirring, the metal salt slurry was added drop-wise to the slurry of ligand over the course of ~5 min. Upon complete addition of the metal salt, all reaction components largely dissolved in solution. The mixture was allowed to stir for 3 h, upon which the solution was cloudy with fine solid (Tb, Dy, Y = colorless; Ho, Er = pink; U = dark blue). The supernatant was decanted off of this solid and 10 mL DME was added to remove LiX. This mixture was stirred for 20 min and then the solid was isolated and dried under vacuum. Sufficient THF (~15-20 mL) was added to dissolve the solid and the resulting solution was filtered over 2 cm diatomaceous earth. Layering of this solution with a 50:50 (v:v) mixture of hexanes and diethyl ether and storage at room temperature resulted in crystals of $M(Bc^{Me})_3$ within 1-3 days. Moderate yields were obtained from a single crystallization, as follows based on metal halide starting material: 0.1113 g (0.5700 mmol) of YCl_3 gave 0.1492 g of $Y(Bc^{Me})_3$ (43%); 0.050 g (0.19 mmol) of $TbCl_3$ gave 0.063 g of $Tb(Bc^{Me})_3$ (48%); 0.050 g (0.19 mmol) of $DyCl_3$ gave 0.076 g of $Dy(Bc^{Me})_3$ (59%); 0.050 g (0.18 mmol) of $HoCl_3$ gave 0.049 g of $Ho(Bc^{Me})_3$ (38%); 0.0462 g (0.169 mmol) of $ErCl_3$ gave 0.0701 g of $Er(Bc^{Me})_3$ (60%); and 0.1135 g (0.1834 mmol) of UCl_3 gave 0.05920 g of $U(Bc^{Me})_3$ (42%). Multiple syntheses reproduced crystalline yields between 40-60% for each complex. A small amount of additional product could often be obtained from a second recrystallization, although decomposition in solution was evident and likely explains the less than optimum yields of the complexes. Calculated for $C_{24}H_{36}B_3N_{12}Y$ (%) C: 46.95, H: 5.91, N: 27.38; found (%) C: 47.08, H: 5.82, N: 27.45. Calculated for $C_{24}H_{36}B_3N_{12}Tb$ (%) C: 42.14, H: 5.31, N: 24.57; found (%) C: 42.10, H: 5.25, N: 24.38. Calculated for $C_{24}H_{36}B_3DyN_{12}$ (%) C: 41.92, H: 5.29, N: 24.45; found (%) C: 41.64, H: 5.14, N: 24.15. Calculated for $C_{24}H_{36}B_3HoN_{12}$ (%) C: 41.78, H: 5.26, N: 24.36; found (%) C: 41.78, H: 5.31, N: 24.18. Calculated for $C_{24}H_{36}B_3ErN_{12}$ (%) C: 41.64, H: 5.24, N: 24.28; found (%) C: 41.69, H: 5.17, N: 24.11. Calculated for $C_{24}H_{36}B_3N_{12}U$ (%) C: 37.78, H: 4.76, N: 22.03; found (%) C: 38.03, H: 4.96, N: 21.82.

Crystallography. Crystals were mounted on Kapton loops and transferred to a Bruker SMART APEX diffractometer, cooled in a nitrogen stream. The SMART program package was used to determine the unit cell parameters and for data collection (10 s/frame scan time for a hemisphere of diffraction data). Data integration was performed by SAINT and the absorption correction provided by SADABS. Subsequent calculations were carried out using the WinGX program, with structure solutions obtained using SIR2004²¹ and subsequent refinements performed using SHELX.²² The structures were solved by direct methods and refined against F^2 by full-matrix least-squares techniques. The analytical scattering factors for neutral atoms were used throughout the analysis. All non-borate Hydrogen atoms were included using a riding model. Electron density corresponding to the borate hydrogen atoms could be found in the Fourier difference map.

Magnetic Measurements. Samples were prepared by adding the powdered crystalline compound to a 5 mm inner diameter/7 mm outer diameter quartz tube with raised quartz

platform. Solid eicosane was added to cover the samples to prevent crystallite torquing and provide good thermal contact between the sample and the bath. The tubes were fitted with Teflon sealable adapters, evacuated using a glove box vacuum pump, and flame sealed under static vacuum. Following flame sealing, the solid eicosane was melted in a water bath held at 40 °C.

Magnetic susceptibility measurements were collected using a Quantum Design MPMS2 SQUID magnetometer. Dc susceptibility data measurements were performed at temperatures ranging from 1.8 to 300 K, using an applied field of 1000 Oe. The amounts of paramagnetic species present in dilute samples was determined by adjusting the mass of the paramagnetic material until the low temperature portions of the dilute dc susceptibility curves overlapped with that of the neat compound. Ac magnetic susceptibility measurements were performed using a 4 Oe switching field. All data were corrected for diamagnetic contributions from the core diamagnetism estimated using Pascal's constants²³ to give $\chi_D = -0.0003378$ emu/mol (Y congeners), -0.0003448 emu/mol (Tb/Dy/Ho congeners), -0.0003438 emu/mol (Er congeners), -0.0003718 emu/mol (U congeners), and -0.00024306 emu/mol (eicosane). Cole-Cole plots were fitted using formulae describing χ_M' and χ_M'' in terms of frequency, constant temperature susceptibility (χ_T), adiabatic susceptibility (χ_S), relaxation time (τ), and a variable representing the distribution of relaxation times (α).²⁴ All data could be fitted to give $\alpha \leq 0.4$ for field-dependent scans, $\alpha \leq 0.32$ for concentrated temperature-dependent scans, and $\alpha \leq 0.25$ for dilute temperature-dependent scans (Tables 3.S3-16).

EPR Measurements. Samples were sealed in quartz tubes with an inner diameter of 4 mm, under Ar, N₂, or static vacuum in the case of solution-phase samples of the Er compounds. EPR spectra were obtained at 2 K with a Varian E-12 spectrometer equipped with flowing liquid He cryostat, an EIP-547 microwave frequency counter, and a Varian E-500 gaussmeter. The data were recorded with a Hewlett-Packard XY plotter, and digitized using the program Un Scan It. The spectrum was fit using a version of the code ABVG modified to use the line shape described by Pilbrow and modified to fit spectra using the downhill simplex method.^{25,26}

Lanthanide M_{5,4}-Edge Measurements. All manipulations were performed with rigorous exclusion of air and moisture using standard Schlenk, glovebox, and glovebag techniques to ensure that trace water or oxygen impurities were removed. Tb₂O₃ was prepared according to the literature method.²⁷ Samples for STXM measurements were encapsulated between two 100 nm Si₃N₄ membranes (Silson), as described previously.²⁸ Single-energy images and lanthanide M_{5,4}-edge XANES spectra were acquired using the STXM instrument at the Molecular Environmental Science Beamline 11.0.2 at the Advanced Light Source, which is operated in tophoff mode at 500 mA, in a < 0.5 atm He filled chamber.²⁹ Energy calibrations were performed at the Ne K-edge for Ne (867.3 eV) or at the Al K-edge for Al foil (1559 eV). The energy resolution (FWHM) was estimated at 0.2 eV, and spectra were collected using elliptically polarized radiation. For these measurements, the x-ray beam was focused with a zone plate onto the sample, and the transmitted x-rays detected. Images at a single energy were obtained by raster-scanning the sample and collecting x-rays as a function of sample position. Spectra at each image pixel or particular regions of interest on the sample image were extracted from the "stack," which is a collection of images recorded at multiple, closely spaced photon energies across the absorption edge. Dwell times used to acquire an image at a single photon energy were < 1 ms per pixel. To quantify the absorbance signal, the measured transmitted intensity (I) was converted to optical density using Beer-Lambert's law: $OD = \ln(I/I_0) = \mu\rho d$, where I_0 is the incident photon flux intensity, d is the sample thickness, and μ and ρ are the mass absorption coefficients and density of the sample material, respectively. Incident beam intensity was measured through the sample-

free region of the Si₃N₄ windows. For Ln(Bp^{Me})₃ and Ln(Bc^{Me})₃, relatively large particles were selected with lateral dimensions $\geq 4 \mu\text{m}^2$. For Ln₂O₃, it was necessary to use smaller particles of area $\leq 0.4 \mu\text{m}^2$ to ensure that they were in the linear regime of the Beer-Lambert law (absorption < 1.5 OD). The branching ratio for Tb₂O₃ (0.60) was smaller than expected from the free ion value (0.74), which may be evidence of small errors due to self-absorption or surface contamination on the small particles. During the STXM experiment, particles showed no sign of radiation damage and each spectrum was reproduced several times on independent particles and different samples. Second-derivative spectra were used as guides to determine the number and position of peaks, and the areas under the M₅ and M₄ edges were determined graphically by integration of the second-derivative spectra (Figure 3.S48) using the program *IGOR 6.0*. Branching ratios were reproduced several times from multiple measurements performed on independent samples.

3.3 Results and Discussion

N-heterocyclic carbene ligands are well-known for their strongly σ -donating character and have found utility in stabilizing high-valent transition metal complexes,³⁰ homogeneous catalysis,³¹ and even actinide-lanthanide differentiation.³² However, *N*-heterocyclic carbene complexes of the f-elements are still fairly sparse, found primarily in heteroleptic systems in which the carbene is tethered to an alkyl chain or stabilized by bulky heteroatom substituents.³³ In one uranyl(VI) β -diketiminato derivative, free methylimidazolate ligands could also be stabilized through “ate” complex formation.³⁴ No prior examples are present in the literature of Tb³⁺ or Dy³⁺ *N*-heterocyclic carbene complexes, and no homoleptic complexes have been characterized for any f-element. Previous metal complexes of the ligand [Bc^{Me}][−] were limited to gold, palladium, and platinum, and in these cases the ligand was not isolated or characterized spectroscopically, but prepared *in situ* by deprotonation of [H₂B(MeIm)₂]I with *n*-butyllithium.¹⁸ Thus, the M(Bc^{Me})₃ complexes reported here represent the first example of *N*-heterocyclic carbene complexes of terbium and dysprosium, and also the first examples of homoleptic *N*-heterocyclic carbene complexes for any f-element.

Our synthetic approach to Li[Bc^{Me}] closely followed the route established by Nieto and coworkers for the synthesis of Li[Bc^{tBu}].¹⁹ Interestingly, the precursor imidazolium salt [H₂B(MeIm)₂]I is an ionic liquid above 100 °C. The compounds Li[Bc^{Me}] and Na[Bc^{Me}] were prepared via deprotonation of [H₂B(MeIm)₂]I with two equivalents of the corresponding diisopropyl amide in diethyl ether at −34 °C. Both salts could be isolated as highly temperature-sensitive crystalline solids, free of organic impurities as indicated by ¹H NMR spectroscopy; however, it was not possible in our hands to isolate LiI-free crystals of Li[Bc^{Me}], as indicated by elemental analysis. In contrast, Na[Bc^{Me}] could be re-crystallized from diethyl ether as pale yellow needles, and proved to be pure by elemental analysis. Due to the greater temperature sensitivity and reactivity of Na[Bc^{Me}], however, only Li[Bc^{Me}] was used in the synthesis of M(Bc^{Me})₃.

Initial attempts to synthesize M(Bc^{Me})₃ in THF at room temperature led to a mixture of products, of which the desired complex was frequently a minor component. Cooling the reaction to −34 °C also did not increase the yield significantly. Instead, it was found that a mixture of diethyl ether and THF (50% diethyl ether or more by volume) led to highly reproducible synthesis of M(Bc^{Me})₃ in moderate yields. Accordingly, a slurry of metal salt in THF was chilled to −34 °C and added dropwise to a stirring slurry of LiI·Li[Bc^{Me}] in diethyl ether, also at −34 °C.

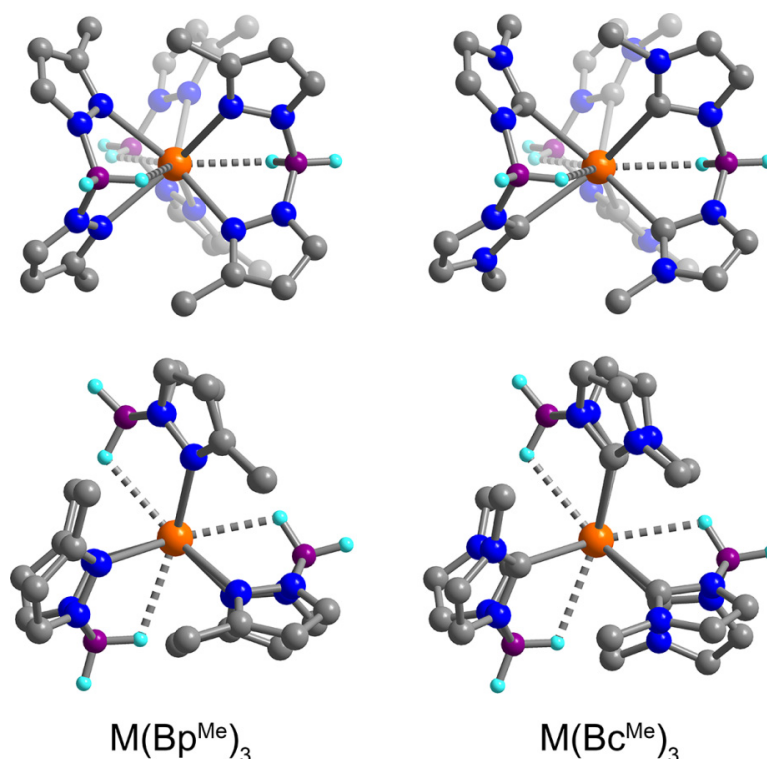


Figure 3.1. Side and top views of x-ray crystal structures of the trigonal prismatic complexes $M(\text{Bp}^{\text{Me}})_3$ and $M(\text{Bc}^{\text{Me}})_3$ for $M = \text{U}$. The lanthanide congeners are isostructural. Orange, grey, blue, purple, and pale blue spheres represent U, C, N, B, and H atoms, respectively; all other hydrogen atoms have been omitted for clarity. The borate hydrogen atoms were found in the Fourier difference map, confirming agostic $M \cdots \text{H}-\text{BH}$ interactions.

After stirring for 3 h, solid $M(\text{Bc}^{\text{Me}})_3$ precipitated from the reaction mixture and could readily be isolated by decanting off the supernatant and stirring the resulting solid in DME to remove excess LiI or LiCl.

Crystals of $M(\text{Bc}^{\text{Me}})_3$ grow in the course of 1-3 days at room temperature, from a THF solution layered with a 50:50 (v:v) mixture of hexanes and diethyl ether. The crystals form as beautiful transparent rectangular blocks with considerable luster, and are deep royal blue for U^{3+} , colorless for Tb^{3+} , Dy^{3+} , and Y^{3+} , and neon and pale pink for Er^{3+} and Ho^{3+} , respectively. When crystalline, these compounds are only minimally soluble in THF and completely insoluble in other ethereal or aromatic solvents. The compounds $M(\text{Bc}^{\text{Me}})_3$ are air and temperature-sensitive and start to decompose within a few days under nitrogen when left in the solid state at room temperature. Interestingly, $\text{Ho}(\text{Bc}^{\text{Me}})_3$ appears bright pink under illumination with a mercury vapor lamp, while under broad spectrum light it is pale yellow (Figure 3.A1), a common phenomenon for Ho^{3+} compounds arising from sharp phosphor-like emission.³⁵

Compounds $M(\text{Bp}^{\text{Me}})_3$ were synthesized at room temperature from the combination of the corresponding metal halide and potassium salt of the ligand in THF. This reaction proceeds cleanly at room temperature, and is not significantly dependent on the identity of the reaction solvent or manner of combination of metal salt and ligand. Further in contrast to $M(\text{Bc}^{\text{Me}})_3$, the

Table 3.1. Selected Bond Lengths (Å) and Angles (deg).

Compound	M–C or N^a	Bite angle	Inter-centroid^b	M...H	M...B	M...M	Normalized bite
U(Bp ^{Me}) ₃	2.588(4)	76.73(9)	3.2105(3)	2.62(4)	3.201(5)	9.427(1)	1.241(2)
U(Bc ^{Me}) ₃	2.662(4)	73.77(9)	3.188(2)	2.75(2)	3.334(4)	8.482(5)	1.200(2)
Tb(Bp ^{Me}) ₃	2.491(3)	78.99(5)	3.1680(1)	2.44(2)	3.113(3)	9.508(1)	1.272(2)
Tb(Bc ^{Me}) ₃	2.578(3)	75.55(5)	3.1533(2)	2.74(2)	3.282(2)	8.699(1)	1.225(2)
Dy(Bp ^{Me}) ₃	2.481(3)	78.94(5)	3.1535(2)	2.48(2)	3.103(3)	9.496(1)	1.271(2)
Dy(Bc ^{Me}) ₃	2.577(4)	75.40(9)	3.148(2)	2.75(3)	3.277(4)	8.919(1)	1.223(2)
Ho(Bp ^{Me}) ₃	2.473(3)	79.12(6)	3.2921(2)	2.43(2)	3.091(3)	9.491(1)	1.277(2)
Ho(Bc ^{Me}) ₃	2.556(3)	75.49(6)	3.1246(1)	2.71(2)	3.273(3)	8.743(1)	1.224(2)
Er(Bp ^{Me}) ₃	2.463(3)	79.11(6)	3.1360(3)	2.42(2)	3.086(2)	9.482(1)	1.274(2)
Er(Bc ^{Me}) ₃	2.545(3)	75.56(5)	3.1183(2)	2.71(2)	3.271(2)	8.771(1)	1.225(2)
Y(Bp ^{Me}) ₃	2.474(1)	78.95(5)	3.1440(2)	2.41(1)	3.100(3)	9.483(3)	1.271(1)
Y(Bc ^{Me}) ₃	2.565(2)	75.39(5)	3.1314(2)	2.71(2)	3.280(3)	8.731(1)	1.223(1)

^a Averages of the two crystallographically independent values.

^b Distance between two centroids defined by upper and lower plane of coordinated carbon (nitrogen) atoms.

$M(\text{Bp}^{\text{Me}})_3$ complexes readily crystallize at low temperature and are highly soluble in THF, with good solubility in DME or 2-MeTHF, and limited solubility in diethyl ether. These species can also be stored indefinitely under nitrogen at room temperature without decomposition. Crystals of the $M(\text{Bp}^{\text{Me}})_3$ complexes grow within 1-3 days at -34°C from a solution of THF or 2-MeTHF layered with hexanes. The crystals also form as rectangular blocks, and are dark burgundy in the case of U^{3+} , colorless for Tb^{3+} , Dy^{3+} , and Y^{3+} , and neon and pale pink for Er^{3+} and Ho^{3+} , respectively; crystals of $\text{Ho}(\text{Bp}^{\text{Me}})_3$ exhibit the same color change as $\text{Ho}(\text{Bc}^{\text{Me}})_3$.

Both $M(\text{Bp}^{\text{Me}})_3$ and $M(\text{Bc}^{\text{Me}})_3$ complexes crystallize in the space group $R\bar{3}$, with idealized C_{3h} symmetry (see Figure 3.1), where the presence of agostic $M\cdots\text{H}-\text{BH}$ interactions leads to an overall tricapped trigonal prismatic coordination geometry, analogous to $\text{U}(\text{Bp})_3$ as discussed in Chapter 2. Such agostic interactions are observed for metal complexes of scorpionate ligands,³⁶ and can be identified as a manifold of infrared stretches in the range of $2200\text{-}2500\text{ cm}^{-1}$ (Figure 3.A2). Electron density corresponding to $-\text{BH}_2$ protons could be found in the Fourier difference map of all complexes, and the resulting $M\cdots\text{H}-\text{BH}$ interaction distances along with metal-donor distances are given in Table 3.1.

The $M-\text{N}^{36,\text{d}}$ or $M-\text{C}^{32,33}$ bond lengths for each complex are in agreement with previously reported values, with the $M-\text{C}$ distances consistently longer than the $M-\text{N}$ distances by as much as 0.1 \AA . Notably, the $M-\text{N}$ separations in the $M(\text{Bp}^{\text{Me}})_3$ complexes are the same within error when the ionic radius of the lanthanide ion is excluded and the same is true for the $M-\text{C}$ distances in $M(\text{Bc}^{\text{Me}})_3$; thus, these metrical parameters alone would suggest that the bonding is best described as ionic for both types of complexes.³⁷ Additional structural features of note are the ligand bite angles, agostic $M\cdots\text{H}$ distances, and nearest neighbor $M\cdots\text{M}$ distances. The ligand bite angles for the $M(\text{Bc}^{\text{Me}})_3$ complexes are smaller by more than 3° when compared to the corresponding $M(\text{Bp}^{\text{Me}})_3$ complexes, and these are accompanied by agostic $M\cdots\text{H}$ interaction distances that are larger on average by $\sim 0.3\text{ \AA}$. Values of the normalized bite angles calculated for all complexes by the method of Kepert (Table 3.1)³⁸ reveal that these differences are statistically significant, with a smaller normalized bite associated with the $M(\text{Bc}^{\text{Me}})_3$ complexes. Furthermore, the distance between centroids defined by the upper and lower nitrogen (carbon) atoms is smaller for $M(\text{Bc}^{\text{Me}})_3$. Thus, coordination of the *N*-heterocyclic carbene ligands leads to formation of a trigonal prism that is more axially compressed than that formed by coordination of the bis(pyrazolyl)borate ligands. From a purely electrostatic argument, we might therefore expect that the crystal field in $M(\text{Bc}^{\text{Me}})_3$ will be more favorable in promoting slow relaxation for oblate f-element ions.

Static Magnetic Susceptibility. Magnetic susceptibility data were collected for the $M(\text{Bp}^{\text{Me}})_3$ and $M(\text{Bc}^{\text{Me}})_3$ compounds under a static field of 1000 Oe (Figures 3.2 and 3.A4). In the case of U^{3+} , these measurements provide information about the splitting of the $J = 9/2$ ground state manifold by the crystal field, which removes the degeneracy of the corresponding M_J states. In C_{3h} symmetry, the $^4I_{9/2}$ ground state forms five Kramers doublets: the $M_J = \pm 1/2$ doublet, two doublets that are mixtures of $M_J = \pm 9/2$ and $\mp 3/2$, and two that are mixtures of $M_J = \pm 7/2$ and $\mp 5/2$.

As the temperature is raised from zero K, $\chi_M T$ increases due to two factors. At the lowest temperatures, only the ground state is populated, and the slope is typically due to temperature independent paramagnetism, the value of which is inversely proportional to the energy gap between the two lowest M_J doublets.³⁹ In this regime, $\chi_M T$ is linear with temperature, as in the $\text{U}(\text{Bc}^{\text{Me}})_3$ data between 0 and 50 K. As the temperature increases, other low-lying states become thermally populated. For these states, the magnitude of the temperature-independent

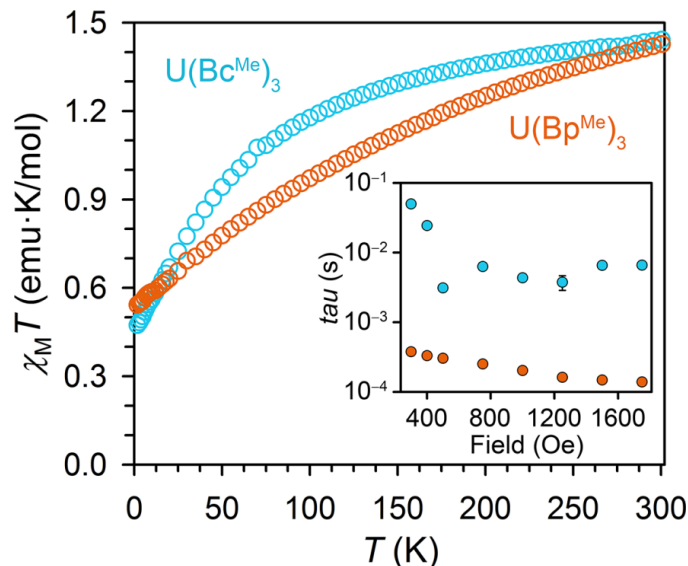


Figure 3.2. Plot of the molar magnetic susceptibility times temperature versus temperature ($\chi_M T$ versus T) for $U(Bc^{Me})_3$ (blue circles) and $U(Bp^{Me})_3$ (orange circles) collected under an applied field of 0.1 T. For free U^{3+} $\chi_M T = 1.63$ emu·K/mol (L–S coupling). (Inset) Plot of the relaxation time versus H_{dc} for $U(Bc^{Me})_3$ and $U(Bp^{Me})_3$ at 1.8 K.

paramagnetism is the same, but it is of opposite sign to that of the ground state, and the slope of $\chi_M T$ versus T will thus decrease, as seen at ~ 70 K for $U(Bc^{Me})_3$.³⁹

As the temperature is increased and $k_B T$ becomes significantly greater than the splitting within the $J = 9/2$ manifold, the Kramers doublets are equivalently populated, and $\chi_M T$ becomes largely temperature independent, approaching the free-ion value.⁴⁰ For both $U(Bp^{Me})_3$ and $U(Bc^{Me})_3$, the room temperature $\chi_M T$ values of 1.43 and 1.44 emu·K/mol, respectively, are significantly lower than the value of 1.63 emu·K/mol calculated for a free f^3 ion, though still within range of previously reported values for U^{3+} complexes (Chapter 2 and Ref. 9, 10). This low room temperature value of $\chi_M T$ may arise from two possibilities. First, if the crystal field splitting is large relative to $k_B T$ at 300 K, the population of the Kramers doublets in the $J = 9/2$ manifold will not be complete, and the plot of $\chi_M T$ versus T will have a significant slope, as is the case for $U(Bp^{Me})_3$. This could suggest a larger crystal field splitting for $U(Bp^{Me})_3$ relative to $U(Bc^{Me})_3$. In the absence of higher temperature data, however, such an observation can only be speculative; for instance, a plateau and subsequent additional rise in $\chi_M T$ could also occur for $U(Bc^{Me})_3$ at higher temperatures, and it is impossible to predict when the plot for $U(Bp^{Me})_3$ may level out.

The presence of significant covalency in the bonding between ligands and the U^{3+} center can also lead to a $\chi_M T$ value much less than that of the free-ion value,⁴¹ as the orbital angular momentum of the occupied f-orbitals is reduced. While the value of $\chi_M T$ for $U(Bc^{Me})_3$ is only slightly temperature dependent at 300 K, consistent with a small crystal field splitting relative to room temperature, that of $U(Bp^{Me})_3$ is still strongly temperature dependent. Interestingly, this observation might suggest that the magnitude of $\chi_M T$ will be greater for $U(Bp^{Me})_3$ when the $J = 9/2$ multiplet is fully populated, and therefore that the bonding in $U(Bc^{Me})_3$ is more covalent.

For $M = Tb^{3+}$, Dy^{3+} , Ho^{3+} , and Er^{3+} , the room temperature $\chi_M T$ values are 11.74 and 12.14 emu·K/mol, 14.05 and 13.90 emu·K/mol, 14.16 and 13.78 emu·K/mol, and 11.62 and 11.58 emu·K/mol for the $M(Bp^{Me})_3$ and $M(Bc^{Me})_3$ complexes, respectively, agreeing well with those

anticipated for the free ions (11.82, 14.17, 14.07, and 11.48 emu·K/mol).⁴² For each metal, the temperature dependence of $\chi_M T$ is similar between isomers (Figure 3.A4) in contrast to the uranium congeners. The similarity of the room temperature moments of $\text{Ln}(\text{Bp}^{\text{Me}})_3$ and $\text{Ln}(\text{Bc}^{\text{Me}})_3$ to the free ion values strongly suggests that covalency is small (compared to $k_B T$ at room temperature) in both sets of compounds. Likewise, the low temperatures at which the $\chi_M T$ versus T plots flatten out strongly suggest that the crystal field splitting is weak for all of the complexes, with the possible exception of the Tb^{3+} species.

Variable-Field Ac Magnetic Susceptibility. A hallmark of single-molecule magnetism is slow magnetic relaxation in the presence of a small oscillating magnetic field, leading to the presence of an out-of-phase component, χ_M'' , to the magnetic susceptibility. In the presence of a 4 Oe oscillating field and zero external field, over the frequency range of 1-1500 Hz no full peak was observed for χ_M'' for $\text{M}(\text{Bp}^{\text{Me}})_3$ or $\text{M}(\text{Bc}^{\text{Me}})_3$. However, many factors can lead to the absence of slow magnetic relaxation under zero applied field, including the presence of dipolar interactions and zero-field tunneling,⁴³ the latter having particular relevance for non-Kramers ions (i.e., ions with an even number of electrons) such as Tb^{3+} and Ho^{3+} . In such cases, application of a dc field can suppress tunneling or break up transverse fields caused by dipolar interactions, and reveal slow magnetic relaxation.⁴³ Indeed, at 1.8 K under a small applied dc field of less than 500 Oe, an out-of-phase signal becomes apparent for the complexes $\text{M}(\text{Bp}^{\text{Me}})_3$ and $\text{M}(\text{Bc}^{\text{Me}})_3$ ($\text{M} = \text{Tb}^{3+}$, Dy^{3+} , and U^{3+}) (Figures 3.A5-3.A12). For the $\text{M}(\text{Bc}^{\text{Me}})_3$ species, the relaxation is generally characterized by high frequency χ_M'' peaks under small applied dc fields, which grow in magnitude and move to lower frequencies as the field is increased. In the cases of Tb and $\text{Dy}(\text{Bp}^{\text{Me}})_3$, only high frequency tails are observed in χ_M'' for fields as high as 1250 Oe, precluding further analysis of the relaxation behavior in the concentrated samples.⁴⁴ However, for all compounds, the relaxation time is notably one to two orders of magnitude slower for $\text{M}(\text{Bc}^{\text{Me}})_3$ than for the corresponding $\text{M}(\text{Bp}^{\text{Me}})_3$ complex (Figures 3.2, inset, and 3.A5-3.A12). Note that the optimum applied magnetic field used below in temperature-dependent measurements corresponds to a simultaneous maximum in χ_M'' and τ .

Variable-Temperature Ac Magnetic Susceptibility. The compounds $\text{M}(\text{Bc}^{\text{Me}})_3$ ($\text{M} = \text{Tb}$, Dy , U) and $\text{U}(\text{Bp}^{\text{Me}})_3$ all demonstrate temperature-dependence in χ_M'' . However, the corresponding plots of $\ln(\tau)$ versus $1/T$ show pronounced deviations from linearity (Figures 3.A22-3.A25), indicating that thermally-activated Orbach relaxation is not the dominant spin-lattice relaxation process. In such a scenario, commonly only the highest temperature points are fit to extract a value of the relaxation barrier, U_{eff} . However, this method provides only an estimate of U_{eff} , making a comprehensive comparison of relaxation behavior challenging. As has been discussed already in chapter 1, by considering the other possible spin-lattice relaxation mechanisms, namely Raman⁴⁵ and direct⁴⁶ processes, it is possible to fit the entire range of temperature-dependent relaxation.^{47,48} This fitting was accomplished by employing Equation 1,⁴⁹ and enabled determination of the contribution from each spin-lattice mechanism in $\text{M}(\text{Bp}^{\text{Me}})_3$ and $\text{M}(\text{Bc}^{\text{Me}})_3$. In this equation, the first, second, and third terms account for the temperature-dependence of direct, Orbach, and two-phonon Raman relaxation processes, respectively. Orbach and Raman processes can both be observed under zero dc field, while in the presence of applied fields the possibility of direct relaxation between out-of-resonance ground states becomes highly relevant. The values of the exponents m and n have been shown to take on various values, with the direct process commonly showing linear or quadratic dependence on temperature ($m = 1$ or 2), while the exponent of the Raman process is highly dependent on the identity of the metal ion and the energy separations between lowest lying Kramers doublets (see Ref 48b and 50).

Table 3.2. Parameters obtained from fitting temperature-dependent ac susceptibility for $M(\text{Bc}^{\text{Me}})_3$ and $M(\text{Bp}^{\text{Me}})_3$.

Compound	U_{eff}^a (cm^{-1})	τ_0 (s)	A ($\text{s}^{-1} \cdot \text{K}^{-1}$)	A ($\text{s}^{-1} \cdot \text{K}^{-2}$)	C ($\text{s}^{-1} \cdot \text{K}^{-5}$)
$\text{U}(\text{Bp}^{\text{Me}})_3$	–	–	1271(3)	–	23.09(4)
11% $\text{U}(\text{Bp}^{\text{Me}})_3$	–	–	262(3)	–	9.69(2)
$\text{U}(\text{Bc}^{\text{Me}})_3$	22.009(1)	1×10^{-7}	77.317(6)	–	1.1294(2)
12% $\text{U}(\text{Bc}^{\text{Me}})_3$	23.163(2)	1×10^{-7}	0	–	0.1863(4)
14% $\text{Tb}(\text{Bp}^{\text{Me}})_3^b$	21(1)	$1(1) \times 10^{-6}$	115.9(7)	–	–
$\text{Tb}(\text{Bc}^{\text{Me}})_3$	44.8(2)	$8.6(2) \times 10^{-6}$	–	0.527(4)	–
11% $\text{Tb}(\text{Bc}^{\text{Me}})_3$	45.2(4)	$6.6(4) \times 10^{-6}$	–	0.23(1)	–
$\text{Dy}(\text{Bc}^{\text{Me}})_3$	32.8(7)	$6(1) \times 10^{-9}$	3.1(3)	–	–
12% $\text{Dy}(\text{Bc}^{\text{Me}})_3^c$	33.6(3)	$4.2(4) \times 10^{-9}$	0.39(9)	–	–

^a Data acquired under $H_{\text{dc}} = 1500$ Oe except in the case of concentrated $\text{U}(\text{Bc}^{\text{Me}})_3$ ($H_{\text{dc}} = 750$ Oe) and $\text{U}(\text{Bp}^{\text{Me}})_3$ ($H_{\text{dc}} = 300$ Oe).

^b Fitting to Equation 1 also gives a small Raman contribution with $C = 0.0013(1) \text{ s}^{-1} \cdot \text{K}^{-7}$.

^c Fitting to Equation 1 also gives a very small Raman contribution with $C = 0.00057(8) \text{ s}^{-1} \cdot \text{K}^{-9}$.

$$\tau^{-1} = AT^m + \tau_0^{-1} \exp(-U_{\text{eff}}/k_{\text{B}}T) + CT^n \quad (3.1)$$

Uranium. Under an applied field of $H_{\text{dc}} = 750$ Oe, a χ_M'' signal is observed from 1.7-4.1 K for $\text{U}(\text{Bc}^{\text{Me}})_3$ (Figure 3.A13). Relaxation times were extracted at each of these temperatures by fitting Cole-Cole plots using a generalized Debye model.²⁴ Fitting a plot of $\ln(\tau)$ versus $1/T$ to Equation 1 reveals that Orbach relaxation dominates at high temperatures with $U_{\text{eff}} = \sim 22 \text{ cm}^{-1}$. A very small contribution from a Raman process is also evident, while direct relaxation occurs at low temperatures (Table 3.2 and Figure 3.A22). In contrast, $\text{U}(\text{Bp}^{\text{Me}})_3$ demonstrates a much weaker temperature dependence under a 300 Oe applied field (Figure 3.A15) and a plot of $\ln(\tau)$ versus $1/T$ can be fit with only direct and Raman contributions (Table 3.2 and Figure 3.A23).⁵⁰

Terbium. The slowest relaxation among all of the compounds occurs for $\text{Tb}(\text{Bc}^{\text{Me}})_3$, for which an applied field of 1500 Oe leads to the presence of a χ_M'' signal from 4-19 K within the measured frequency range (Figure 3.A17). $\text{Tb}(\text{Bc}^{\text{Me}})_3$ also exhibits the largest relaxation barrier at $U_{\text{eff}} = 44.8(2) \text{ cm}^{-1}$ (Table 3.2 and Figure 3.A24).

Dysprosium. Under a 1500 Oe applied field, $\text{Dy}(\text{Bc}^{\text{Me}})_3$ relaxes slowly over the temperature range 2.5-4.6 K. Values of the α parameter at this field indicate a narrow distribution of relaxation times ($\alpha \leq 0.2$),²⁴ although a clearly resolved second process grows in at low frequencies, accounting for a very small magnitude of the total susceptibility (Figure 3.A20).⁵¹ Fitting of the temperature-dependence of the dominant process reveals that the relaxation is thermally activated, with $U_{\text{eff}} = 32.8(7) \text{ cm}^{-1}$ and $\tau_0 = 6(1) \times 10^{-9} \text{ s}$ (Table 3.2 and Figure 3.A25).

Dilution Studies. To further aid in the comparison of relaxation behavior, ac susceptibility measurements were performed on crystalline dilute samples prepared with $\text{Y}(\text{Bc}^{\text{Me}})_3$ and $\text{Y}(\text{Bp}^{\text{Me}})_3$. These measurements confirm the molecular origins of the observed slow magnetic relaxation, and provide even stronger evidence of the advantage of the *N*-heterocyclic carbene ligand. At 1.8 K the relaxation time for 12 mol% $\text{U}(\text{Bc}^{\text{Me}})_3$ is orders of magnitude slower than in the concentrated species and field-dependent frequency scans at 3.5 K reveal only a single peak indicating uniform relaxation (Figure 3.A26). Fitting of the temperature-dependent relaxation data collected at 1500 Oe reveals predominantly Orbach relaxation with $U_{\text{eff}} \sim 23 \text{ cm}^{-1}$, and the

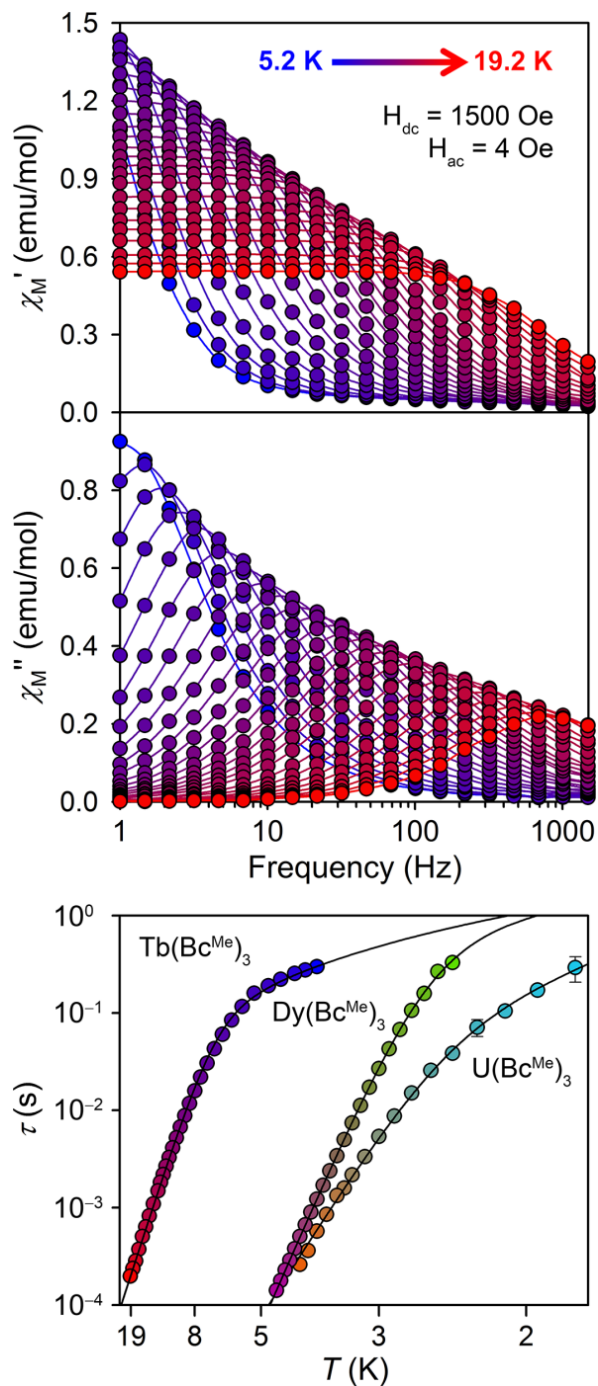


Figure 3.3. (Upper) Plot of the in-phase (χ_M') and out-of-phase (χ_M'') magnetic susceptibility for 11 mol% $\text{Tb}(\text{Bc}^{\text{Me}})_3$ under an applied field of 1500 Oe. (Lower) Plot of the relaxation time τ (log scale) versus T (inverse scale) for samples of 11% Tb, 12% Dy, and 12% $\text{U}(\text{Bc}^{\text{Me}})_3$ under $H_{dc} = 1500$ Oe. Percentages represent molar quantities of the paramagnetic complex present in a matrix of $\text{Y}(\text{Bc}^{\text{Me}})_3$. Fitting to Equation 3.1 yields $U_{\text{eff}} = 45.2(4) \text{ cm}^{-1}$ ($\text{Tb}(\text{Bc}^{\text{Me}})_3$), $33.6(3) \text{ cm}^{-1}$ ($\text{Dy}(\text{Bc}^{\text{Me}})_3$), and $\sim 23 \text{ cm}^{-1}$ ($\text{U}(\text{Bc}^{\text{Me}})_3$) with $\tau_0 = 6.6(4) \times 10^{-6} \text{ s}$, $4.2(4) \times 10^{-9} \text{ s}$, and $1 \times 10^{-7} \text{ s}$, respectively.

process is no longer operative (Figure 3.3, Table 3.2, and Figure 3.A34). For a sample of 11 mol% U(Bp^{Me})₃ in Y(Bp^{Me})₃, the relaxation time is slowed only by a factor of four and the direct process remains dominant (Figures 3.A32 and 3.A35).

For 11 mol% Tb(Bc^{Me})₃ co-crystallized with Y(Bc^{Me})₃, slow relaxation is present under zero applied dc field as a tail at the highest frequencies. Under an applied field of 1500 Oe, the temperature range of observable χ_M'' signal extends from 5.2-19.2 K (Figure 3.3) and the relaxation time has increased below 8 K compared to the concentrated sample. Moreover, the contribution of the direct process is now half of what it was in the concentrated sample and the relaxation barrier increases to $U_{\text{eff}} = 45.2(4) \text{ cm}^{-1}$ (Table 3.2). Dilution of Tb(Bp^{Me})₃ results in observable χ_M'' signal from 1.7 to 7.45 K under an applied field of 1500 Oe (Figure 3.A39), although the relaxation occurs largely via direct and Raman processes. A small contribution from Orbach relaxation is fit at the highest temperatures (Figure 3.A41), yet still the estimated barrier is less than half of that for Tb(Bc^{Me})₃ (Table 3.2).

A sample of 11 mol% Dy(Bp^{Me})₃ in Y(Bp^{Me})₃ displays only very broad and featureless peaks under applied fields, precluding any analysis of relaxation behavior. However, for a 12 mol% sample of Dy(Bc^{Me})₃ in Y(Bc^{Me})₃ the relaxation time slows greatly and χ_M'' signal can be seen even under zero dc field, although only at the highest measured frequencies, as observed for Tb(Bc^{Me})₃. This peak is very broad, suggesting multiple relaxation processes; however, application of a 1500 Oe field results in uniform peaks from 2.4-4.6 K (Figure 3.A44). For this sample, the coefficient for the direct process decreases by nearly an order of magnitude (Table 3.2) and the relaxation is clearly dominated by an Orbach process (Figures 3.3 and 3.A46). From this data, a $U_{\text{eff}} = 33.6(3) \text{ cm}^{-1}$ and $\tau_0 = 4.24 \times 10^{-9} \text{ s}$ are calculated, in good agreement with the concentrated sample.

The relaxation parameters determined from fitting the data for each complex are summarized in Table 3.2. Taking the parameters obtained from the dilute samples, which more closely represent molecular relaxation, the experimental values of U_{eff} are small, although within range of those previously reported for mononuclear systems.⁵² In the case of U(Bc^{Me})₃, the relaxation barrier of $\sim 23 \text{ cm}^{-1}$ is the highest yet reported for a mononuclear uranium species. Notably, the observation of slow magnetic relaxation only for the Tb³⁺, Dy³⁺, and U³⁺ compounds supports the underlying principle that an axial ligand field is favorable for the oblate f-element ions.⁵³ However, the relaxation is significantly slower for the corresponding M(Bc^{Me})₃ compounds and is dominated by an Orbach process, despite closer inter-ion distances compared to M(Bp^{Me})₃. Clearly, the presence of a carbon donor in the M(Bc^{Me})₃ complexes serves to lengthen τ and facilitates relaxation through thermal means. Considering again a crystal field model, it could be argued that the much slower relaxation for M(Bc^{Me})₃ results in large part from the axial compression of this crystal field relative to M(Bp^{Me})₃ (vide supra). In order to further probe electronic differences in these two complexes, we turned to M_{5,4}-edge, EPR, and ¹H NMR spectroscopies.

Lanthanide XANES. Of the experimental approaches to evaluate electronic structure in lanthanide materials, XANES has historically formed an important component of the characterization of complex systems with many-electron or open-shell configurations.⁵⁴ Exciting electrons from 3d core orbitals at the M₅ and M₄ edges is a particularly effective method because it probes the valence 4f orbitals directly with electric dipole-allowed transitions of $\Delta l \pm 1$.⁵⁵ For the free ion, these M_{5,4}-edge transitions can be described as $3d^{10}4f^n \rightarrow 3d^94f^{n+1}$ excitations, which are split into two primary M₅ ($3d_{5/2} \rightarrow 4f_{7/2}$ and $3d_{5/2} \rightarrow 4f_{5/2}$) and M₄ ($3d_{3/2} \rightarrow 4f_{5/2}$) edges due to differences in the stabilization of the spin-orbit split $3d_{5/2}$ and $3d_{3/2}$ core hole (Figure 3.4,

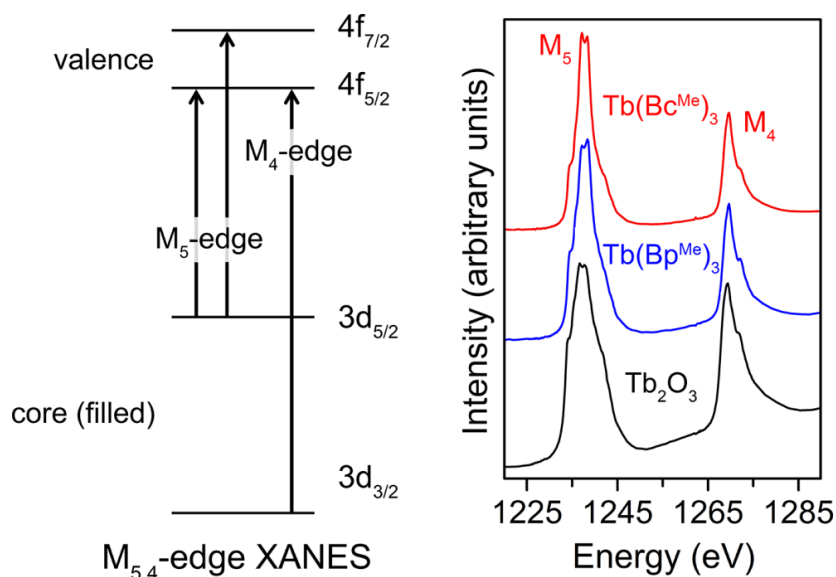


Figure 3.4. Left: Qualitative energy level diagram showing allowed electronic transitions at the $M_{5,4}$ -edges. Spin-orbit coupling with the core-hole splits the $3d_{3/2}$ and $3d_{5/2}$ orbitals by ~ 20 - 40 eV (for Tb through Er). To a lesser extent, spin-orbit coupling, ligand-field, and multiplet effects causes scrambling of the valence $4f_{5/2}$ and $4f_{7/2}$ levels. Right: Background subtracted terbium $M_{5,4}$ -edge XANES spectra from $Tb(Bc^{Me})_3$, $Tb(Bp^{Me})_3$, and Tb_2O_3 .

left).⁵⁶ Previous studies have shown that the ratio of intensities for the lower energy M_5 and higher energy M_4 edges are sensitive to changes in the local chemical environment dictated by spin-orbit and covalency effects.⁵⁷

Chemical bonding and electronic structure were evaluated for $Ln(Bp^{Me})_3$ and $Ln(Bc^{Me})_3$ by determining the branching ratios from $M_{5,4}$ -edge XANES. This approach has been successful in detailed studies of lanthanide oxides,^{57a,58} metals,^{56a} and various other lanthanide-containing materials.⁵⁹ The sesquioxides Ln_2O_3 ($Ln = Tb, Dy, Ho, Er$) were measured as a reference, given that the lanthanide ions in this environment are well-described by a rigorously trivalent electronic configuration.^{57a,60} Accurate measurements were facilitated by using a scanning transmission x-ray microscope (STXM). Figure 3.4 shows the background subtracted $M_{5,4}$ -edge spectra for $Tb(Bc^{Me})_3$, $Tb(Bp^{Me})_3$, and Tb_2O_3 (see Figure 3.A47 for $Ln = Dy, Ho, Er$) obtained using STXM. For each of the compounds, the strong spin-orbit interaction in the core hole separates the M_5 and M_4 edges into two distinct regions, with separations of approximately 32 eV for Tb and 42 eV for Er. At first glance, each of the spectral profiles is similar to those expected based on predictions for the free ions,^{57a} with M_5 and M_4 edges exhibiting many multiplet features. The low energy M_5 edges exhibit considerable structure and a characteristic saw-tooth pattern, followed by a tail that decreases mostly to zero. However, the well-defined sharp features on the M_5 edge belie an extremely complex underlying spectrum consisting of hundreds or even thousands of unique transitions.^{56a,57a} At high energy, the M_4 edge does not exhibit the same quantity of multiplet features, but it is clearly asymmetric in appearance and likely composed of multiple transitions.

The branching ratios $A_5/(A_5+A_4)$, where A_5 and A_4 are the areas under the M_5 and M_4 peaks, were determined using a graphical approach based on integration of the 2nd derivative spectrum (Figure 3.A48).^{57b} The branching ratios determined for $Ln(Bc^{Me})_3$, $Ln(Bp^{Me})_3$, and Ln_2O_3 ($Ln =$

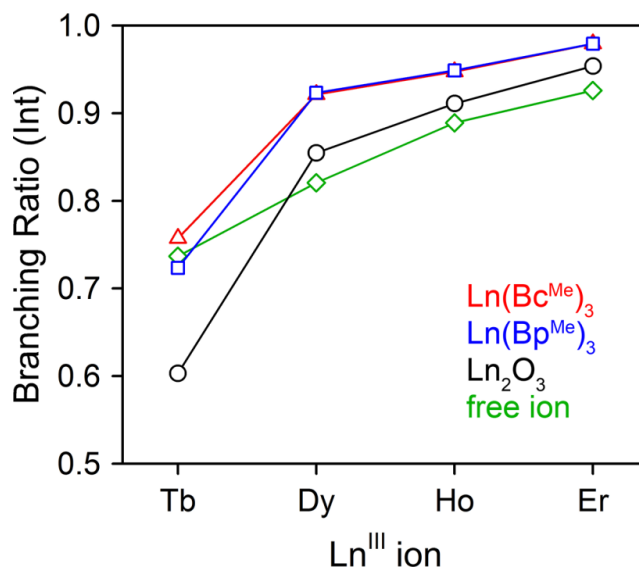


Figure 3.5. Plot of the branching ratios determined from the experimental $M_{5,4}$ -edge XANES spectra of $\text{Ln}(\text{Bc}^{\text{Me}})_3$, $\text{Ln}(\text{Bp}^{\text{Me}})_3$, and Ln_2O_3 for $\text{Ln} = \text{Tb, Dy, Ho, and Er}$. The experimentally determined branching ratio for Tb_2O_3 (0.60) is smaller than expected based on theoretical free ion values (see Section 3.2). Theoretical free ion values are taken from reference 56a.

Tb, Dy, Ho, Er) are listed in Table 3.A3 and plotted in Figure 3.5 as a function of the number of 4f electrons in the initial state. For all three sets of compounds, larger branching ratios are observed with increases in atomic number and the concomitant increase in the number of 4f electrons in the initial state. This trend is consistent with previous studies,^{56a,57a,58,59} which have shown that the branching ratio approaches unity as the lanthanide series is traversed from left to right because the $4f_{5/2}$ states are filled first and the probability of the $3d_{3/2} \rightarrow 4f_{5/2}$ (M_4) excitation decreases. This phenomenon is exemplified by the case of Yb^{3+} ($4f^{13}$), in which the $4f_{5/2}$ states are filled completely and only the $3d_{5/2} \rightarrow 4f_{7/2}$ (M_5) excitation is allowed.^{56a}

Although the three sets of compounds exhibit the anticipated trend towards increasing branching ratios, values for individual lanthanides were uniformly higher for $\text{Ln}(\text{Bp}^{\text{Me}})_3$ and $\text{Ln}(\text{Bc}^{\text{Me}})_3$ relative to the corresponding oxides (Figure 3.5). For example, values determined for both $\text{Tb}(\text{Bp}^{\text{Me}})_3$ (0.76) and $\text{Tb}(\text{Bc}^{\text{Me}})_3$ (0.72) were significantly higher than those for Tb_2O_3 (0.60). Toward the end of the series, the branching ratio measured for Er_2O_3 (0.95) was lower than that of either $\text{Er}(\text{Bp}^{\text{Me}})_3$ or $\text{Er}(\text{Bc}^{\text{Me}})_3$ (both 0.98). Although changes in crystal field are unlikely to be reflected in branching ratios,^{56b} trends towards increasing branching ratios may be rationalized by enhanced covalent mixing with high-energy donor orbitals on the $[\text{Bp}^{\text{Me}}]^-$ and $[\text{Bc}^{\text{Me}}]^-$ ligands. Electrons will preferentially occupy the $4f_{5/2}$ levels, which decreases the probability of the $3d_{3/2} \rightarrow 4f_{5/2}$ (M_4) transitions and increases the branching ratios in $\text{Ln}(\text{Bp}^{\text{Me}})_3$ and $\text{Ln}(\text{Bc}^{\text{Me}})_3$ relative to Ln_2O_3 .^{57a,58,61} Although electronic structure calculations and additional spectroscopic measurements are needed to fully validate this interpretation, the $M_{5,4}$ -edge XANES results suggest that the $[\text{Bp}^{\text{Me}}]^-$ and $[\text{Bc}^{\text{Me}}]^-$ ligands both provide a more strongly donating ligand field in comparison with the trivalent Ln_2O_3 .

EPR Spectroscopy and Metal Ion Anisotropy. EPR can be a powerful experimental probe to understand low temperature slow magnetic relaxation in single-molecule magnets, allowing for assessment of magnetic anisotropy through determination of the electronic g -values and the magnetic ground state.⁶² Low temperature X-band EPR spectra were collected for compounds of

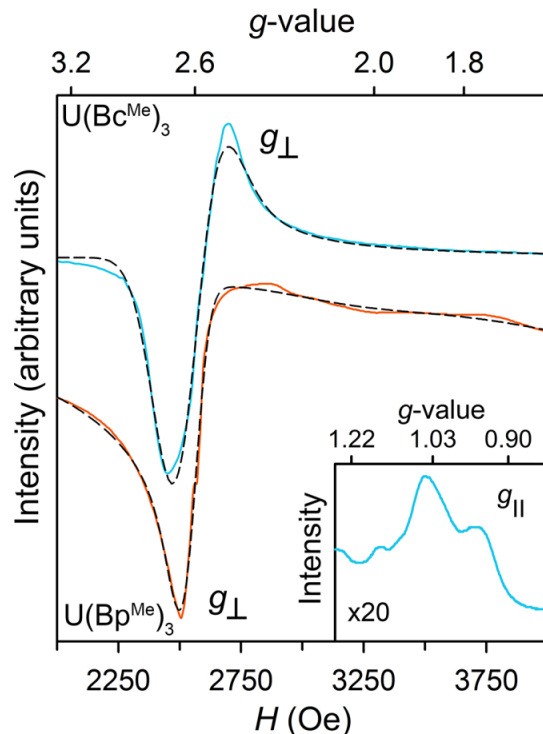


Figure 3.6. X-band EPR spectra of microcrystalline powder samples of $\text{U}(\text{Bc}^{\text{Me}})_3$ (blue lines) and $\text{U}(\text{Bp}^{\text{Me}})_3$ (orange line) collected at 1.8 K with a microwave frequency of 9.2175 GHz, power of 10 mW, and a modulation amplitude of 1 G. Dashed black lines correspond to simulations of the data resulting in values of $g_{\perp}/g_{\parallel} = 2.57 / 1.03$ for $\text{U}(\text{Bc}^{\text{Me}})_3$ and $2.62 / 1.76$ for $\text{U}(\text{Bp}^{\text{Me}})_3$.

the Kramers ions Dy^{3+} , Er^{3+} , and U^{3+} . Data collected at 2 K reveal anisotropic signals for Er^{3+} (Figure 3.A49-3.A51) and U^{3+} (Figure 3.6), each with dominant transverse anisotropy ($g_{\perp} > g_{\parallel}$). Both $\text{Dy}(\text{Bp}^{\text{Me}})_3$ and $\text{Dy}(\text{Bc}^{\text{Me}})_3$ are EPR silent, and we note that this result and the presence of a spectrum for the Er^{3+} complexes is consistent with the EPR spectra of the lanthanide ethylsulfate complexes and anhydrous chloride complexes, which also possess C_{3h} symmetry.⁶² In contrast to the Er^{3+} and U^{3+} complexes, all the other compounds have strong axial anisotropy, which can be rationalized by the change in the ordering of the ^1H NMR resonances in the Er^{3+} compounds relative to the other lanthanides, as discussed below.

The resulting spectra and corresponding simulations are given in Figure 3.6 for both U^{3+} complexes. From the extracted g -values, the ground state magnetic moment for each compound was calculated using Equation 3.3 and compared to the moment determined from the magnetic susceptibility, $\chi_{\text{M}}T$, extrapolated to 0 K using Equation 3.4.

$$\mu_{\text{eff}}^2 = (g_1^2 + g_2^2 + g_3^2)/4 \quad (3.3)$$

$$\mu_{\text{eff}}^2 = 7.997 \cdot (\chi_{\text{M}}T)_{(T=0)} \quad (3.4)$$

This analysis gives $\mu_{\text{eff}} = 2.05$ and $1.89 \mu_{\text{B}}$ for $\text{U}(\text{Bp}^{\text{Me}})_3$ and $\text{U}(\text{Bc}^{\text{Me}})_3$, respectively, which are in very good agreement with the values of $1.92(2) \mu_{\text{B}}$ and $2.07(1) \mu_{\text{B}}$ determined from the magnetic susceptibility measurements.⁶³

The compounds $\text{U}(\text{Bp}^{\text{Me}})_3$ and $\text{U}(\text{Bc}^{\text{Me}})_3$ possess similar values of $g_{\perp} = 2.62$ and 2.57 , respectively, revealing a large transverse contribution to the anisotropy. The observation of slow

magnetic relaxation only under an applied dc field can thus be understood as arising from tunneling of the magnetization facilitated by the large transverse anisotropy. Despite similar g_{\perp} values, however, $\text{U}(\text{Bc}^{\text{Me}})_3$ is more anisotropic than $\text{U}(\text{Bp}^{\text{Me}})_3$ with a smaller $g_{\parallel} = 1.03$ (compared to $g_{\parallel} = 1.76$). This difference suggests that the much slower relaxation observed for $\text{U}(\text{Bc}^{\text{Me}})_3$ is a result of greater magnetic anisotropy, as also proposed below for the lanthanide compounds.

The idealized symmetry for the trigonal prismatic coordination geometry of both compounds is C_{3h} . The behavior of Nd^{3+} in C_{3h} symmetry has been extensively studied,^{64,65} and can be applied to the behavior of $\text{U}(\text{Bc}^{\text{Me}})_3$ and $\text{U}(\text{Bp}^{\text{Me}})_3$ to determine the magnetic ground state for these compounds. As noted above, a C_{3h} crystal field will split the $^4I_{9/2}$ ground state of U^{3+} into M_J states of $^5/2, ^{-7/2}; ^1/2$; and $^9/2, ^{-3/2}$, although only the first two states satisfy the EPR selection rule ($\Delta M_J = \pm 1$). The g -values for the $^1/2$ state^{62,66} are $g_{\parallel} = 0.73$ and $g_{\perp} = 3.65$, which do not match well with the experimentally observed values.⁶⁷ On the other hand, the $^5/2, ^{-7/2}$ state provides good, but not exact, agreement with the observed g -values (see Table 3.A4). For $\text{U}(\text{Bc}^{\text{Me}})_3$, this agreement is improved by allowing the symmetry to decrease to C_3 ,⁶⁸ therefore allowing the $^{-1/2}$ state to mix with the $^5/2, ^{-7/2}$ state. The same lowering of the symmetry does not improve the agreement for $\text{U}(\text{Bp}^{\text{Me}})_3$.⁶⁹ Nevertheless, both complexes possess a ground state that is largely composed of $M_J = \pm 5/2$. A similar result has been demonstrated previously using an effective point charge model to simulate magnetic susceptibility data for other U^{3+} scorpionate-based compounds.⁷⁰

Fitting U^{III} Dc Susceptibility with CONDON. As discussed already, the program CONDON has been demonstrated as a powerful means to determine the energy level structure of mononuclear systems exhibiting slow magnetic relaxation, through the use of a so-called “full model” Hamiltonian.⁷¹ The low-lying electronic structure of most scorpionate-based uranium systems exhibiting slow magnetic relaxation has been elucidated via ligand field calculations^{70,72} or other computational methods (for example Ref 9e). It was therefore of interest to fit the dc susceptibility data for $\text{U}(\text{Bc}^{\text{Me}})_3$ and $\text{U}(\text{Bp}^{\text{Me}})_3$ using CONDON in order to have a basis for comparison and to gain further insight into the electronic influences of carbon and nitrogen as donor atoms in the same symmetry. Fitting was carried out by assuming ideal C_{3h} symmetry and using corresponding ligand field parameters reported for $\text{U}(\text{Bp})_3$ in Ref. 70 as starting points. The dc susceptibility data for $\text{U}(\text{Bc}^{\text{Me}})_3$ and $\text{U}(\text{Bp}^{\text{Me}})_3$ is reproduced in Figure 3.7 along with fits obtained from CONDON and the calculated electronic structure of the ground $J = 9/2$. Agreeing well with the EPR results of the previous section and prior calculations on U^{III} scorpionate complexes, the ground state was determined to be a mixture of $M_J = \pm 5/2$ and $\mp 7/2$.

Another notable result of the calculations is that the crystal field splitting for $\text{U}(\text{Bc}^{\text{Me}})_3$ is predicted to be larger than that of $\text{U}(\text{Bp}^{\text{Me}})_3$ by $\sim 300 \text{ cm}^{-1}$, revealing the limitations inherent in the qualitative analysis of the dc susceptibility data in Section 3.3 (wherein it was supposed that $\text{U}(\text{Bp}^{\text{Me}})_3$ might exhibit the greater crystal field splitting). While the results of the calculations must also be taken with a few grains of salt in the absence of supporting spectroscopic data, if the ligand field splitting is indeed larger for $\text{U}(\text{Bc}^{\text{Me}})_3$, this result supports the original notion that the N -heterocyclic carbene donor should provide a stronger ligand field for U^{III} . Additionally, if relaxation of the magnetization could be observed through the full ground J for each complex, then employing the N -heterocyclic carbene ligand is certainly an advantageous strategy. Of course the results of the ac susceptibility measurements revealed thermally-dependent relaxation only for $\text{U}(\text{Bc}^{\text{Me}})_3$, and the $U_{\text{eff}} = 23 \text{ cm}^{-1}$ is much smaller than the calculated ground to first excited state M_J separation of 74 cm^{-1} . In the case of $\text{U}(\text{Bp}^{\text{Me}})_3$, for which no Orbach process was fit using Equation 3.1, the calculated ground to first excited state splitting is 192 cm^{-1} , more than

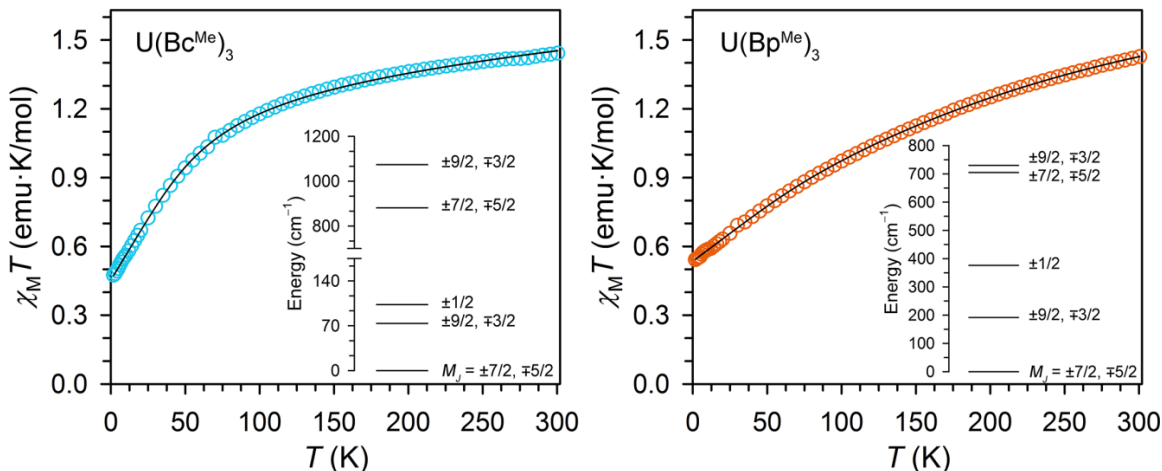


Figure 3.7. Plot of $\chi_M T$ versus T for $U(\text{Bc}^{\text{Me}})_3$ (left) and $U(\text{Bp}^{\text{Me}})_3$ (right) along with the fits obtained using CONDON (black lines). The corresponding electronic structure of the ground $J = 9/2$ is given as an inset in each plot.

double that of $U(\text{Bc}^{\text{Me}})_3$. Thus, as was observed generally for mononuclear actinide compounds in Chapter 1, Raman relaxation again appears to be the default for $U(\text{Bc}^{\text{Me}})_3$ and $U(\text{Bp}^{\text{Me}})_3$ over the examined frequency and temperature range. No doubt moving away from scorpionate ligands and even trigonal symmetry will aid in developing a further understanding of the relaxation of these unique systems and the maximizing of actinide single-ion magnetic anisotropy.

^1H NMR Spectroscopy. While paramagnetic transition metal complexes often possess long electron spin-lattice relaxation times leading to difficulty in the interpretation of their NMR spectra, this is not the case for the lanthanides. Indeed, large spin-orbit coupling contributes to short relaxation times and thus peaks can often be readily observed and assigned.⁷³ The chemical shift of a given nucleus in a paramagnetic complex can be broken down into dipolar (or pseudocontact) and contact contributions. The former is a through-space interaction and arises from coupling of the nuclear and electronic magnetic moments, while the contact (or Fermi contact) shift arises as a consequence of delocalization of unpaired electron spin density from the metal center. In magnetically anisotropic systems, the dipolar contribution is especially important and may be a useful metric in evaluating magnetic anisotropy in isostructural compounds.⁷⁴ Room temperature ^1H NMR spectra were collected for $M(\text{Bc}^{\text{Me}})_3$ and $M(\text{Bp}^{\text{Me}})_3$ in $\text{THF}-d_8$. In the case of the paramagnetic lanthanides, all complexes demonstrate broad peaks over a wide range of chemical shifts, from -400 to $+400$ ppm (Figure 3.8). The spectra possess four peaks each, suggesting that the solid-state structure is maintained in solution, although only one chemical shift is observed due to the borate hydrogen(s).⁷⁵ Integration of the $\text{Ho}(\text{Bp}^{\text{Me}})_3$ and $\text{Er}(\text{Bp}^{\text{Me}})_3$ spectra enabled assignments of all observed peaks. Incident protons appear in the same regions of spectral space for the Tb^{3+} , Dy^{3+} , and Ho^{3+} compounds, such that the borate proton(s) are most upfield while the methyl protons are most downfield. This order is reversed for Er^{3+} , however, where the borate proton is now furthest downfield, and the methyl protons furthest upfield. This reversal is due to the presence of dominant transverse anisotropy, as confirmed by EPR spectroscopy, in contrast to the axial anisotropy of the other compounds.^{73,74}

The most notable difference is found when comparing spectra for a given metal, wherein the chemical shift for all protons is greater for $\text{Ln}(\text{Bc}^{\text{Me}})_3$ than $\text{Ln}(\text{Bp}^{\text{Me}})_3$. For instance, in the case of

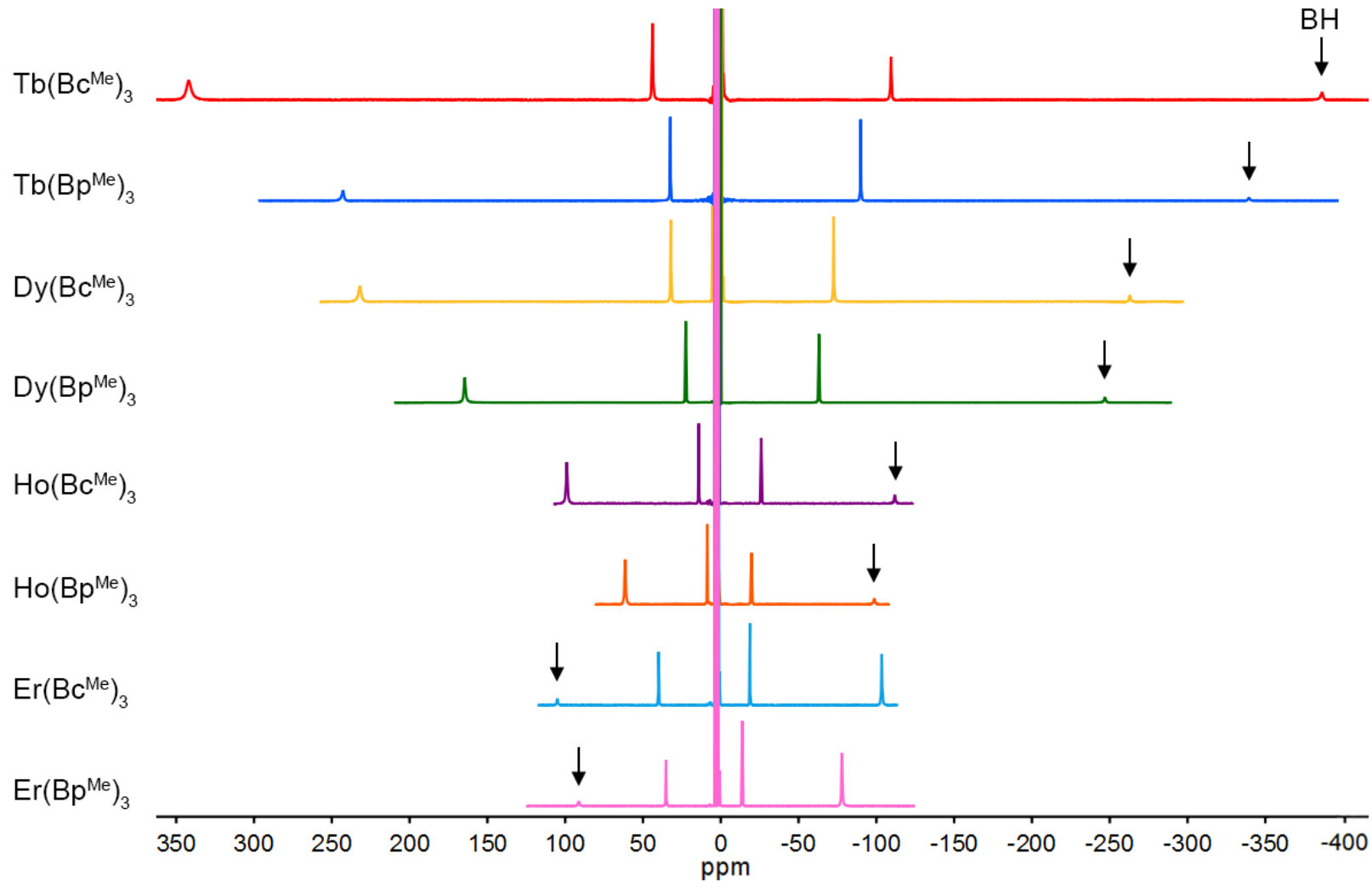


Figure 3.8. ^1H NMR spectra for $\text{Ln}(\text{Bc}^{\text{Me}})_3$ and $\text{Ln}(\text{Bp}^{\text{Me}})_3$ demonstrating much larger chemical shift values for $\text{Ln}(\text{Bc}^{\text{Me}})_3$, which are likely due to a greater dipolar contribution to the chemical shift for this series of compounds.

Tb(Bc^{Me})₃ the methyl proton resonance appears at 340 ppm, while in Tb(Bp^{Me})₃ the same resonance is shifted upfield by nearly 100 ppm. Notably, this effect is pronounced for the methyl and borate protons while almost insignificant for the aromatic protons (Figure 3.A52). A dominant dipolar contribution to the chemical shift is especially common in the case of the highly anisotropic lanthanides, where contact contributions arising from covalency are generally expected to be small. In this respect, the XANES results indeed suggest that differences between Ln(Bc^{Me})₃ and Ln(Bp^{Me})₃ are minimal. Thus, the greater chemical shift for the protons in Ln(Bc^{Me})₃ can be interpreted as arising from a greater dipolar contribution compared to Ln(Bp^{Me})₃. The dipolar field experienced by the protons within each molecule will depend heavily on the main magnetic anisotropy axis orientation at room temperature, this observation might be interpreted further as evidence of greater magnetic anisotropy in Ln(Bc^{Me})₃. Such a hypothesis can aid in rationalizing the differences in magnetic relaxation between Ln(Bc^{Me})₃ and Ln(Bp^{Me})₃, as a larger magnetocrystalline anisotropy in the latter should afford slower relaxation.

For U(Bc^{Me})₃ and U(Bp^{Me})₃, three ¹H NMR peaks integrating in an approximate 2:2:6 ratio appear between 0 and 14 ppm (Figure 3.A53), assigned to the aromatic and methyl protons, respectively, suggesting again that the solid state structure is maintained in solution. Two more broad resonances are also observed in each spectrum with integration values close to 1, which we have assigned to the borate protons in each compound. Relative to the methyl protons in the corresponding diamagnetic Y³⁺ spectra, the methyl peak for U(Bc^{Me})₃ is notably shifted downfield, while that for U(Bp^{Me})₃ is shifted upfield. While analysis of the spectra and assessment of magnetic anisotropy magnitude is complicated due to disparity in chemical shifts, the relative positions of the methyl protons might be attributed to opposing signs of the dipolar contribution to the chemical shift.⁷⁴

3.4 Conclusions and Outlook

Two series of isostructural compounds M(Bc^{Me})₃ and M(Bp^{Me})₃ have been synthesized with the f-elements Tb, Dy, Ho, Er, and U and fully characterized to examine how donor strength influences slow magnetic relaxation. From dynamic magnetic susceptibility measurements, the presence of a strongly donating *N*-heterocyclic carbene ligand in M(Bc^{Me})₃ has been shown to be advantageous in the promotion of slow magnetic relaxation for compounds of the oblate ions U³⁺, Tb³⁺, and Dy³⁺ when compared with M(Bp^{Me})₃. Interestingly, static magnetic susceptibility characterization of both U³⁺ complexes might indicate greater covalency in the case of the *N*-heterocyclic carbene species. Additional characterization utilizing lanthanide M_{5,4}-edge XANES, EPR, and ¹H NMR spectroscopies reveals that differences in covalency between the two sets of lanthanide compounds are not as significant. Rather, the *N*-heterocyclic carbene ligand promotes greater magnetic anisotropy for the complexes M(Bc^{Me})₃ (M = Tb, Dy, U) and therefore slower magnetic relaxation. Fitting the temperature-dependent relaxation data to account for Raman, Direct, and Orbach processes suggests that Orbach relaxation is active for M(Bc^{Me})₃, while use of the program CONDON to fit dc susceptibility data for the U^{III} congeners reveals that true Orbach relaxation may elude these latter molecules. Thus, fitting a relatively small temperature range of ac data for all the compounds discussed here may paint too simple a picture regarding the actual mechanism of relaxation. Even still it is clear that thermally-dependent relaxation is favored for M(Bc^{Me})₃ in both concentrated and dilute forms. These results reveal that for uranium and even the lanthanides, donor type and strength is a factor of import in the design of new single-molecule magnets. Though relatively short relaxation times and small anisotropy

barriers characterize the slowly relaxing systems presented here, the conclusions reached can perhaps be applied to further systems demonstrating relaxation under zero field, through the exploitation of a more strongly-donating ligand field of appropriate symmetry.

3.5 Acknowledgements

The NSF Graduate Fellowship Program is acknowledged for support of K.R.M, Prof. R. A. Andersen for valuable discussions, Dr. A. DiPasquale for x-ray structure assistance, and McDonald's Corporation for the drinking straws employed in magnetic sample loading. Dr. Stefan G. Minasian (Lawrence Berkeley National Lab) and Dr. Stosh Kozimor (Los Alamos National Lab) are gratefully acknowledged for carrying out the XANES studies and analysis. Dr. Wayne W. Lukens (Lawrence Berkeley National Lab) is gratefully acknowledged for conducting EPR experiments and data analysis.

3.6 References

- (1) (a) Rinehart, J. D.; Long, J. R. *Chem. Sci.* **2011**, *2*, 2078. (b) Jiang, S.-D.; Wang, B.-W.; Sun, H.-L.; Wang, Z.-M.; Gao, S. *J. Am. Chem. Soc.* **2011**, *133*, 4730. (c) Baldoví, J. J.; Cardona-Serra, S.; Clemente-Juan, J. M.; Coronado, E.; Gaita-Ariño, A.; Palií, A. *Inorg. Chem.* **2012**, *51*, 12565. (d) Chilton, N. F.; Langley, S. K.; Moubaraki, B.; Soncini, A.; Batten, S. R.; Murray, K. S. *Chem. Sci.* **2013**, *4*, 1719. (e) Chilton, N. F.; Collison, D.; McInnes, E. J. L.; Winpenny, R. E. P.; Soncini, A. *Nat. Commun.* **2013**, *4*, 2551.
- (2) Liu, J.-L.; Chen, Y.-C.; Zheng, Y.-Z.; Lin, W.-Q.; Ungur, L.; Wernsdorfer, W.; Chibotaru, L. F.; Tong, M.-L. *Chem. Sci.* **2013**, *4*, 3310.
- (3) Rinehart, J. D.; Long, J. R. *J. Am. Chem. Soc.* **2009**, *131*, 12558.
- (4) Pereira, L. C. J.; Camp, C.; Coutinho, J. T.; Chatelain, L.; Maldivi, P.; Almeida, M.; Mazzanti, M. *Inorg. Chem.* **2014**, DOI: 10.1021/ic501520c.
- (5) Antunes, M. A.; Pereira, L. C. J.; Santos, I. C.; Mazzanti, M.; Marçalo, J.; Almeida, M. *Inorg. Chem.* **2011**, *50*, 9915.
- (6) Moro, F.; Mills, D. P.; Liddle, S. T.; Van Slageren, J. *Angew. Chem. Int. Ed.* **2013**, *52*, 3430.
- (7) (a) Lukens, W. W.; Edelstein, N. M.; Magnani, N.; Hayton, T. W.; Fortier, S.; Seaman, L. *J. Am. Chem. Soc.* **2013**, *135*, 10742. (b) Behrle, A. C.; Barnes, C. L.; Kaltsoyannis, N.; Walensky, J. R. *Inorg. Chem.* **2013**, *52*, 10623. (c) Neidig, M. L.; Clark, D. L.; Martin, R. L. *Coord. Chem. Rev.* **2013**, *257*, 394. (d) Minasian, S. G.; Keith, J. M.; Batista, E. R.; Boland, K. S.; Clark, D. L.; Kozimor, S. A.; Martin, R. L.; Shuh, D. K.; Tylliszczak, T. *Chem. Sci.* **2014**, *5*, 351; and references therein.
- (8) Zadrozny, J. M.; Xiao, D. J.; Atanasov, M.; Long, G. J.; Grandjean, F.; Neese, F.; Long, J. R. *Nature Chem.* **2013**, *5*, 577.
- (9) (a) Rinehart, J. D.; Long, J. R. *J. Am. Chem. Soc.* **2009**, *131*, 12558. (b) Rinehart, J. D.; Meihaus, K. R.; Long, J. R. *J. Am. Chem. Soc.* **2010**, *132*, 7572. (c) Meihaus, K. R.; Rinehart, J. D.; Long, J. R. *Inorg. Chem.* **2011**, *50*, 8484-8489. (d) Antunes, M. A.; Pereira, L. C. J.; Santos, I. C.; Mazzanti, M.; Marçalo, J.; Almeida, M. *Inorg. Chem.* **2011**, *50*, 9915. (e) Coutinho, J. T.; Antunes, M. A.; Pereira, L. C. J.; Bolvin, H.; Marçalo, J.; Mazzanti, M.; Almeida, M. *Dalton Trans.* **2012**, *41*, 13568. (f) Rinehart, J.

- D.; Long, J. R. *Dalton Trans.* **2012**, *41*, 13572. (g) Coutinho, J. T.; Antunes, M. A.; Pereira, L. C. J.; Marçalo, J.; Almeida, M. *Chem. Commun.* **2014**, *50*, 10262.
- (10) (a) Mills, D. P.; Moro, F.; McMaster, J.; van Slageren, J.; Lewis, W.; Blake, A. J.; Liddle, S. T. *Nat. Chem.* **2011**, *3*, 454. (b) Moro, F.; Mills, D. P.; Liddle, S. T.; van Slageren, J. *Angew. Chem. Int. Ed.* **2013**, *52*, 3430.
- (11) (a) Jeletic, M.; Lin, P.-H.; Le Roy, J. J.; Korobkov, I.; Gorelsky, S. I.; Murugesu, M. *J. Am. Chem. Soc.* **2011**, *133*, 19286. (b) Jiang, S.-D.; Liu, S.-S.; Zhou, L.-N.; Wang, B.-W.; Wang, Z.-M.; Gao, S. *Inorg. Chem.* **2012**, *51*, 3079. (c) Le Roy, J. J.; Jeletic, M.; Gorelsky, S. I.; Korobkov, I.; Ungur, L.; Chibotaru, L. F.; Murugesu, M. *J. Am. Chem. Soc.* **2013**, *135*, 3502. (d) Layfield, R. A. *Organometallics* **2014**, *33*, 1084.
- (12) (d) Tuna, F.; Smith, C. A.; Bodensteiner, M.; Ungur, L.; Chibotaru, L. F.; McInnes, E. J. L.; Winpenny, R. E. P.; Collison, D.; Layfield, R. A. *Angew. Chem. Int. Ed.* **2012**, *51*, 6976.
- (13) Smith, J. M. *Comments Inorg. Chem.* **2008**, *29*, 189.
- (14) Cloke, F. G. N.; Hitchcock, P. B. *J. Am. Chem. Soc.* **2002**, *124*, 9352.
- (15) Spedding, F. H.; Newton, A. S.; Warf, J. C.; Johnson, O.; Nottorf, R. W.; Johns, I. B.; Daane, A. H. *Nucleonics* **1949**, *4*, 4.
- (16) Munguia, T.; Bakir, Z. A.; Cervantes-Lee, F.; Metta-Magana, A.; Pannell, K. H. *Organometallics*, **2009**, *28*, 5777.
- (17) Niedenzu, K.; Niedenzu, P. M.; Warner, K. R. *Inorg. Chem.* **1985**, *24*, 1604.
- (18) Fränkel, R.; Kniczek, J.; Ponikwar, W.; Nöth, H.; Polborn, K.; Fehlhammer, W. P. *Inorg. Chim. Acta.* **2001**, *312*, 23.
- (19) Nieto, I.; Bontchev, R. P.; Smith, J. M. *Eur. J. Inorg. Chem.* **2008**, 2476.
- (20) Assuming the presence of no organic impurities, using the crystalline solid isolated directly from the reaction of $[H_2B(MeIm)_2]I$ and LDA, a starting amount of metal reagent was chosen to be $1/3$ of the molar amount of theoretical $Li[Bc^{Me}]$ present.
- (21) Burla, M. C.; Caliendo, R.; Camalli, M.; Carrozzini, B.; Cascarano, G. L.; De Caro, L.; Giacovazzo, C.; Polidori, G.; Spagna, R. *J. Appl. Cryst.* **2005**, *38*, 381.
- (22) Sheldrick, G. M. *Acta Cryst.* **2008**, *A64*, 112.
- (23) Bain, G. A. and Berry, J. F. *J. Chem. Ed.* **2008**, *85*, 532.
- (24) D. Gatteschi, R. Sessoli, J. Villain, *Molecular Nanomagnets*, Oxford University Press, Oxford, **2006**.
- (25) Daul, C.; Schlapfer, C. W.; Mohos, B.; Ammeter, J.; Gamp, E. *Comput. Phys. Commun.* **1981**, *21*, 385.
- (26) Pilbrow, J. R. *Transition Ion Electron Paramagnetic Resonance*; Clarendon Press: Oxford, 1990.
- (27) Gasgnier, M.; Schiffmacher, G.; Albert, L.; Caro, P. E.; Dexpert, H.; Esteva, J. M.; Blancard, C.; Karnatak, R. C. *J. Less-Common Met.* **1989**, *156*, 59.
- (28) (a) Bugaris, D. E.; Choi, E. S.; Copping, R.; Glans, P.-A.; Minasian, S. G.; Tylliszczak, T.; Kozimor, S. A.; Shuh, D. K.; Ibers, J. A. *Inorg. Chem.* **2011**, *50*, 6656. (b) Gianetti, T. L.; Nocton, G.; Minasian, S. G.; Tomson, N. C.; Kilcoyne, A. L. D.; Kozimor, S. A.; Shuh, D. K.; Tylliszczak, T.; Bergman, R. G.; Arnold, J. *J. Am. Chem. Soc.* **2013**, *135*, 3224. (c) Minasian, S. G.; Keith, J. M.; Batista, E. R.; Boland, K. S.; Bradley, J. A.; Daly, S. R.; Kozimor, S. A.; Lukens, W. W.; Martin, R. L.; Nordlund, D.; Seidler, G. T.; Shuh,

- D. K.; Sokaras, D.; Tylliszczak, T.; Wagner, G. L.; Weng, T.-C.; Yang, P. *J. Am. Chem. Soc.* **2013**, *135*, 1864. (d) Minasian, S. G.; Keith, J. M.; Batista, E. R.; Boland, K. S.; Clark, D. L.; Kozimor, S. A.; Martin, R. L.; Shuh, D. K.; Tylliszczak, T. *Chem. Sci.* **2014**, *5*, 351.
- (29) Bluhm, H.; Andersson, K.; Araki, T.; Benzerara, K.; Brown, G. E.; Dynes, J. J.; Ghosal, S.; Gilles, M. K.; Hansen, H.-Ch.; Hemminger, J. C.; Hitchcock, A. P.; Ketteler, G.; Kilcoyne, A. L. D.; Kneedler, E.; Lawrence, J. R.; Leppard, G. G.; Majzlam, J.; Mun, B. S.; Myneni, S. C. B.; Nilsson, A.; Ogasawara, H.; Ogletree, D. F.; Pecher, K.; Salmeron, M.; Shuh, D. K.; Tonner, B.; Tylliszczak, T.; Warwick, T.; Yoon, T. H. *J. Electron. Spectrosc. Relat. Phenom.* **2006**, *150*, 86.
- (30) (a) Nieto, I.; Ding, F.; Bontchev, R. P.; Wang, H.; Smith, J. M. *J. Am. Chem. Soc.* **2008**, *130*, 2716. (b) Scepaniak, J. J.; Fulton, M. D.; Bontchev, R. P.; Duesler, E. N.; Kirk, M. L.; Smith, J. M. *J. Am. Chem. Soc.* **2008**, *130*, 10515. (c) Scepaniak, J. J.; Young, J. A.; Bontchev, R. P.; Smith, J. M. *Angew. Chem. Int. Ed.* **2009**, *48*, 3158. (d) Scepaniak, J. J.; Vogel, C. S.; Khusniyarov, M. M.; Heinemann, F. W.; Meyer, K.; Smith, J. M. *Science* **2011**, *331*, 1049. (e) Li, S.; Wang, Z.; Hor, T. S. A.; Zhao, J. *Dalton Trans.* **2012**, *41*, 1454.
- (31) (a) Grubbs, R. H. *Angew. Chem. Int. Ed.* **2006**, *45*, 3760. (b) Bantreil, X.; Broggi, J.; Nolan, S. P. *Annu. Rep. Prog. Chem., Sect. B: Org. Chem.* **2009**, *105*, 232. (c) Fortman, G. C.; Nolan, S. P.; *Chem. Soc. Rev.* **2011**, *40*, 5151.
- (32) (a) Mehdoui, T.; Berthet, J.-C.; Thuéry, P.; Ephritikhine, M. *Chem. Comm.* **2005**, 2860. (b) Arnold, P. L.; Turner, Z. R.; Germeroth, A. I.; Casely, I. J.; Bellabarba, R.; Tooze, R. P. *Dalton Trans.* **2010**, *39*, 6808.
- (33) (a) Arnold, P. L.; Liddle, S. T. *Chem Comm.* **2006**, 3959, and references therein. (b) Arnold, P. L.; Casely, I. J.; Turner, Z. R.; Carmichael, C. D. *Angew. Chem. Int. Ed.* **2008**, *14*, 10415.
- (34) Schettini, M. F.; Wu, G.; Hayton, T. W. *Chem. Comm.* **2012**, *48*, 1484.
- (35) Rai, S. B. *Spectrochim. Acta, Part A* **2002**, *58*, 1559.
- (36) (a) Carvalho, A.; Domingos, A.; Gaspar, P.; Marques, N.; Pires de Matos, A.; Santos, I. *Polyhedron* **1992**, *11*, 1481. (b) Sun, Y.; Takats, J.; Eberspacher, T.; Day, V. *Inorg. Chim. Acta.* **1995**, *229*, 315. (c) Sessler, J. L.; Melfi, P. J.; Pantos, G. D. *Coord. Chem. Rev.* **2006**, *250*, 816. (d) Pettinari, C. *Scorpionates II: Chelating Borate Ligands*; Imperial College Press: London, 2008. (e) Tsoureas, N.; Nunn, J.; Bevis, T.; Haddow, M. F.; Hamilton, A.; Owen, G. R. *Dalton Trans.* **2011**, *40*, 951.
- (37) Raymond, K. N.; Eigenbrot, C. W. *Acc. Chem. Res.* **1980**, *13*, 276.
- (38) Kepert, D. L. *Inorganic Stereochemistry*; Springer-Verlag Berlin: Heidelberg, 1982.
- (39) van Vleck, J. H. *The Theory of Electric and Magnetic Susceptibilities*; Oxford University Press: London, 1932.
- (40) The small slope can be ascribed to TIP due to mixing of the $J = 11/2$ state into the $J = 9/2$ ground state by the crystal field.
- (41) Stevens, K. W. H. *Proc. R. Soc. A.* **1953**, *219*, 542.
- (42) Kahn, O. *Molecular Magnetism*; Wiley-VCH: New York, 1993.
- (43) (a) Gatteschi, D.; Sessoli, R. *Angew. Chem. Int. Ed.* **2003**, *42*, 268. (b) Sessoli, R.; Powell, A. K. *Coord. Chem. Rev.* **2009**, *253*, 2328.

- (44) A low frequency rise can be observed for both complexes at 1.8 K and applied fields. However, this signal appears to be intermolecular in origin, as this tail rapidly goes to zero with increase in temperature.
- (45) The temperature-dependence of the relaxation time is $\tau \propto T^n$, where $n = 9$ (7) if the metal ion is Kramers (non-Kramers). $\tau \propto T^5$ is also sometimes observed for Kramers ions (see for example Ref. 7 and Yersin, H.; Strasser, J. *Coord. Chem. Rev.* **2000**, 208, 331).
- (46) For a direct process, typically $\tau \propto T$; however, $\tau \propto T^2$, a so-called bottle-neck direct process, is also possible.
- (47) (a) Harman, W. H.; Harris, T. D.; Freedman, D. E.; Fong, H.; Chang, A.; Rinehart, J. D.; Ozarowski, A.; Sougrati, M. T.; Grandjean, F.; Long, G. J.; Long, J. R.; Chang, C. J. *J. Am. Chem. Soc.* **2010**, 132, 18115. (b) Zadrozny, J. M.; Atanasov, M.; Bryan, A. M.; Lin, C.-Y.; Rekker, B. D.; Power, P. P.; Neese, F.; Long, J. R. *Chem. Sci.* **2013**, 4, 125.
- (48) Alternate relaxation processes such as Raman and direct mechanisms were first identified in a Dy³⁺ tetramer: (a) Guo, Y.-N.; Xu, G.-F.; Gamez, P.; Zhao, L.; Lin, S.-Y.; Deng, R.; Tang, J.; Zhang, H.-J. *J. Am. Chem. Soc.* **2010**, 132, 8538. Recently, a comprehensive study on the effect of ligand functionalization on slow relaxation for Er³⁺ presented evidence for the dominance of a Raman process for variously functionalized complexes of the trensal³⁻ ligand (H₃trensal = 2,2',2''-tris(salicylideneimino)triethylamine): (b) Pedersen, K. S.; Ungur, L.; Sigrist, M.; Sundt, A.; Schau-Magnussen, M.; Vieru, V.; Mutka, H.; Rols, S.; Weihe, H.; Waldmann, O.; Chibotaru, L. F.; Bendix, J.; Dreiser, J. *Chem. Sci.* **2014**, 5, 1650.
- (49) This explicit equation was first used to fit field-dependent relaxation data for some LnCl₃ in: Bohan, T. L.; Stapleton, H. J. *Phys. Rev.* **1969**, 182,385.
- (50) For all uranium samples, a Raman exponent $m = 5$ was found to give a better fit than $m = 9$. A T^5 temperature dependence has been rationalized by Orbach for a multi-level Kramers system in which Raman relaxation occurs between two states that are not time-reversed Kramers states. See Orbach, R.; Blume, M. *Phys. Rev. Lett.* **1962**, 8, 478.
- (51) This process goes away with dilution, suggesting that it is of dipolar origin.
- (52) Woodruff, D. N.; Winpenny, R. E.; Layfield, R. A. *Chem. Rev.* **2013**, 113, 5110.
- (53) While Ho³⁺ might also be considered an “oblate” ion, the 100% abundant $I = 7/2$ nuclear spin could contribute to very fast relaxation and hence the lack of slow relaxation observed for Ho(Bc^{Me})₃ or Ho(Bp^{Me})₃.
- (54) (a) Fuggle, J. C.; Hillebrecht, F. U.; Esteva, J. M.; Karnatak, R. C.; Gunnarsson, O.; Schonhammer, K. *Phys. Rev. B* **1983**, 27, 4637. (b) Bradley, J. A.; Moore, K. T.; Lipp, M. J.; Mattern, B. A.; Pacold, J. I.; Seidler, G. T.; Chow, P.; Rod, E.; Xiao, Y.; Evans, W. *J. Phys. Rev. B* **2012**, 85, 100102. (c) Hu, Z. W.; Kaindl, G.; Meyer, G. *J. Alloys Compd.* **1997**, 246, 186. (d) Gordon, R. A.; Seidler, G. T.; Fister, T. T.; Nagle, K. P. *J. Electron. Spectrosc. Relat. Phenom.* **2011**, 184, 220.
- (55) (a) Kaindl, G.; Brewer, W. D.; Kalkowski, G.; Holtzberg, F. *Phys. Rev. Lett.* **1983**, 51, 2056. (b) Bradley, J. A.; Moore, K. T.; van der Laan, G.; Bradley, J. P.; Gordon, R. A. *Phys. Rev. B* **2011**, 84, 205105.
- (56) (a) Thole, B. T.; Vanderlaan, G.; Fuggle, J. C.; Sawtzky, G. A.; Karnatak, R. C.; Esteva, J. M. *Phys. Rev. B* **1985**, 32, 5107. (b) Thole, B.T.; van der Laan, G. *Phys. Rev. B* **1988**, 38, 3158.

- (57) (a) Kotani, A.; Ogasawara, H. *J. Electron. Spectrosc. Relat. Phenom.* **1992**, *60*, 257. (b) Fortner, J. A.; Buck, E. C. *Appl. Phys. Lett.* **1996**, *68*, 3817.
- (58) Manoubi, T.; Colliex, C.; Rex, P. *J. Electron. Spectrosc. Relat. Phenom.* **1990**, *50*, 1.
- (59) (a) Kaindl, G.; Kalkowski, G.; Brewer, W. D.; Perscheid, B.; Holtzberg, F. *J. Appl. Phys.* **1984**, *55*, 1910. (b) Ayala, P.; Kitaura, R.; Nakanishi, R.; Shiozawa, H.; Ogawa, D.; Hoffmann, P.; Shinohara, H.; Pichler, T. *Phys. Rev. B* **2011**, *83*, 085407. (c) Nakamura, T.; Hirono, T.; Kinoshita, T.; Narumi, Y.; Hayashi, M.; Nojiri, H.; Mitsuda, A.; Wada, H.; Kodama, K.; Kindo, K.; Kotani, A. *J. Phys. Soc. Jpn.* **2012**, *81*, 103705.
- (60) (a) Karnatak, R. C. *J. Alloys Compd.* **1993**, *192*, 64. (b) Gasgnier, M.; Schiffmacher, G.; Albert, L.; Caro, P. E.; Dexpert, H.; Esteva, J. M.; Blancard, C.; Karnatak, R. C. *J. Less-Common Met.* **1989**, *156*, 59. (c) Gasgnier, M.; Eyring, L.; Karnatak, R. C.; Dexpert, H.; Esteva, J. M.; Caro, P.; Albert, L. *J. Less-Common Met.* **1987**, *127*, 367. (d) Dexpert, H.; Karnatak, R. C.; Esteva, J. M.; Connerade, J. P.; Gasgnier, M.; Caro, P. E.; Albert, L. *Phys. Rev. B* **1987**, *36*, 1750.
- (61) Shim, J. H.; Haule, K.; Kotliar, G. *Europhys. Lett.* **2009**, *85*, 17007.
- (62) Abragam, A.; Bleaney, B. *Electron Paramagnetic Resonance of Transition Ions*; Clarendon Press: Oxford, 1970.
- (63) Extrapolation of the dc susceptibility data for Tb, Dy, and Ho compounds was attempted in the same way, utilizing Equations 3 and 4 and assuming $g_{\perp} = 0$. However, a small amount of torqueing could not be resolved at low temperature in the Tb data, and small mass uncertainty in the case of all complexes makes such a calculation unreliable in the absence of other supporting data such as EPR. However, the ^1H NMR results clearly testify to the presence of axial anisotropy for these complexes, and a greater anisotropy in the case of $\text{M}(\text{Bc}^{\text{Me}})_3$.
- (64) Judd, B. R. *Proc. R. Soc. A* **1955**, *232*, 458.
- (65) Elliott, R. J.; Stevens, K. W. H. *Proc. R. Soc. A* **1953**, *219*, 387.
- (66) Defined as $g_{\perp} = 5g_{\parallel} = 5g_J$ (where g_J is the Landé g -value = $8/11$ for f^3).
- (67) The agreement may be improved somewhat by including the effect of mixing the $^{11/2}, 1/2$ state into the $^{9/2}, 1/2$ state by the crystal field, however here the agreement is still poor.
- (68) This symmetry relaxing also more accurately represents the true molecular symmetry of the compound, which lacks a horizontal mirror plane.
- (69) It is also possible that mixing of the relevant $J = 11/2$ states into the ground state would improve the agreement, but this possibility cannot be examined as the resulting state uses three parameters rather than the single parameter needed for the $5/2, -7/2$ state.
- (70) Baldoví, J. J.; Cardona-Serra, S.; Clemente-Juan, J. M.; Coronado, E.; Gaita-Ariño, A. *Chem. Sci.* **2013**, *4*, 938.
- (71) This “full model” accounts for electronic repulsion, spin-orbit coupling, the ligand field, and the Zeeman effect. (a) Schilder, H.; Lueken, H. *J. Magn. Magn. Mater.* **2004**, *281*, 17. (b) Speldrich, M.; Schilder, H.; Lueken, H.; Kögerler, P. *Isr. J. Chem.* **2011**, *51*, 215. (c) van Leusen, J.; Speldrich, M.; Schilder, H.; Kögerler, P. *Coord. Chem. Rev.* **2014**, DOI: 10.1016/j.ccr.2014.10.011.
- (72) Apostolidis, C.; Morgenstern, A.; Rebizant, J.; Kanellakopulos, B.; Walter, O.; Powietzka, B.; Karbowski, M.; Reddmann, H.; Amberger, H.-D. *Z. Anorg. Allg. Chem.* **2010**, *636*, 201.

- (73) La Mar, G. N.; Horrocks, W. DeW. Jr.; Holm, R. H. *NMR of Paramagnetic Molecules*; Academic Press: New York, 1973.
- (74) Bertini, I.; Luchinat, C. *NMR of Paramagnetic Molecules in Biological Systems*; Benjamin/Cummings Publishing Company, Inc: Menlo Park, 1986.
- (75) In the case of the $\text{Er}(\text{Bc}^{\text{Me}})_3$ spectra, for instance, the four peaks were found to have integration values of $\sim 6:2:2:1$ (corresponding to the most upfield peak, the two central most intense peaks, and most downfield resonance, respectively). It is therefore possible that the second borate proton resonance is too broad to be observed on the time-scale of these experiments; or alternatively that the two borate protons are indistinguishable and the integration value challenging to determine reliably, due to the broadness of the peak.

Chapter 3 Appendix

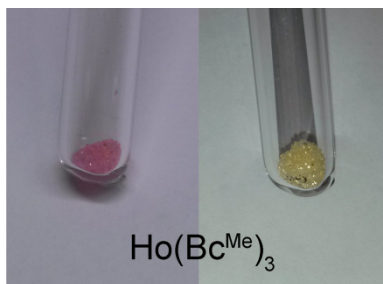


Figure 3.A1. Ho(Bc^{Me})₃ crystals photographed with (left) and without (right) a camera flash.

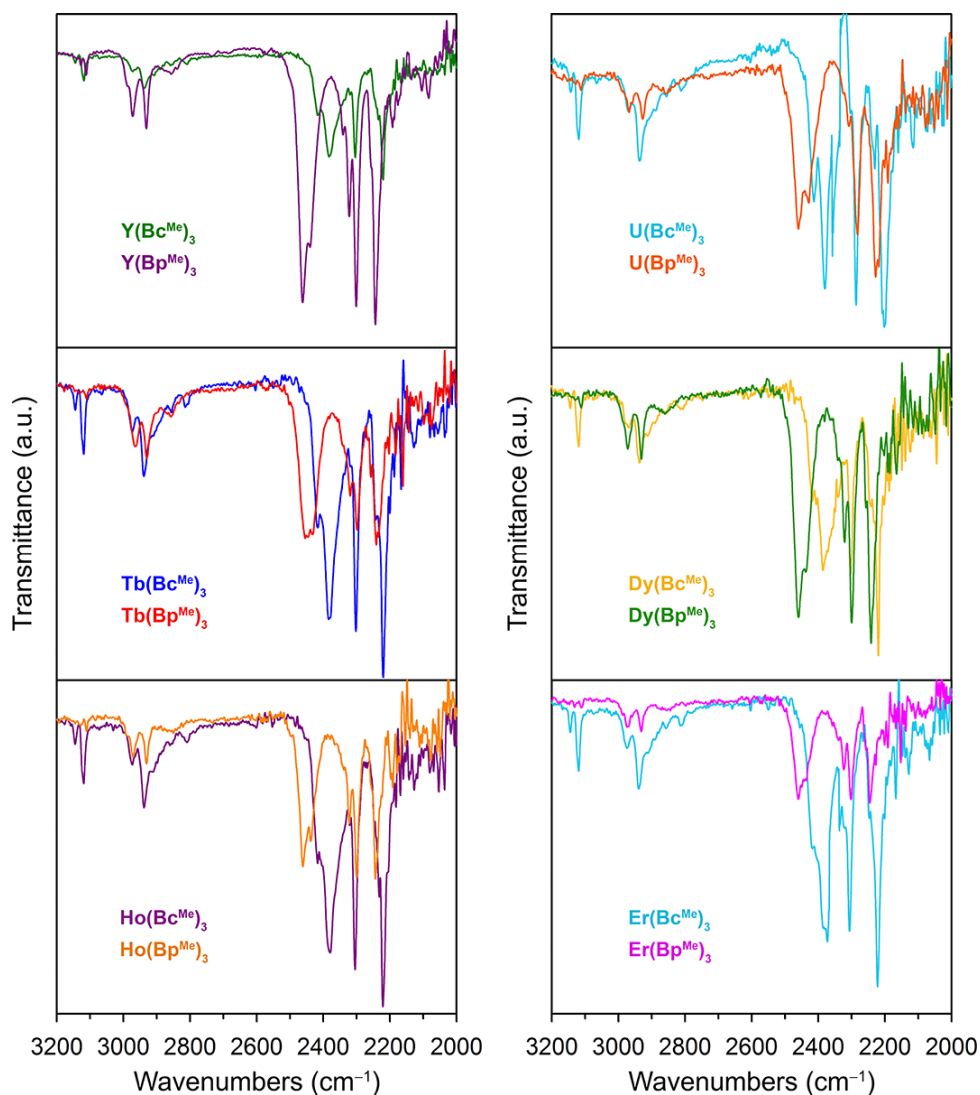


Figure 3.A2. IR spectra of M(Bc^{Me})₃ and M(Bp^{Me})₃. Spectra were collected under N₂ at room temperature, using a Perkin Elmer Avatar Spectrum 400 FTIR Spectrometer enclosed in a nitrogen glove-bag.

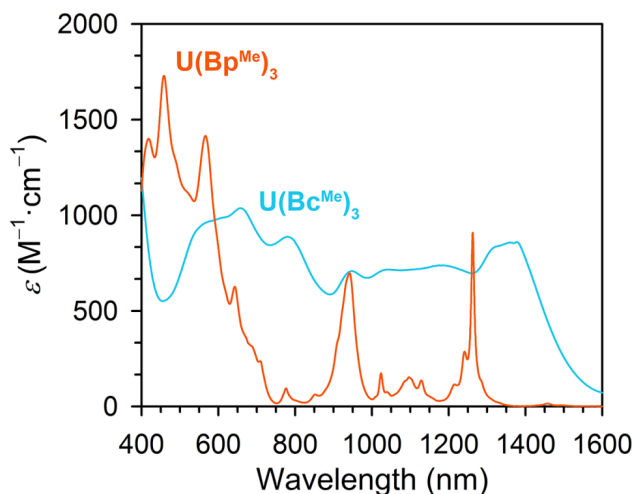


Figure 3.A3. Room temperature UV-Vis/NIR spectra of THF solutions of $\text{U}(\text{Bc}^{\text{Me}})_3$ (0.25 mM) and $\text{U}(\text{Bp}^{\text{Me}})_3$ (0.5 mM).

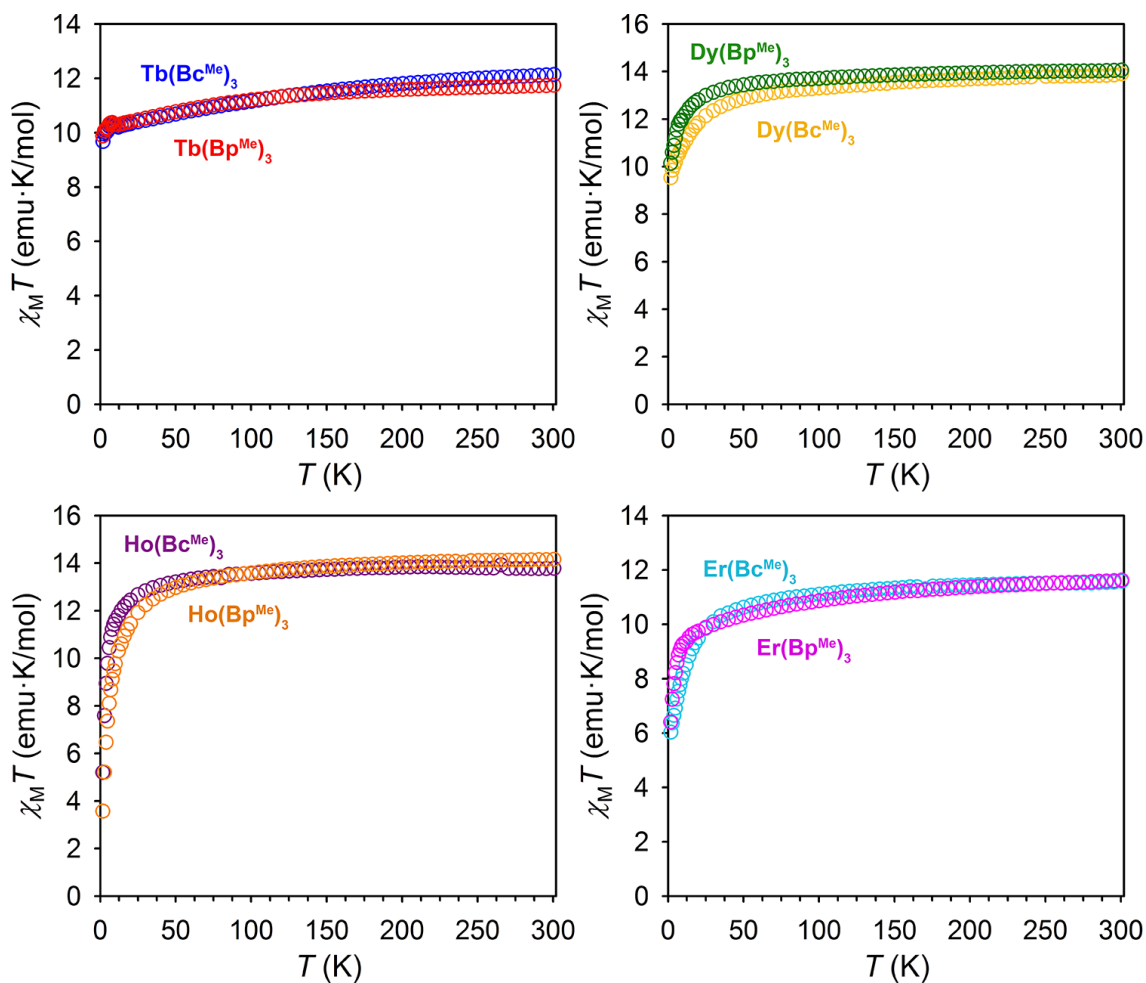


Figure 3.A4. Plot of the molar magnetic susceptibility times temperature versus temperature ($\chi_{\text{M}}T$ versus T) for $\text{Ln}(\text{Bc}^{\text{Me}})_3$ and $\text{Ln}(\text{Bp}^{\text{Me}})_3$ collected under an applied field of 0.1 T.

Table 3.A1. Crystal data and structure refinement for **M(Bc^{Me})₃** and **M(Bp^{Me})₃**.

	Dy(Bc^{Me})₃	Dy(Bp^{Me})₃	Er(Bc^{Me})₃	Er(Bp^{Me})₃	Ho(Bc^{Me})₃	Ho(Bp^{Me})₃
Empirical formula	C ₂₄ H ₃₆ B ₃ DyN ₁₂	C ₂₄ H ₃₆ B ₃ DyN ₁₂	C ₂₄ H ₃₆ B ₃ ErN ₁₂	C ₂₄ H ₃₆ B ₃ ErN ₁₂	C ₂₄ H ₃₆ B ₃ HoN ₁₂	C ₂₄ H ₃₆ B ₃ HoN ₁₂
Formula weight	687.58	687.58	692.34	692.34	690.01	690.01
Temperature (K)	100(2)	100(2)	100(2)	100(2)	100(2)	100(2)
Wavelength (Å)	0.71073	0.71073	0.71073	0.71073	0.71073	0.71073
Crystal system	Hexagonal	Hexagonal	Hexagonal	Hexagonal	Hexagonal	Hexagonal
Space group	R-3	R-3	R-3	R-3	R-3	R-3
<i>a</i> (Å)	16.214(9)	16.0669(8)	16.0352(9)	16.0538(18)	16.0584(7)	16.0584(10)
<i>b</i> (Å)	16.214(9)	16.0669(8)	16.0352(9)	16.0538(18)	16.0584(7)	16.0584(10)
<i>c</i> (Å)	19.624(11)	19.8473(10)	19.4744(11)	19.783(2)	19.4547(8)	19.8205(13)
α (°)	90	90	90	90	90	90
β (°)	90	90	90	90	90	90
γ (°)	120	120	120	120	120	120
Volume (Å ³)	4468(4)	4437.1(4)	4336.5(4)	4415.4(9)	4344.7(3)	4426.4(5)
<i>Z</i>	6	6	6	6	6	6
ρ_{calcd} (mg/m ³)	1.533	1.544	1.591	1.562	1.582	1.553
μ (mm ⁻¹)	2.545	2.563	2.941	2.888	2.769	2.718
F(000)	2070	2070	2082	2082	2076	2076
Theta range (°)	2.51- 25.32	1.79-25.38	1.80-25.35	1.79-25.36	1.80-25.35	1.79-25.35
Reflections	9154	23570	31139	20467	20100	11698
Independent reflections	1828 [R(int) = 0.0236]	11736 [R(int) = 0.0225]	1731 [R(int) = 0.0229]	1742 [R(int) = 0.0385]	1725 [R(int) = 0.0263]	1772 [R(int) = 0.0338]
Final R indices [I > 2 σ (I)]	R1 = 0.0198 wR2 = 0.0470	R1 = 0.0139 wR2 = 0.0328	R1 = 0.0123 wR2 = 0.0308	R1 = 0.0162 wR2 = 0.0376	R1 = 0.0142 wR2 = 0.0340	R1 = 0.0177 wR2 = 0.0407
R indices (all data)	R1 = 0.0235 wR2 = 0.0484	R1 = 0.0141 wR2 = 0.0329	R1 = 0.0126 wR2 = 0.0309	R1 = 0.0178 wR2 = 0.0382	R1 = 0.0149 wR2 = 0.0343	R1 = 0.0199 wR2 = 0.0414

Table 3.A2. Crystal data and structure refinement for **M(Bc^{Me})₃** and **M(Bp^{Me})₃**.

	Tb(Bc^{Me})₃	Tb(Bp^{Me})₃	U(Bc^{Me})₃	U(Bp^{Me})₃	Y(Bc^{Me})₃	Y(Bp^{Me})₃
Empirical formula	C ₂₄ H ₃₆ B ₃ TbN ₁₂	C ₂₄ H ₃₆ B ₃ TbN ₁₂	C ₂₄ H ₃₆ B ₃ UN ₁₂	C ₂₄ H ₃₆ B ₃ UN ₁₂	C ₂₄ H ₃₆ B ₃ YN ₁₂	C ₂₄ H ₃₆ B ₃ YN ₁₂
Formula weight	684.00	684.00	763.11	763.11	613.99	613.99
Temperature (K)	100(2)	100(2)	100(2)	100(2)	100(2)	100(2)
Wavelength (Å)	0.71073	0.71073	0.71073	0.71073	0.71073	0.71073
Crystal system	Hexagonal	Hexagonal	Hexagonal	Hexagonal	Hexagonal	Hexagonal
Space group	R-3	R-3	R-3	R-3	R-3	R-3
<i>a</i> (Å)	16.0909(8)	16.0883(6)	16.412(10)	16.2056(15)	16.0838(10)	16.0508(8)
<i>b</i> (Å)	16.0909(8)	16.0883(6)	16.412(10)	16.2056(15)	16.0838(10)	16.0508(8)
<i>c</i> (Å)	19.4144(10)	19.8659(7)	19.192(11)	19.9312(18)	19.4499(12)	19.8200(11)
α (°)	90	90	90	90	90	90
β (°)	90	90	90	90	90	90
γ (°)	120	120	120	120	120	120
Volume (Å ³)	4353.3(4)	4453.1(3)	4477(5)	4533.1(7)	4357.4(5)	4422.1(4)
<i>Z</i>	6	6	6	6	6	6
ρ_{calcd} (mg/m ³)	1.565	1.530	1.698	1.677	1.404	1.383
μ (mm ⁻¹)	2.474	2.419	5.475	5.407	2.045	2.015
F(000)	2064	2064	2226	2226	1908	1908
Theta range (°)	1.80- 25.36	1.79-28.27	2.48-25.50	1.77-25.33	1.80-25.34	1.79-25.35
Reflections	102181	17648	11296	17685	18556	180932
Independent reflections	1786 [R(int) = 0.0292]	2218 [R(int) = 0.0287]	1843 [R(int) = 0.0231]	1780 [R(int) = 0.0392]	1720 [R(int) = 0.0337]	1786 [R(int) = 0.0495]
Final R indices [I > 2 σ (I)]	R1 = 0.0135 wR2 = 0.0322	R1 = 0.0194 wR2 = 0.0428	R1 = 0.0153 wR2 = 0.0363	R1 = 0.0210 wR2 = 0.0513	R1 = 0.0201 wR2 = 0.0548	R1 = 0.0248 wR2 = 0.0586
R indices (all data)	R1 = 0.0137 wR2 = 0.0325	R1 = 0.0216 wR2 = 0.0437	R1 = 0.0179 wR2 = 0.0371	R1 = 0.0248 wR2 = 0.0531	R1 = 0.0214 wR2 = 0.0556	R1 = 0.0294 wR2 = 0.0603

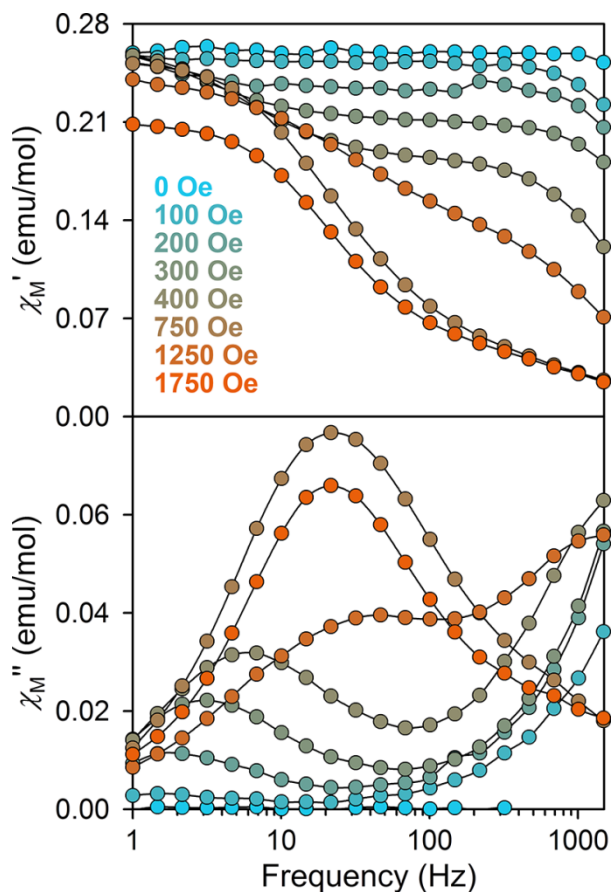


Figure 3.A5. Plot of the molar in- (χ_M') and out-of-phase susceptibility (χ_M'') versus frequency collected at 1.8 K for $U(Bc^{Me})_3$ at various applied fields. Black lines are guides for the eyes.

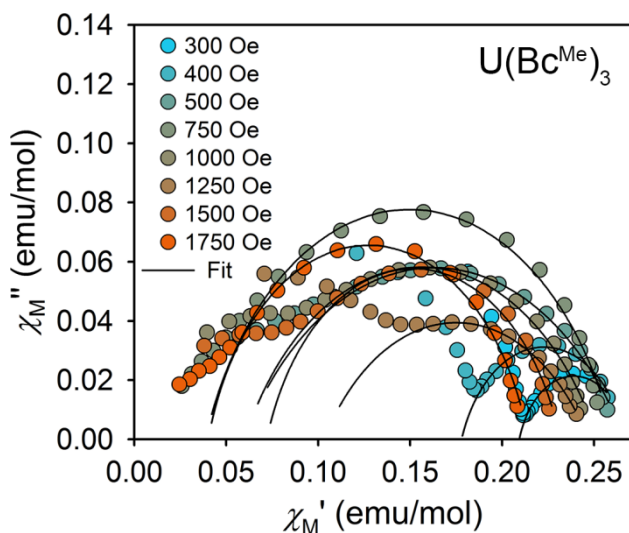


Figure 3.A6. Cole-Cole (Argand) plots for ac susceptibility data collected at 1.8 K and varying fields for $U(Bc^{Me})_3$. Experimental data points are represented by colored circles and the points representing the fit are connected by a solid black line.

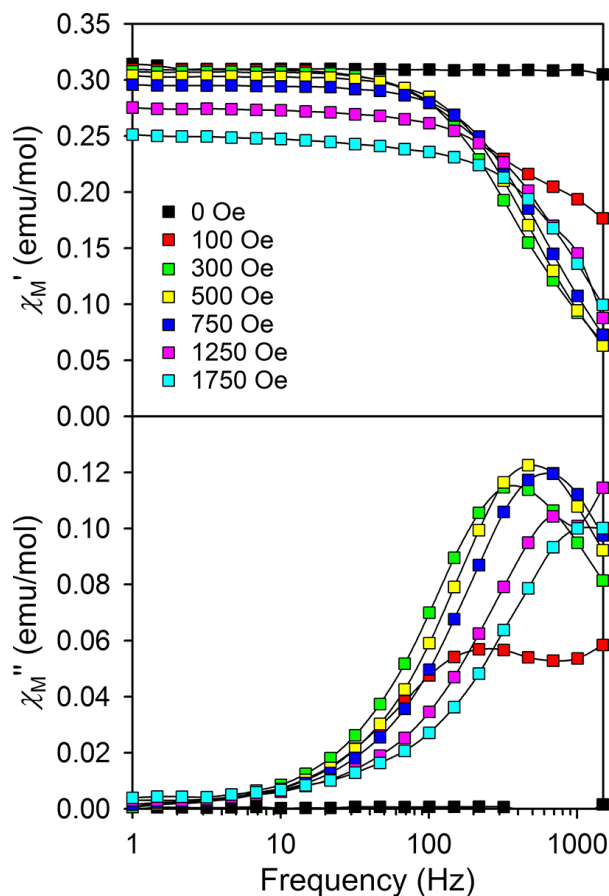


Figure 3.A7. Plot of the molar in- (χ_M') and out-of-phase susceptibility (χ_M'') versus frequency collected at 1.8 K for $U(Bp^{Me})_3$ at various applied fields. Black lines are guides for the eyes.

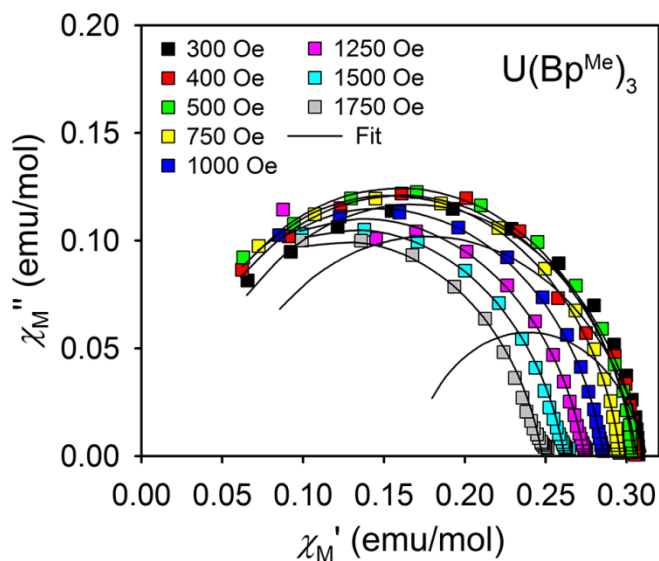


Figure 3.A8. Cole-Cole (Argand) plots for ac susceptibility data collected at 1.8 K and varying fields for $U(Bp^{Me})_3$. Experimental data points are represented by colored circles and the points representing the fit are connected by a solid black line.

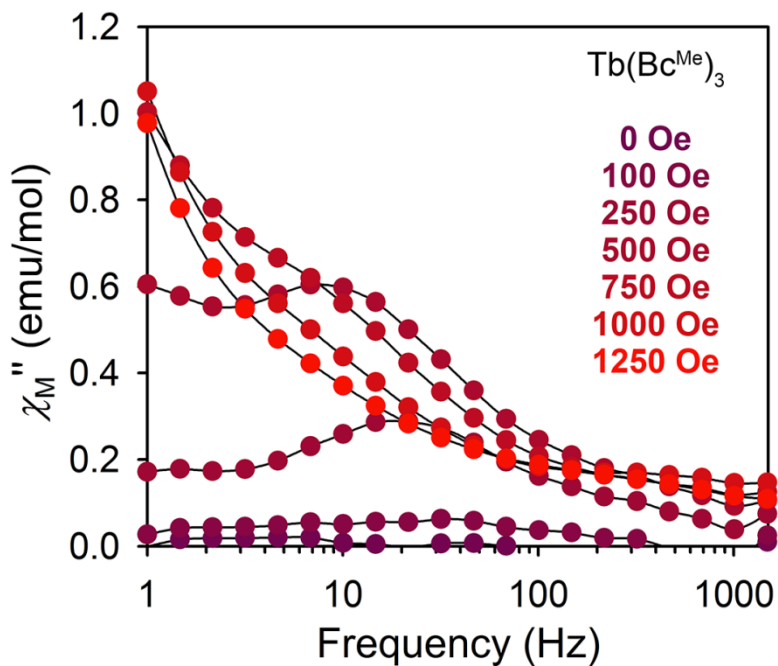


Figure 3.A9. Plot of the out-of-phase susceptibility χ_M'' versus frequency collected at 1.8 K for $\text{Tb}(\text{Bc}^{\text{Me}})_3$. Black lines are guides for the eyes.

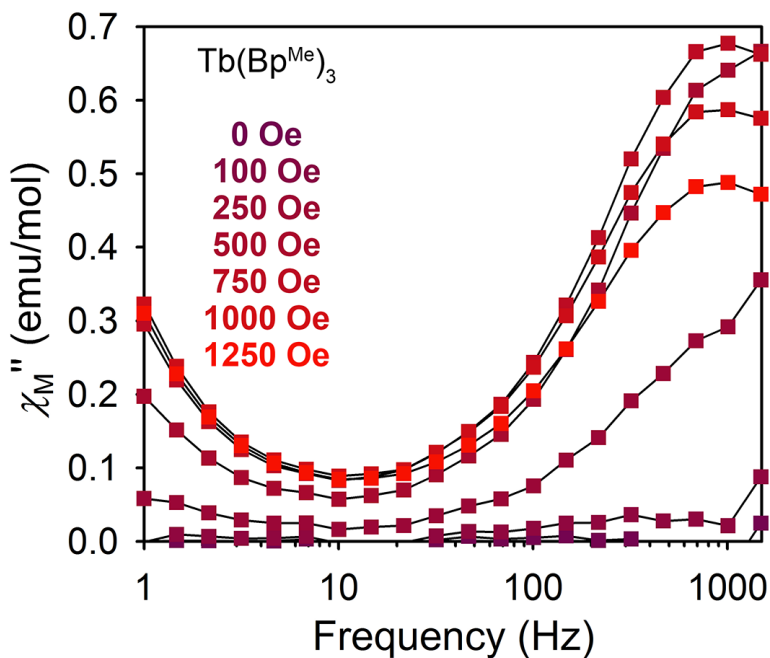


Figure 3.A10. Plot of the out-of-phase susceptibility χ_M'' versus frequency collected at 1.8 K for $\text{Tb}(\text{Bp}^{\text{Me}})_3$. Black lines are guides for the eyes.

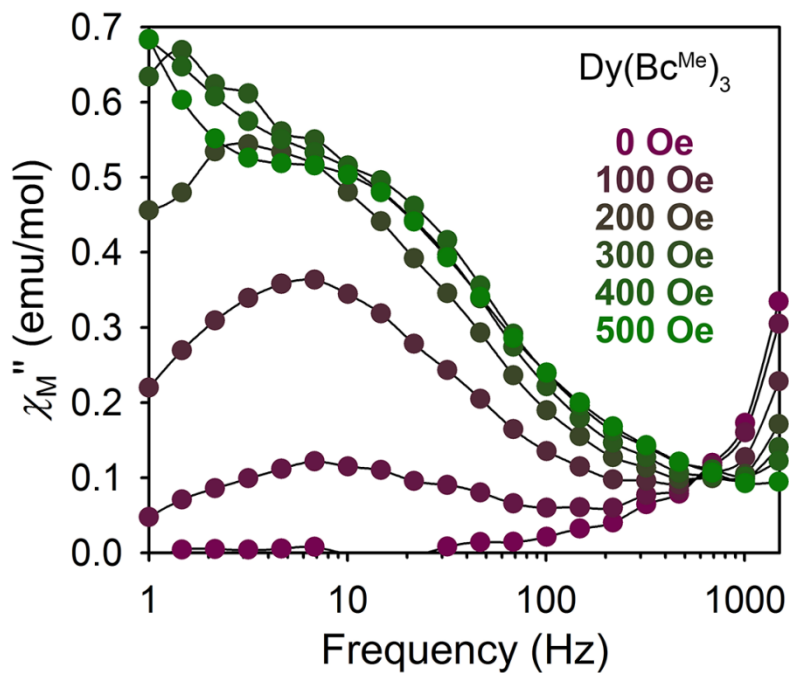


Figure 3.A11. Plot of the out-of-phase susceptibility χ_M'' versus frequency collected at 1.8 K for $\text{Dy}(\text{Bc}^{\text{Me}})_3$. Black lines are guides for the eyes.

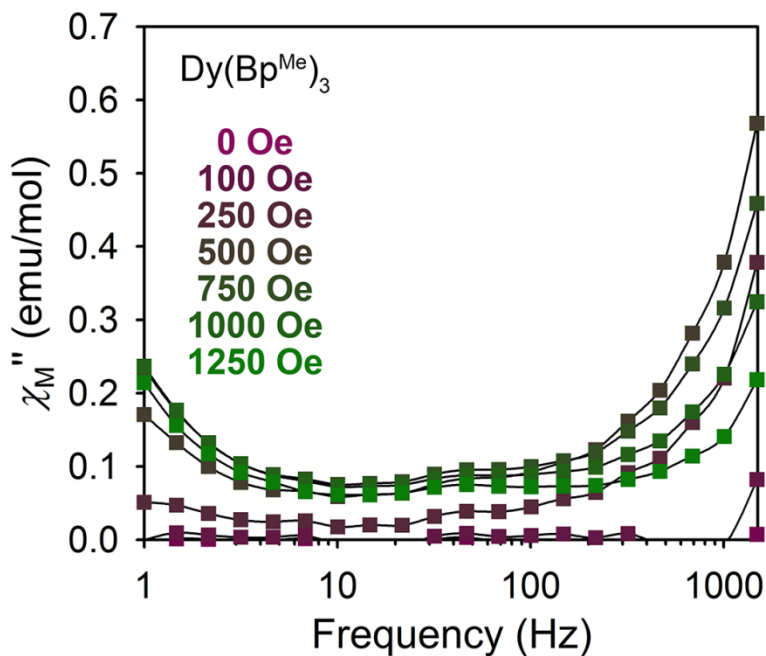


Figure 3.A12. Plot of the out-of-phase susceptibility χ_M'' versus frequency collected at 1.8 K for $\text{Dy}(\text{Bp}^{\text{Me}})_3$. Black lines are guides for the eyes.

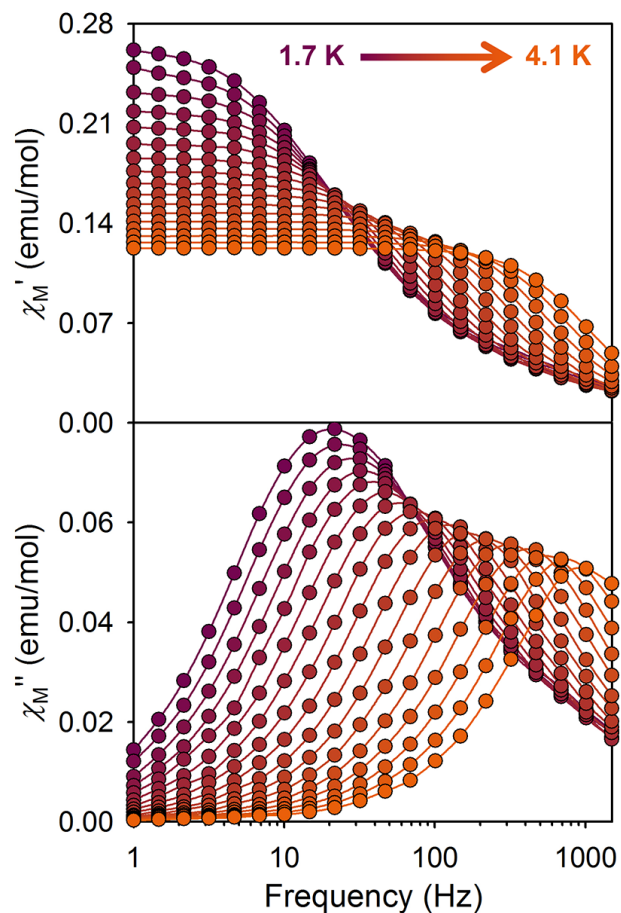


Figure 3.A13. Plot of the in-phase (χ_M') and out-of-phase (χ_M'') magnetic susceptibility for $U(Bc^{Me})_3$ under an applied field of 750 Oe and various temperatures.

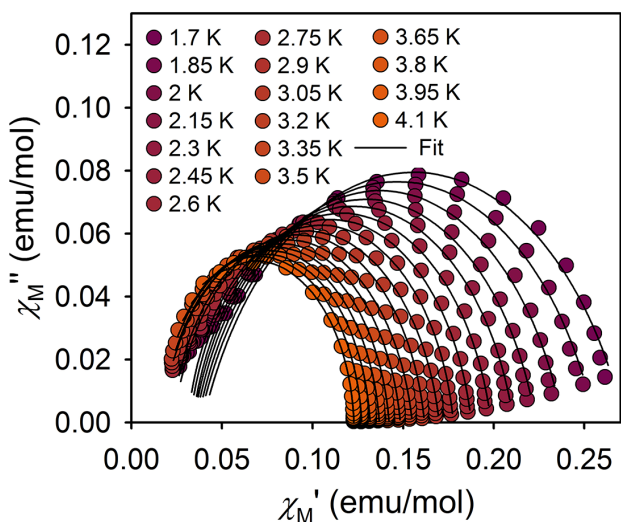


Figure 3.A14. Cole-Cole (Argand) plots for ac susceptibility data collected at 750 Oe and varying temperatures for $U(Bc^{Me})_3$.

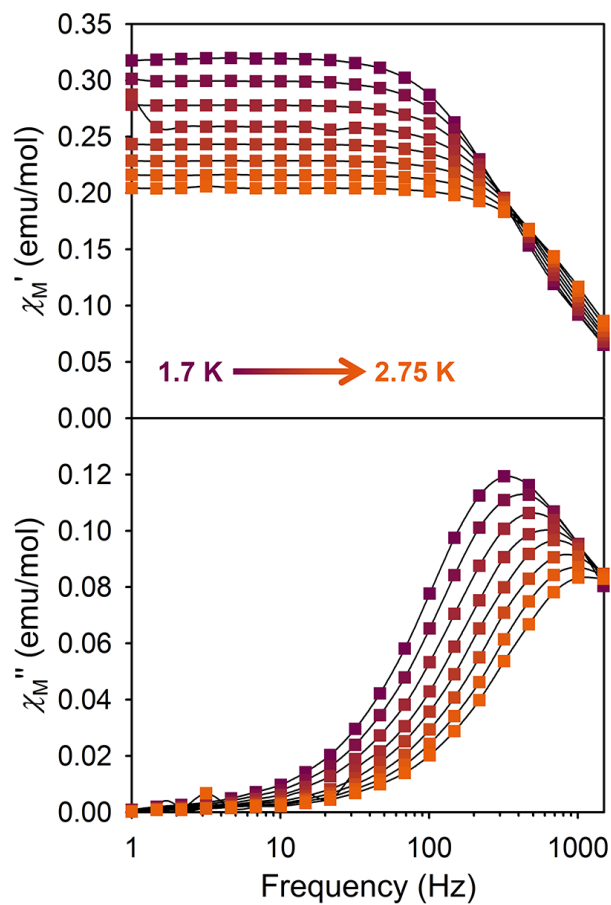


Figure 3.A15. Plot of the in-phase (χ_M') and out-of-phase (χ_M'') magnetic susceptibility for $U(Bp^{Me})_3$ under an applied field of 300 Oe and various temperatures.

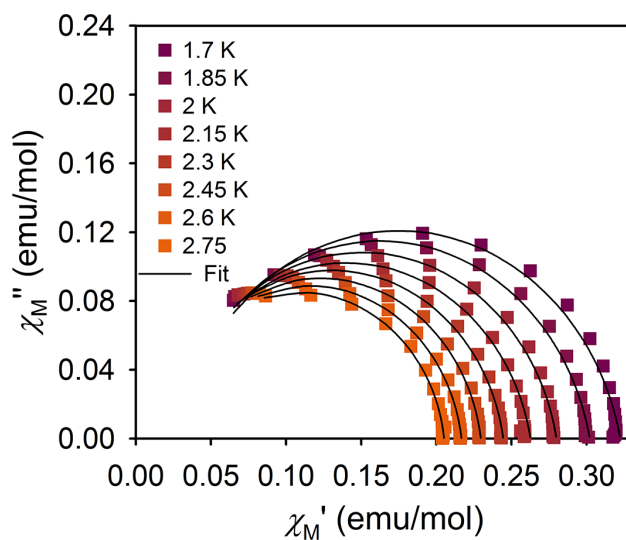


Figure 3.A16. Cole-Cole plots for ac susceptibility data collected at 300 Oe and varying temperatures for $U(Bp^{Me})_3$. Points representing the fit are connected by a solid black line.

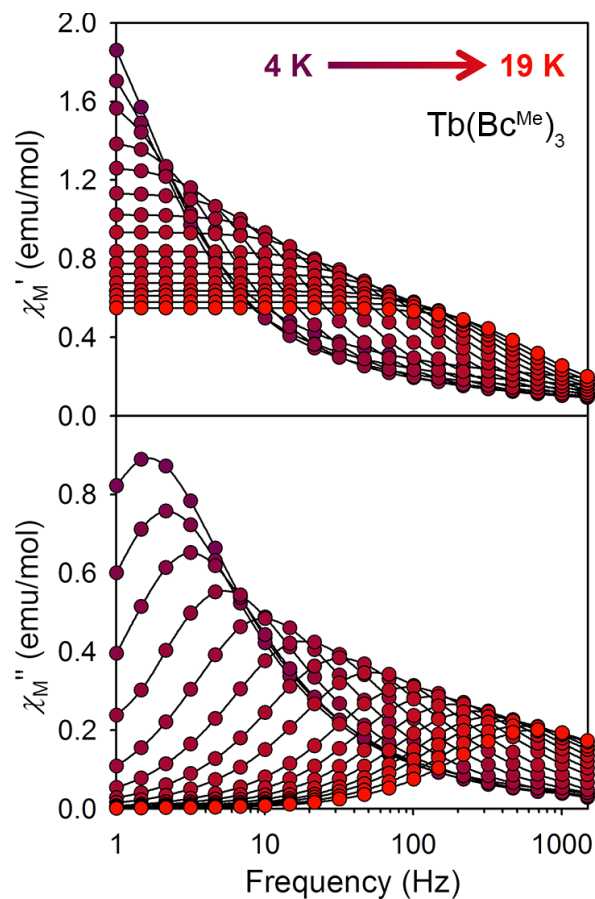


Figure 3.A17. Plot of the in-phase (χ_M') and out-of-phase (χ_M'') magnetic susceptibility for $\text{Tb}(\text{Bc}^{\text{Me}})_3$ at 1500 Oe and various temperatures. Black lines are guides for the eyes.

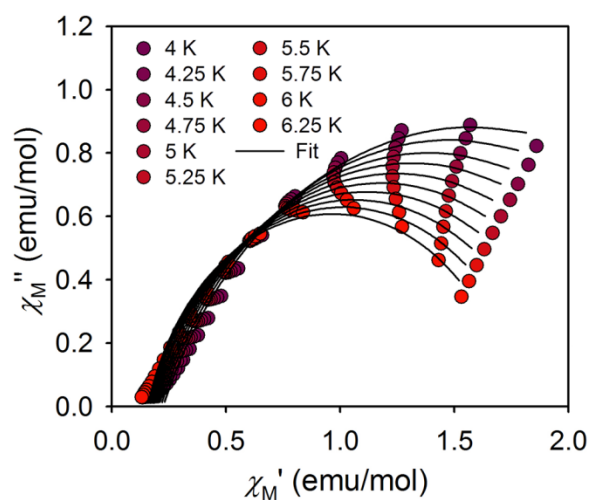


Figure 3.A18. Cole-Cole plots for ac susceptibility data collected at 1500 Oe and varying temperatures for $\text{Tb}(\text{Bc}^{\text{Me}})_3$. Experimental data points are represented by colored circles and the points representing the fit are connected by a solid black line.

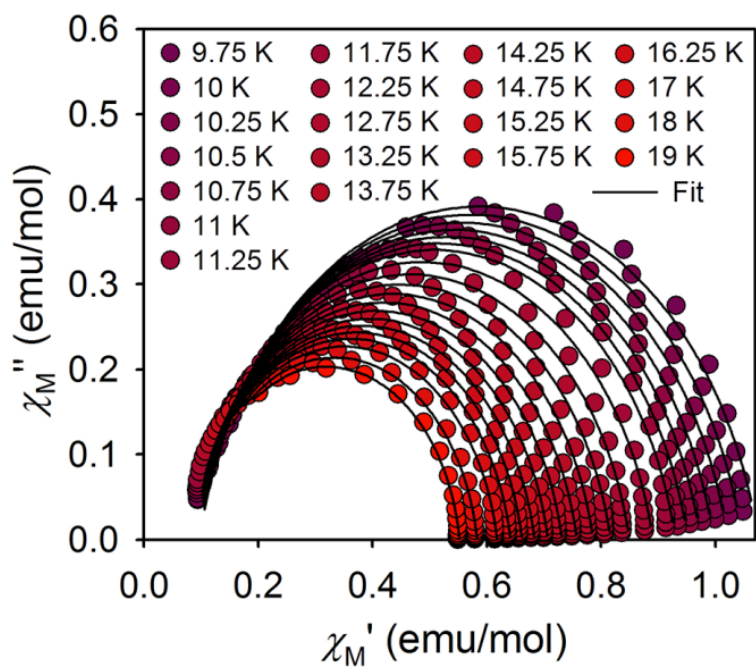
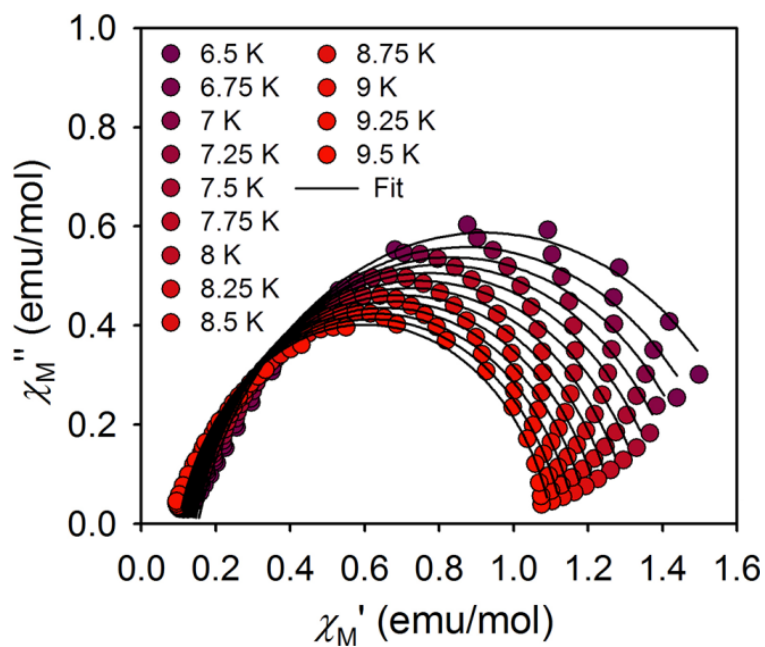


Figure 3.A19. Cole-Cole plots for ac susceptibility data collected at 1500 Oe and varying temperatures for $\text{Tb}(\text{Bc}^{\text{Me}})_3$. Experimental data points are represented by colored circles and the points representing the fit are connected by a solid black line.

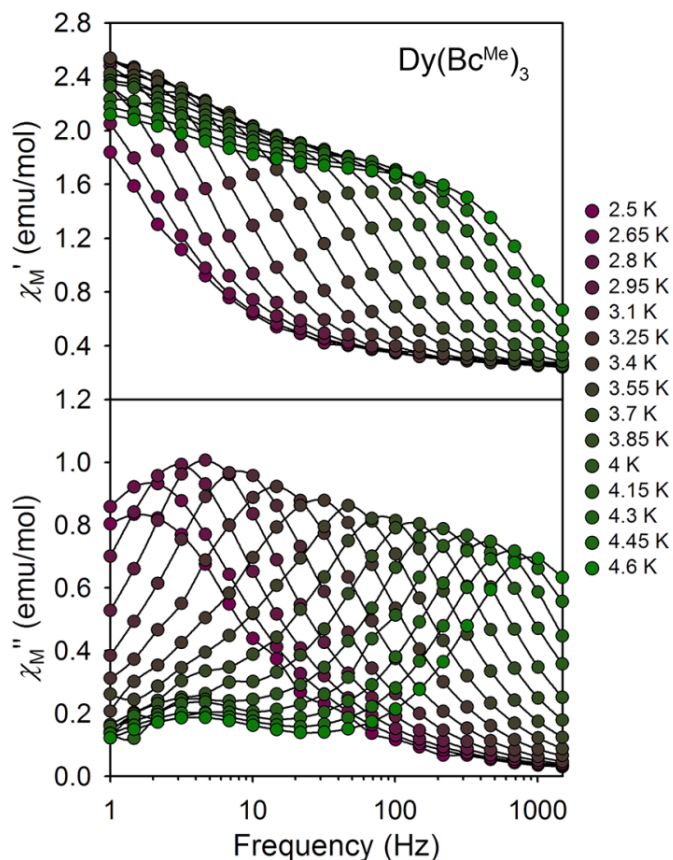


Figure 3.A20. Plot of the in-phase (χ_M') and out-of-phase (χ_M'') magnetic susceptibility for $\text{Dy}(\text{Bc}^{\text{Me}})_3$ at 1500 Oe and various temperatures. Black lines are guides for the eyes.

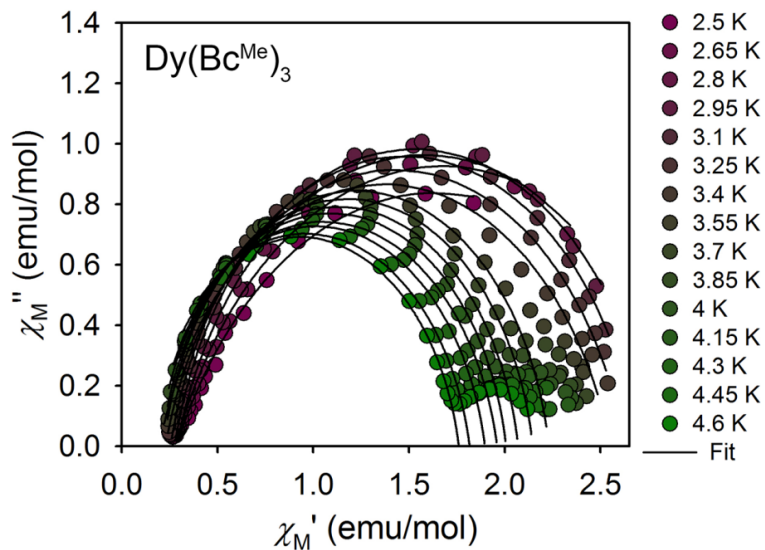


Figure 3.A21. Cole-Cole plots for ac susceptibility data collected at 1500 Oe and varying temperatures for $\text{Dy}(\text{Bc}^{\text{Me}})_3$. Experimental data points are represented by colored circles and the points representing the fit are connected by a solid black line.

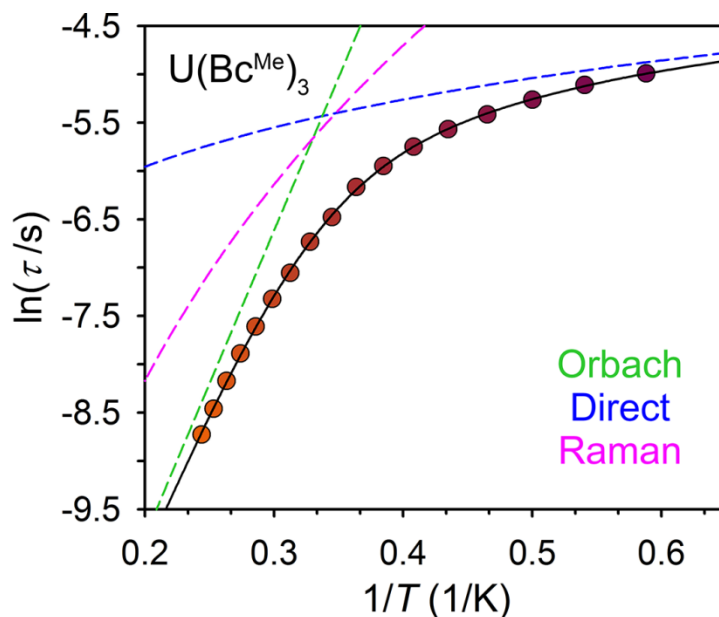


Figure 3.A22. Plot of $\ln(\tau)$ versus $1/T$ for $U(\text{Bc}^{\text{Me}})_3$ under an applied field of 750 Oe. The black line represents the fit to the experimental data using Equation 1 (main text). Green, pink, and blue dashed lines represent individual Orbach, Raman, and Direct fits, respectively. A Raman exponent of $m = 7$ was found to afford the best fit to all U^{3+} relaxation data.

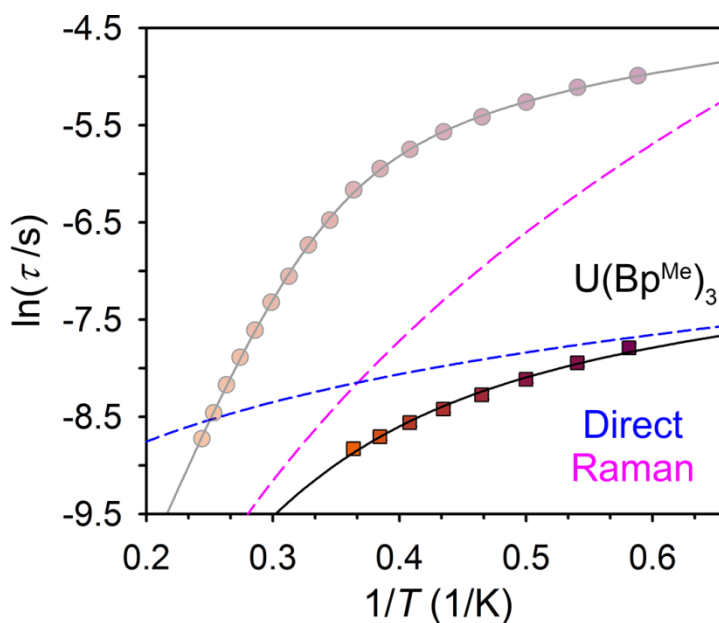


Figure 3.A23. Plot of $\ln(\tau)$ versus $1/T$ for $U(\text{Bp}^{\text{Me}})_3$ under an applied field of 300 Oe. The black line represents the fit to the experimental data using Equation 1 (main text). Pink and blue dashed lines represent individual Raman and Direct fits, respectively. Temperature-dependent data for $U(\text{Bc}^{\text{Me}})_3$ under an applied field of 750 Oe is shown in circles with corresponding fit for comparison.

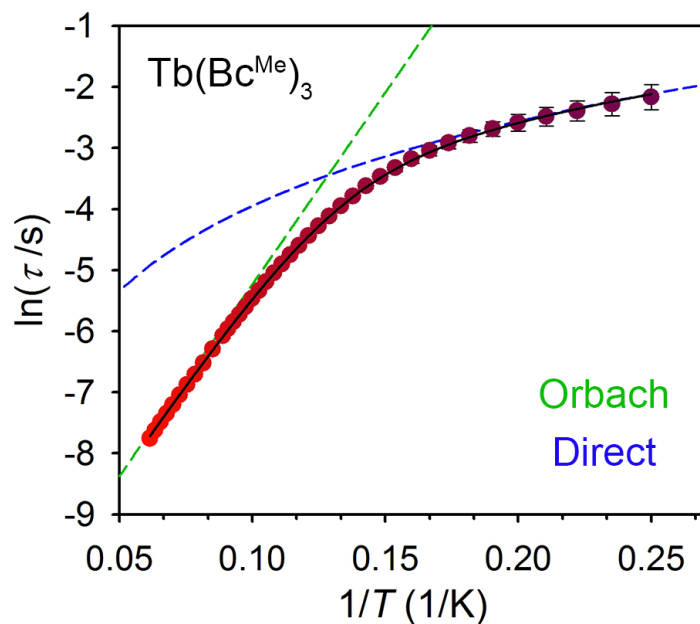


Figure 3.A24. Plot of $\ln(\tau)$ versus $1/T$ for $\text{Tb}(\text{Bc}^{\text{Me}})_3$, obtained under an applied field of 1500 Oe over the temperature range 4-19 K. The black line represents the fit to the experimental data using Equation 1 (main text). Green and blue dashed lines represent individual Orbach and Direct fits, respectively.

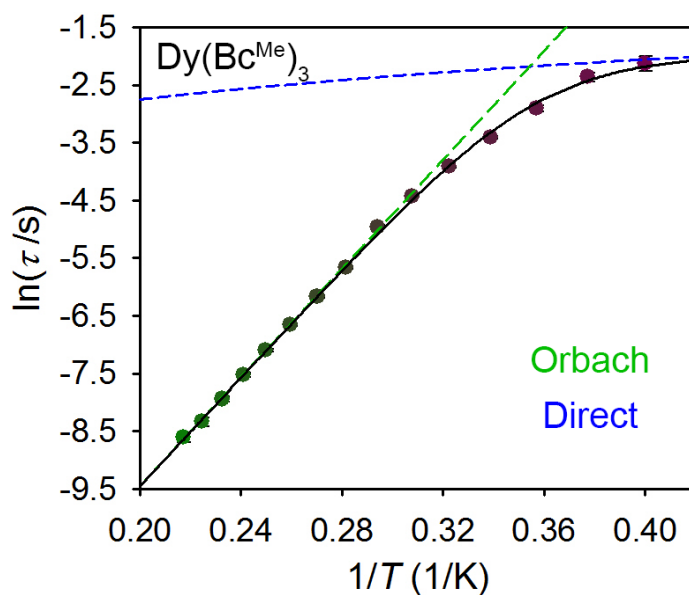


Figure 3.A25. Plot of $\ln(\tau)$ versus $1/T$ for $\text{Dy}(\text{Bc}^{\text{Me}})_3$, obtained under an applied field of 1500 Oe. The black line represents the fit to the experimental data using Equation 1 (main text). Green and blue dashed lines represent individual Orbach and direct fits, respectively.

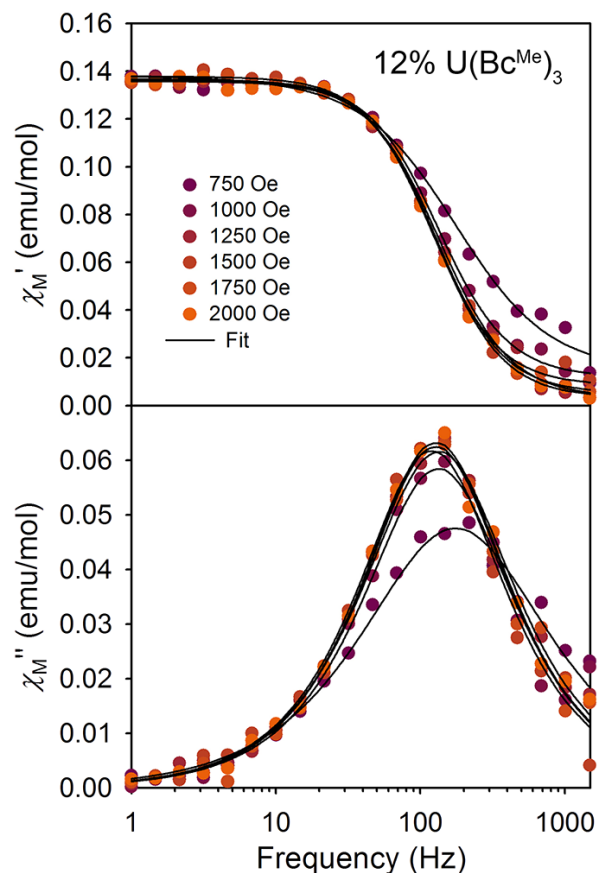


Figure 3.A26. Plot of the in-phase (χ_M') and out-of-phase (χ_M'') magnetic susceptibility for 12% $U(Bc^{Me})_3$ in $Y(Bc^{Me})_3$ at 3.5 K and various applied fields.

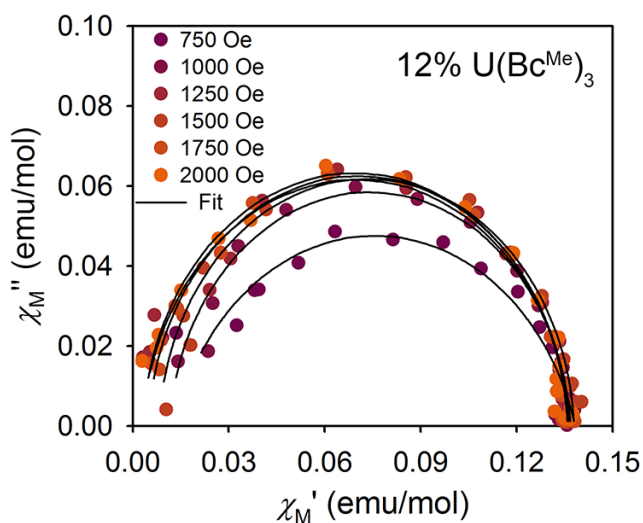


Figure 3.A27. Cole-Cole plots for ac susceptibility data collected at 3.5 K and varying fields for 12% $U(Bc^{Me})_3$ in $Y(Bc^{Me})_3$ at 3.5 K and various applied fields. Experimental data points are represented by colored circles and the points representing the fit are connected by a solid black line.

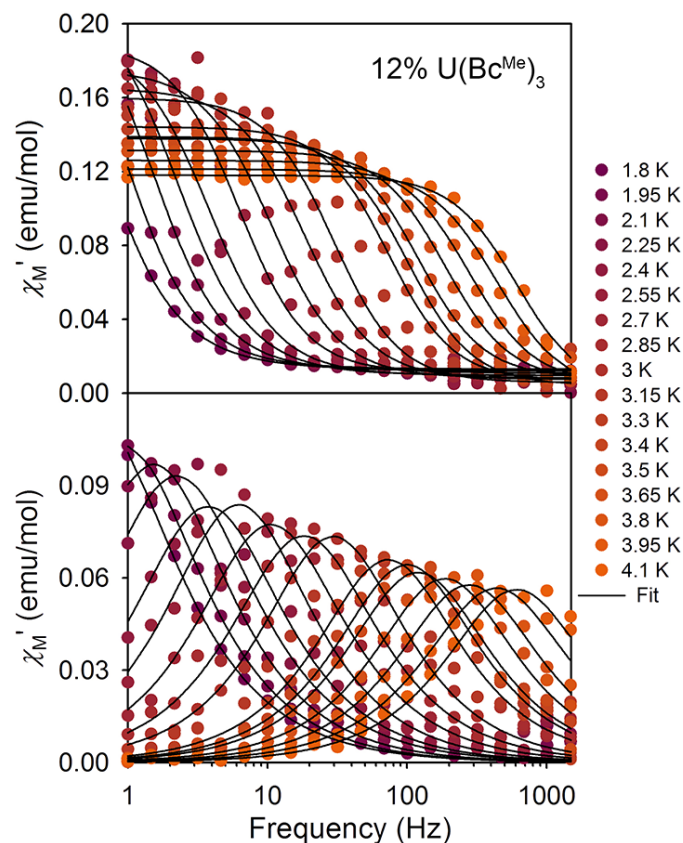


Figure 3.A28. Plot of the in-phase (χ_M') and out-of-phase (χ_M'') magnetic susceptibility for 12% $U(Bc^{Me})_3$ in $Y(Bc^{Me})_3$ under an applied field of 1500 Oe.

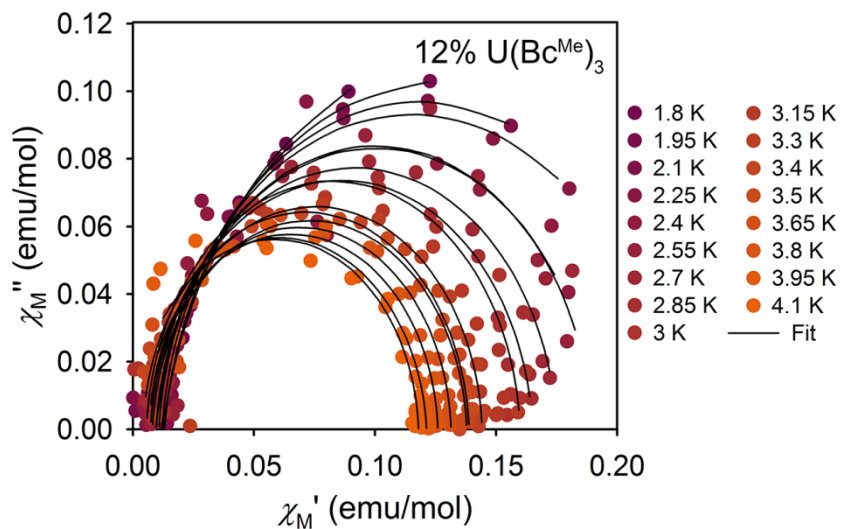


Figure 3.A29. Cole-Cole (Argand) plots for ac susceptibility data collected at 1500 Oe and varying temperatures for 12% $U(Bc^{Me})_3$ in $Y(Bc^{Me})_3$. Experimental data points are represented by colored circles and the points representing the fit are connected by a solid black line.

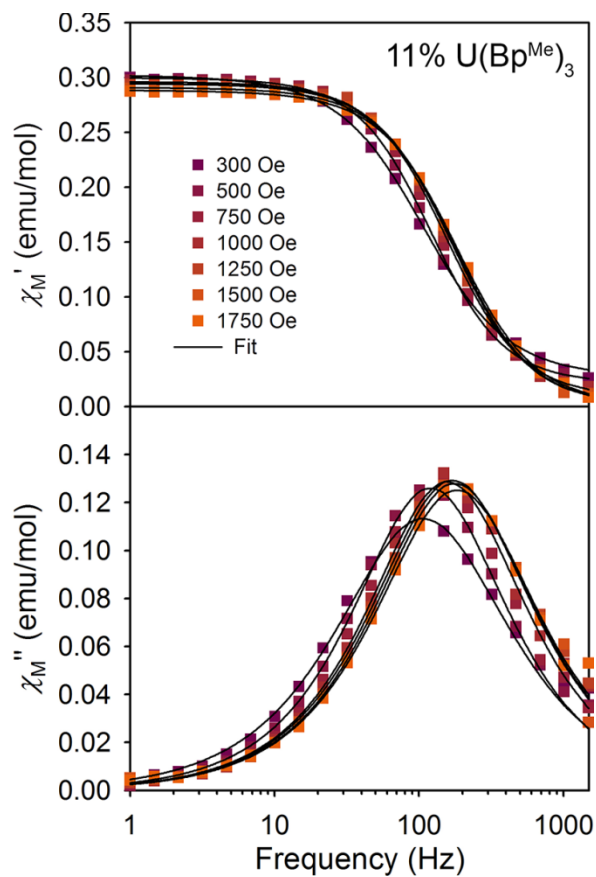


Figure 3.A30. Plot of the in-phase (χ_M') and out-of-phase (χ_M'') magnetic susceptibility for 11% $U(Bp^{Me})_3$ in $Y(Bp^{Me})_3$ at 1.8 K and various fields. Black lines represent fits to a generalized Debye model.

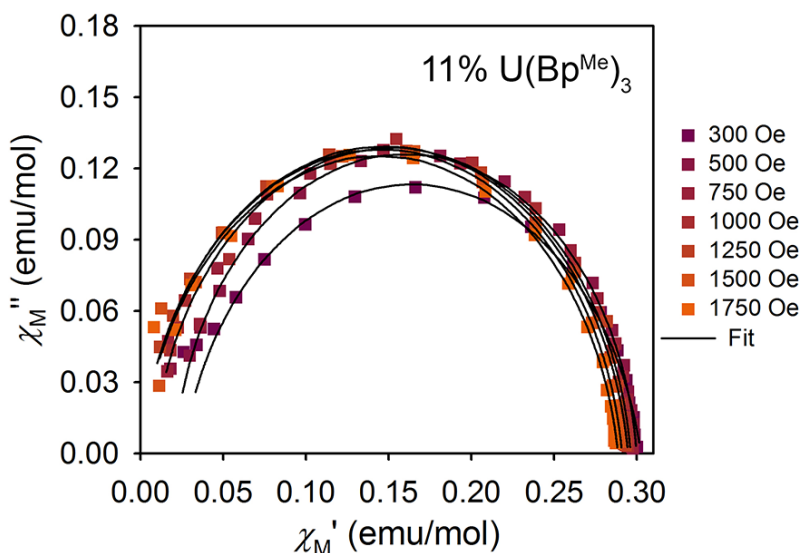


Figure 3.A31. Cole-Cole (Argand) plots for ac susceptibility data collected at 1.8 K and varying applied fields 11% $U(Bp^{Me})_3$ in $Y(Bp^{Me})_3$ at 1.8 K. Experimental data points are represented by colored squares and the points representing the fit are connected by a solid black line.

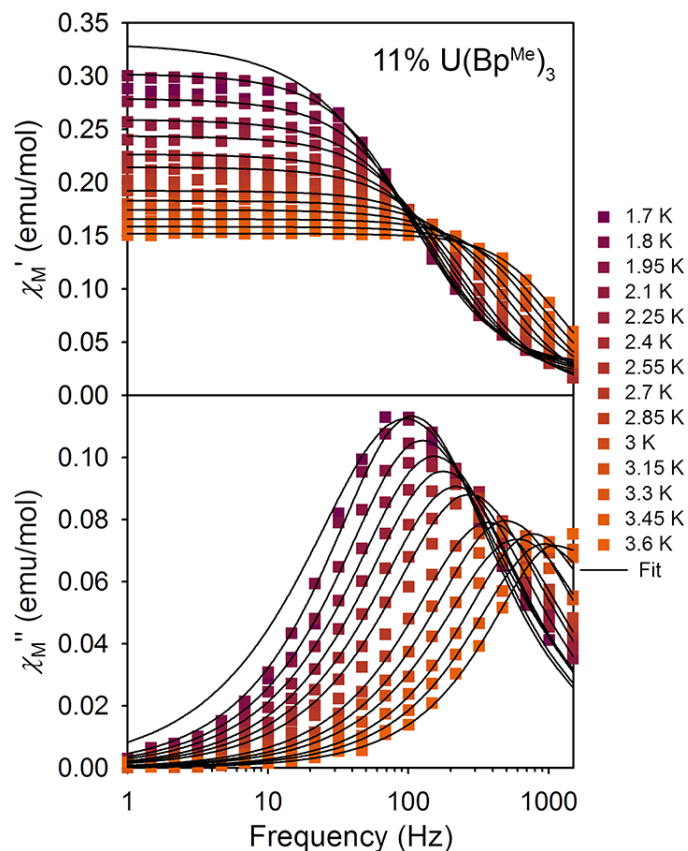


Figure 3.A32. Plot of the in-phase (χ_M') and out-of-phase (χ_M'') magnetic susceptibility for 11% U(Bp^{Me})₃ in Y(Bp^{Me})₃ at 300 Oe and various temperatures. Black lines represent fits to a generalized Debye model.

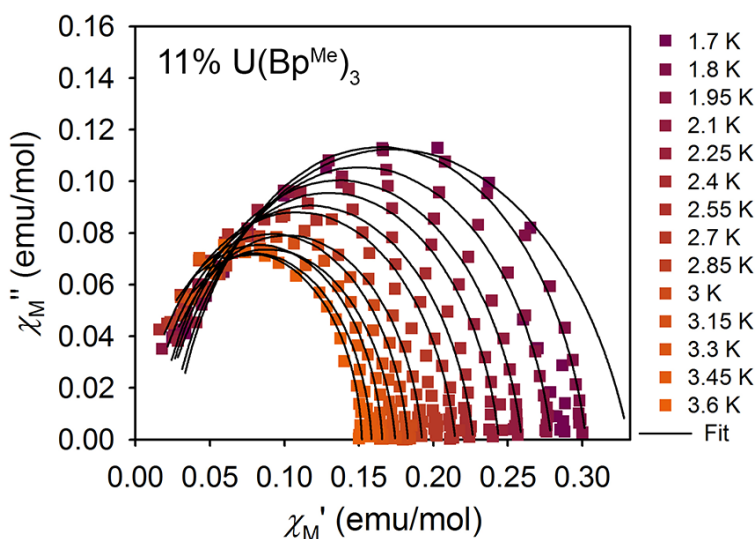


Figure 3.A33. Cole-Cole (Argand) plots for ac susceptibility data collected at 300 Oe and varying temperatures for 11% U(Bp^{Me})₃ in Y(Bp^{Me})₃. Experimental data points are represented by colored squares and the points representing the fit are connected by a solid black line.

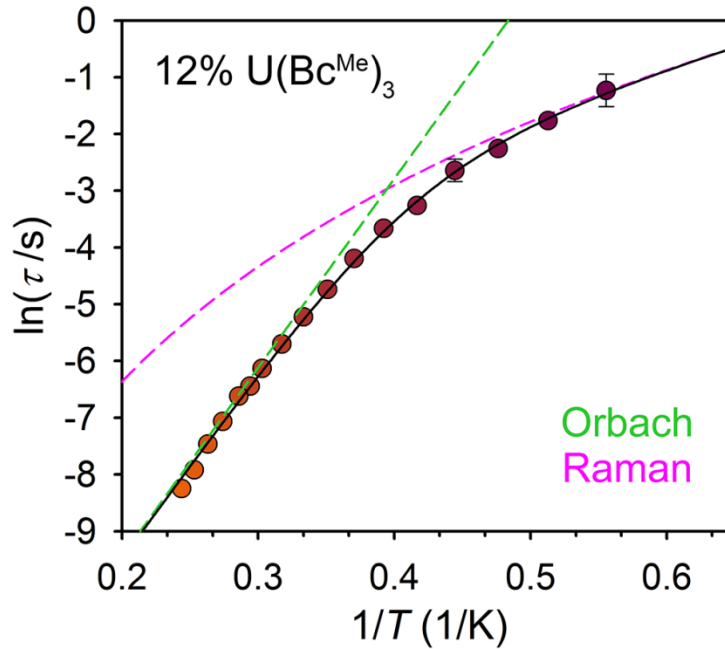


Figure 3.A34. Plot of $\ln(\tau)$ versus $1/T$ for 12% $U(Bc^{Me})_3$ in $Y(Bc^{Me})_3$ under an applied field of 1500 Oe. The black line represents the fit to the experimental data using Equation 1 (main text). Green and pink lines represent individual Orbach and Raman fits, respectively.

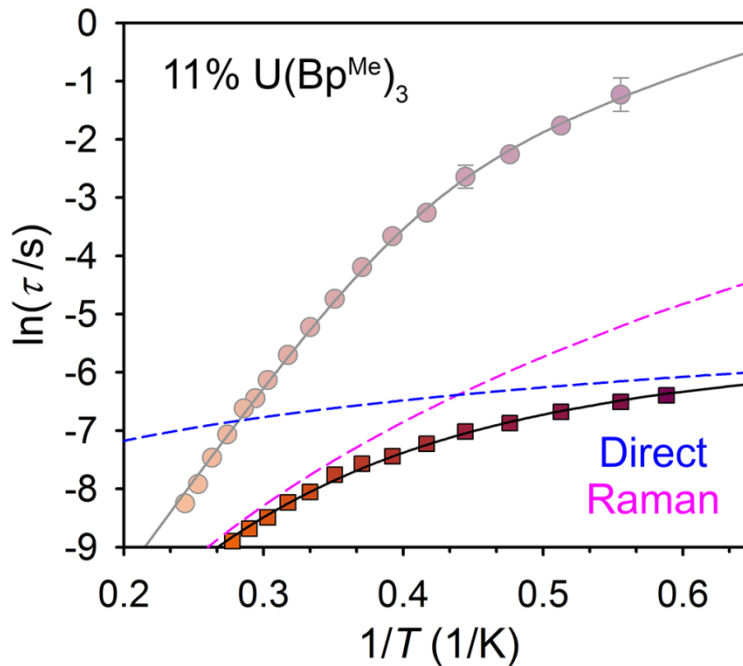


Figure 3.A35. Plot of $\ln(\tau)$ versus $1/T$ for 11% $U(Bp^{Me})_3$ in $Y(Bp^{Me})_3$ obtained under an applied field of 300 Oe, together with 12% $U(Bc^{Me})_3$ in $Y(Bc^{Me})_3$ (faded circles, $H_{dc} = 1500$ Oe). The black line represents the fit to the experimental data using Equation 1 (main text). Pink and blue dashed lines represent individual Raman and Direct fits, respectively.

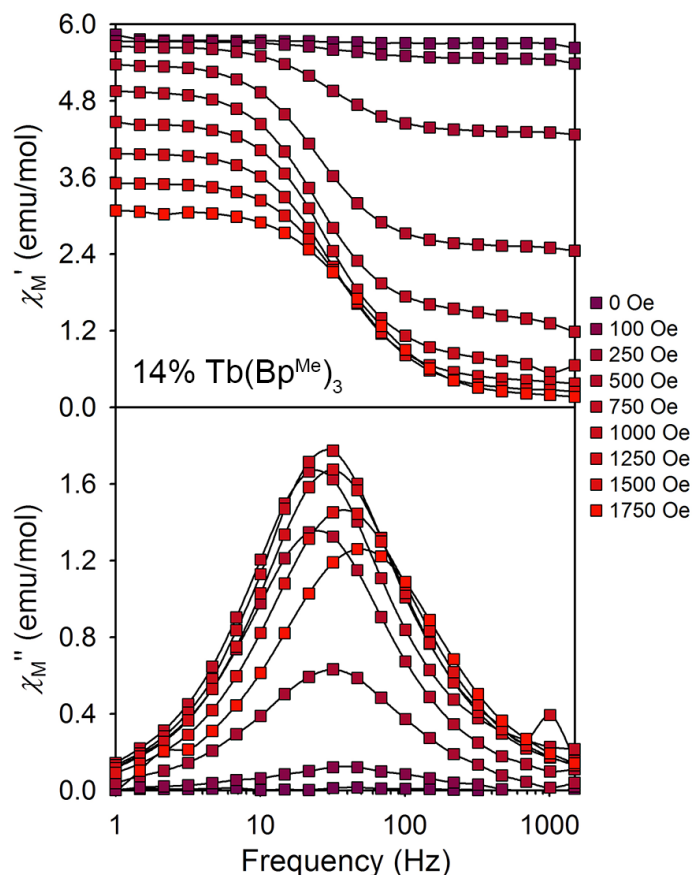


Figure 3.A36. Plot of the in-phase (χ_M') and out-of-phase (χ_M'') magnetic susceptibility for 14% $\text{Tb}(\text{Bp}^{\text{Me}})_3$ in $\text{Y}(\text{Bp}^{\text{Me}})_3$ at 1.8 K and various fields. Black lines are guides for the eyes.

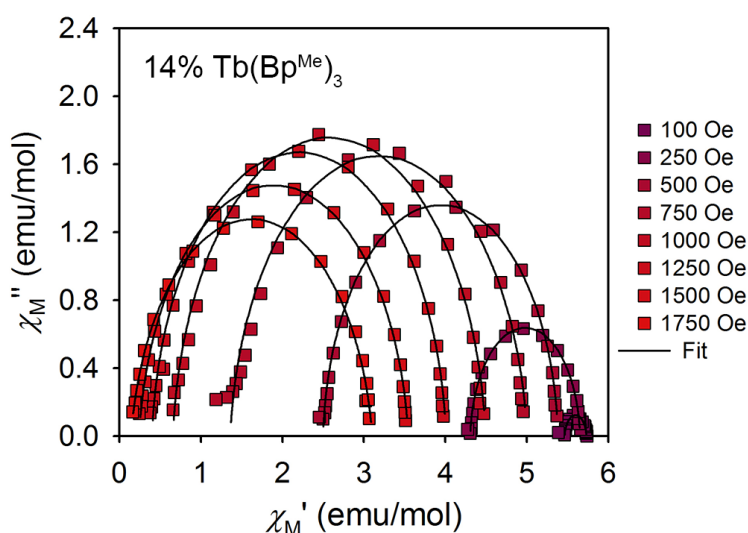


Figure 3.A37. Cole-Cole plots for ac susceptibility data collected at 1.8 K and varying fields for 14% $\text{Tb}(\text{Bp}^{\text{Me}})_3$ in $\text{Y}(\text{Bp}^{\text{Me}})_3$. Experimental data points are represented by colored squares and the points representing the fit are connected by a solid black line.

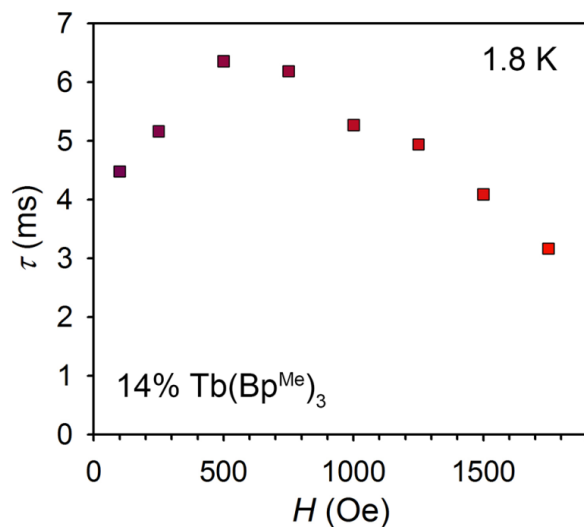


Figure 3.A38. Plot of the relaxation time, τ , versus applied dc field for 14% Tb(Bp^{Me})₃ in Y(Bp^{Me})₃, obtained at a temperature of 1.8 K. The maximum in the relaxation time occurs for $H_{dc} = 500$ Oe, however the full magnitude of the out-of-phase signal is not represented at this field.

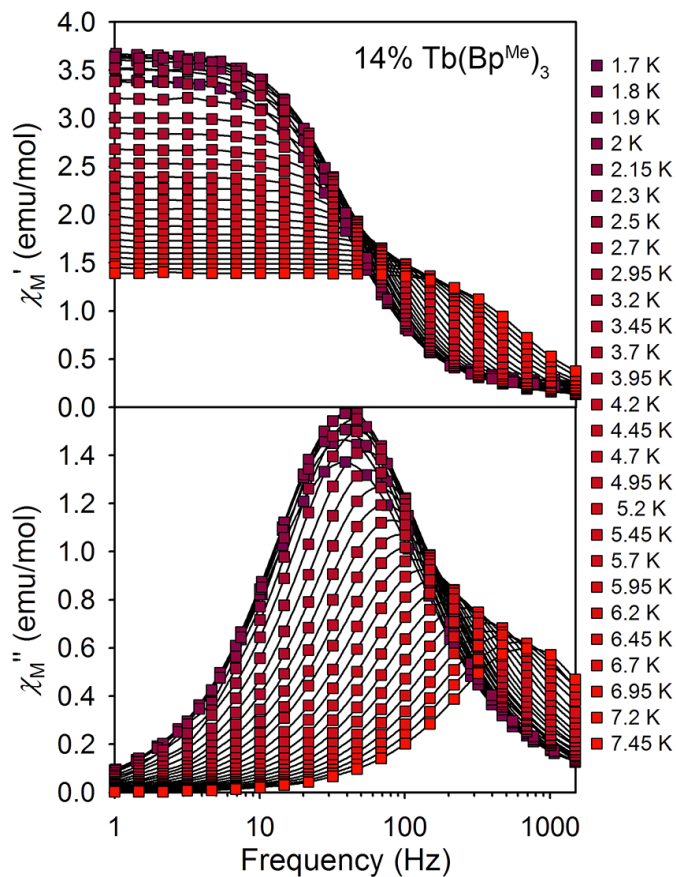


Figure 3.A39. Plot of the in-phase (χ_M') and out-of-phase (χ_M'') magnetic susceptibility for 14% Tb(Bp^{Me})₃ in Y(Bp^{Me})₃ at 1500 Oe and various temperatures. Black lines are guides for the eyes.

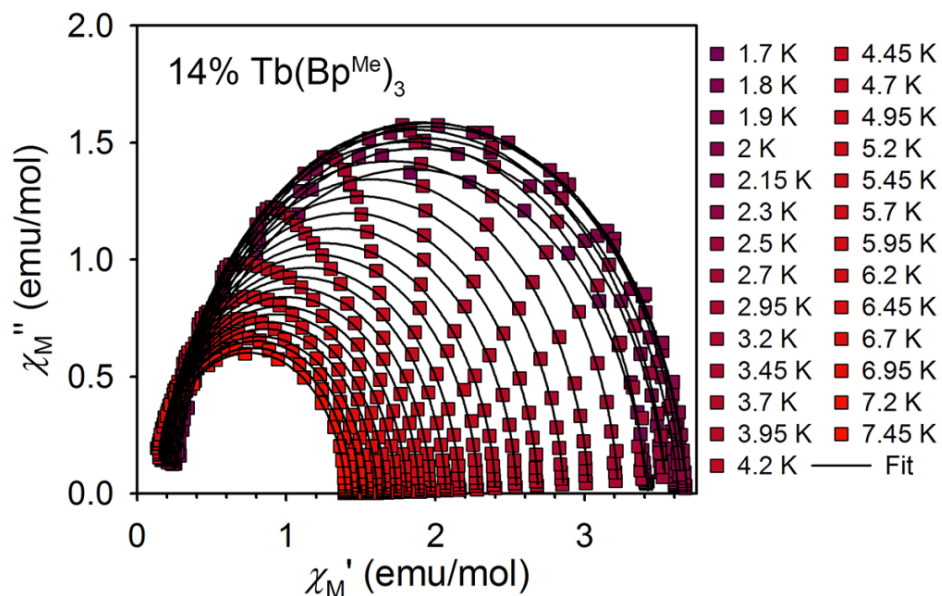


Figure 3.A40. Cole-Cole plots for ac susceptibility data collected at 1500 Oe and varying temperatures for 14% Tb(Bp^{Me})₃ in Y(Bp^{Me})₃. Experimental data points are represented by colored squares and the points representing the fit are connected by a solid black line.

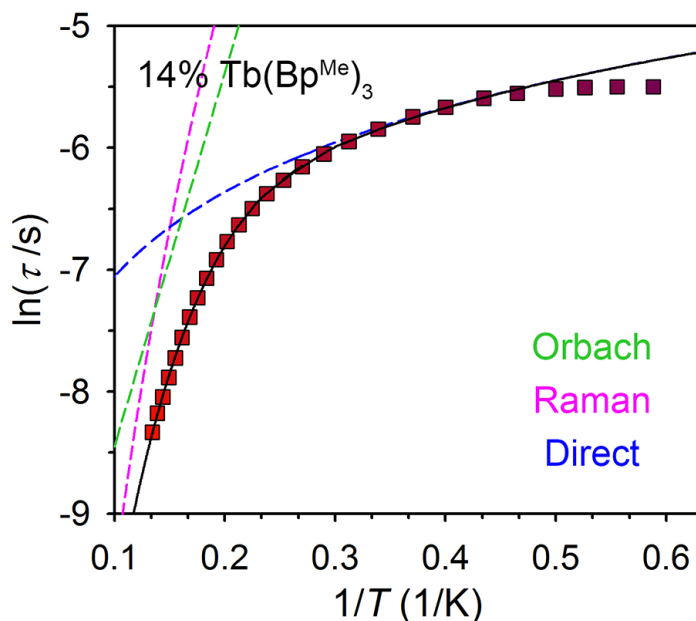


Figure 3.A41. Plot of $\ln(\tau)$ versus $1/T$ for 14% Tb(Bp^{Me})₃ in Y(Bp^{Me})₃, obtained under an applied field of 1500 Oe. The black line represents the fit to the experimental data using Equation 1 (main text). Green, pink and blue dashed lines represent individual Orbach, Raman and direct fits, respectively. A good fit could be obtained only by omitting the lowest five temperature points. This could be due to the presence of a pure tunneling mechanism below 2.3 K, for which Equation 3.1 does not account.

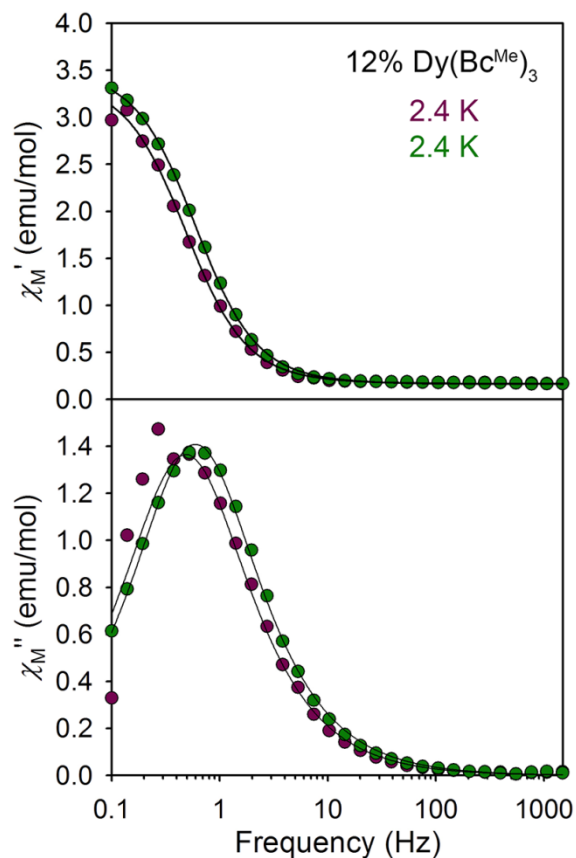


Figure 3.A42. Plot of the in-phase (χ_M') and out-of-phase (χ_M'') magnetic susceptibility for 12 mol% $\text{Dy}(\text{Bc}^{\text{Me}})_3$ in $\text{Y}(\text{Bc}^{\text{Me}})_3$ at 1500 Oe and temperatures of 2.4 and 2.5 K. Black lines represent fits to the data.

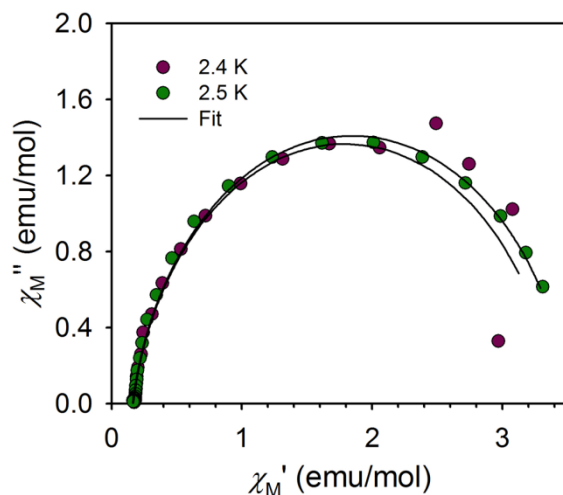


Figure 3.A43 Cole-Cole (Argand) plots for ac susceptibility data collected at 1500 Oe and varying temperatures for 12 mol% $\text{Dy}(\text{Bc}^{\text{Me}})_3$ in $\text{Y}(\text{Bc}^{\text{Me}})_3$. Experimental data points are represented by colored circles and the points representing the fit are connected by a solid black line.

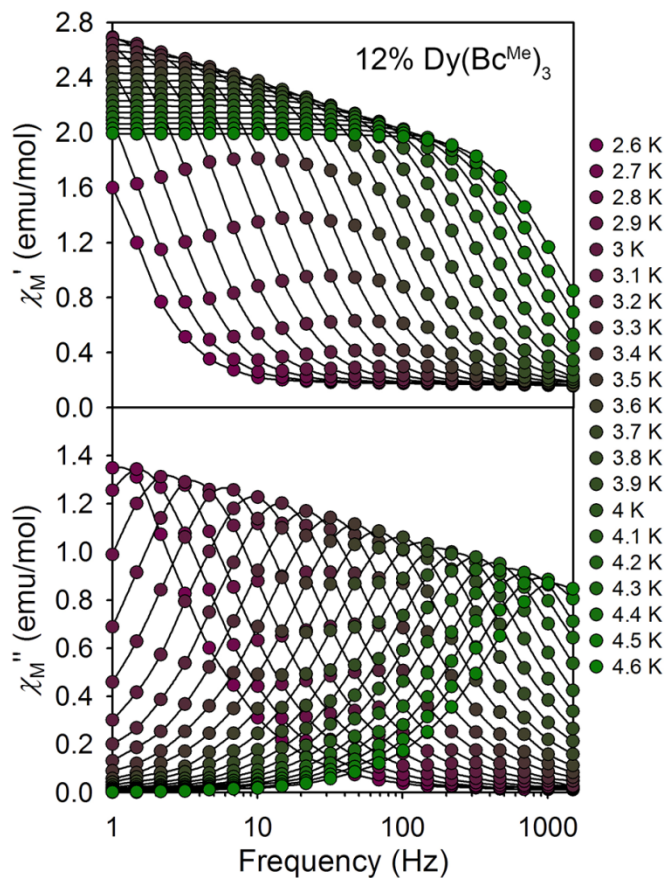


Figure 3.A44. Plot of the in-phase (χ_M') and out-of-phase (χ_M'') magnetic susceptibility for 12 mol% Dy(Bc^{Me})₃ in Y(Bc^{Me})₃ at an applied field of 1500 Oe and various temperatures. Black lines are guides for the eyes.

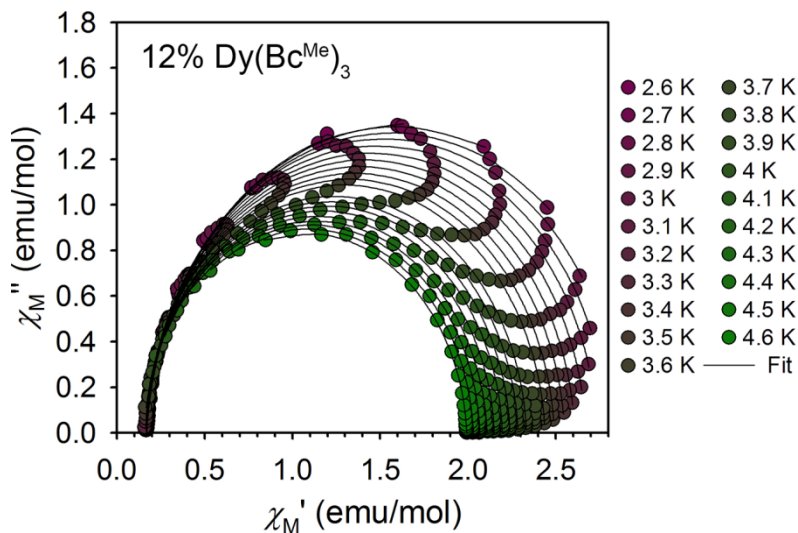


Figure 3.A45. Cole-Cole plots for ac susceptibility data collected at 1500 Oe and varying temperatures for 12 mol% Dy(Bc^{Me})₃ in Y(Bc^{Me})₃. Experimental data points are represented by colored circles and the points representing the fit are connected by a solid black line.

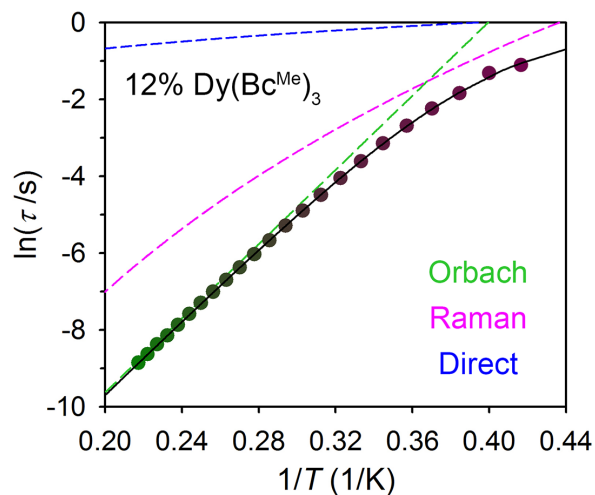


Figure 3.A46. Plot of $\ln(\tau)$ versus $1/T$ for 12 mol% $\text{Dy}(\text{Bc}^{\text{Me}})_3$ in $\text{Y}(\text{Bc}^{\text{Me}})_3$ obtained under $H_{\text{dc}} = 1500$ Oe. The black line represents the fit to the experimental data using Equation 3.1. Green, pink, and blue dashed lines represent individual Orbach, Raman, and direct fits, respectively.

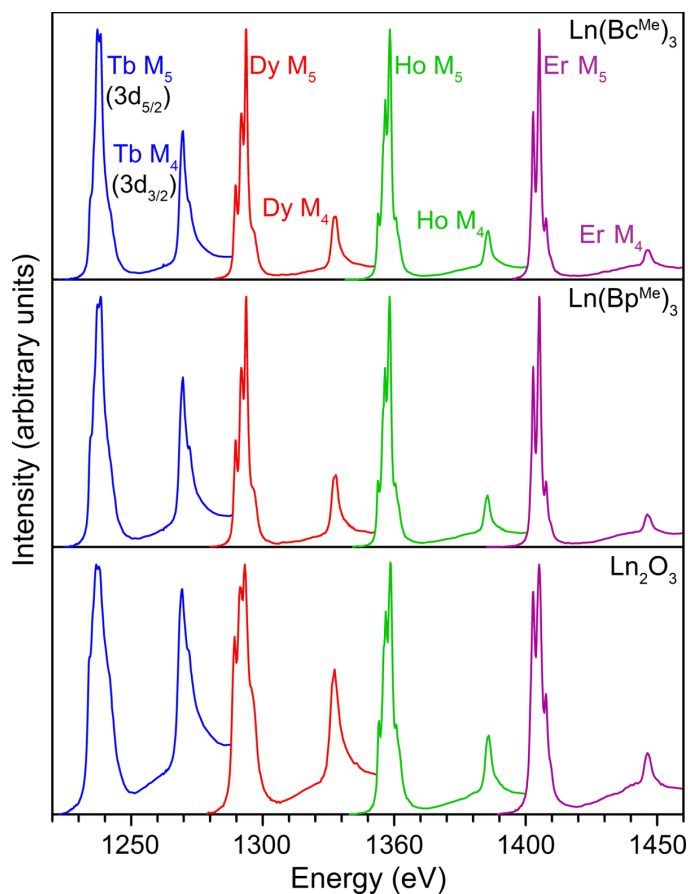


Figure 3.A47. Background subtracted $M_{5,4}$ -edge XANES spectra from $\text{Ln}(\text{Bc}^{\text{Me}})_3$, $\text{Ln}(\text{Bp}^{\text{Me}})_3$, and Ln_2O_3 , for $\text{Ln} = \text{Tb}, \text{Dy}, \text{Ho}, \text{and Er}$. Spectra are normalized to the maximum of the corresponding Tb M_5 -edge.

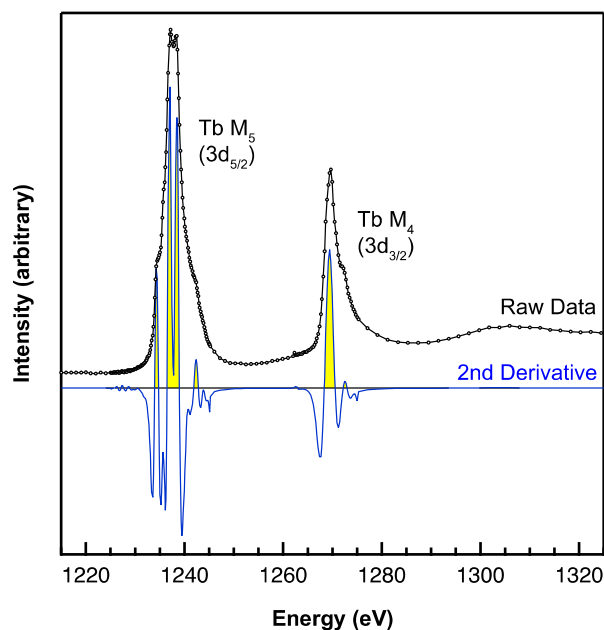


Figure 3.A48. Plot of the terbium $M_{5,4}$ -edge XANES raw experimental data obtained using STXM (black circles) for $Tb(Bc^{Me})_3$, showing how the area beneath the $M_{5,4}$ -edges (shaded yellow) was determined graphically from the 2nd derivative (blue trace).

Table 3.A3. A summary of data taken from the Tb, Dy, Ho, and Er $M_{5,4}$ -edge XANES spectra of $Ln(Bc^{Me})_3$, $Ln(Bp^{Me})_3$, and Ln_2O_3 .

Cmpd	M_5 and M_4 Energies (eV)								M_5^a	M_4^a	$M_5/(M_5+M_4)^b$	M_5/M_4^b
$Tb(Bc^{Me})_3$	1234.4	1235.7	1237.0	1238.4	1239.9	1242.0	1269.4	1272.0	1238.4	1270.7	0.76	3.2
$Tb(Bp^{Me})_3$	1234.4	1235.7	1237.0	1238.5	1240.3	1242.2	1269.4	1272.2	1238.5	1270.7	0.72	2.6
Tb_2O_3	1234.1	1235.3	1236.3	1237.8	1239.2	1241.9	1269.0	1271.9	1238.2	1270.6	0.60	1.5
$Dy(Bc^{Me})_3$	1289.7	1291.9	1293.7	1294.8	1296.4	1327.3			1293.1	1328.0	0.92	11.9
$Dy(Bp^{Me})_3$	1289.6	1291.9	1293.7	1294.6	1296.5	1327.4			1293.1	1328.1	0.92	12.0
Dy_2O_3	1289.2	1291.3	1293.2	1294.2	1296.0	1327.0			1292.8	1328.0	0.85	6.2
$Ho(Bc^{Me})_3$	1343.9	1345.6	1346.6	1348.3	1350.5	1351.7	1385.6		1347.7	1385.6	0.95	18.0
$Ho(Bp^{Me})_3$	1343.9	1345.5	1346.5	1348.2	1350.3	1351.6	1385.4		1347.6	1385.4	0.95	18.6
Ho_2O_3	1344.1	1345.8	1346.8	1348.5	1350.7	1351.7	1385.8		1348.1	1385.8	0.91	10.7
$Er(Bc^{Me})_3$	1402.8	1405.2	1407.7	1409.8	1446.4				1404.8	1446.4	0.98	47.3
$Er(Bp^{Me})_3$	1402.8	1405.2	1407.7	1409.8	1446.4				1404.8	1446.4	0.98	47.2
Er_2O_3	1402.7	1405.2	1407.7	1409.3	1446.4				1404.9	1446.4	0.95	20.6

^a Centroid (eV).

^b Int.

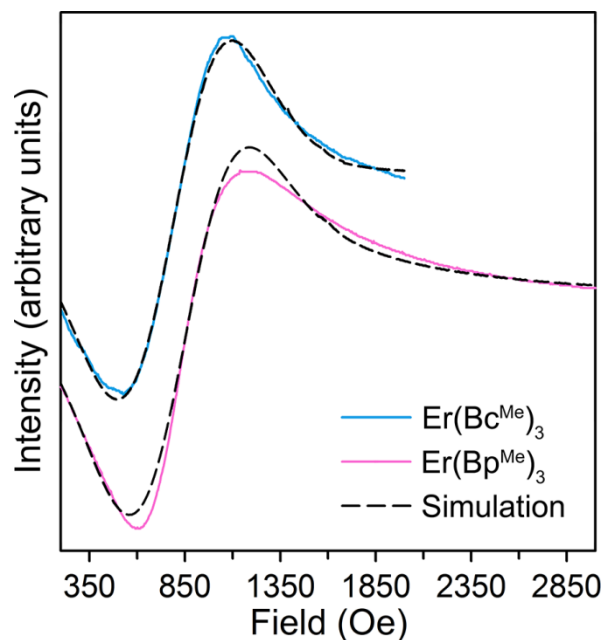


Figure 3.A49. EPR spectra for neat $\text{Er}(\text{Bc}^{\text{Me}})_3$ and $\text{Er}(\text{Bp}^{\text{Me}})_3$. For $\text{Er}(\text{Bc}^{\text{Me}})_3$, $g_{\perp} = 8.2$ and $g_{\parallel} < 0.6$; for $\text{Er}(\text{Bp}^{\text{Me}})_3$, $g_{\perp} = 8.0$ and $g_{\parallel} < 0.6$. Spectra were collected at 1.5 K with a microwave frequency of 9.21507 GHz ($\text{Er}(\text{Bc}^{\text{Me}})_3$) and 9.21588 GHz ($\text{Er}(\text{Bp}^{\text{Me}})_3$), power of 10 mW, and modulation amplitude of 4 G.

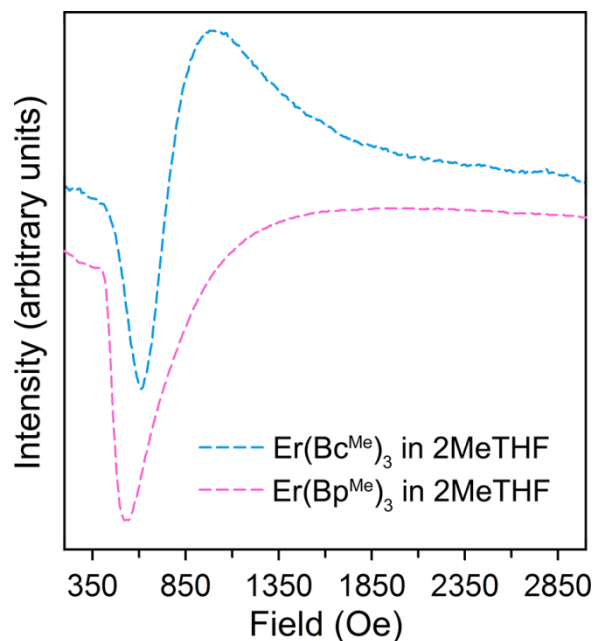


Figure 3.A50. EPR spectra for $\text{Er}(\text{Bc}^{\text{Me}})_3$ and $\text{Er}(\text{Bp}^{\text{Me}})_3$ obtained from frozen solutions in 2MeTHF (1 mM concentration). Spectra were collected at 1.9 K with a microwave frequency of 9.21565 GHz ($\text{Er}(\text{Bc}^{\text{Me}})_3$) and 9.21803 GHz ($\text{Er}(\text{Bp}^{\text{Me}})_3$), power of 10 mW, and modulation amplitude of 10 G.

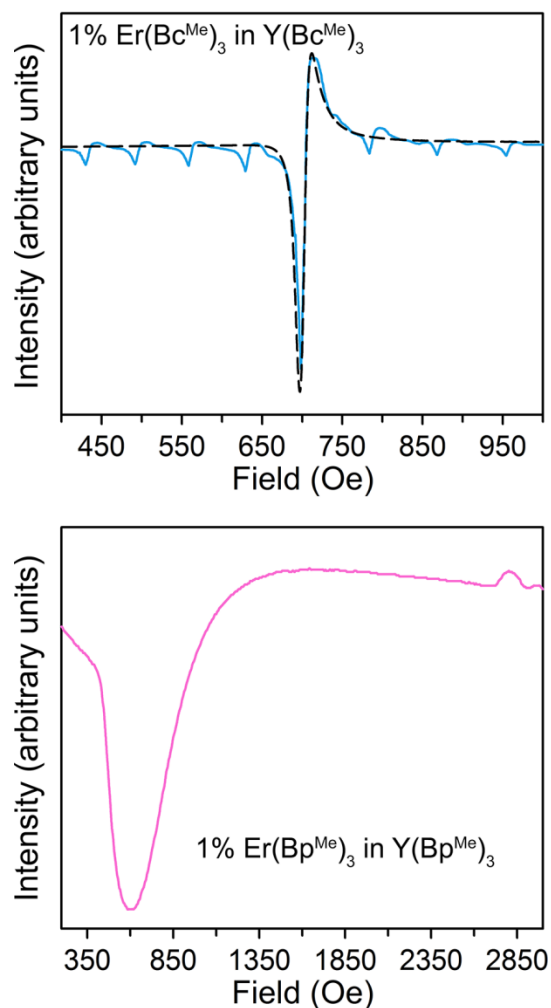


Figure 3.A51. EPR spectra for $\text{Er}(\text{Bc}^{\text{Me}})_3$ and $\text{Er}(\text{Bp}^{\text{Me}})_3$ doped into the yttrium analogues (~ 1 mol% Er in Y). For $\text{Er}(\text{Bc}^{\text{Me}})_3$, $g_{\perp} = 9.4$ and $g_{\parallel} < 0.6$. Additional lines in the $\text{Er}(\text{Bc}^{\text{Me}})_3$ spectrum are due to hyperfine coupling to Er-167 ($I = 7/2$, 23% natural abundance). Spectra were collected at 1.9 K with a microwave frequency of 9.21962 GHz ($\text{Er}(\text{Bc}^{\text{Me}})_3$) and 9.21896 GHz ($\text{Er}(\text{Bp}^{\text{Me}})_3$), power of 10 mW, and modulation amplitude of 1 G ($\text{Er}(\text{Bc}^{\text{Me}})_3$) and 10 G ($\text{Er}(\text{Bp}^{\text{Me}})_3$).

Table 3.A4. EPR results and ground state wave functions of $\text{U}(\text{Bc}^{\text{Me}})_3$ and $\text{U}(\text{Bp}^{\text{Me}})_3$.

Compound	Symmetry	Experiment		Calculated		$ \frac{5}{2}\rangle$	M_J contribution	
		g_{\parallel}	g_{\perp}	g_{\parallel}	g_{\perp}		$ \frac{7}{2}\rangle$	$ \frac{1}{2}\rangle$
$\text{U}(\text{Bc}^{\text{Me}})_3$	C_{3h}	1.03	2.57	-1.06	2.66	0.84	0.54	–
$\text{U}(\text{Bc}^{\text{Me}})_3$	C_3	1.03	2.57	-1.03	2.57	0.83	0.54	0.12
$\text{U}(\text{Bp}^{\text{Me}})_3$	C_{3h}	1.76	2.62	-1.68	2.43	0.88	0.47	–
$\text{U}(\text{Bp}^{\text{Me}})_3$	C_3	1.76	2.62	-1.68	2.43	0.88	0.47	0.00

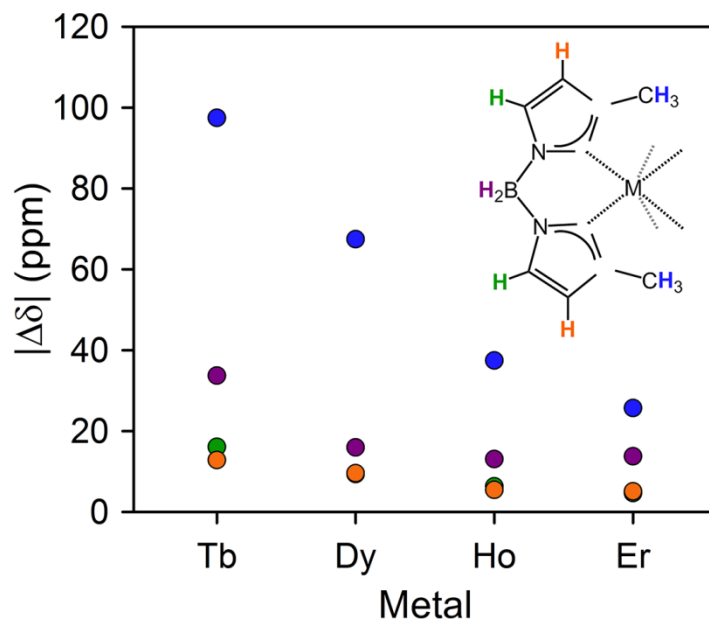


Figure 3.A52. Plot of the difference in chemical shift ($\Delta\delta$) for matching protons in $\text{Ln}(\text{Bc}^{\text{Me}})_3$ and $\text{Ln}(\text{Bp}^{\text{Me}})_3$ ($\Delta\delta$ defined as $\delta_{\text{Ln}(\text{Bc}^{\text{Me}})_3} - \delta_{\text{Ln}(\text{Bp}^{\text{Me}})_3}$). The difference is most pronounced for protons closest to the metal center, namely methyl and borate protons, and decreases in magnitude upon going from Tb^{3+} to Er^{3+} .

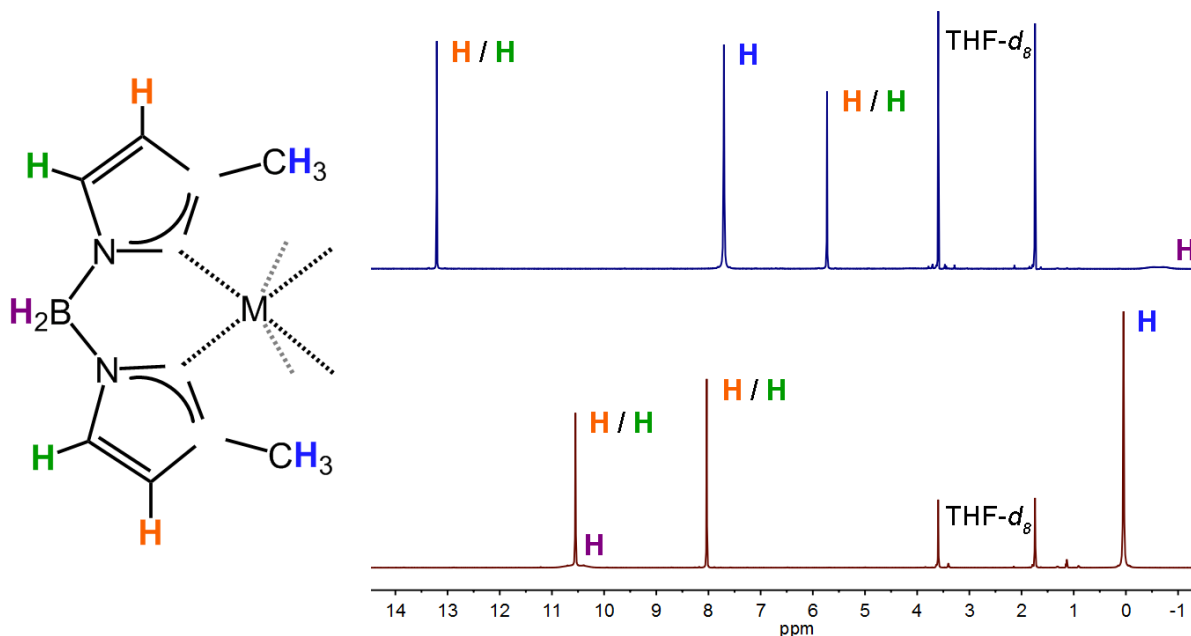
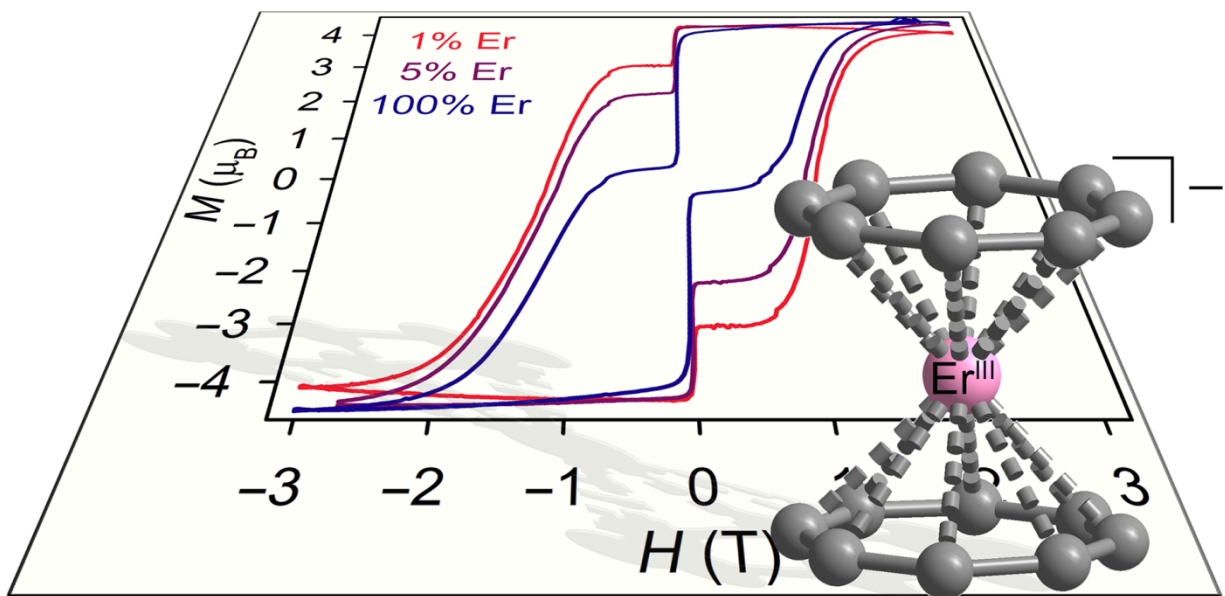


Figure 3.A53. Plot of ^1H NMR peaks in the region -1 to 14 ppm for $\text{U}(\text{Bc}^{\text{Me}})_3$ (top) and $\text{U}(\text{Bp}^{\text{Me}})_3$ (bottom). One of the two BH resonances observed for each complex are indicated with purple H labels. The other two observed resonances are shifted further down field at 31.6 ppm and 80.4 ppm, respectively.

Chapter 4: Magnetic Blocking above 9 K in Salts of the Bis(η^8 -cyclooctatetraenide) Complex $[\text{Er}(\text{COT})_2]^-$



4.1 Introduction

Recall from Chapter 1, when considering which of the trivalent lanthanides to use in the pursuit of mononuclear single-molecule magnets, those with an odd number of unpaired electrons (Kramers ions), large magnetic anisotropies, and ground states with a large J are an excellent place to start. Tb^{III} and Dy^{III} are most ubiquitous in the literature to date, a result that stems from their large anisotropies, the Kramers nature of Dy^{III} , and the utility of D_{4d} symmetry in engineering a doubly-degenerate ground state and slow relaxation for Tb^{III} .¹ The relative paucity of Er^{III} compounds, until recently, then comes as somewhat of a surprise; indeed, Er^{III} is also a Kramers ion like Dy^{III} with a $J = 15/2$ ground state and large magnetic anisotropy. However Er^{III} is among the lanthanides with a prolate electron density distribution, and thus the common ligands and symmetries employed successfully for oblate Dy^{III} and Tb^{III} will necessarily engender weaker magnetic anisotropy for the former (and vice versa).^{2,3} As discussed at some length in Chapter 1, following the discovery of slow magnetic relaxation in the molecule $\text{ErCp}^*(\text{COT})$ ($[\text{Cp}^*]^-$ = pentamethylcyclopentadienide anion), there has been renewed interest in mono- and recently multinuclear complexes of Er^{III} .^{3g,h,4} In the case of $\text{ErCp}^*(\text{COT})$, the Er^{III} center is coordinated by one η^8 -cyclooctatetraenide ligand and one η^5 -pentamethylcyclopentadienide ligand. In spite of the low symmetry (C_s) of this complex, $\text{ErCp}^*(\text{COT})$ exhibits a large relaxation barrier of $U_{\text{eff}} = 224 \text{ cm}^{-1}$ and magnetic hysteresis up to 5 K.⁵ The origin of this slow relaxation was found to derive from an Ising ground state of $M_J = 15/2$ that is well-separated from an $M_J = 13/2$ excited state, as determined by modeling dc susceptibility assuming a molecular symmetry of $C_{\infty v}$. Recently, angular-resolved magnetometry experiments have elegantly confirmed easy-axis anisotropy in $\text{ErCp}^*(\text{COT})$.⁶ From an electrostatic standpoint, the well-isolated M_J ground state can be seen to arise from the arrangement of the π -bonding molecular orbitals of the COT^{2-} and $[\text{Cp}^*]^-$ ligands, which should engender a predominance of electron density in the xy-plane of the Er^{III} (the z-axis defined as the symmetry axis of the COT^{2-} ligand), favoring stabilization of the most prolate $M_J = 15/2$ state of Er^{III} . Indeed, ab initio calculations demonstrated that in the (symmetrized) homoleptic complex $[\text{Dy}(\text{COT})_2]^-$, the ligand field is more equatorial than axial.^{3f} It was therefore of interest to characterize the analogous cyclooctatetraenide species for Er^{III} , namely $[\text{Er}(\text{COT})_2]^-$, as replacing the $[\text{Cp}^*]^-$ ligand with COT^{2-} holds the potential of enhancing symmetry, all the while maintaining the advantageous equatorial ligand field.

As described in this chapter, $[\text{Er}(\text{COT})_2]^-$ indeed exhibits thermally-activated slow magnetic relaxation under zero dc field and magnetic hysteresis. Interestingly, it was possible to isolate two different forms of the molecule depending on the crystallization conditions, namely $[\text{K}(18\text{-c-6})][\text{Er}(\text{COT})_2] \cdot 2\text{THF}$ and $[\text{K}(18\text{-c-6})(\text{THF})_2][\text{Er}(\text{COT})_2]$ with inner- and outer-sphere potassium counterions, respectively. In spite of slightly differing symmetries for the two salts, the compounds exhibit indistinguishable relaxation dynamics under ac and dc fields. Most impressive is the observation of magnetic hysteresis as high as 10 K, double the highest temperature hysteresis for $\text{ErCp}^*(\text{COT})$. While a drastic zero-field drop in the magnetization occurs for both concentrated species of $[\text{Er}(\text{COT})_2]^-$, magnetic dilution with $[\text{Y}(\text{COT})_2]^-$ leads to opening of the loop at zero field for all temperatures. Thus, $[\text{Er}(\text{COT})_2]^-$ also exhibits one of the highest blocking temperatures to date for any mononuclear single-molecule magnet.

4.2 Experimental Section

All reactions and subsequent manipulations were performed under anaerobic and anhydrous conditions in a nitrogen-atmosphere glove box. THF and hexanes were dried by passage over activated molecular sieves using a custom-built solvent system. LnCl₃ was purchased from Strem Chemicals, and cyclooctatetraene and 18-crown-6 were purchased from Sigma Aldrich. All chemicals were used as received. ¹H NMR spectra were recorded on a Bruker AV 600 spectrometer. Elemental analyses were performed by the Micro-Mass Facility at the University of California, Berkeley on a Perkin-Elmer 2400 Series II combustion analyzer. Quartz tubes used for magnetic samples were custom-made by D&G Glassblowing, Inc.

K₂COT was prepared from modification of the original method of Katz,⁷ whereupon an excess of two equivalents of potassium metal was added to a stirring solution of cyclooctatetraene in THF. Over the course of 24 hours, the pale yellow cyclooctatetraene solution took on a dark yellow-brown color, indicative of the dianion formation. After filtering off excess potassium metal, concentration of the resulting solution and storage at -34 °C resulted in formation of large transparent beige crystals of K₂COT, which were dried thoroughly under vacuum and used in subsequent reactions. K[Ln(COT)₂] (Ln = Er, Sm, Tb, Dy, Ho, Yb, Y) was prepared by modification of the literature procedure.⁸ To a stirring slurry of LnCl₃ in THF was added dropwise a chilled (-34 °C) solution of K₂COT in THF. After stirring for three hours, the reaction mixture was allowed to settle and a cloudy precipitate filtered over a layer of celite (4 cm). After removal of the solvent in vacuo, yellow (Er, Tb, Dy, Ho), brown (Sm), dark blue (Yb), and pale yellow-green (Y) powders were isolated.

K[Er(COT)₂]. ErCl₃ (221.6 mg, 0.8099 mmol) in THF (4 mL) was combined with K₂COT (295.3 mg, 1.619 mmol) in THF (4 mL) as described above. The yellow solution quickly took on a cloudy appearance. After stirring for three hours, the solution was filtered and dried to obtain 228.7 mg of bright yellow, microcrystalline K[Er(COT)₂] (68.1% yield). A proton NMR spectrum collected on this power in THF-*d*₈ exhibited a single broad peak at -88.825 ppm.

[K(18-c-6)(THF)₂][Ln(COT)₂]. Addition of one equivalent of 18-crown-6 to K[Ln(COT)₂] and subsequent recrystallization from concentrated THF resulted in the formation of [K(18-c-6)(THF)₂][Ln(COT)₂] for Y^{III}, Dy^{III}, and Sm^{III}. In the case of Er^{III}, [K(18-c-6)][Er(COT)₂]·2THF was isolated, containing an inner sphere potassium counterion (Tb^{III}, Ho^{III}, and Yb^{III} congeners were found to be isostructural). Treatment of [K(18-c-6)][Er(COT)₂]·2THF with an additional equivalent of 18-crown-6 and recrystallization from concentrated THF at -34°C resulted in isolation of [K(18-c-6)(THF)₂][Er(COT)₂]. Elemental analysis of [K(18-c-6)][Er(COT)₂]·2THF upon drying under vacuum: Calculated for ErC₂₈H₄₀O₆K (%) C: 49.53, H: 5.95; found (%) C: 49.67, H: 6.01. [K(18-c-6)(THF)₂][Er(COT)₂]: Calculated for ErC₂₈H₄₀O₆K (%) C: 49.53, H: 5.95; found (%) C: 49.53, H: 5.83.

Dilute Sample Preparation. (Er:Y) 1:20 dilution: 325.4 mg of [(18-c-6)][Y(COT)₂] was combined with 18.5 mg [(18-c-6)][Er(COT)₂] in 80 mL of THF. The resulting solution was filtered over celite (1 cm) and stored in the freezer (-34 °C). Pale neon yellow block-shaped crystals grew within 5 days. After drying for 20 minutes under vacuum, these crystals were used in magnetic sample preparation. From the overlay of temperature-dependent dc susceptibility data for this dilution and [(18-c-6)][Er(COT)₂], the measured magnetic sample was determined to contain 2.5 mg of the paramagnetic compound. This same value reproduced well the ac susceptibility and dc relaxation data. [(18-c-6)][Y(COT)₂] crystallizes in P-1, the same space group as the outer-sphere potassium species, but with a unit cell distinct from the latter and the inner-sphere compound. A unit cell obtained for the 1:20 dilution matches with that of [(18-c-

6)] $[Y(COT)_2]$, however, thus excess Y^{III} dictates the overall molecular symmetry of dilute samples.

(Er:Y) 1:85 dilution – 130.5 mg of the Y^{III} compound was combined with 1.6 mg [(18-c-6)] $[Er(COT)_2]$ in 40 mL of THF. The resulting solution was filtered over celite (1 cm) and stored in the freezer ($-34\text{ }^\circ\text{C}$). Pale neon yellow block-shaped crystals grew within 5 days. After drying for 20 minutes under vacuum, these crystals were used in magnetic sample preparation. From the overlay of temperature-dependent dc susceptibility data for this dilution and [(18-c-6)] $[Er(COT)_2]$, the measured magnetic sample was determined to contain 0.8 mg of the latter. It was found for the dc relaxation data, however, that a value of 0.7 mg better reproduced the magnetization magnitude at 1.8 K. Given that the error on the analytical balance used for sample preparation is on the order of 0.1 mg, this difference is reasonable. Additionally, use of either 0.7 or 0.8 mg in work-up of several temperatures of ac susceptibility data did not change the relaxation time τ for this sample. Based on the number of nearest neighbors determined out to 22 Å for the Y^{III} species, the inter-ion spacing for Er^{III} is $\geq 20\text{ }\text{Å}$.

Dilution *via* Precipitation: $K[Y(COT)_2]$ (64.1 mg, 0.191 mmol) of was dissolved with $K[Er(COT)_2]$ (0.9 mg, 0.02 mmol) in THF (3 mL). The resulting solution was filtered through a pipette plugged with a 1 cm^2 piece of kimwipe to remove particulates, and then added with stirring to 18-crown-6 (52.1 mg, 0.197 mmol). Within less than a minute, pale yellow crystalline powder had precipitated, however the solution still remained strongly yellow colored. After two hours of stirring, more yellow solid was present and the solution a pale yellow. The solid was allowed to settle and the THF supernatant decanted off. After rinsing with diethyl ether (3 times) the resulting pale yellow microcrystalline solid was dried under vacuum and used directly in magnetic sample preparation. Though prepared as a 1:85 (Er:Y) dilution, the resulting molar ratio was determined to be 1:70 from magnetic measurements.

Crystallography. Crystals were mounted on Kapton loops and transferred to a Bruker SMART APEX diffractometer, cooled in a nitrogen stream. The SMART program package was used to determine the unit cell parameters and for data collection (10 s/frame scan time for a hemisphere of diffraction data). Data integration was performed by SAINT and the absorption correction provided by SADABS. Subsequent calculations were carried out using the WinGX program. The structures were solved by direct methods and refined against F^2 by full-matrix least-squares techniques. The analytical scattering factors for neutral atoms were used throughout the analysis. Hydrogen atoms were included using a riding model. Full crystal data is presented for complexes all compounds except for Tb^{III} , Ho^{III} , and Yb^{III} congeners, which were found to be isostructural with ell data revealed these to be isostructural with $[K(18-c-6)] [Er(COT)_2] \cdot 2THF$. In the case of $[K(18-c-6)] [Er(COT)_2] \cdot 2THF$, one of the COT^{2-} rings is disordered over staggered and eclipsed positions, while for $[K(18-c-6)(THF)_2] [Er(COT)_2]$ and $[K(18-crown-6)] [Sm(COT)_2]$, one 18-crown-6 molecule is severely disordered. Thus, the corresponding carbon atoms were left isotropic during refinement.

Magnetic Measurements. Magnetic sample were prepared by adding crystalline powder compound to a 7 mm quartz tube with raised quartz platform. Solid eicosane was added to cover the samples to prevent crystallite torqueing and provide good thermal contact between the sample and the bath. The tubes were fitted with Teflon sealable adapters, evacuated using a glove box vacuum pump, and flame sealed under static vacuum. Following flame sealing, the solid eicosane was melted in a water bath held at $40\text{ }^\circ\text{C}$. Magnetic susceptibility measurements were collected using a Quantum Design MPMS2 SQUID magnetometer. Dc susceptibility data measurements were performed at temperatures ranging from 1.8 to 300 K, using an applied field

of 1000 Oe. Dc relaxation measurements were performed starting at fields of 5 and 1 T. The amounts of paramagnetic species present in dilute samples was determined by adjusting the mass of the paramagnetic material until the low temperature portions of the dilute dc susceptibility curves overlapped with that of the neat compound. Ac magnetic susceptibility measurements were performed using a 4 Oe switching field. All susceptibility data were corrected for diamagnetic contributions from the core diamagnetism estimated using Pascal's constants⁹ to give $\chi_D = -0.0003438$ emu/mol ($[\text{K}(18\text{-c-6})][\text{Er}(\text{COT})_2]$), -0.0003378 emu/mol ($[(18\text{-c-6})][\text{Y}(\text{COT})_2]$), -0.0003448 emu/mol ($[(18\text{-c-6})][\text{Dy}(\text{COT})_2]$), and -0.00024306 emu/mol (eicosane). Cole-Cole plots were fitted using formulae describing χ_M' and χ_M'' in terms of frequency, constant temperature susceptibility (χ_T), adiabatic susceptibility (χ_S), relaxation time (τ), and a variable representing the distribution of relaxation times (α).¹⁰ All data could be fitted to give $\alpha \leq 0.31$ in the case of $[(18\text{-c-6})][\text{Dy}(\text{COT})_2]$ and $\alpha \leq 0.09$ for both Er^{III} complexes.

4.3 Results and Discussion

The synthesis of $\text{K}[\text{Ln}(\text{COT})_2]$ was pioneered in 1973 by Streitwieser,⁸ though this work did not report the Er^{III} congener and it was over three decades before structural characterization of the first homoleptic complex $[\text{Er}(\text{COT})_2]^-$, isolated as a 1,3-diisopropylimidazolium ($[(N\text{-}^i\text{Pr})_2\text{Im}]^+$) salt.¹¹ The potassium salt of the $[\text{Er}(\text{COT})_2]^-$ complex reported here was synthesized by a modification of the published method for other lanthanides,⁸ *via* slow addition of a THF solution of K_2COT at -34 °C to a stirring slurry of ErCl_3 in THF. When combined with one equivalent of 18-crown-6, crystals of $[\text{K}(18\text{-c-6})][\text{Er}(\text{COT})_2] \cdot 2\text{THF}$ formed over the course of 3-5 days from a concentrated THF solution stored at -34 °C. X-ray analysis of a single crystal revealed a triple-decker sandwich structure, with an $[\text{Er}(\text{COT})_2]^-$ complex capped by an $[\text{K}(18\text{-crown-6})]^+$ unit (Figure 4.1, left). The inner-sphere complex crystallizes in the orthorhombic space group *Pnma*, with one of the COT^{2-} rings experiencing static disorder over eclipsed and staggered positions with respect to the other. The COT^{2-} rings are not perfectly coplanar, forming a dihedral angle of just $2.8(2)^\circ$, significantly less than the 8° dihedral angle observed in $\text{ErCp}^*(\text{COT})$.⁵ The Er–C bond lengths range from 2.575(7)-2.606(6) Å for the ordered COT^{2-} ring, similar to those reported for $[(N\text{-}^i\text{Pr})_2\text{Im}][\text{Er}(\text{COT})_2]$ though varying over a smaller range.¹¹ The Er– COT^{2-} (centroid) distances are 1.8835(3) Å and 1.8483(3) Å, identical within error to those in $[(N\text{-}^i\text{Pr})_2\text{Im}][\text{Er}(\text{COT})_2]$.¹¹

Dc magnetic susceptibility data were collected for the inner-sphere compound under an applied field of 1000 Oe over the temperature range 1.8-300 K (Figure 4.2, left). At room temperature, the value of $\chi_M T$ is 10.9 emu·K/mol, lower than that expected for a $4f^{11}$ configuration with a $J = 15/2$ ground state (11.48 emu·K/mol). The moment decreases very slightly as the temperature is lowered, until about 10 K where it drops precipitously to a final value of 0.75 emu·K/mol at 1.8 K. This sudden drop in $\chi_M T$ is indicative of magnetic blocking, where a barrier to reorientation of the magnetic moment leads to pinning of the moment along the easy axis of each molecule.

Ac magnetic susceptibility scans collected in the range 1-1500 Hz under zero applied dc field exhibit a single peak in the out-of-phase susceptibility, χ_M'' , between 15 and 27 K (see Figure 4.A1 for Cole-Cole plots). This result is in contrast to $\text{ErCp}^*(\text{COT})$, which shows two relaxation modes arising from crystallographically distinct disordered conformers.⁵ The relaxation time, τ , at each temperature was extracted by fitting the corresponding plots of χ_M' and χ_M'' using a generalized Debye model.¹⁰ A plot of the natural log of τ versus $1/T$ is linear (Figure 4.A2), suggesting that the relaxation is dominated by the thermally activated Orbach process.¹²

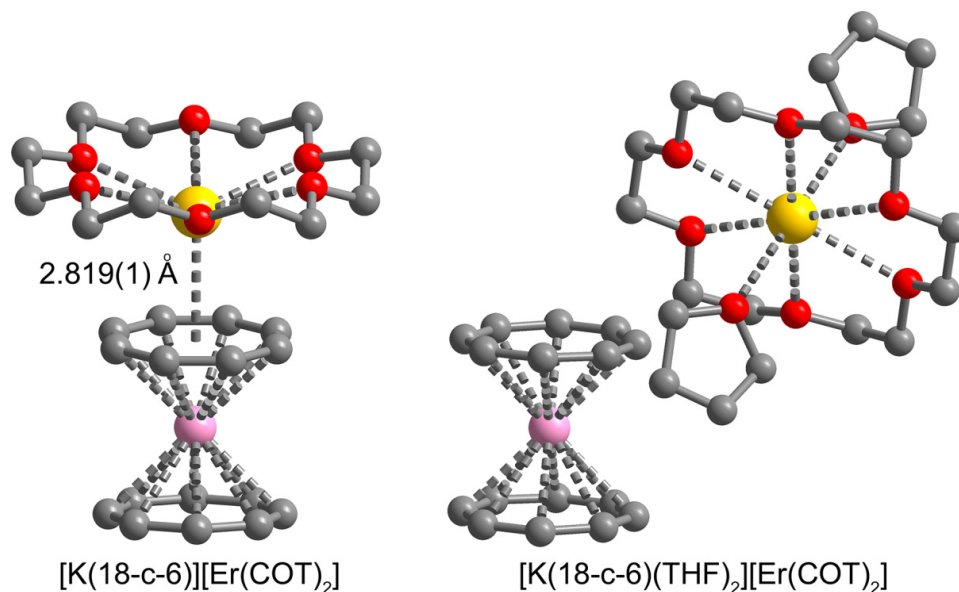


Figure 4.1. X-ray structures of inner-sphere (left) and outer-sphere (right) potassium complexes of $[\text{Er}(\text{COT})_2]^-$, with pink, yellow, grey and red spheres representing Er, K, C, and O, respectively; hydrogen atoms have been omitted for clarity. Two molecules of THF that co-crystallize with each formula unit of the inner-sphere complex are not shown. The upper COT^{2-} ring in the latter is disordered over staggered and eclipsed conformations, while the outersphere K^+ complex possesses eclipsed COT^{2-} rings with no disorder.

Additionally, for all temperatures $\alpha \leq 0.08(1)$ indicates a narrow distribution of relaxation times.¹⁰ An Arrhenius fit of the temperature-dependent relaxation time gives a barrier of $U_{\text{eff}} = 147(1) \text{ cm}^{-1}$, which falls in between the two relaxation barriers of 224.6 cm^{-1} and 137.2 cm^{-1} observed for $\text{ErCp}^*(\text{COT})$. However, a very slight curvature is apparent in the data and a $\tau_0 = 8.3(6) \times 10^{-8} \text{ s}$ suggests that the relaxation is not purely Orbach in character.¹³ The slight curvature is likely a result of small contributions from additional relaxation mechanisms, as discussed below.

Extrapolating the Arrhenius data to low temperatures, the relaxation time is 100 seconds at 10.1 K, suggesting magnetic hysteresis may be apparent below this temperature. Variable-field magnetization measurements performed up to 3 T indeed revealed a waist-restricted magnetic hysteresis loop from 1.8 to 10 K at a sweep rate of 0.78 mT/s (Figure 4.2, right). For all temperatures, the moment plummets to near zero as the field is removed, however, resulting in a coercive field of only 0.7 T at 1.8 K while at 10 K and zero field the loop is completely closed. This loss of remanence is ubiquitous among single-molecule magnets, as has been discussed already in Chapter 1.

Magnetic hysteresis does not provide a quantitative measure of the relaxation time below 15 K, though extracting relaxation times for these lower temperatures was of interest to discern relaxation mechanism(s) operative in the absence of an Orbach process. A measurement that can be performed on a conventional SQUID magnetometer to extract such low temperature relaxation times is a dc relaxation experiment. This experiment involves first heating the magnetic sample to a temperature where relaxation dynamics are fast (here, 30 K was chosen), under a large dc field (e.g. 5 T); second, the sample is cooled to the measurement temperature of interest; and finally the dc magnetic field is removed and the time decay of the magnetization is

Table 4.1. Selected distances (Å) and angles (°) for Er^{III} and Y^{III} complexes.

	[K(18-c-6)][Er(COT) ₂] ₂ ·2THF	[K(18-c-6)(THF) ₂][Er(COT) ₂]	Y ^{III}
M···M ^a	7.240(7)	7.789(2)	7.319(1)
Dihedral angle	2.8(2)	0.00(6)	1.642(1)/0.000(2)
M–COT ^{2–b}	1.87(2)	1.8744(3)	1.9102(0)/1.894(5)
M–C ^c	2.59(1)	2.62(1)	2.64(2)/2.654(7)

^a Nearest neighbor distance.

^b Average from COT^{2–} centroid to metal.

^c Average value.

recorded.¹⁰ This measurement affords the relaxation time under zero dc field. Alternatively, a variation is to track the time decay of the magnetization upon going from one magnetic field, H_1 (with associated M_1), to another field H_2 (M_2). In both cases, typically, the magnetization will decay in an exponential fashion and the M versus time elapsed can be fit to extract a relaxation time.¹⁰ Depending on the strength of the initial applied field, it can take anywhere from ~300–700 seconds on a conventional magnetometer to zero the field. For ErCp*(COT), the low-temperature relaxation time was found to be a constant between 1.8 K and 3.5 K, indicating tunneling of the magnetization.

For inner-sphere [Er(COT)₂][–], a dc relaxation experiment was initially performed using the first method described above, namely magnetizing the sample with a 5 T field at 30 K, subsequently cooling to 1.8 K, and then removing the magnetic field. Under these conditions, the time decay of the magnetization was non-exponential due to a drastic loss in M upon removal of the magnetic field (Figure 4.A3). Indeed, after ~760 seconds, the time necessary to ramp the magnetic field to zero from 5 T, the magnetization dropped to 2% of its initial value; using a weaker starting field of only 1 T resulted in the same behavior, and in as little as 262 seconds, the magnetization had again reached 2% of its initial value. This drastic loss of magnetization is perhaps unsurprising, given the evidence of rapid zero-field relaxation in the magnetic hysteresis data. A similar phenomenon was observed in dc relaxation measurements performed on the radical-bridged single-molecule magnet [{ [(Me₃Si)₂N]₂(THF)Dy }₂(μ-N₂)][–],¹⁴ and was suggested to arise from a magnetic avalanche, a phenomenon in which heat released upon spin relaxation promotes the relaxation of additional spins.¹⁵ This phenomenon has been well-studied in Mn₁₂O₁₂, though it is characterized by a sudden and complete reversal of the magnetization, interrupting slow magnetization reversal or steps in the magnetic hysteresis.¹⁶ While tunneling of the magnetization can trigger the onset of a magnetic avalanche,¹⁷ this phenomenon is typically stochastic when occurring during a conventional magnetic hysteresis sweep, unless intentionally triggered via sample heating.¹⁵ In contrast, the drop at zero field in the hysteresis for [Er(COT)₂][–] does not correspond to a complete reversal of the magnetization, and is reproducible over different sweep rates and samples. Thus, there is little evidence here to support the eruption of a magnetic avalanche for [Er(COT)₂][–]. The very rapid relaxation near zero field is then most readily ascribed to tunneling, as in the case of ErCp*(COT). In an effort to further elucidate the magnetization loss for [Er(COT)₂][–], two approaches were used. First, it is well-known that tunneling of the magnetization can be facilitated by intrinsic molecular symmetry,^{18,19} thus a second complex of [Er(COT)₂][–] was synthesized in which the anion is isolated from the potassium counterion, to determine what role, if any, symmetry plays in the drop in the hysteresis. Tunneling of the magnetization can also be mediated by dipolar interactions,¹⁸ and

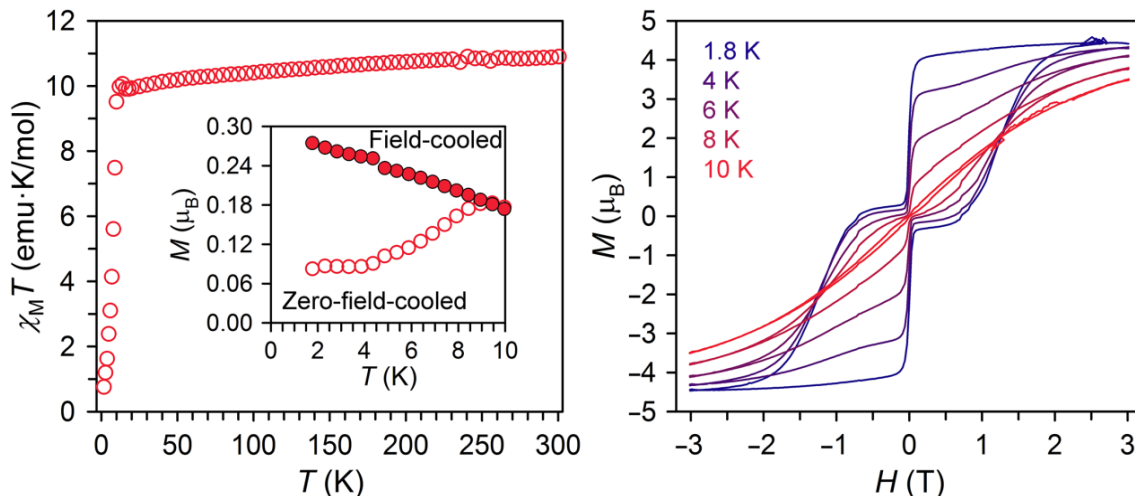


Figure 4.2. (Right) Temperature dependence of the static magnetic susceptibility times temperature ($\chi_M T$) for the inner-sphere complex under an applied field of 1000 Oe. Inset: comparison of the zero-field-cooled and field-cooled magnetization curves from 10 to 1.8 K under an applied field of 1000 Oe, showing a divergence around 9 K. (Left) Variable-field magnetization data measured at various temperatures and fields ranging from 3 to -3 T; for all temperatures but 10 K, the loop is open at zero field.

thus magnetically diluted samples of $[\text{Er}(\text{COT})_2]^-$ were prepared with the diamagnetic complex $[\text{Y}(\text{COT})_2]^-$.

The compound $[\text{K}(18\text{-c-}6)(\text{THF})_2][\text{Er}(\text{COT})_2]$ was isolated through recrystallization of $\text{K}[\text{Er}(\text{COT})_2]$ with two equivalents of 18-crown-6. Only one equivalent of the crown ether is present in the resulting structure, which crystallizes in the $P-1$ space group with an outer-sphere potassium counter-ion encapsulated by an 18-crown-6 and two THF molecules (Figure 4.1, right). Closely approaching the point group D_{8h} , the molecular symmetry of the $[\text{Er}(\text{COT})_2]^-$ anion in this outer-sphere compound is higher than in the corresponding inner-sphere species, with eclipsed COT^{2-} rings that are nearly coplanar with a dihedral angle of $0.00(6)^\circ$. As anticipated given the separation between anion and cation in the former, the nearest-neighbor $\text{Er}\cdots\text{Er}$ distance is larger than in the inner-sphere compound by more than 0.5 \AA (Table 4.1). For $[\text{K}(18\text{-c-}6)(\text{THF})_2][\text{Er}(\text{COT})_2]$, the $\text{Er}-\text{C}$ bond lengths range from $2.605(3)$ - $2.632(3) \text{ \AA}$, similar to the inner-sphere species and again close to the range previously reported for $[(N\text{-}^i\text{Pr})_2\text{Im}][\text{Er}(\text{COT})_2]$.¹¹ Even with the structural differences between $[\text{Er}(\text{COT})_2]^-$ salts reported here, a full examination of $[\text{K}(18\text{-c-}6)(\text{THF})_2][\text{Er}(\text{COT})_2]$ through static and dynamic susceptibility measurements reveals the magnetism to be essentially indistinguishable from the inner-sphere species (with the room temperature $\chi_M T$ product also agreeing for both). Importantly, this result seems to suggest that tunneling due to deviations from ideal D_{8h} symmetry is not a notable source of the hysteresis drop. Otherwise, a greater deviation in site symmetry for the inner-sphere species might be expected to promote different hysteresis behavior when compared with $[\text{K}(18\text{-c-}6)(\text{THF})_2][\text{Er}(\text{COT})_2]$.

Diluted samples of $[\text{Er}(\text{COT})_2]^-$ were prepared in Er:Y molar ratios of 1:20 and 1:85 by co-crystallization with the corresponding Y^{III} compound $[\text{K}(18\text{-c-}6)(\text{THF})_2][\text{Y}(\text{COT})_2]$ (Figure 4.A4).

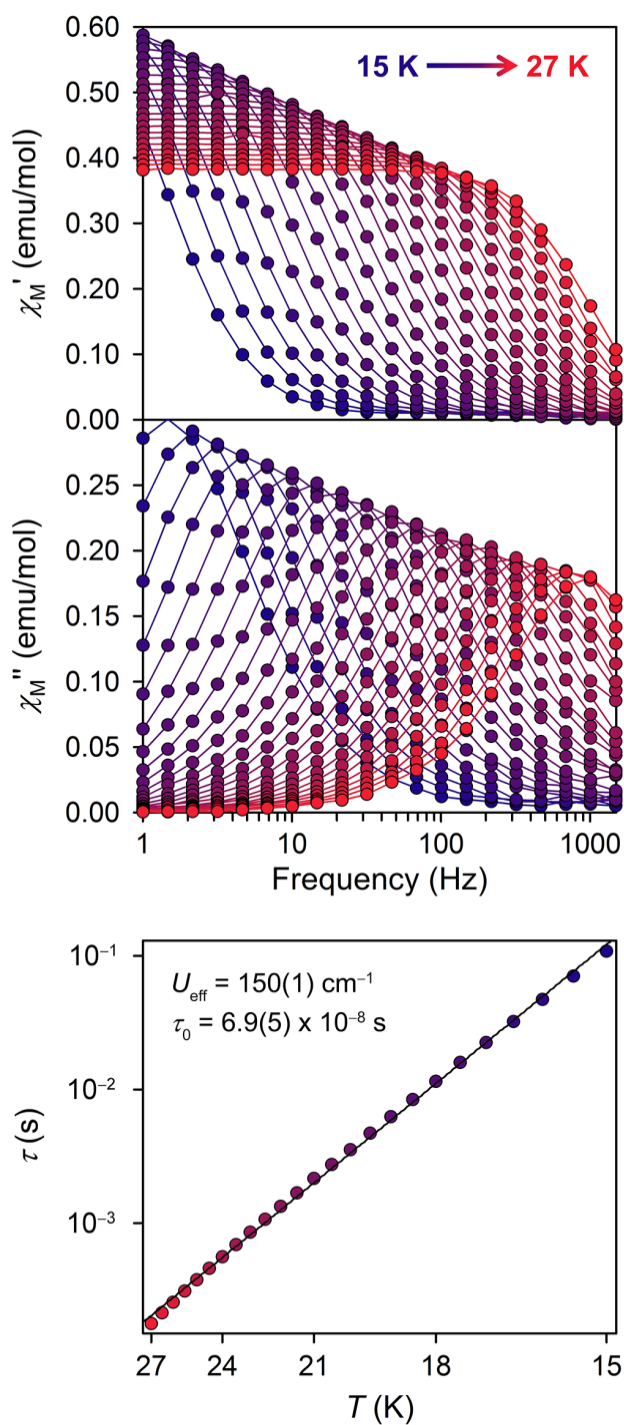


Figure 4.3. (Top) Plot of the in-phase (χ_M') and out-of-phase (χ_M'') susceptibility from 15 to 27 K for a 1:20 (Er:Y) dilution of $[\text{Er}(\text{COT})_2]^-$ under zero dc field. (Bottom) Plot of τ (log scale) versus T (inverse scale) for a 1:20 (Er:Y) dilution of $[\text{Er}(\text{COT})_2]^-$. A fit to the Arrhenius expression $\ln(\tau) = \ln(\tau_0) + U_{\text{eff}}/(k_B T)$ gives $U_{\text{eff}} = 150(1) \text{ cm}^{-1}$ and $\tau_0 = 6.9(5) \times 10^{-8} \text{ s}$.

Despite crystallization via the same route as the inner-sphere $[\text{Er}(\text{COT})_2]^-$ complex, the Y^{III} species crystallizes in the same space group as $[\text{K}(18\text{-c-6})(\text{THF})_2][\text{Er}(\text{COT})_2]$, namely P-1, while the unit cell exhibits two unique molecules. Characterization of magnetically dilute samples prepared with $[\text{K}(18\text{-c-6})(\text{THF})_2][\text{Y}(\text{COT})_2]$ reveals ac relaxation behavior nearly indistinguishable from either $[\text{Er}(\text{COT})_2]^-$ complex. This observation can be ascribed to the fact that each molecule in the unit cell for the Y^{III} complex possesses metrical parameters very close to both $[\text{Er}(\text{COT})_2]^-$ polymorphs (Table 4.1), and the ac behavior of the latter two was already shown to be insignificantly influenced by differences in symmetry. Thus, the crystallographic differences do not appear to impede an effective dilution study of the $[\text{Er}(\text{COT})_2]^-$ complex. For a 1:20 dilution, out-of-phase signal occurs over the same temperature range of 15-27 K as in the concentrated samples (Figure 4.3, upper) and the relaxation time increases only slightly from the concentrated samples at the lowest temperatures. Indeed, fitting the temperature-dependent relaxation data to an Arrhenius law yielded almost identical parameters compared with the concentrated sample, namely $U_{\text{eff}} = 150(1) \text{ cm}^{-1}$ and $\tau_0 = 6.9(5) \times 10^{-8} \text{ s}$ (Figure 4.3, lower). A notable difference is in the variable-field magnetization data for the dilute sample, for which there is no longer the same drastic loss of magnetization at zero field, and the remnant magnetization is nearly double that of the concentrated samples (Figure 4.A5). Dc magnetization relaxation data at 1.8 K still exhibit a sharp drop after removal of the field (Figure 4.A6), although the decline in magnetization with time is more gradual than in the concentrated sample, which could be attributed to diminished tunneling of the magnetization.

Relaxation times obtained for a 1:85 dilution of $[\text{Er}(\text{COT})_2]^-$ are, within error, the same as those of the 1:20 dilution, although variable-field magnetization data reveal an even further increase in the remnant magnetization (Figure 4.4, left). Indeed, at 1.8 K, the remnant magnetization and coercive field are $3.53 \mu_{\text{B}}$ and 1.1 T, respectively, and open hysteresis is now observed up to 10 K. The blocking temperature of a single-molecule magnet can be defined either as the maximum temperature for which hysteresis is open at zero applied field (assuming a conventional sweep rate) or the temperature at which the relaxation time is 100 s.^{2,10} Estimated in this fashion, both hysteresis measurements and extrapolation of the relaxation times measured by ac susceptibility result in a blocking temperature of 10 K. Even still, at this dilution a small drop in the magnetization close to zero field is observed for all temperatures.²⁰

Dc relaxation measurements were again performed by magnetizing the sample ($H_0 = 3 \text{ T}$) and then zeroing the field, for temperatures $\geq 6 \text{ K}$. For this highest dilution, the sample exhibits a much more gradual magnetization decay relative to the concentrated samples (as high as 9 K), allowing for fitting of the magnetization to extract relaxation times. Notably, it was still not possible to obtain satisfactory fits assuming a simple exponential decay of τ ($M(t) = M_0 \cdot \exp(-t/\tau)$), though excellent fits were obtained using an expression for a stretched exponential decay, given by Equation 4.1, known as the Kohlrausch function,²¹ where $0 < \beta < 1$ (Figures 4.4, right, and 4.A8).¹⁰

$$M(t) = M_0 \cdot \exp[-(t/\tau)^\beta] \quad (4.1)$$

Originally introduced by Rudolf Kohlrausch to describe the relaxation of charges in a Leiden jar,²² the stretched exponential function has been found to be useful in discussing relaxation of the magnetization in single-domain particles²³ and Nd-Fe-B thin films,²⁴ spin relaxation in organic superconductors,²⁵ and commonly spin glasses¹⁰ or spin ices²⁶ as well as a host of other systems.²⁷ A previous theoretical paper investigating physical meaning for the β parameter has

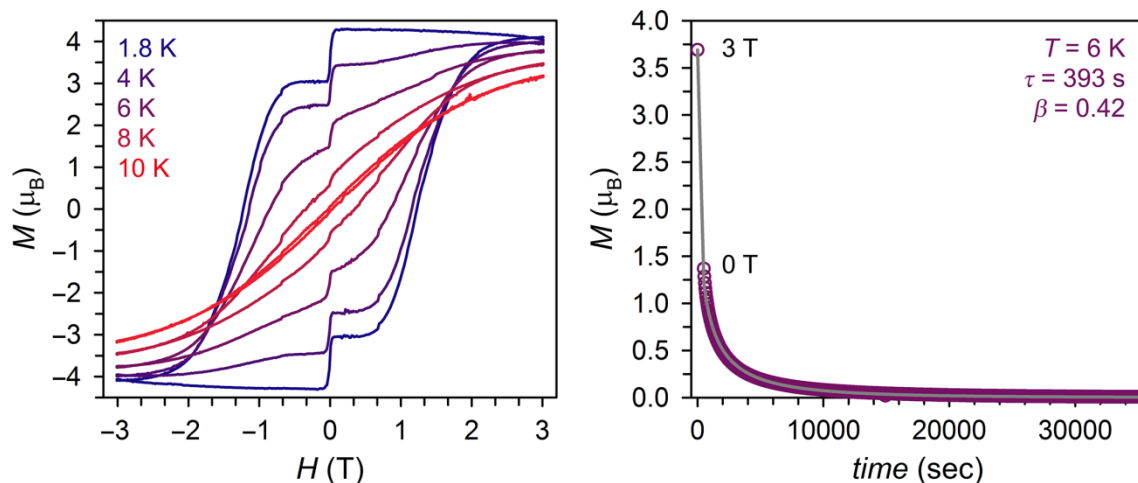


Figure 4.4. (Left) Variable-field magnetization for the 1:85 dilution of $[\text{Er}(\text{COT})_2]^-$, collected at a sweep rate of 0.78 mT/s. (Right) Dc relaxation curve for the 1:85 dilution with $H_0 = 3$ T (purple circles) along with a fit to the stretched exponential function given in Equation 4.1 (gray line). The time between the first and second magnetization points is $t = 8.36$ s.

also pointed out that a sum of discrete exponentials may fit a decay curve equally well when compared with a stretched exponential curve, and care must be taken when using the latter to fit data.²⁸ It must be acknowledged that in the absence of any further experiment or theory, in the case of $[\text{Er}(\text{COT})_2]^-$ this fit is necessarily phenomenological; however, a distribution of relaxation times²⁵ or energy barrier heights²⁴ have previously been invoked to rationalize the stretched exponential nature of the relaxation, and indeed a sum of exponential decay curves would also suggest a distribution of relaxation times.²⁹ A final interesting paper investigating nuclear spin-lattice relaxation in carbon nanomaterials has demonstrated that observed stretched exponential decay can be correlated with interactions between nuclear spins and paramagnetic defects, facilitating nuclear spin relaxation.³⁰ While an imperfect analogue to the system described here, it is interesting to consider how the non-zero ^{167}Er nuclear spin ($I = 7/2$, $\sim 23\%$ abundant) may play a role in the low-temperature relaxation dynamics, facilitating inhomogeneous relaxation of the electron spins.

With the relaxation times extracted from the stretched exponential fit, it was possible to extend the Arrhenius plot for $[\text{Er}(\text{COT})_2]^-$ to temperatures below 15 K (Figure 4.A9). Again, defining the blocking temperature as the value corresponding to $\tau = 100$ s, from the dc data a blocking temperature of ~ 9.25 K could be deduced for $[\text{Er}(\text{COT})_2]^-$. This value is lower than that estimated from both hysteresis and ac measurements, and highlights the importance of adopting a uniform definition for the blocking temperature. Even still, significantly this represents one of the highest blocking temperatures yet measured for a mononuclear single-molecule magnet.^{5,31}

Even with the drastic opening of the hysteresis loop for the 1:85 dilution, the remaining drop reveals that not all of the fast relaxation at zero field has been quenched. Given the large separation between magnetic ions (on average ~ 20 Å or more³²), it is unlikely that dipolar interactions are implicit in the remaining tunneling drop. It is interesting then to return to the possible role of the ^{167}Er nuclear spin in facilitating quantum tunneling. As introduced in Chapter 1 (see in particular Section 1.2 and Ref. 30), while hyperfine interactions have long been known to play a role in tunneling,¹⁰ the first experimental verification of this for a mononuclear lanthanide system exhibiting magnetic hysteresis was accomplished only recently for

[Dy(tta)₃(L)]·C₆H₁₄ (tta⁻ = 2-thenoyltrifluoroacetate, L = 4,5-bis(propylthio)-tetrathiafulvaene-2-(2-pyridal)-benzimidazole methyl-2-pyridine).³³ A combination of magnetic dilution (via solution measurements) and complete isotopic enrichment of [Dy(tta)₃(L)] with ¹⁶¹Dy ($I = 5/2$) or ¹⁶⁴Dy ($I = 0$) revealed that the presence of Dy nuclear spin enhances tunneling near zero field. Thus, enrichment of a sample of [Er(COT)₂]⁻ with any of the five additional isotopes with $I = 0$ would serve as a further fundamental inquiry into the source of the magnetization drop and the unique way in which it is mitigated by magnetic dilution.

To gain insight into the specificity of the COT²⁻ ligand field for Er^{III}, the magnetic behavior of the compounds [K(18-c-6)][Ln(COT)₂] for Ln = Sm, Yb, Tb, Dy (Figure 4.A10) and Ho were also investigated.⁸ Out of these, the Kramers ions Sm^{III} and Yb^{III} exhibit the greatest prolate character in their maximal M_J states, and thus are potential candidates for exhibiting slow magnetic relaxation in this equatorial ligand field. As non-Kramers ions, Tb^{III} and Ho^{III} are least likely to show zero-field slow relaxation, particularly in this ligand field, due to maximal M_J states that are largely oblate in character (recall Chapter 1, Section 1.4).² Interestingly, magnetic measurements performed on all of the compounds revealed zero-field slow relaxation only for the Dy^{III} analogue, at low temperatures with weak thermal dependence, while a relaxation barrier of $U_{\text{eff}} = 9(1) \text{ cm}^{-1}$ was extracted by fitting the four highest temperature points in a plot of $\ln(\tau)$ versus $1/T$ (Figure 4.A11). Although dipolar interactions are likely involved in speeding up the relaxation for this complex, the COT²⁻ ligand field does not engender strong uniaxial magnetic anisotropy as for [Er(COT)₂]⁻, and in fact the equatorial ligand field would be anticipated to stabilize a non-maximal M_J ground state of more prolate character for Dy^{III}. Indeed, a subsequent study on homoleptic lanthanide bis(cyclooctatetraenide) complexes included ab initio calculations, which determined the ground state of the Dy^{III} molecule is predominantly $M_J = 9/2$, separated by $\sim 20 \text{ cm}^{-1}$ from the first excited $M_J = 11/2$.^{3h,34} The observation of $U_{\text{eff}} = 9 \text{ cm}^{-1}$ at high temperatures and the near temperature independence below 3.2 K suggests then that the relaxation is preferentially occurring via Raman and tunneling and/or Direct mechanisms.

4.4 Conclusions and Outlook

In summary, the homoleptic Er^{III} sandwich complex in [K(18-c-6)][Er(COT)₂]-2THF and [K(18-c-6)(THF)₂][Er(COT)₂] exhibits slow magnetic relaxation under zero field, much like its heteroleptic predecessor ErCp*(COT),⁵ supporting the rationale that the equatorial COT²⁻ ligand field preferentially stabilizes the prolate $M_J = 15/2$ state of Er^{III}. [Er(COT)₂]⁻ demonstrates a single ac feature dominated by thermal relaxation at high temperatures, in contrast to the two ac peaks exhibited by ErCp*(COT), and this data is reminiscent of more recent studies on mononuclear Er^{III} systems.^{3g,h} At low temperatures the relaxation is heavily influenced by dipolar interactions that facilitate zero-field tunneling as evidenced by dc relaxation and variable-field magnetization measurements. This result serves as a reminder that the multifaceted role of dipolar interactions in modifying slow relaxation is still being established, as demonstrated for U^{III} in Chapter 2. Simply through magnetic dilution of [Er(COT)₂]⁻, the drop in magnetic hysteresis was significantly reduced, opening the loop at zero field as high as 10 K. Magnetic dilution also enabled fitting of dc relaxation data to extract the most reliable blocking temperature of 9.25 K. Er^{III} thus holds tremendous promise for the design of new single-molecule magnets with even higher blocking temperatures, through the development of stronger equatorial ligand fields than imposed here by two COT²⁻ ligands. As the development of this area continues, both dilution

and isotopic enrichment studies may be essential to better understanding low-temperature relaxation.

4.5 Acknowledgements

The NSF Graduate Fellowship Program is acknowledged for support of K.R.M, Dr. Antonio DiPasquale for assistance with crystal structure determination, and McDonald's Corporation for the drinking straws employed in magnetic sample loading.

4.6 References

- (1) Woodruff, D. N.; Winpenny, R. E. P.; Layfield, R. A. *Chem. Rev.* **2013**, *113*, 5110.
- (2) Rinehart, J. D.; Long, J. R. *Chem. Sci.* **2011**, *2*, 2078.
- (3) (a) Ishikawa, N.; Sugita, M.; Ishikawa, T.; Koshihara, S.-y.; Kaizu, Y. *J. Am. Chem. Soc.* **2003**, *125*, 8694. (b) Ishikawa, N.; Sugita, M.; Okubo, T.; Iino, T.; Kaizu, Y. *Inorg. Chem.* **2003**, *42*, 2440. (c) Ishikawa, N.; Sugita, M.; Ishikawa, T.; Koshihara, S.-y.; Kaizu, Y. *J. Phys. Chem. B* **2004**, *108*, 11265. (d) AlDamen, M. A.; Clemente-Juan, J. M.; Coronado, E.; Martí-Gastaldo, C.; Gaita-Ariño, A. *J. Am. Chem. Soc.* **2008**, *130*, 8874. (e) AlDamen, M. A.; Cardona-Serra, S.; Clemente-Juan, J. M.; Coronado, E.; Gaita-Ariño, A.; Martí-Gastaldo, C.; Luis, F.; Montero, O. *Inorg. Chem.* **2009**, *48*, 3467. (f) Le Roy, J. J.; Jeletic, M.; Gorelsky, S. I.; Korobkov, I.; Ungur, L.; Chibotaru, L. F.; Murugesu, M. *J. Am. Chem. Soc.* **2013**, *135*, 3502. (g) Le Roy, J. J.; Korobkov, I.; Murugesu, M. *Chem. Commun.* **2014**, *50*, 1602. (h) Ungur, L.; Le Roy, J. J.; Korobkov, I.; Murugesu, M.; Chibotaru, L.F. *Angew. Chem. Int. Ed.* **2014**, *53*, 4413.
- (4) Le Roy, J. J.; Ungur, L.; Korobkov, I.; Chibotaru, L.F.; Murugesu, M. *J. Am. Chem. Soc.* **2014**, *136*, 8003.
- (5) Jiang, S.-D.; Wang, B.-W.; Sun, H.-L.; Wang, Z.-M.; Gao, S. *J. Am. Chem. Soc.* **2011**, *133*, 4730.
- (6) Boulon, M.-E.; Cucinotta, G.; Liu, S.-S.; Jiang, S.-D.; Ungur, L.; Chibotaru, L. F.; Gao, S.; Sessoli, R. *Chem. Eur. J.* **2013**, *19*, 13726.
- (7) Katz, T.J. *J. Am. Chem. Soc.* **1960**, *82*, 3784.
- (8) Hodgson, K. O.; Mares, F.; Starks, D. F. Streitwieser, Jr., A. *J. Am. Chem. Soc.* **1973**, *95*, 8560.
- (9) Bain, G. A. and Berry, J. F. *J. Chem. Ed.* **2008**, *85*, 532.
- (10) D. Gatteschi, R. Sessoli, J. Villain, *Molecular Nanomagnets*, Oxford University Press, Oxford, **2006**.
- (11) Jones, P. G.; Hrib, C. G.; Panda, T. K.; Tamm, M. *Acta Cryst.E.* **2007**, *63*, m2059.
- (12) Orbach, R. *Proc. R. Soc. Lond. A* **1961**, *264*, 458.
- (13) Attempts to fit the entire temperature regime by accounting for a contribution from Raman relaxation led to a poorer fit than obtained assuming pure Arrhenius behavior.
- (14) Rinehart, J. D.; Fang, M.; Evans, W. J.; Long, J. R. *Nat. Chem.* **2011**, *3*, 538.
- (15) McHugh, S.; Sarachik, M. P. *Mod.Phys. Lett. B* **2011**, *25*, 1795.
- (16) Sarachik, M. Magnetic Avalanches in Molecular Magnets. In *Molecular Magnets: Physics and Applications*; Bartolomé, J.; Luis, F.; Fernández, J. F., Eds. Springer: New York, 2014 and references therein.

- (17) Suzuki, Y. Magnetic Avalanches in Mn12-acetate, “Magnetic Deflagration.” Ph.D. Thesis, City University of New York, New York, NY, 2007.
- (18) Gatteschi, D.; Sessoli, R. *Angew. Chem. Int. Ed.* **2003**, *42*, 268.
- (19) Ungur, L.; Chibotaru, L. F. *Phys. Chem. Chem. Phys.* **2011**, *13*, 20086.
- (20) To exclude the possibility that this drop occurs due to inefficient isolation of paramagnetic centers during slow crystallization, we prepared a dilute sample by rapid precipitation (see Appendix). Magnetic hysteresis measurements on this sample display a magnetization loss similar to the 1:85 dilution sample (Figure 4.A7).
- (21) Kohlrausch, R. *Pogg. Ann. Phys. Chem.* **1854**, *91*, 179.
- (22) A Leiden (or Leyden) jar was the earliest form of a capacitor.
- (23) Klik, I.; Yao, Y. D. *J. Magn. Magn. Mater.* **2000**, *209*, 25.
- (24) Yao, Q.; Grössinger, R.; Liu, W.; Cui, W. B.; Yang, F.; Zhao, X. G.; Zhang, Z. D. *J. Magn. Magn. Mater.* **2012**, *324*, 2854.
- (25) Gezo, J.; Lui, T.-K.; Wolin, B.; Slichter, C. P.; Giannetta, R. *Phys. Rev. B* **2013**, *88*, 140504.
- (26) Revell, H. M.; Yaraskavitch, L. R.; Mason, J. D.; Ross, K. A.; Noad, H. M. L.; Dabkowska, H. A.; Gaulin, B. D.; Henelius, P.; Kycia, J. B. *Nature Phys.* **2012**, *9*, 34.
- (27) This is by no means intended to be a comprehensive list of the sundry systems investigated in conjunction with stretched exponential relaxation behavior, but is rather a sampling. The author was new to this topic until very recently, and finds it interesting. While use of the stretched exponential in this work can hardly represent anything more than a phenomenological description of the relaxation of the $[\text{Er}(\text{COT})_2]^-$, it is the hope that some well-trained eyes may examine this information and have their curiosity piqued to investigate the physics of this system further. See Phillips, J. C. *Rep. Prog. Phys.* **1996**, *59*, 1133 for a nice discussion of the stretched exponential in systems such as spin glasses, polymers, and supercooled liquids. This reference also seeks to provide a more concrete description of the β parameter.
- (28) Johnston, D. C. *Phys. Rev. B* **2006**, *74*, 184430.
- (29) Attempts to fit the 6 K data, for instance, using a sum of exponentials (two or three) led to somewhat unrealistic values for the highest values of τ , in excess of 1000 s. The stretched exponential also more accurately estimates τ near the estimated blocking temperature from hysteresis and ac measurements.
- (30) Panich, A. M.; Furman, G. B. *Diamond Relat. Mater.* **2012**, *23*, 157.
- (31) The single-molecule magnet $[\text{Zn}_2\text{DyL}_2(\text{MeOH})]^+$ (see Liu, J.-L.; Chen, Y.-C.; Zheng, Y.-Z.; Lin, W.-Q.; Ungur, L.; Wernsdorfer, W.; Chibotaru, L. F.; Tong, M.-L. *Chem. Sci.* **2013**, *4*, 3310; L = 2,2',2''-(((nitrilotris(ethane-2,1-diyl))tris(azanediy))tris(methylene))tris-(4-bromophenol) was reported to show waist-restricted magnetic hysteresis to 11 K, which would represent the current record for a mononuclear lanthanide complex. Though, the loop is closed at zero field and the data was collected at a sweep rate nearly two orders of magnitude faster than that reported here (0.78 versus 20 mT/s) and the 0.92 mT/s and 0.53 mT/s sweep rates reported for $\text{ErCp}^*(\text{COT})$. Thus, it is not possible to say whether the temperature corresponding to 100 s relaxation for this Dy^{III} compound would out-compete $[\text{Er}(\text{COT})_2]^-$. However,

these compounds represent the most successful in the literature based on highest hysteresis temperature for any mononuclear compound.

- (32) As estimated from the number of nearest neighbors for the Y^{III} complex.
- (33) Pointillart, F.; Bernot, K.; Golhen, S.; Le Guennic, B.; Guizouarn, T.; Ouahab, L.; Cador, O. *Angew. Chem. Int. Ed.* **2015**, *54*, 1504.
- (34) Interestingly, the shape of the electron density for the $M_J = 9/2$ state for Dy^{III} closely resembles the maximal $M_J = 15/2$ state for Er^{III}, see Ref. 2.

Chapter 4 Appendix

Table 4.A1. Crystal data and structure refinement for Chapter 4, designated by anion.

	[Er(COT) ₂] ⁻ innersphere	[Er(COT) ₂] ⁻ outersphere	[Y(COT) ₂] ⁻	[Dy(COT) ₂] ⁻	[Sm(COT) ₂] ⁻
Empirical formula	C ₃₆ H ₅₆ ErKO ₈	C ₃₆ H ₅₆ ErKO ₈	C ₂₇ H ₄₂ K _{0.75} O ₆ Y _{0.75}	C ₂₇ H ₄₂ Dy _{0.75} K _{0.75} O ₆	C ₂₇ H _{42.25} K _{0.75} O ₆ Sm _{0.75}
Formula weight	823.17	823.19	558.61	613.81	604.97
Temperature (K)	238(2)	239(2)	100(2)	238(2)	100(2)
Wavelength (Å)	0.71073	0.71073	0.71073	0.71073	0.71073
Crystal system	Orthorhombic	Triclinic	Triclinic	Triclinic	Triclinic
Space group	<i>Pnma</i>	<i>P</i> -1	<i>P</i> -1	<i>P</i> -1	<i>P</i> -1
<i>a</i> (Å)	20.002(3)	7.789 (2)	13.0729(4)	13.271(3)	13.162(2)
<i>b</i> (Å)	11.449(2)	9.337 (2)	15.5542(5)	15.830(3)	15.616(3)
<i>c</i> (Å)	16.359(2)	13.184(3)	15.7380(5)	15.868(3)	15.635(3)
α (°)	90	84.992(3)	72.594(1)	72.624(3)	72.467(3)
β (°)	90	83.644(3)	77.347(1)	66.105(3)	67.322(2)
γ (°)	90	89.270(3)	67.149(1)	76.991(3)	78.121(3)
Volume (Å ³)	3746.1(9)	949.4(3)	2794.6(2)	2888.2(1)	2812.7(8)
<i>Z</i>	4	1	4	4	4
ρ_{calcd} (mg/m ³)	1.460	1.440	1.328	1.412	1.429
μ (mm ⁻¹)	2.398	2.366	1.724	2.094	1.724
F(000)	1692	423	1182	1263	1252
Theta range (°)	1.61- 25.41	1.56-25.37	1.46-25.35	1.44-25.38	1.37-25.33
Reflections	41609	15108	46288	45686	33780
Independent reflections	3630 [R(int) = 0.0347]	3478 [R(int) = 0.0188]	10148 [R(int) = 0.0217]	10556 [R(int) = 0.0231]	10111 [R(int) = 0.0337]
Final R indices [I>2 σ (I)]	R1 = 0.0331 wR2 = 0.0794	R1 = 0.0177 wR2 = 0.0455	R1 = 0.0764 wR2 = 0.2080	R1 = 0.0287 wR2 = 0.0736	R1 = 0.0513 wR2 = 0.1310
R indices (all data)	R1 = 0.0385 wR2 = 0.0840	R1 = 0.0178 wR2 = 0.0455	R1 = 0.0819 wR2 = 0.2139	R1 = 0.0324 wR2 = 0.0770	R1 = 0.0632 wR2 = 0.1433

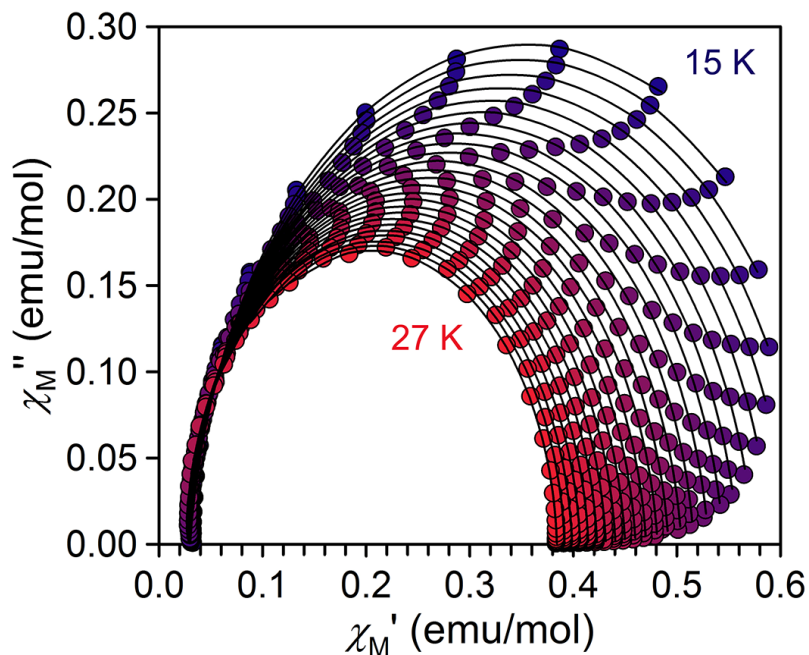


Figure 4.A1. Cole-Cole plots for [K(18-c-6)][Er(COT)₂] under zero dc field and varying temperatures. Experimental data points are represented by colored circles and the points representing the fit are connected by a solid black line.

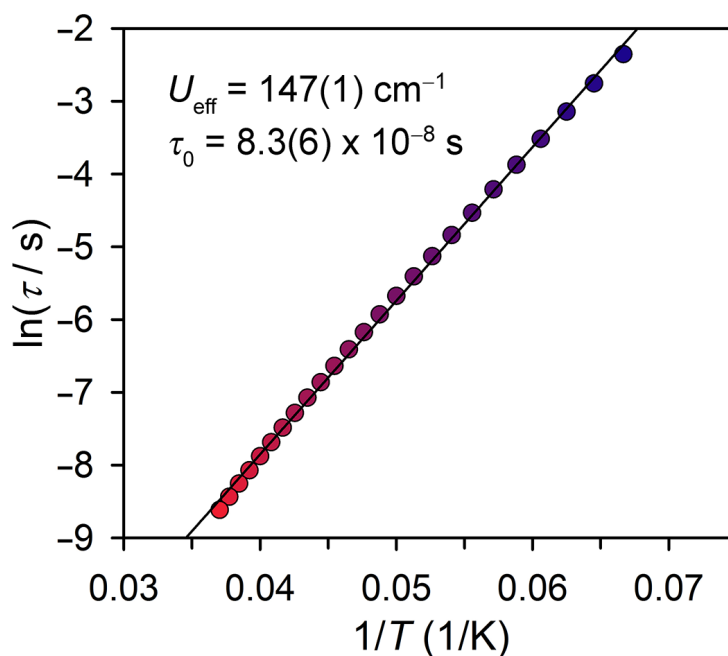


Figure 4.A2. Plot of the natural log of the relaxation time, $\ln(\tau)$, versus $1/T$ for [K(18-c-6)][Er(COT)₂] under zero applied dc field.

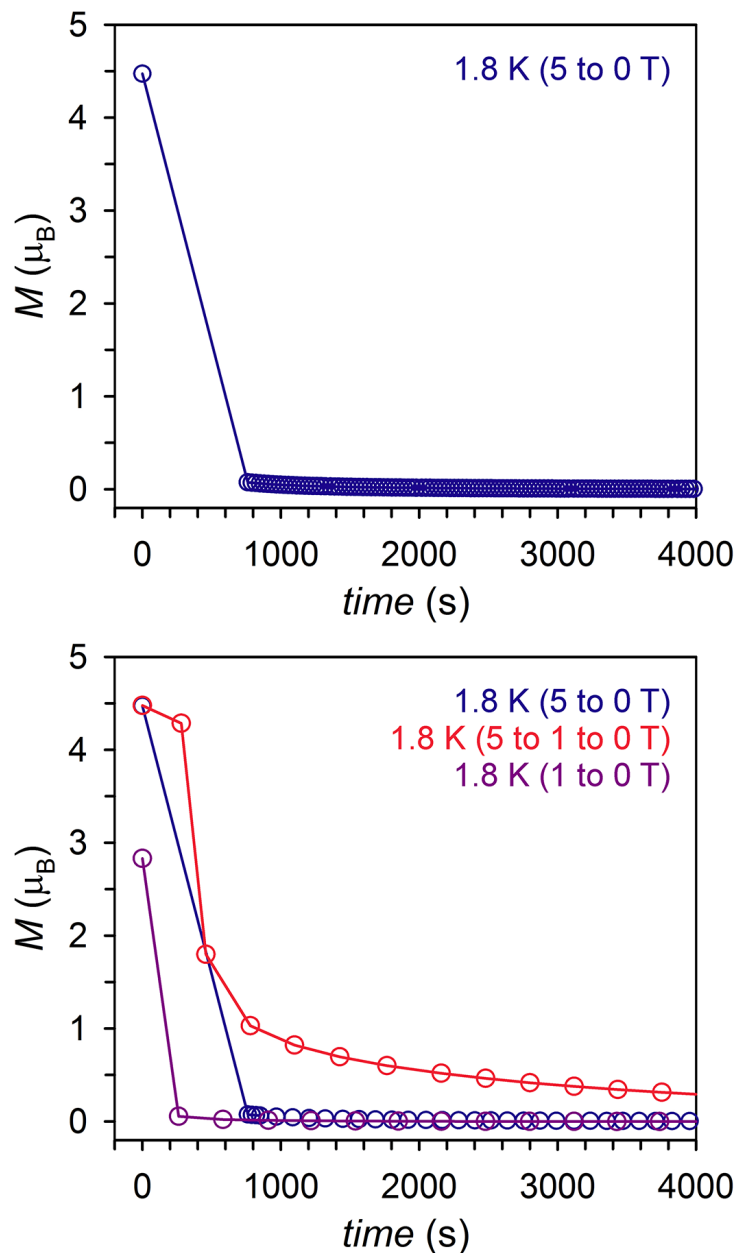


Figure 4.A3. (Top) Decay of the magnetization versus time for $[\text{K}(18\text{-c-6})][\text{Er}(\text{COT})_2]$, obtained by applying a magnetic field of 5 T to the sample at a temperature of 30 K, cooling the sample to 1.8 K, and then removing the magnetic field, which takes 12.7 min. (Bottom) Comparison of the time decay of the magnetization for different fields. By changing the field from $5 \rightarrow 1 \rightarrow 0$ T, the decay begins to look more exponential with longer times (pink circles), however a discontinuity still occurs (1 T and $t = 4.7$ min). Starting from a field of 1 T (purple circles) reveals an even sharper discontinuity at $t = 4.4$ min.

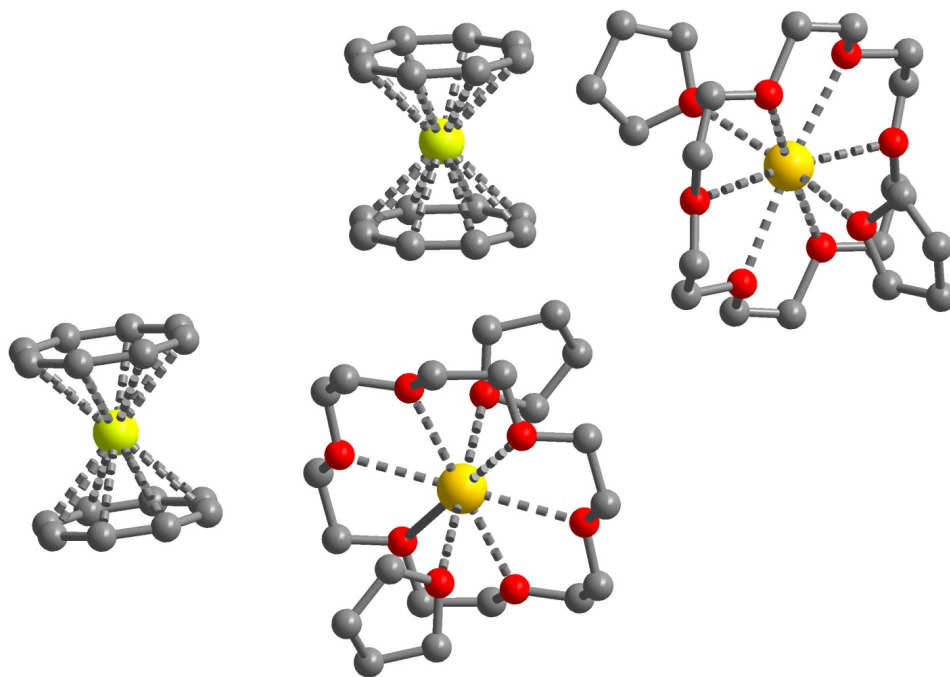


Figure 4.A4. X-ray structure of [K(18-c-6)(THF)₂][Y(COT)₂]. Hydrogen atoms are omitted for clarity; yellow-green, yellow, grey and red spheres represent Y, K, C, and O, respectively.

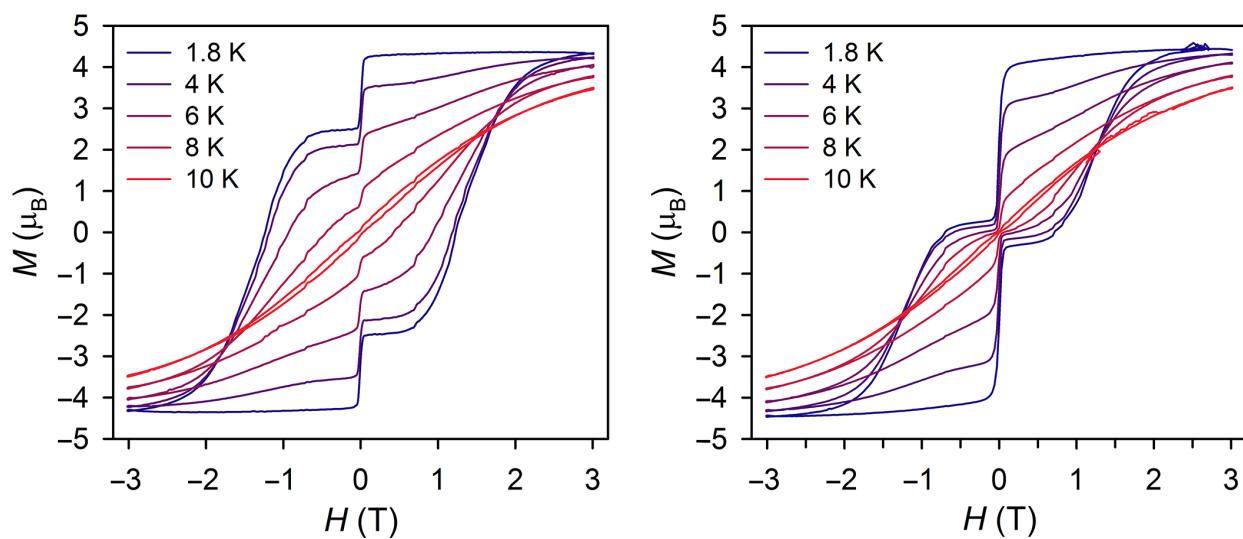


Figure 4.A5. Comparison of variable field magnetization for a 1:20 (Er:Y) dilution (left) and compound [Er(COT)₂]⁻ (right) at the indicated temperatures.

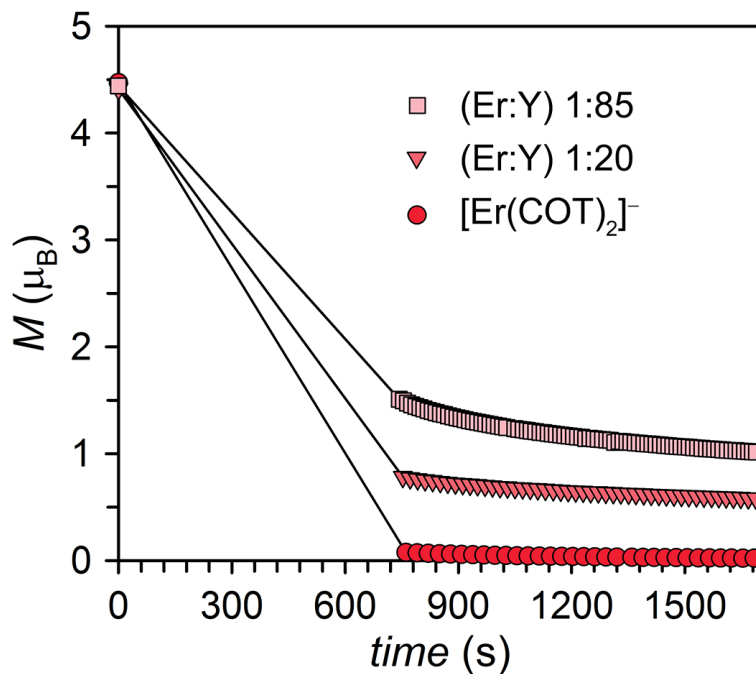


Figure 4.A6. Decay of the magnetization versus time for concentrated and dilute samples of $[\text{Er}(\text{COT})_2]^-$. Data was obtained by applying a magnetic field of 5 T to each sample at 30 K, cooling to 1.8 K, and then zeroing the field.

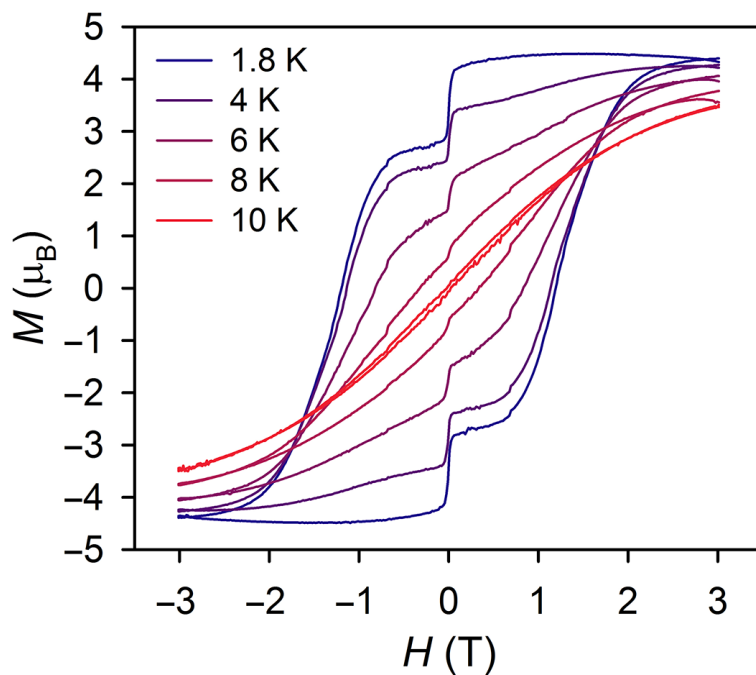


Figure 4.A7. Variable field magnetization for the 1:70 (Er:Y) precipitated dilution sample, collected at the indicated temperatures.

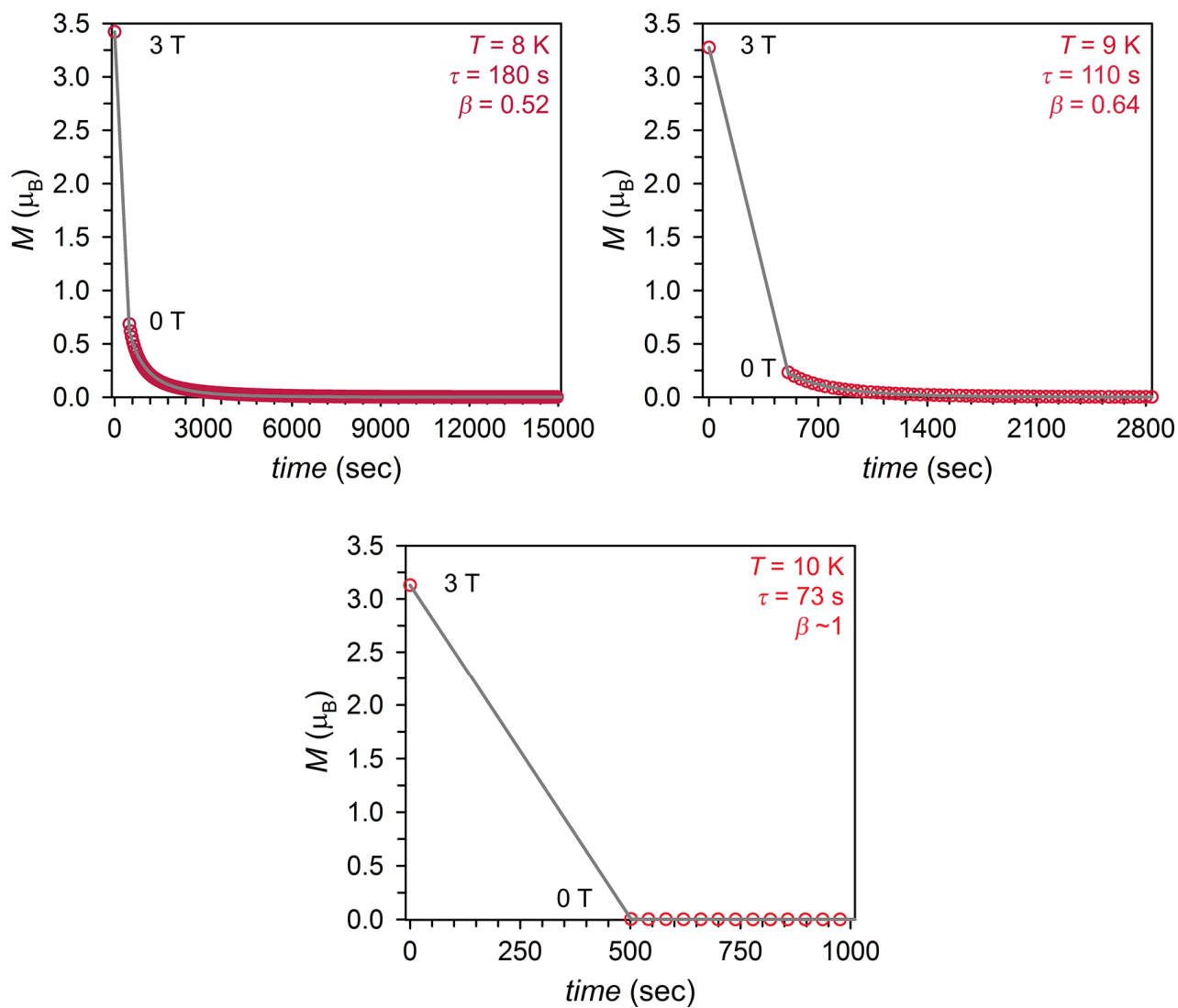


Figure 4.A8. Dc relaxation curves for the 1:85 dilution of $[\text{Er}(\text{COT})_2]^-$ at various temperatures with $H_0 = 3 \text{ T}$ (colored circles) and fits to the stretched exponential function given in Equation 4.1 (gray lines).

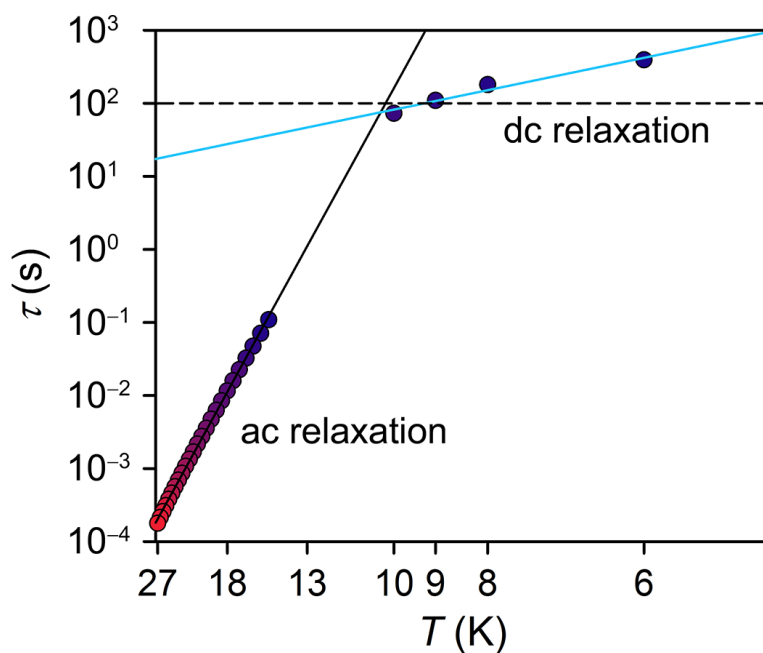


Figure 4.A9. Plot of τ (log scale) versus T (inverse scale) for ac points collected for the 1:20 (Er:Y) dilution of $[\text{Er}(\text{COT})_2]^-$ and dc points collected for the 1:85 dilution (ac relaxation times were the same within error between both dilutions). The dc measurements enable the extension of the Arrhenius plot as low as 6 K and an estimate of the true blocking temperature of 9.25 K, corresponding to $\tau = 100$ s.

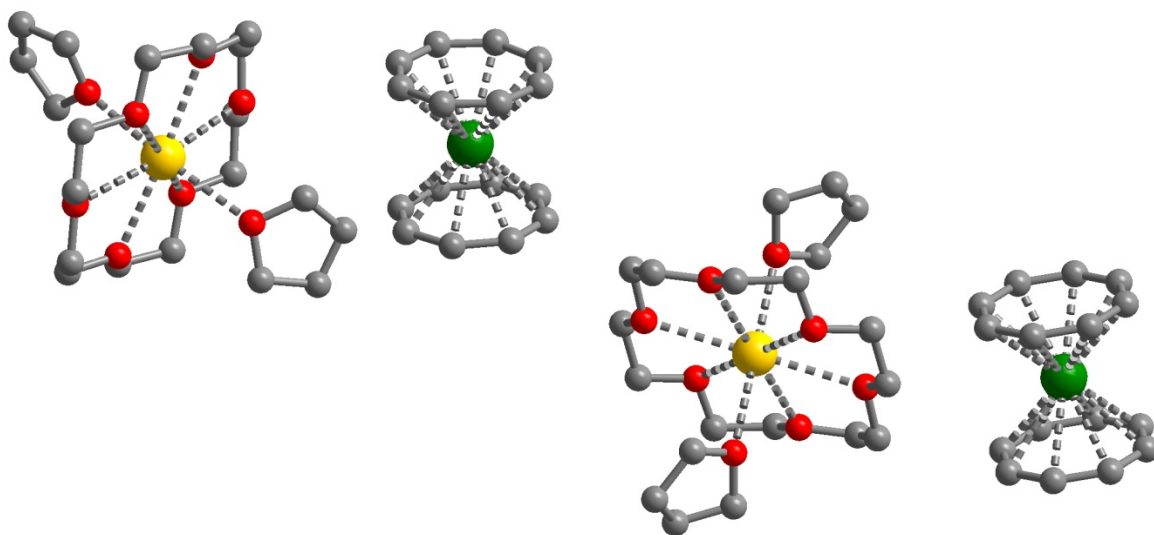


Figure 4.A10. X-ray structure of $[\text{K}(18\text{-c-}6)(\text{THF})_2][\text{Dy}(\text{COT})_2]$. Hydrogen atoms are omitted for clarity; green, yellow, grey and red spheres represent Dy, K, C, and O, respectively. The dihedral angles for each unique $[\text{Dy}(\text{COT})_2]^-$ unit are $0.0(1)$ and $1.7(1)^\circ$, respectively, with corresponding intramolecular COT^{2-} ring distances of $3.838(6)$ and $3.806(6)$ Å. The closest inter-ion Dy \cdots Dy distance is $7.454(1)$ Å.

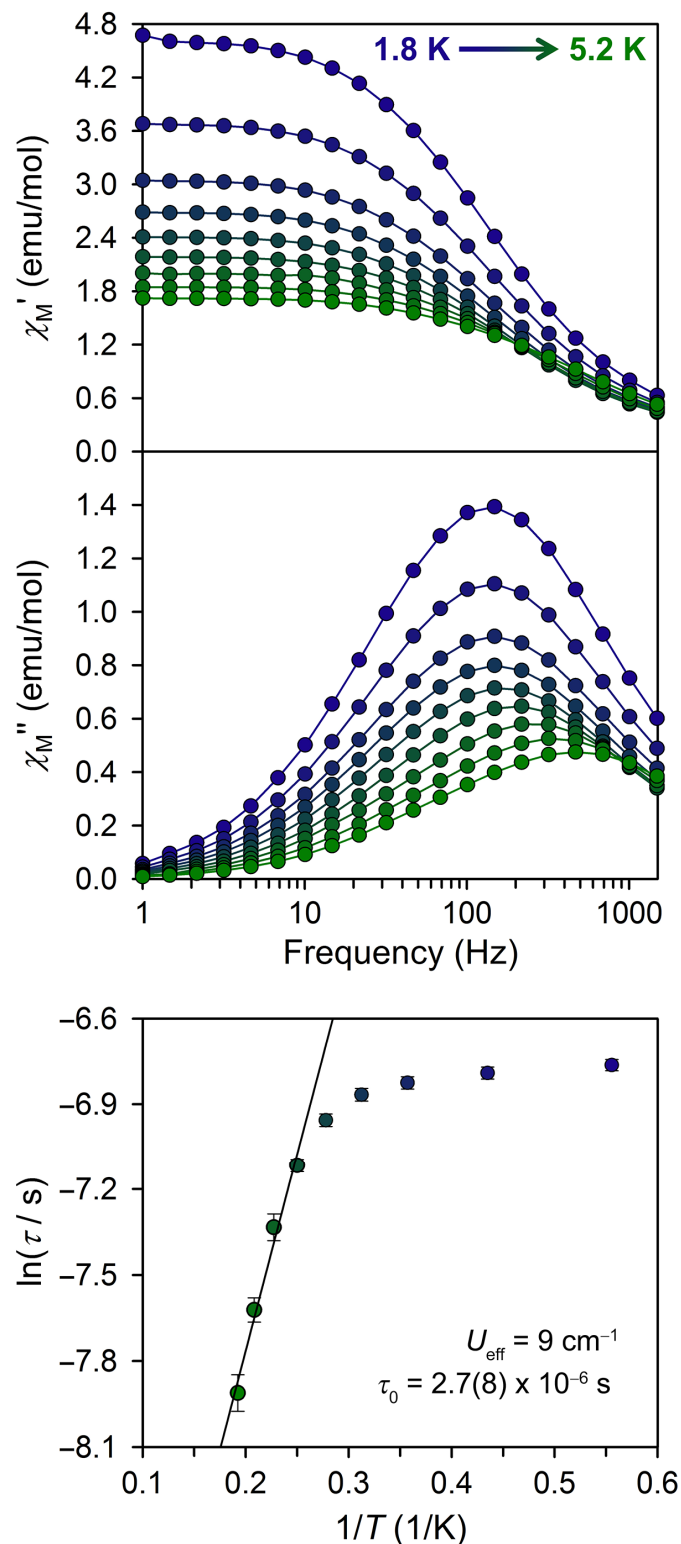
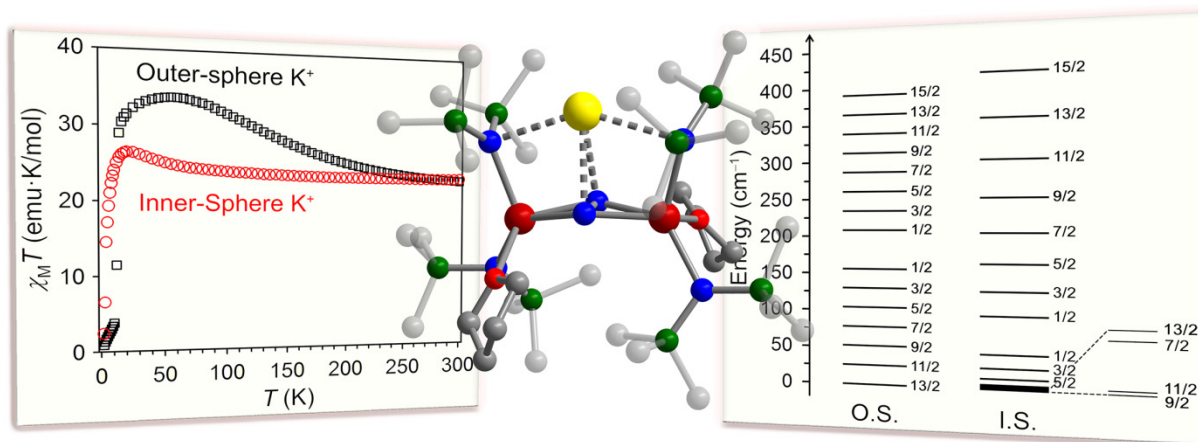


Figure 4.A11. (Top) Plot of the in-phase (χ_M') and out-of-phase (χ_M'') magnetic susceptibility from 1.8 to 5.2 K for $[\text{K}(18\text{-c-6})][\text{Dy}(\text{COT})_2]$ under zero dc field. (Bottom) Corresponding plot of the natural log of the relaxation time, $\ln(\tau)$, versus $1/T$.

Chapter 5: Influence of an Inner-Sphere K^+ Ion on the Magnetic Behavior of N_2^{3-} Radical-Bridged Dilanthanide Complexes



5.1 Introduction

Unraveling the relationship between structure and magnetic properties is a fundamental goal in the study of lanthanide molecular magnetism. In mononuclear lanthanide species, the combination of inherently large magnetic anisotropy with the appropriate ligand field symmetry has been used to rationalize slow magnetic relaxation in many different coordination environments, as already discussed in Chapter 1.¹ Even for multinuclear complexes, single-ion anisotropy and symmetry often trump exchange interactions as the most relevant criteria for promoting slow relaxation,² due to the contracted nature of the 4f orbitals and resulting weak magnetic exchange.³ The advent of a small contingent of dinuclear radical-bridged lanthanide complexes has recently demonstrated that strong magnetic exchange can be facilitated by diffuse 2,2'-bipyrimidine⁻ or N₂³⁻ radical units.^{4,5} As introduced in Chapter 1, currently the record blocking temperature of 14 K is held by the N₂³⁻ radical-bridged species [K(18-crown-6)(THF)₂]{[(Me₃Si)₂N)₂Tb(THF)₂(μ-N₂)},^{5b} while the Gd^{III} congener exhibits the strongest magnetic exchange coupling observed to date for any Gd^{III} compound, with $J_{\text{Gd-radical}} = -27 \text{ cm}^{-1}$.^{5a} DFT calculations for the Gd^{III} complex suggest that the coupling interaction is a result of overlap of the lanthanide 4f orbitals with the N₂³⁻ ligand orbitals and thus, as the dihedral angle between the lanthanide and radical ligand deviates from planarity, the strength of the coupling is predicted to decrease.⁶

As a probe of this computational result, it was of interest to magnetically characterize the complexes {[(Me₃Si)₂N)₂Ln(THF)₂(μ-N₂)K} (Ln = Gd^{III}, Tb^{III}, Dy^{III}),⁷ which are crystallized in the absence of coordinating solvent resulting in an un-solvated, inner-sphere K⁺ ion. Coordination of the potassium to the N₂³⁻ unit and amides from each lanthanide center leads to a folding of the planar Ln₂N₂ unit present in the [K(18-crown-6)(THF)₂]⁺ salt.⁸ Full magnetic characterization of the series reveals that, while the strength of the Ln^{III}-N₂³⁻ coupling remains unchanged (as determined for Gd^{III}), the bending of the Ln-radical-Ln unit facilitates non-negligible antiferromagnetic coupling between Ln^{III} centers, a result which leads to significantly lower magnetic relaxation barriers and blocking temperatures for the Tb^{III} and Dy^{III} congeners of the inner-sphere compound.

5.2 Experimental

Magnetic Measurements. Magnetic samples were prepared by adding powdered crystalline compounds to a 7 mm diameter quartz tube with a raised quartz platform. All sample manipulations were carried out in a glove box with N₂ or Ar atmosphere, or on a Schlenk line. Solid eicosane (pump-heat-freeze, three cycles) was added to cover the samples to prevent crystallite torqueing and provide good thermal contact between the sample and the cryogenic bath. The tubes were fitted with Teflon sealable adapters, evacuated on a Schenk line or using a glove box vacuum pump, and sealed under vacuum using an H₂/O₂ flame. Following flame sealing, the solid eicosane was melted in a water bath held at 40 °C. Dc magnetic susceptibility measurements were performed at temperatures ranging from 1.8 to 300 K, under applied fields of 0.1, 0.5, and 1 T. Ac magnetic susceptibility measurements were performed using a 4 Oe switching field over the frequency range 1-1500 Hz and at a range of temperatures. All data for {[(Me₃Si)₂N)₂Ln(THF)₂(μ-N₂)K} were corrected for diamagnetic contributions from the core diamagnetism estimated using Pascal's constants to give $\chi_D = -0.00065194 \text{ emu/mol (Gd}^{\text{III}}\text{)}, -0.00065687 \text{ emu/mol (Tb}^{\text{III}}\text{)}, -0.00066181$

emu/mol (Dy^{III}), and -0.00024306 emu/mol (eicosane). Cole-Cole plots were fitted using formulae describing χ' and χ'' in terms of frequency, constant temperature susceptibility (χ_T), adiabatic susceptibility (χ_S), relaxation time (τ), and a variable representing the distribution of relaxation times (α).⁹ All data could be fitted to α values of ≤ 0.1 , indicating a narrow distribution of relaxation processes.

5.3 Results and Discussion

The synthesis of the complexes $\{[(\text{Me}_3\text{Si})_2\text{N})_2\text{Ln}(\text{THF})_2(\mu\text{-N}_2)\text{K}\}$ has been reported elsewhere,^{7,10} and is accomplished by potassium graphite reduction of the corresponding neutral (N_2^{2-}) -bridged complexes $\{[(\text{Me}_3\text{Si})_2\text{N})_2\text{Ln}(\text{THF})_2(\mu\text{-N}_2)\}$ ¹¹ followed by recrystallization from toluene. Notably, as described in Ref. 7, it was found for these molecules (and a handful of other anisotropic lanthanide compounds) that rapid crystallization of pure material could be induced by use of a $\text{Nd}_2\text{Fe}_{13}\text{B}$ magnet. This technique rests on the fact that paramagnetic molecules will be much more strongly attracted to a magnet than say, diamagnetic impurities, or less paramagnetic substances (e.g. complexes with smaller spin). A magnet-driven concentration gradient in solution should thus lead to more rapid and preferential crystallization of the most paramagnetic substance. What is fascinating to note is that in some cases for the crystallization images reported in Ref.7, individual crystallites seem to form in a pattern defined by magnetic field lines. Structural characterization of $\{[(\text{Me}_3\text{Si})_2\text{N})_2\text{Ln}(\text{THF})_2(\mu\text{-N}_2)\text{K}\}$ revealed similar metrical parameters when compared with the outer-sphere analogues. However, one notable difference was the folding of the previously planar Ln_2N_2 core unit found in the outer-sphere species, leading to dihedral angles between the two LnN_2 planes of 13.64° in (Gd^{III}), 16.12° (Tb^{III} , Figure 5.1), and 15.27° (Dy^{III}).

Static Magnetic Susceptibility Measurements. Temperature-dependent dc magnetic susceptibility measurements were carried out for the inner-sphere complexes between 1.8 and 300 K at fields of 0.1 or 1 T. Comparison of the resulting $\chi_{\text{M}}T$ versus T data with that previously reported for $\{[(\text{Me}_3\text{Si})_2\text{N})_2\text{Ln}(\text{THF})_2(\mu\text{-N}_2)\}^-$ reveals stark differences in the magnetism of the two series (Figure 5.2). For $\{[(\text{Me}_3\text{Si})_2\text{N})_2\text{Gd}(\text{THF})_2(\mu\text{-N}_2)\text{K}\}$, $\chi_{\text{M}}T$ is 16.28 emu·K/mol at 300 K, larger than that observed for its forerunner (15.25 emu·K/mol)^{5a} and corresponding to the value of 16.31 emu·K/mol expected for two uncoupled $S = 7/2$ Gd^{III} centers and an $S = 1/2$ radical bridge. A shallow minimum occurs at 185 K upon lowering the temperature, significantly below the > 300 K minimum for $\{[(\text{Me}_3\text{Si})_2\text{N})_2\text{Gd}(\text{THF})_2(\mu\text{-N}_2)\}^-$,^{5b} but greater than the 135 K minimum observed for the bipyrimidine radical-bridged species $\{[(\text{C}_5\text{Me}_5)_2\text{Gd}]_2(\mu\text{-bpym})\}^+$.⁴ The susceptibility rises to a maximum of 18.25 emu·K/mol at 18 K for the inner-sphere species, much lower than the 9 K maximum of 23.83 emu·K/mol for the outer-sphere analogue. The latter corresponds well to the value of 24.38 emu·K/mol expected for an $S = 13/2$ ground state arising from strong antiferromagnetic coupling between Gd^{III} and the N_2^{3-} radical bridge.^{5a} In contrast, the $\chi_{\text{M}}T$ maximum for $\{[(\text{Me}_3\text{Si})_2\text{N})_2\text{Gd}(\text{THF})_2(\mu\text{-N}_2)\text{K}\}$ is closer to the expected value for an $S = 11/2$ ground state (17.88 emu·K/mol), which is not reasonable assuming simple antiferromagnetic coupling between the Gd^{III} centers and the N_2^{3-} . Another distinct feature in the $\chi_{\text{M}}T$ data for $\{[(\text{Me}_3\text{Si})_2\text{N})_2\text{Gd}(\text{THF})_2(\mu\text{-N}_2)\text{K}\}$ is the presence of a downturn following the maximum at 18 K, which might be attributed to the presence of competing exchange interactions.¹²

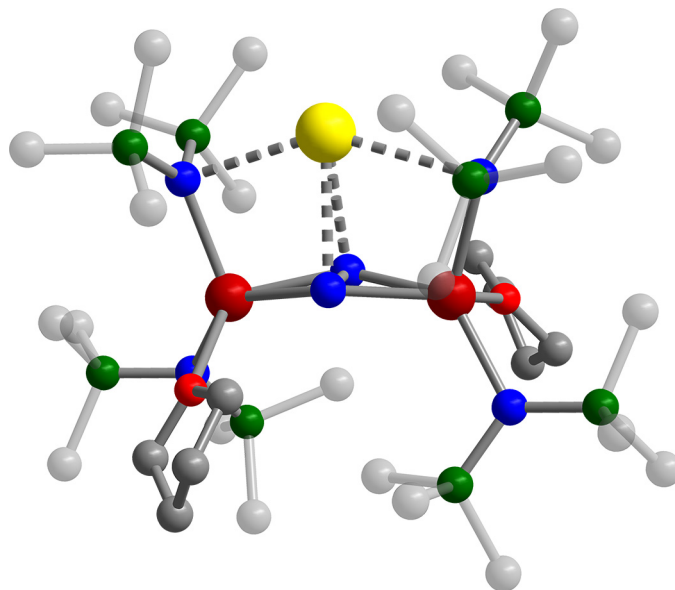


Figure 5.1. X-ray structure of $\{[(\text{Me}_3\text{Si})_2\text{N})_2\text{Gd}(\text{THF})]_2(\mu\text{-N}_2)\text{K}\}$. Dark red, blue, green, red, grey, and yellow spheres represent Tb, N, Si, O, C, and K, respectively. H atoms have been omitted for clarity.

With its half-filled 4f shell, Gd^{III} possesses no angular momentum, thus enabling analysis of its magnetic behavior using a standard spin-only model. Previously, dc susceptibility data for the outer-sphere Gd^{III} species were modeled using the isotropic Heisenberg-Dirac-Van Vleck Hamiltonian $\hat{H} = -2J\hat{S}_{\text{radical}} \cdot (\hat{S}_{\text{Gd1}} + \hat{S}_{\text{Gd2}})$.^{5a} Assuming all coupling interactions are accounted for, this Hamiltonian represents a reasonable model for complexes containing paramagnetic centers with no orbital angular momentum, such as $^8\text{S}_{7/2} \text{Gd}^{\text{III}}$ and an $S = 1/2 \text{N}_2^{3-}$ radical bridge. However, use of this Hamiltonian resulted in a satisfactory fit of the experimental data only above 40 K for $\{[(\text{Me}_3\text{Si})_2\text{N})_2\text{Gd}(\text{THF})]_2(\mu\text{-N}_2)\text{K}\}$. Addition of a second term accounting for a weak intermolecular interaction^{5a} still did not enhance the fit below 40 K. Considering the dihedral angle between the two GdN_2 planes present in the latter, intramolecular $\text{Gd}^{\text{III}}\text{-Gd}^{\text{III}}$ coupling might also contribute to the overall magnetic susceptibility, and therefore the system would be better modeled as a triangle of paramagnetic centers with $(\text{N}_2)^{3-}$ at the apex. This scenario can be described by the Hamiltonian $\hat{H} = -J(\hat{S}_{\text{radical}} \cdot \hat{S}_{\text{Gd1}} + \hat{S}_{\text{radical}} \cdot \hat{S}_{\text{Gd2}}) - J'(\hat{S}_{\text{Gd1}} \cdot \hat{S}_{\text{Gd2}})$,¹³ where the first constant J represents coupling between Gd^{III} and the N_2^{3-} radical, while J' quantifies the intramolecular coupling between the two Gd^{III} centers. With the inclusion of a very small intermolecular coupling constant of $J'' = 0.020(1) \text{ cm}^{-1}$, this model provides a good fit to the magnetic susceptibility data over the entire temperature range of 1.8 to 300 K yielding $J = -27.1(4) \text{ cm}^{-1}$ and $J' = -2.28(1) \text{ cm}^{-1}$ (Figure 5.2). The improvement in the fit (largely below 40 K) with the inclusion of this intramolecular term indicates that the coupling between Gd^{III} centers is significant only below this temperature,¹⁴ and therefore, such an interaction is also likely to influence the magnetic relaxation behavior of the Tb^{III} and Dy^{III} complexes.

Notably, the $\text{Gd}^{\text{III}}\text{-(N}_2^{3-})$ coupling constant obtained for $\{[(\text{Me}_3\text{Si})_2\text{N})_2\text{Gd}(\text{THF})]_2(\mu\text{-N}_2)\text{K}\}$ matches the value of $J = -27 \text{ cm}^{-1}$ previously reported for $\{[(\text{Me}_3\text{Si})_2\text{N})_2\text{Gd}(\text{THF})]_2(\mu\text{-N}_2)\}^-$.^{5a} Thus, the small bend in the $\text{Gd}^{\text{III}}\text{-(N}_2^{3-})\text{-Gd}^{\text{III}}$ unit appears to have little impact on the strength of the $\text{Gd}^{\text{III}}\text{-(N}_2^{3-})$ coupling. Indeed, DFT calculations predicted that this coupling

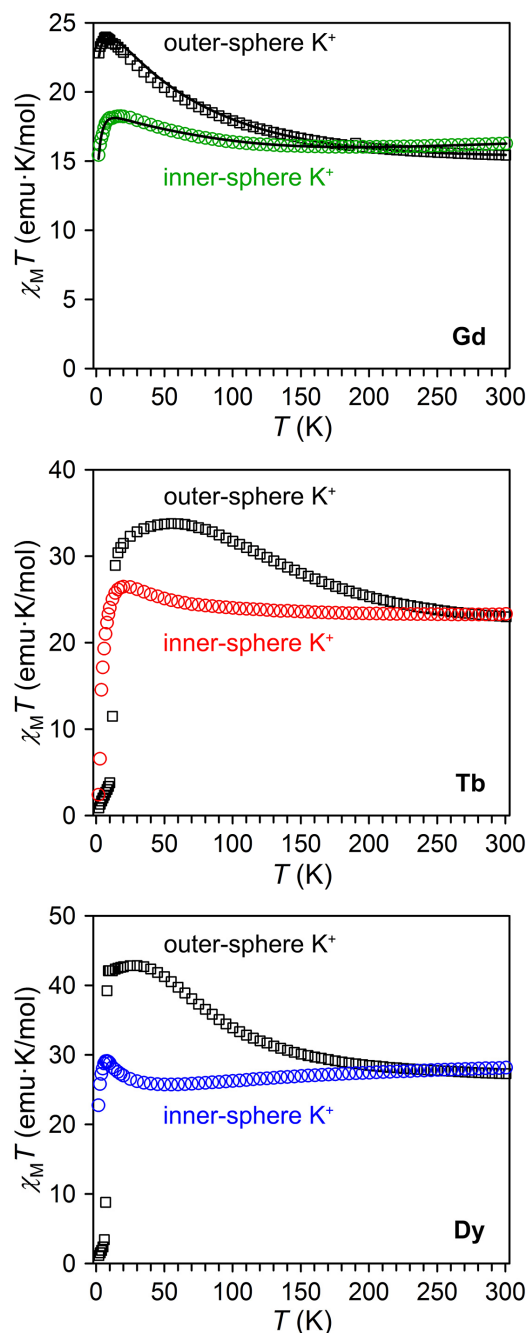


Figure 5.2. Plot of the molar magnetic susceptibility times temperature ($\chi_M T$) versus T for $\{[(\text{Me}_3\text{Si})_2\text{N})_2\text{Ln}(\text{THF})_2(\mu\text{-N}_2)\text{K}]\}$ (colored circles) and $\{[(\text{Me}_3\text{Si})_2\text{N})_2\text{Ln}(\text{THF})_2(\mu\text{-N}_2)]^-\}$ (black squares). Data for Gd^{III} and Dy^{III} complexes were collected under $H_{\text{dc}} = 0.1$ T, while data for the Tb^{III} complexes were collected under $H_{\text{dc}} = 1$ T. Fits using the Hamiltonian described in the text are represented by black lines. For $\{[(\text{Me}_3\text{Si})_2\text{N})_2\text{Gd}(\text{THF})_2(\mu\text{-N}_2)\text{K}]\}$, a good fit to the data is achieved by considering intramolecular $\text{Gd}^{\text{III}}\text{-}(\text{N}_2^{3-})$ and $\text{Gd}^{\text{III}}\text{-Gd}^{\text{III}}$ coupling, resulting in $J = -27.1(4)$ cm^{-1} and $J' = -2.28(1)$ cm^{-1} , respectively, with $g = 2.17$. When the data is adjusted for a mass error of ~ 2 mg, $g = 2.09$, while the values of J and J' do not change within error, thus the larger g -value obtained from fitting is likely the result of a small mass error.

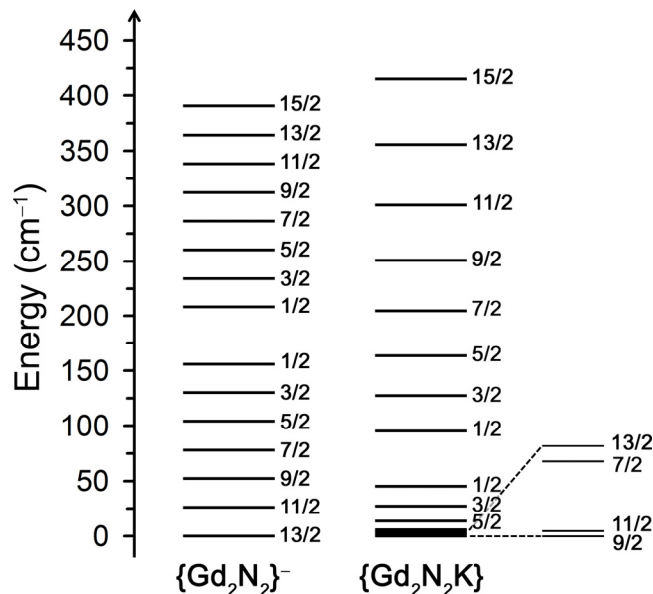


Figure 5.3. Spin state energy level diagrams for Gd^{III} complexes, obtained from fits using the Hamiltonians described in the text and Ref. 5a. The outer-sphere complex exhibits a well-isolated $S = 13/2$ ground state, while competing antiferromagnetic coupling between the Gd^{III} centers in $\{[(\text{Me}_3\text{Si})_2\text{N})_2\text{Gd}(\text{THF})_2(\mu\text{-N}_2)\text{K}]\}$ result in an $S = 9/2$ ground state that is nearly degenerate with the first excited state of $S = 11/2$.

strength should decrease by only $\sim 5 \text{ cm}^{-1}$ with a dihedral angle of 13.5° .⁶ A less intuitive result of fitting the dc susceptibility data is the occurrence of significant exchange coupling directly between the Gd^{III} centers, which was not necessary to include in modeling the data for $\{[(\text{Me}_3\text{Si})_2\text{N})_2\text{Gd}(\text{THF})_2(\mu\text{-N}_2)]\}^-$, and was predicted by DFT calculations⁶ to be just -0.5 cm^{-1} . While literature data are sparse for exchange coupling between Gd^{III} centers, the magnitude of the experimental value of $-2.28(1) \text{ cm}^{-1}$ dwarfs recently reported values for antiferromagnetic superexchange mediated by semiquinone radical,¹⁵ phenoxylate,¹⁶ or carboxylate¹⁷ bridges. Much work has also been done to characterize the nature of the magnetic coupling in Ln^{III} nitronyl nitroxide chains,¹⁸ and notably in some cases antiferromagnetic next-nearest-neighbor Gd^{III}-Gd^{III} exchange has been observed that is even stronger than the metal-radical exchange interaction, on the order of $J = -0.98 \text{ cm}^{-1}$.^{18c,f} Very recently, a comparable antiferromagnetic exchange interaction with $J = -1.22 \text{ cm}^{-1}$ has also been shown between Gd^{III} ions bridged by hydride ligands, where the Gd^{III}...Gd^{III} separation is $3.4140(6) \text{ \AA}$.¹⁹ Given the large separation of 4.267 \AA between Gd^{III} centers in $\{[(\text{Me}_3\text{Si})_2\text{N})_2\text{Gd}(\text{THF})_2(\mu\text{-N}_2)\text{K}]\}$, it appears the coupling mechanism here is likely via superexchange through the N_2^{3-} ligand. For comparison, an exchange of $J = -0.49 \text{ cm}^{-1}$ was observed for the planar (N_2^{2-})-bridged species,^{5a} indicating that the strength of the exchange increases considerably upon reduction of the bridging intermediary to N_2^{3-} and folding of the Gd_2N_2 core unit.

The competing Gd^{III}-Gd^{III} exchange interaction that arises in $\{[(\text{Me}_3\text{Si})_2\text{N})_2\text{Gd}(\text{THF})_2(\mu\text{-N}_2)\text{K}]\}$ has a dramatic effect on its magnetic susceptibility data, as manifested in a suppression of the magnetic moment at low temperatures. The origin of this effect is apparent upon comparing plots of the spin state energy level structures obtained from fits to the susceptibility data, as shown in Figure 5.3. Here, the simple level ordering of

$\{[(\text{Me}_3\text{Si})_2\text{N})_2\text{Gd}(\text{THF})]_2(\mu\text{-N}_2)\}^-$ expected for strong antiferromagnetic exchange between an $S = 1/2$ radical and two $S = 7/2$ Gd^{III} centers is disrupted by the antiferromagnetic $\text{Gd}^{\text{III}}\text{-Gd}^{\text{III}}$ exchange. Namely, whereas the $S = 13/2$ ground state of $\{[(\text{Me}_3\text{Si})_2\text{N})_2\text{Gd}(\text{THF})]_2(\mu\text{-N}_2)\}^-$ is well-isolated from an $S = 11/2$ excited state, for $\{[(\text{Me}_3\text{Si})_2\text{N})_2\text{Gd}(\text{THF})]_2(\mu\text{-N}_2)\text{K}\}$, the ground state is a lower spin $S = 9/2$ state that is separated by only 0.29 cm^{-1} from an $S = 11/2$ excited state. Variable-field magnetization measurements performed at low temperature up to 7 T for confirm the calculated $S = 9/2$ ground state (Figure 5.A1). Additionally, at temperatures of 2, 4, and 6 K, the $M(H)$ curves for $\{[(\text{Me}_3\text{Si})_2\text{N})_2\text{Gd}(\text{THF})]_2(\mu\text{-N}_2)\text{K}\}$ exactly overlay with the Brillouin curves expected for an $S = 9/2$ system until fields beyond 1 T, when the experimental curve passes through $S = 11/2$ at (~ 3.5 T) before meeting with $S = 13/2$.

Dc magnetic susceptibility measurements performed on the Tb^{III} and Dy^{III} congeners of this inner-sphere species reveal similar trends to those observed for Gd^{III} (Figure 5.2). While significant magnetic anisotropy precludes fitting of the $\chi_{\text{M}}T$ data using a spin-only approximation, the general results obtained for Gd^{III} may be extended to gain a qualitative understanding of the magnetism. In particular, it is anticipated for these compounds that the moment of the ground state is reduced as a result of antiferromagnetic $\text{Tb}^{\text{III}}\text{-Tb}^{\text{III}}$ and $\text{Dy}^{\text{III}}\text{-Dy}^{\text{III}}$ exchange interactions. At room temperature, the $\chi_{\text{M}}T$ values are $23.77 \text{ emu}\cdot\text{K/mol}$ and $28.17 \text{ emu}\cdot\text{K/mol}$ for Tb^{III} and Dy^{III} , respectively, very close to those expected for two uncoupled Ln^{III} centers and an $S = 1/2$ radical ($24.0 \text{ emu}\cdot\text{K/mol}$ and $28.7 \text{ emu}\cdot\text{K/mol}$, respectively). Maxima in $\chi_{\text{M}}T$ are encountered for at 10 K (Tb^{III}) and 8 K (Dy^{III}), with corresponding $\chi_{\text{M}}T$ values of $28.44 \text{ emu}\cdot\text{K/mol}$ and $29.12 \text{ emu}\cdot\text{K/mol}$. These maxima are much less than those for the corresponding outer-sphere species ($33.76 \text{ emu}\cdot\text{K/mol}$ and $42.54 \text{ emu}\cdot\text{K/mol}$) consistent with competing antiferromagnetic interactions between Ln^{III} centers. One also observes an extraordinary suppression in the magnitudes of the magnetic moments (Figure 5.2), again highlighting the impact of $\text{Ln}^{\text{III}}\text{-Ln}^{\text{III}}$ coupling upon bending of the Ln_2N_2 core unit. Considering just the susceptibility behavior of the inner-sphere species, the $\chi_{\text{M}}T$ maximum for Tb^{III} hints at stronger magnetic coupling relative to Dy^{III} , an observation supported by the temperature-dependence of $\chi_{\text{M}}T$ below these maxima. For Tb^{III} , $\chi_{\text{M}}T$ falls abruptly to a final value of $4.71 \text{ emu}\cdot\text{K/mol}$ at 1.8 K, while a very small decline in the case of Dy^{III} yields a value of $\chi_{\text{M}}T = 22.75 \text{ emu}\cdot\text{K/mol}$ at the same temperature. The sharp decline for the former is indicative of magnetic blocking, however, the same phenomenon is lacking for Dy^{III} in the range of temperatures accessible by the SQUID magnetometer, indicating the latter has a much lower blocking temperature.

Dynamic Magnetic Susceptibility Measurements. To probe for slow relaxation of the magnetization in the anisotropic $\{[(\text{Me}_3\text{Si})_2\text{N})_2\text{Ln}(\text{THF})]_2(\mu\text{-N}_2)\text{K}\}$ complexes, ac susceptibility measurements were carried out over a range of temperatures using a 4 Oe switching field and frequencies from 1 to 1500 Hz. Out-of-phase signal (χ_{M}'') is observed under zero applied field for both complexes (Figure 5.4, top, and Figure 5.A2), although at much lower temperatures and over a narrower range than observed for the previously reported radical complexes.⁵ Relaxation times (τ) were extracted for at the various temperatures by fitting the frequency-dependent χ_{M}' and χ_{M}'' data using a generalized Debye model.⁹ Small values of the alpha (α) parameter (≤ 0.1) revealed the relaxation to be uniform over the temperature and frequency range probed. Indeed, a plot of the natural logarithm of τ versus $1/T$ is linear for both compounds; thus, relaxation occurs predominantly through a thermally activated Orbach process.²⁰ Fitting to an Arrhenius law yielded barriers of $U_{\text{eff}} = 41.13(4) \text{ cm}^{-1}$ (Tb^{III}) and $U_{\text{eff}} = 14.95(8) \text{ cm}^{-1}$ (Dy^{III}) (Figure 5.4), substantially reduced

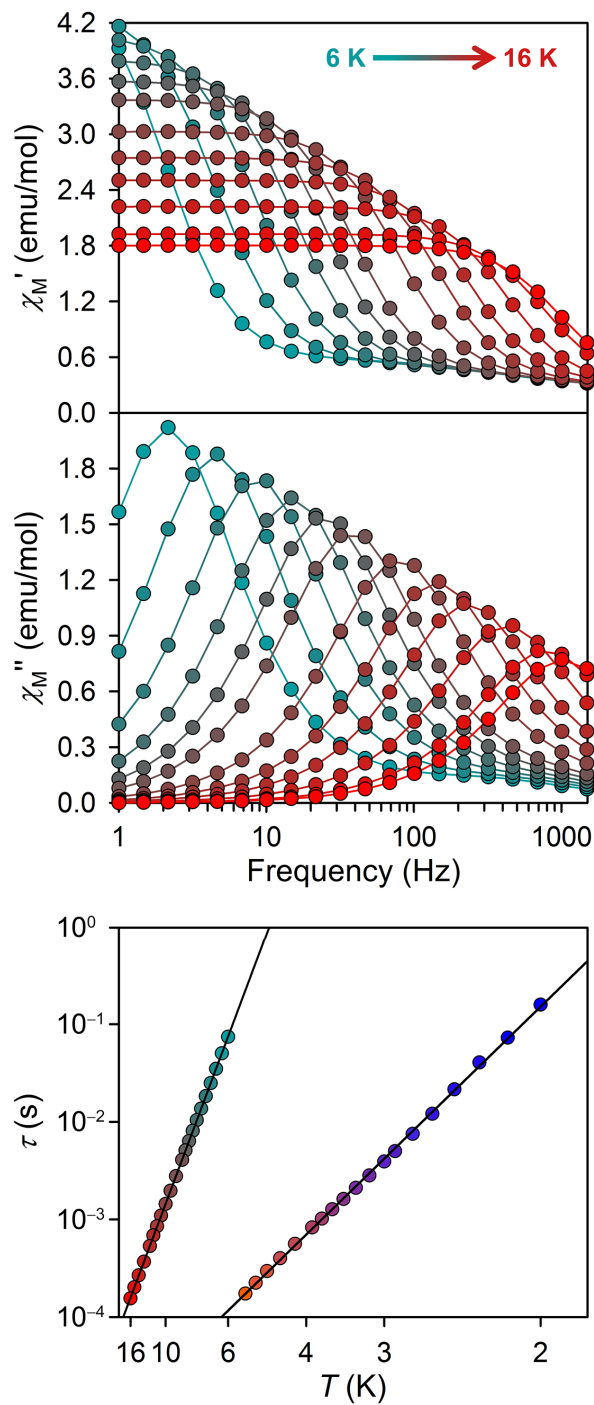


Figure 5.4. (Top) Plot of the molar in-phase (χ_M') and out-of-phase (χ_M'') magnetic susceptibility versus frequency of the oscillating field for $\{[(\text{Me}_3\text{Si})_2\text{N})_2\text{Tb}(\text{THF})]_2(\mu\text{-N}_2)\text{K}\}$ over the temperature range 6-16 K and frequencies between 1 and 1500 Hz under zero-applied dc field. (Bottom) Plot of the relaxation time (log scale) versus T (inverse scale) for $\{[(\text{Me}_3\text{Si})_2\text{N})_2\text{Ln}(\text{THF})]_2(\mu\text{-N}_2)\text{K}\}$ (Tb^{III} and Dy^{III}) under zero applied dc field.

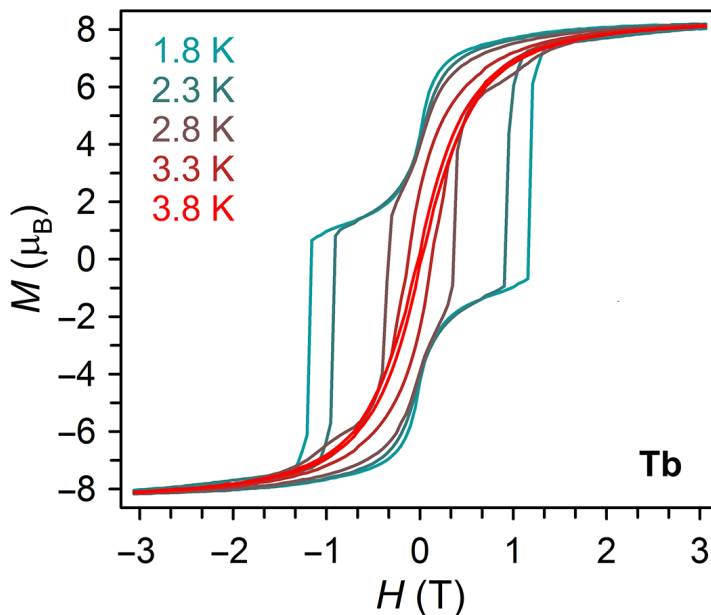


Figure 5.5. Variable-field magnetization for $\{[(\text{Me}_3\text{Si})_2\text{N})_2\text{Tb}(\text{THF})]_2(\mu\text{-N}_2)\text{K}\}$ collected at a sweep rate of 1 mT/s. At 1.8 K, the remnant magnetization and coercive field are $4.28 \mu_{\text{B}}$ and 1.1 T.

from those of the parent outer-sphere complexes at $227.0(4) \text{ cm}^{-1}$ (Tb^{III})^{5b} and 123 cm^{-1} (Dy^{III})^{5a}, though within range of many terbium and dysprosium single-molecule magnets described in the literature.^{1f} The much faster relaxation and smaller barriers observed for both compounds is a direct testimony to the influence of the competing antiferromagnetic coupling interaction on the energy landscape. Additionally, while the outer-sphere potassium complexes both exhibit τ_0 values on the order of 10^{-9} s ,⁵ corresponding well to pure Orbach relaxation, τ_0 values of $3.89(2) \times 10^{-6}$ and $3.2(1) \times 10^{-7} \text{ s}$ for $\{[(\text{Me}_3\text{Si})_2\text{N})_2\text{Tb}(\text{THF})]_2(\mu\text{-N}_2)\text{K}\}$ and $\{[(\text{Me}_3\text{Si})_2\text{N})_2\text{Dy}(\text{THF})]_2(\mu\text{-N}_2)\text{K}\}$, respectively, suggest that additional relaxation mechanisms may be active at the temperatures and frequencies probed. At high ac frequencies, such a conclusion is also supported by an additional small increase in χ_M'' for both complexes and the non-zero value of χ_M' for $\{[(\text{Me}_3\text{Si})_2\text{N})_2\text{Tb}(\text{THF})]_2(\mu\text{-N}_2)\text{K}\}$.

While the relaxation time for the inner-sphere Dy^{III} compound is still within the ac frequency range near the lowest temperatures accessible by our SQUID magnetometer, ac relaxation for Tb^{III} is only apparent above 6 K. In order to probe relaxation at lower temperatures, variable-field magnetization measurements were carried out from 1.8 K at a sweep rate of 1 mT/s. As anticipated, an open magnetic hysteresis loop is observed that remains open to temperatures as high as 3.8 K (Figure 5.5). This maximum hysteresis temperature is only a fraction of that observed for $\{[(\text{Me}_3\text{Si})_2\text{N})_2\text{Tb}(\text{THF})]_2(\mu\text{-N}_2)\}^-$ at $\sim 14 \text{ K}$,^{5b} again emphasizing the lower moment and weaker overall coupling engineered by the bridging K^+ counterion.

An interesting feature in the magnetic hysteresis of the inner-sphere Tb^{III} complex, not observed for the parent species, is the presence of two steps, one centered at zero field for all temperatures. Such drops in the magnetization indicate rapid relaxation, often ascribed to tunneling of the magnetization.²¹ Indeed, the energy separation between ground and first excited S in $\{[(\text{Me}_3\text{Si})_2\text{N})_2\text{Gd}(\text{THF})]_2(\mu\text{-N}_2)\text{K}\}$ (0.29 cm^{-1}) is on the order of the tunnel

splitting in some molecular magnets.²² A similar separation between ground and excited M_J states for the Tb^{III} species, generated in the presence of low temperature $\text{Tb}^{\text{III}}\text{-Tb}^{\text{III}}$ exchange, could be considered an effective tunnel splitting, promoting tunneling and hence a magnetization drop at zero field. Another possibility is the presence of non-negligible dipolar interactions, which could create a small bias and allow for tunneling at zero field.

Field-dependent ac susceptibility scans suggest²³ that the second, much more drastic magnetization drop is mediated by resonant tunneling of the magnetization, a possibility that could again be rationalized by considering the energy landscape determined for $\{[(\text{Me}_3\text{Si})_2\text{N})_2\text{Gd}(\text{THF})]_2(\mu\text{-N}_2)\text{K}\}$ as a model. Given the presence of a few closely spaced excited states in $\{[(\text{Me}_3\text{Si})_2\text{N})_2\text{Ln}(\text{THF})]_2(\mu\text{-N}_2)\text{K}\}$ (spanning $\sim 5\text{ cm}^{-1}$ for Gd^{III}) arising from the competing $\text{Ln}^{\text{III}}\text{-Ln}^{\text{III}}$ exchange, for the anisotropic lanthanide ions, resonant M_J states are more likely to occur than in the outer-sphere species, where strong concerted exchange effects a much greater separation between ground and first excited state (see Table 5.A1).²⁴ Due to the potential relevance of dipolar interactions in promoting tunneling²¹ several attempts were made to characterize dilute solution samples prepared in both toluene and 2-methyltetrahydrofuran glasses. However, $\{[(\text{Me}_3\text{Si})_2\text{N})_2\text{Tb}(\text{THF})]_2(\mu\text{-N}_2)\text{K}\}$ was found to decompose rapidly in these solutions, precluding further characterization. Detailed theoretical analysis will certainly be necessary to validate any of these interpretations and fully understand the magnetic hysteresis behavior.

5.4 Conclusions and Outlook

The compounds $\{[(\text{Me}_3\text{Si})_2\text{N})_2\text{Ln}(\text{THF})]_2(\mu\text{-N}_2)\text{K}\}$ were magnetically characterized for comprehensive comparison with the previously reported $\{[(\text{Me}_3\text{Si})_2\text{N})_2\text{Ln}(\text{THF})]_2(\mu\text{-N}_2)\}^-$. While the Tb^{III} and Dy^{III} congeners exhibit zero-field slow magnetic relaxation like their parent compounds, they also exhibit substantially shorter relaxation times and much smaller relaxation barriers. Fitting of static magnetic susceptibility data for $\{[(\text{Me}_3\text{Si})_2\text{N})_2\text{Gd}(\text{THF})]_2(\mu\text{-N}_2)\text{K}\}$ reveals strong antiferromagnetic $\text{Gd}^{\text{III}}\text{-(N}_2^{3-})$ radical coupling that is the same magnitude as in the parent compound, with $J \sim -27\text{ cm}^{-1}$. However, the folded $\text{Gd}^{\text{III}}\text{-(N}_2^{3-})\text{-Gd}^{\text{III}}$ unit also introduces a small antiferromagnetic coupling interaction directly between Gd^{III} centers, which competes with the parallel alignment of Gd^{III} spins enforced by the antiferromagnetic $\text{Gd}^{\text{III}}\text{-(N}_2^{3-})$ radical coupling. The resulting energy spectrum of $\{[(\text{Me}_3\text{Si})_2\text{N})_2\text{Gd}(\text{THF})]_2(\mu\text{-N}_2)\text{K}\}$ consists of an $S = 9/2$ ground state with a low-lying excited state $S = 11/2$, and it is this absence of a well-isolated, higher-moment ground state that is likely the source of faster relaxation and smaller blocking temperatures for the Tb^{III} and Dy^{III} molecules. These results reveal the importance of a planar $\text{Ln}^{\text{III}}\text{-(N}_2^{3-})\text{-Ln}^{\text{III}}$ unit to promote strong concerted exchange and very slow magnetic relaxation,⁵ and perhaps more importantly highlight how a simple alkali metal cation such as potassium can be used to dramatically affect magnetic behavior.

5.5 Acknowledgments

The National Science Foundation is acknowledged for support under grant CHE-1111900, McDonald's Corporation for the drinking straws employed in magnetic sample loading, and Wayne W. Lukens for valuable discussions. Jordan Corbey and Prof. Bill Evans at the University of California, Irvine, are gratefully acknowledged for providing the complexes for

magnetic analysis as well as x-ray structure data, and for conducting studies of crystallization in the presence of a Nd₂Fe₁₃B magnet.

5.6 References

- (1) (a) Ishikawa, N.; Sugita, M.; Ishikawa, T.; Koshihara, S.-y.; Kaizu, Y. *J. Am. Chem. Soc.* **2003**, *125*, 8694. (b) AlDamen, M. A.; Clemente-Juan, J. M.; Coronado, E.; Martí-Gastaldo, C.; Gaita-Ariño, A. *J. Am. Chem. Soc.*, **2008**, *130*, 8874. (c) Jiang, S.-D.; Wang, B.-W.; Sun, H.-L.; Wang, Z.-M.; Gao, S. *J. Am. Chem. Soc.* **2011**, *133*, 4730. (d) Baldoví, J. J.; Borrás-Almenar, J. J.; Clemente-Juan, J. M.; Coronado, E.; Gaita-Ariño, A. *Dalton Trans.* **2012**, *41*, 13705. (e) Chilton, N. F.; Langley, S. K.; Moubaraki, B.; Soncini, A.; Batten, S. R.; Murray, K. S. *Chem. Sci.* **2013**, *4*, 1719. (f) Woodruff, D. N.; Winpenny, R. E.; Layfield, R. A. *Chem. Rev.* **2013**, *113*, 5110.
- (2) Blagg, R. J.; Ungur, L.; Tuna, F.; Speak, J.; Comar, P.; Collison, D.; Wernsdorfer, W.; McInnes, E. J. L.; Chibotaru, L. F.; Winpenny, R. E. *P. Nat. Chem.* **2013**, *5*, 673.
- (3) Sessoli, R.; Powell, A. K. *Coord. Chem. Rev.* **2009**, *253*, 2328.
- (4) Demir, S.; Zadrozny, J. M.; Nippe, M.; Long, J. R. *J. Am. Chem. Soc.* **2012**, *134*, 18546.
- (5) (a) Rinehart, J. D.; Fang, M.; Evans, W. J.; Long, J. R. *Nat. Chem.* **2011**, *3*, 538. (b) Rinehart, J. D.; Fang, M.; Evans, W. J.; Long, J. R. *J. Am. Chem. Soc.* **2011**, *133*, 14236.
- (6) Rajeshkumar, T.; Rajaraman, G. *Chem. Comm.* **2012**, *48*, 7856.
- (7) Meihaus, K. R.; Corbey, J. F.; Fang, M.; Ziller, J.W.; Long, J.R.; Evans, W. J. *Inorg. Chem.* **2014**, *53*, 3099.
- (8) Fang, M.; Bates, J. E.; Lorenz, S. E.; Lee, D. S.; Rego, D. B.; Ziller, J. W.; Furche, F.; Evans, W. *Inorg. Chem.* **2011**, *50*, 1459.
- (9) Gatteschi, D.; Sessoli, R.; Villain, J. *Molecular Nanomagnets*, Oxford University Press, Oxford, **2006**.
- (10) Evans, W. J.; Fang, M.; Zucchi, G.; Furche, F.; Ziller, J. W.; Hoekstra, R. M.; Zink, J. I. *J. Am. Chem. Soc.* **2009**, *131*, 11195.
- (11) (a) Evans, W. J.; Zucchi, G.; Ziller, J. W. *J. Am. Chem. Soc.* **2003**, *125*, 10. (b) Evans, W. J.; Lee, D. S.; Rego, D. B.; Perotti, J. M.; Kozimor, S. A.; Moore, E. K.; Ziller, J. W. *J. Am. Chem. Soc.* **2004**, *126*, 14574.
- (12) Milios, C. J.; Gass, I. A.; Vinslava, A.; Budd, L.; Parsons, S.; Wernsdorfer, W.; Perlepes, S. P.; Christou, G.; Brechin, E. K. *Inorg. Chem.* **2007**, *46*, 6215.
- (13) Kahn, O. *Molecular Magnetism*, VCH Publishers, Inc.: New York, **1993**.
- (14) Benelli, C.; Gatteschi, D. *Chem. Rev.* **2002**, *102*, 2369.
- (15) Dei, A.; Gatteschi, D.; Massa, C. A.; Pardi, L. A.; Poussereau, S.; Sorace, L. *Chem. Eur. J.* **2000**, *6*, 4580.
- (16) (a) Chandrasekhar, V.; Bag, P.; Speldrich, M.; van Leusen, J.; Kögerler, P. *Inorg. Chem.* **2013**, *52*, 5035. (b) Long, J.; Habib, F.; Lin, P.-H.; Korobkov, I.; Enright, G.; Ungur, L.; Wernsdorfer, W.; Chibotaru, L. F.; Murugesu, M. *J. Am. Chem. Soc.* **2011**, *133*, 5319.
- (17) Cañadillas-Delgado, L.; Fabelo, O.; Pasán, J.; Delgado, F. S.; Lloret, F.; Julve, M.; Ruiz-Pérez, C. *Dalton Trans.* **2010**, *39*, 7286.

- (18) (a) Benelli, C.; Caneschi, A.; Gatteschi, D.; Pardi, L.; Rey, P.; Shum, D. P.; Carlin, R. L. *Inorg. Chem.* **1989**, *28*, 272. (b) Benelli, C.; Caneschi, A.; Gatteschi, D.; Pardi, L.; Rey, P. *Inorg. Chem.* **1989**, *28*, 275. (c) Benelli, C.; Caneschi, A.; Gatteschi, D.; Pardi, L.; Rey, P. *Inorg. Chem.* **1990**, *29*, 4223. (d) Benelli, C.; Caneschi, A.; Gatteschi, D.; Pardi, L. *Inorg. Chem.* **1992**, *31*, 741. (e) Benelli, C.; Caneschi, A.; Gatteschi, D.; Sessoli, R. *Inorg. Chem.* **1993**, *32*, 4797. (f) Benelli, C.; Gatteschi, D.; Sessoli, S.; Rettori, A.; Pini, M. G.; Bartolomé, F.; Bartolomé, J. *J. Magn. Magn. Mat.* **1995**, *140-144*, 1649.
- (19) Venugopal, A.; Tuna, F.; Spaniol, T. P.; Ungur, L.; Chibotaru, L. F.; Okuda, J.; Layfield, R. A. *Chem. Comm.* **2013**, *49*, 901.
- (20) Orbach, R. *Proc. R. Soc. Lond. A* **1961**, *264*, 458.
- (21) Gatteschi, D.; Sessoli, R. *Angew. Chem., Int. Ed.* **2003**, *42*, 268.
- (22) del Barco, E.; Kent, A. D.; Hill, S.; North, J. M.; Dalal, N. S.; Rumberger, E. M.; Hendrickson, D. N.; Chakov, N.; Christou, G. *J. Low Temp. Phys.* **2005**, *140*, 119.
- (23) For illustration, ac frequency scans were collected at 2.8 K and fields ranging from 2700-3750 Oe (spanning the sharpest magnetization drop in the hysteresis at this temperature). These scans reveal ac peaks between 3 and 5 Hz and corresponding relaxation times with very minimal field dependence (see Figure S13). The relaxation time decreases gradually upon traversing the fields where the drop in magnetization occurs, as might be expected for the occurrence of tunneling.
- (24) Lukens, W. W.; Walter, M. D. *Inorg. Chem.* **2010**, *49*, 4458.

Chapter 5 Appendix

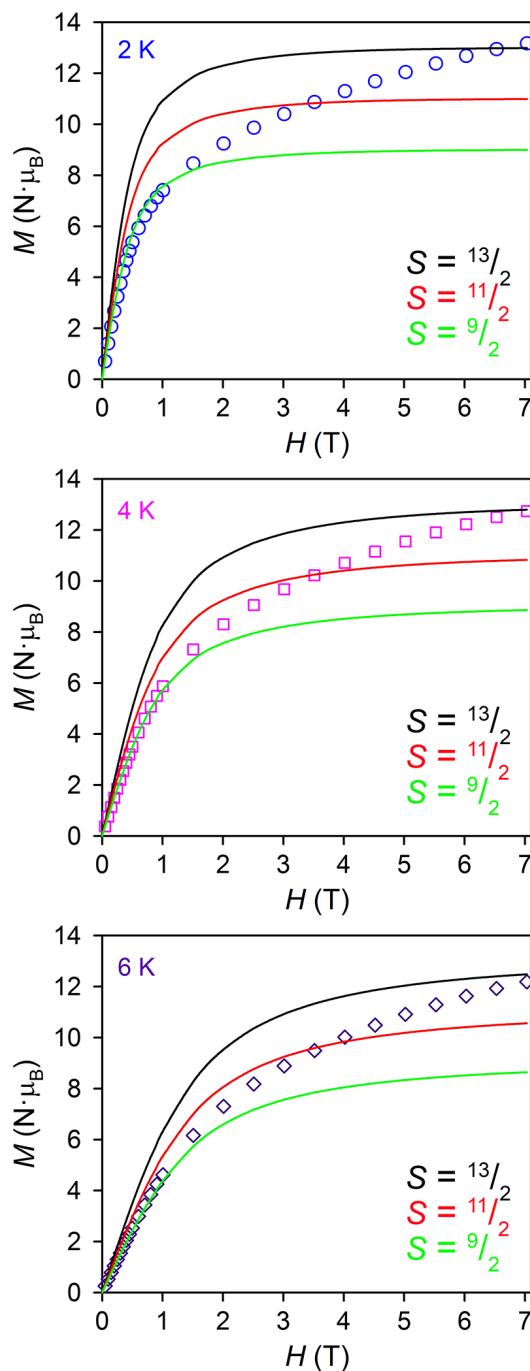


Figure 5.A1. Plot of $M(H)$ for $\{[(\text{Me}_3\text{Si})_2\text{N})_2\text{Gd}(\text{THF})]_2(\mu\text{-N}_2)\text{K}\}$ at 2 K (top, blue circles), 4 K (middle, pink squares), and 6 K (bottom, purple diamonds). Solid black, red, and lime green curves represented the calculated Brillouin functions for $S = 13/2$, $S = 11/2$, and $S = 9/2$, respectively. The low field portion of the $M(H)$ curve at each temperature follows that of the $S = 9/2$ Brillouin function, until it diverges between 1 and 1.5 T, suggesting a level crossing between the closely-spaced $S = 9/2$ and $S = 11/2$ lowest energy levels. At high fields, $M(H)$ approaches the $S = 13/2$ Brillouin function.

Table 5.A1. Spin manifolds and energy levels for $\{[(\text{Me}_3\text{Si})_2\text{N})_2\text{Gd}(\text{THF})_2(\mu\text{-N}_2)]^-\}$ and $\{[(\text{Me}_3\text{Si})_2\text{N})_2\text{Gd}(\text{THF})_2(\mu\text{-N}_2)\text{K}]\}$ highlighting the drastic change in magnetic ground state that occurs with the introduction of competing antiferromagnetic exchange between Gd^{III} centers.

$\{[(\text{Me}_3\text{Si})_2\text{N})_2\text{Gd}(\text{THF})_2(\mu\text{-N}_2)]^-\}$		$\{[(\text{Me}_3\text{Si})_2\text{N})_2\text{Gd}(\text{THF})_2(\mu\text{-N}_2)\text{K}]\}$	
S	E (cm ⁻¹)	S	E (cm ⁻¹)
$13/2$	-188.55	$9/2$	-74.347
$11/2$	-162.54	$11/2$	-74.052
$9/2$	-136.54	$7/2$	-70.042
$7/2$	-110.53	$13/2$	-69.157
$5/2$	-84.523	$5/2$	-61.138
$3/2$	-58.516	$3/2$	-47.634
$1/2$	-32.509	$1/2$	-29.53
$1/2$	19.5053	$1/2$	20.4777
$3/2$	45.5124	$3/2$	52.3811
$5/2$	71.5194	$5/2$	88.8842
$7/2$	97.5265	$7/2$	129.987
$9/2$	123.534	$9/2$	175.69
$11/2$	149.541	$11/2$	225.992
$13/2$	175.548	$13/2$	280.895
$15/2$	201.555	$15/2$	340.397

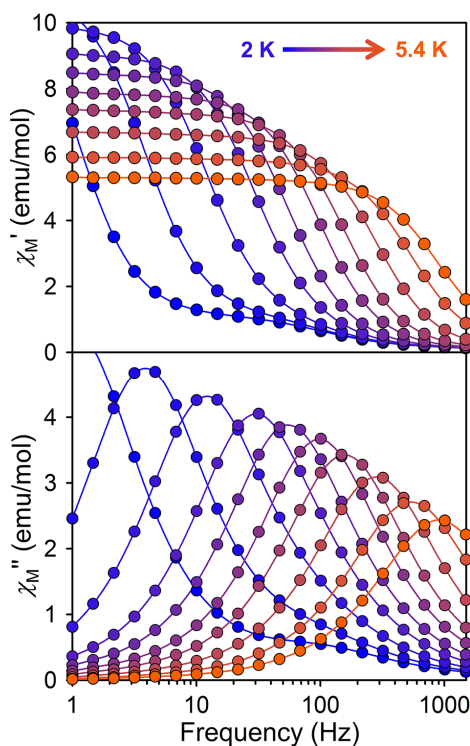


Figure 5.A2. Plot of the molar in-phase (χ_M') and out-of-phase (χ_M'') magnetic susceptibility versus frequency of the oscillating field for $\{[(\text{Me}_3\text{Si})_2\text{N})_2\text{Dy}(\text{THF})_2(\mu\text{-N}_2)\text{K}]\}$ over the temperature range 2-5.4 K and frequencies between 1 and 1500 Hz under zero-applied dc field.

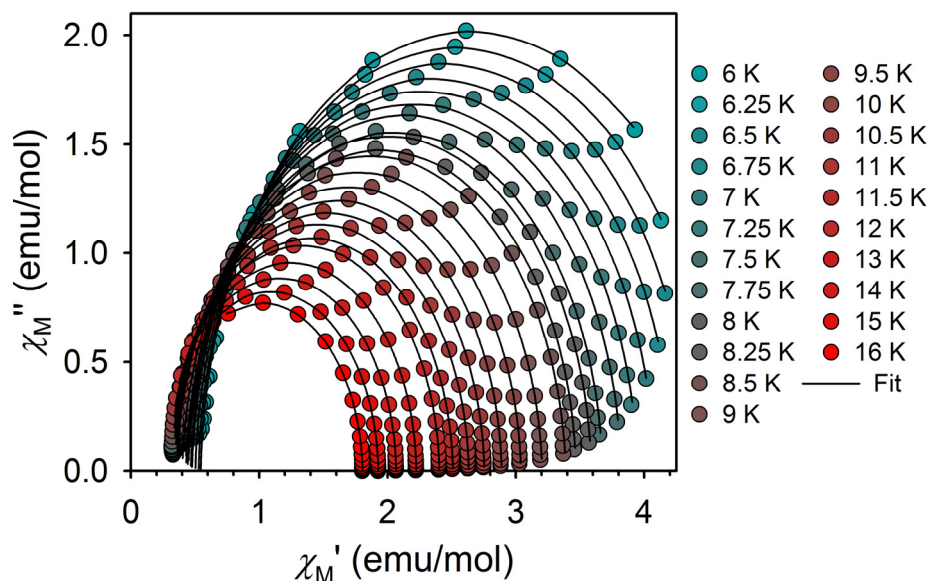


Figure 5.A3. Cole-Cole (Argand) plots for $\{[(\text{Me}_3\text{Si})_2\text{N})_2\text{Tb}(\text{THF})]_2(\mu\text{-N}_2)\text{K}\}$ under zero applied dc field and varying temperatures. Experimental data points are represented by colored circles and the points representing the fit are connected by a solid black line.

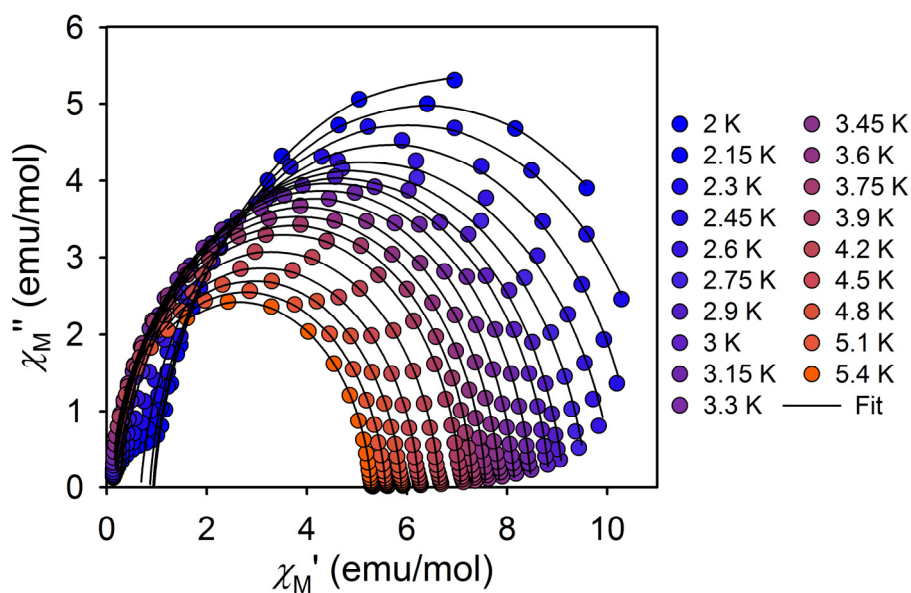


Figure 5.A4. Cole-Cole (Argand) plots for $\{[(\text{Me}_3\text{Si})_2\text{N})_2\text{Dy}(\text{THF})]_2(\mu\text{-N}_2)\text{K}\}$ under zero applied dc field and varying temperatures. Experimental data points are represented by colored circles and the points representing the fit are connected by a solid black line.

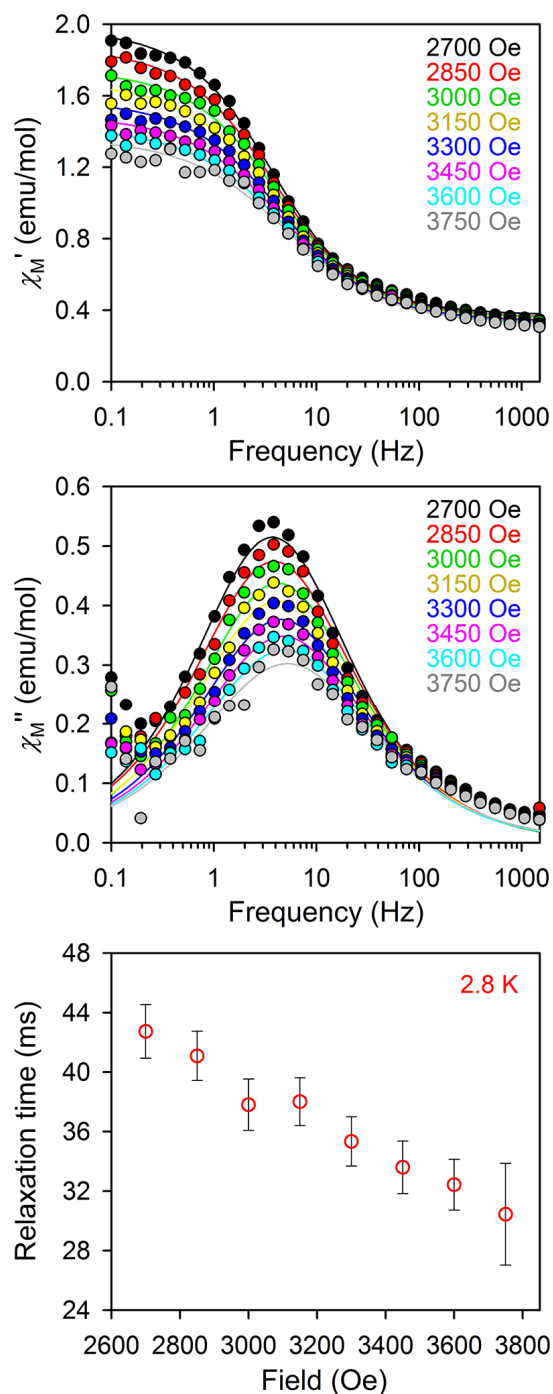


Figure 5.A5. (Top) Molar in-phase (χ_M') and out-of-phase (χ_M'') variable-field magnetic susceptibility versus frequency for $\{[(\text{Me}_3\text{Si})_2\text{N})_2\text{Tb}(\text{THF})_2(\mu\text{-N}_2)\text{K}]\}$, at an illustrative temperature of 2.8 K. (Bottom) Relaxation time versus applied field at 2.8 K. Fields were chosen to span regions prior to, in the middle of, and after the drop in the magnetic hysteresis at this temperature. The corresponding ac signal and relaxation times demonstrate very weak field dependence, while the relaxation time decreases concurrent with the magnetization drop, suggestive of tunneling.